Experimental assessment of enhanced benthic weathering of calcite and dunite in the south western Baltic Sea

Dissertation

zur Erlangung des Doktorgrades

der Mathematisch-Naturwissenschaftlichen Fakultät der Christian-Albrechts-Universität zu Kiel

vorgelegt von

Michael Fuhr

Kiel, 2024

Erster Gutachter: Prof. Dr. Klaus Wallmann
Zweiter Gutachter: Priv.-Doz. Dr. Mark Schmidt

Eingereicht: 21.05.2024
Tag der Disputation: 12.07.2024
Zum Druck freigegeben: 12.07.2024

Ort, Datum, Das Dekanat

Für Omma

Satius est supervacua scire quam nihil!

Erklärung

Hiermit erkläre ich an Eides statt, dass die beigefügte Arbeit, abgesehen von der Beratung durch meine Betreuer und die Zuhilfenahme der angegebenen Mittel, nach Inhalt und Form selbständig verfasst wurde. Ich versichere, dass ich die beigefügte Arbeit ausschließlich in diesem und keinem anderen Promotionsverfahren vorgelegt habe. Diesem Promotionsverfahren ist kein gescheitertes Promotionsverfahren vorausgegangen und mir ist noch kein akademischer Grad entzogen worden. Die Arbeit ist im Rahmen der Regeln guter wissenschaftlicher Praxis der Deutschen Forschungsgemeinschaft entstanden.

Teile dieser Arbeit sind bereits in einer Fachzeitschrift veröffentlicht, oder wurden zur Veröffentlichung eingereicht.

Kiel,_____

Michael Fuhr

Deus non facit differentiam inter simplicem loquelam et iuramentum!

Table of Contents

Abstract

Over the last 120 years, a steady increase in atmospheric CO_2 and an associated increase in mean global surface temperatures has amplified the need to not only reduce CO_2 emissions but also to establish negative emission technologies (NET) in order to limit global warming. This thesis delves into the potential of enhanced benthic weathering (EBW), which has amongst other NETs been proposed as a viable strategy for carbon dioxide removal (CDR) in the Baltic Sea. A series of three laboratory experiments and a long-term benthocosm study were therefore carried out to shed light on the dissolution behavior of various potentially usable alkaline minerals, under controlled and quasi-natural conditions.

Initially, experiments focused on the dissolution kinetics of olivine contained in ultramafic sand (UMS), in artificial seawater, revealing intriguing patterns of total alkalinity (TA) decline attributed to the precipitation of several secondary minerals in the form of calcium carbonate, phyllosilicates and iron hydroxide. These unexpected findings highlighted the complex interplay between mineral dissolution and secondary phase formation, challenging conventional assumptions about TA production solely from mineral dissolution. Furthermore, they underpinned the idea of EBW on organic rich sediments, where metabolically formed CO_2 might inhibit secondary mineral precipitation. In light of these findings, biogeochemical processes within surface sediments were explored in the framework of an incubation experiment under oxygenated conditions to understand alkaline mineral dissolution in natural sediment from Boknis Eck (Baltic Sea, Germany). Microbial activity emerged as a key driver of enhanced weathering, with distinct microbial communities impacting pH dynamics and mineral dissolution rates. In contrast, experiments simulating late summer conditions characterized by hypoxia to anoxia showed that corrosive bottom waters with respect to calcite are the ultimate driver for dissolution kinetics. Calcite and dunite exhibited elevated dissolution rates, compared to the oxygenated experiment, indicating the potential for enhanced CO_2 uptake and alkalinity release during anoxic phases. Quantitative assessment of dissolution kinetics yielded first-order rate constants consistent with literature values, supporting their applicability in EBW modeling efforts. During a long-term benthocosm experiment, mineral dissolution rates closely followed temperature as long as bottom waters were oxygenated. This, combined with the fact that the temperature sensitivity was stronger than reported for laboratory experiments in the absence of biota, substantiates the principle function of the benthic weathering engine in the investigated sediments. A modelling approach assessing the efficiency of EBW in a potential application area in Eckernförde Bay and subsequent economic analysis underscored the cost-effectiveness of calcite as a preferred material for EBW, offering promising prospects for marine CDR implementation in coastal environments in the Baltic Sea.

Overall, the findings of this thesis provide valuable insights into the feasibility and efficiency of EBW as a practical approach for climate change mitigation in Baltic Sea sediments and, potential, to fine-grained coastal sediments in general. By elucidating the underlying mechanisms driving mineral dissolution and assessing economic viability, the results described here further augment the perception of EBW as a CDR method and inform future modeling and implementation efforts.

Zusammenfassung

In den letzten 70 Jahren hat ein kontinuierlicher Anstieg von atmosphärischem CO_2 und eine damit verbundene Zunahme der mittleren globalen Oberflächentemperaturen die Notwendigkeit verstärkt, nicht nur Emissionen zu reduzieren, sondern auch negative Emissionstechnologien (NET) zu etablieren, um die globale Erwärmung zu begrenzen. Diese Arbeit untersucht das Potenzial der verstärkten benthischen Verwitterung (VBV), die neben anderen NETs als eine mögliche Strategie zur Entfernung von Kohlendioxid (EKD) in der Ostsee vorgeschlagen wurde. Eine Reihe von drei Laborversuchen und eine langfristige Benthokosmos-Studie wurden daher durchgeführt, um das Lösungsverhalten verschiedener potenziell verwendbarer alkalischer Minerale unter kontrollierten und quasi-natürlichen Bedingungen zu beleuchten. Zunächst konzentrierten sich die Experimente auf die Lösungskinetik von Olivin, der in ultramafischem Sand (UMS) enthalten ist, in künstlichem Meerwasser, wobei interessante Muster des Gesamtalkalität (TA)-Rückgangs auf die Ausfällung mehrerer Sekundärminerale in Form von Calciumcarbonat, Phyllosilikaten und Eisenhydroxid hinwiesen. Diese unerwarteten Ergebnisse betonten das komplexe Zusammenspiel zwischen Mineralauflösung und Bildung sekundärer Phasen und revidierten herkömmliche Annahmen über die TA-Produktion aus Mineralauflösung. Darüber hinaus untermauerten sie die Idee der VBV in organisch reichen Sedimenten, wo metabolisch gebildetes CO_2 die Ausfällung sekundärer Minerale hemmen könnte. Daraufhin wurden biogeochemische Prozesse in Oberflächensedimenten im Rahmen eines Inkubationsexperiments unter oxischen Bedingungen erforscht, um ihren Einfluss auf die Auflösung alkalischer Minerale zu verstehen. Mikrobielle Aktivität erwies sich als treibende Kraft für eine verstärkte Verwitterung, wobei unterschiedliche mikrobielle Gemeinschaften pH-Dynamik und Lösungsraten der Minerale beeinflussten. Im Gegensatz dazu zeigten Experimente, die spätsommerliche Bedingungen in der Ostsee simulierten, gekennzeichnet durch Hypoxie bis Anoxie und korrosive Bodenwasserchemie, dass letztere der ultimative Treiber für die Lösungskinetik ist. Calcit und Dunit wiesen erhöhte Lösungsraten im Vergleich zum sauerstoffhaltigen Experiment auf, was auf das Potenzial für eine verstärkte CO_2-Aufnahme und Alkalinitätsfreisetzung während anoxischer Phasen hindeutet. Eine quantitative Bewertung der Lösungskinetik ergab Konstanten erster Ordnung, die mit Literaturwerten übereinstimmen und ihre Anwendbarkeit in der VBV-Modellierung unterstützen. Während des langfristigen Benthokosmos-Experiments folgten die Lösungsraten der Temperatur, solange das Bodenwasser sauerstoffhaltig war. In Kombination mit der Tatsache, dass die Temperatursensitivität stärker war als in Laborversuchen ohne Biota, untermauert dies die prinzipielle Funktion des „benthischen Verwitterungsmotors“ in den untersuchten Sedimenten. Ein Modellierungsansatz zur Bewertung der Effizienz von VBV in einem potenziellen Anwendungsgebiet in der Eckernförder Bucht und anschließende ökonomische Analysen unterstrichen die Kosteneffizienz von Calcit als bevorzugtem Material für VBV und bieten vielversprechende Aussichten für die Implementierung von EKD in marinen Umgebungen. Insgesamt liefern die Ergebnisse dieser Arbeit wertvolle Einblicke in die Durchführbarkeit und Effizienz von VBV als praktischem Ansatz zur Minderung des Klimawandels in Ostseesedimenten und ähnlichen Küstenumgebungen. Durch die Aufklärung der zugrunde liegenden Mechanismen der Mineralauflösung und die Bewertung der wirtschaftlichen Tragfähigkeit tragen sie darüber hinaus zum Verständnis von VBV als EKD-Methode bei und unterstützen zukünftige Modellierungs- und Umsetzungsprojekte.

I. Introduction

I.1. Theoretical background and state-of-the-art

I.1.1. Climate change and negative emission technologies

Over the past 120 years, mean global surface temperatures have steadily increased along with increasing CO_2 concentrations in the atmosphere (Hansen et al., 2010; Howe, 2015; Keeling et al., 2001; MacFarling Meure et al., 2006; Petit et al., 1999; Valipour et al., 2021). The first observations of a causal link between these two variables was first established in 1896 (Arrhenius, 1896). CO_2 has by now been identified as a major driver for the 'anthropogenic greenhouse effect' (Krupa and Kickert, 1989; Lindzen, 2007; Solomon et al., 2009). The term describes the portion of global warming that is not caused by natural variability, but by human activity (Wigley and Raper, 1990). Due to the severe consequences of the observed temperature increase (Hansen and Stone, 2016; Magnan et al., 2021), a 1.5 °C goal was declared during the 2015 Paris Climate Change Conference COP21. This goal can only be reached if zero net emissions of CO_2 are attained between 2030-2050 (Rhodes, 2016). Thus, in addition to a drastic reduction of emissions, it is necessary to actively sequester CO_2 from the atmosphere in form of negative emissions (Friedlingstein et al., 2011; IPCC, 2018) to remove past CO_2 contributions, but also to out-balance future emissions that are difficult to abate, for instance from shipping and aviation. A significant number of studies have aimed to evaluate different strategies to achieve these negative emissions via carbon dioxide removal (CDR) (Campbell et al., 2022; Feng et al., 2017; Fuss et al., 2018; Iizuka et al., 2004; Lackner, 2003; Lal, 2004; Saran et al., 2017) and implemented them in integrated assessment models (IAMs) (Azar et al., 2006; Kriegler et al., 2014, 2013; van Vuuren et al., 2007). The techno-economical focus of these IAMs clarifies that negative emission technologies (NETs) do not only have to fulfill the requirement to reduce atmospheric CO_2 but also need to be economically feasible and competitive on a growing negative emission market (Carton et al., 2020). To assess these extended requirements, it is necessary to identify the target residual emissions that a certain method is capable to reduce. These target residual emissions can be categorized as point-sourced and non-point-sourced (Buck et al., 2023; Feng et al., 2023; Luderer et al., 2018; Woodard et al., 2014). For point-sources, carbon capture and storage (CCS) has been identified as a techno-economically feasible technology, where emitted CO_2 is captured directly at the source, liquified and stored in underground geological formations (Anderson and Newell, 2004; Budinis et al., 2018; Leeson et al., 2017). Alternatively, reactor based solutions have been proposed, where CO_2 is neutralized via carbonization (Santos et al., 2013). These methods, however, cannot address non-point-sourced emissions as they rely on already purified CO_2. To tackle these diffuse emissions, it is hence necessary to either extract CO_2 from the atmosphere or create a sink for atmospheric CO_2.

One proposed NET to achieve the former is direct air capture and carbon storage (DACCS). This process extracts CO_2 from the air either physically via membranes, or chemically, e.g. by carbonizing and decarbonizing quicklime or adsorption on suitable resins (Ignatusha et al., 2024; Okesola et al., 2018). Yet, these technologies are rather energy-intensive and costly (Fuss et al., 2018). The expansion of natural sinks for CO_2 has therefore gained attention as these methods rely on processes that in principle take place without human assistance, which is why the only energy demand would be the enhancement of the existing sink, rather than the process itself. The biosphere has been identified as a major sink for atmospheric CO_2 (Taylor and Lloyd, 1992). Hence, afforestation has been proposed as a possible measure to mitigate climate change with the co-benefit of restoring valuable ecosystems (Zomer et al., 2008). For this approach, spatial

limitations may lead to conflicts in land use and compromise the overall uptake potential (Doelman et al., 2020). Furthermore, the storage time of CO_2 in biomass is relatively short and the effect of these measures therefore short-lived (Kemena et al., 2018). A more promising idea is increasing the biomass stored in the ocean, e.g via iron fertilization, where addition of the micro nutrient Fe^{2+} added to Fe-limited waters fosters phytoplankton blooms and thus CO_2 sequestration from the atmosphere (Martin et al., 1990). Critical analysis of this idea, though, has revealed that CO_2 leakage, deoxygenation and increased ocean acidification may be adverse side effects (Oschlies et al., 2010). These have also been identified as possible negative impacts of artificial upwelling that aims to foster primary production in the surface waters by transporting nutrient rich deep water to the surface via wave-driven pumps.

On geological timescales, a major driver for atmospheric CO_2 levels is terrestrial rock weathering (Chenot et al., 2018; Cox et al., 2016). Boosting natural weathering has thus been proposed as a possible CDR method. The potential of enhanced weathering (EW) to serve as a cheap and effective way to support climate mitigation has been subject to a vast amount of studies (Amann et al., 2020; Harrington et al., 2023; Hartmann and Kempe, 2008; Minx et al., 2018; Renforth, 2012; Renforth et al., 2015; Renforth and Henderson, 2017; Strefler et al., 2018 and cited therein). The idea was initially raised by Schuiling and Krijgsman (2006), who suggested enhanced weathering of olivine on land as a possibly cheap and effective way to reduce atmospheric CO_2.

The theoretical approach is that the process produces dissolved cations which are ultimately transported to the ocean and thus contribute to ocean alkalinity (Dickson, 1981; Wolf-Gladrow et al., 2007). Ultimately, EW is therefore one way to achieve CO_2 uptake via ocean alkalinity enhancement (OAE) as originally proposed by Kheshgi (1995).

1.1.1. CO_2 in the ocean: The carbonate system and alkalinity

Based on the solubility of ideal gases in water (Bohr, 1899), the ocean has long been known to be in chemical equilibrium with the atmosphere and therefore constitutes a sink for CO_2 added to the atmosphere by the consumption of fossil fuels (Revelle and Suess, 1957). In the aqueous phase, CO_2 reacts with water to form carbonic acid which subsequently dissociates as described by e.g. Kanwisher (1960) in three steps, following:

$$CO_2 + H_2O \leftrightarrow H_2CO_3 \quad (1)$$

$$H_2CO_3 \leftrightarrow H^+ + HCO_3^- \quad (2)$$

$$HCO_3^- \leftrightarrow H^+ + CO_3^{2-} \quad (3)$$

As inferable from the involvement of protons (H^+), these reactions are pH sensitive and at the same time buffer the sea water to pH values where bicarbonate (HCO_3^-) is the prevailing species. The relatively low CO_2 concentrations in the atmosphere lead to an average surface pH of 8.1 in sea water (Zeebe and Wolf-Gladrow, 2001a). Equations 1 – 3 also imply that the amount of CO_2 that can be dissolved in sea water is dependent on the proton activity, which again is driven by the activity of proton acceptors. This activity of

proton acceptors has been described as alkalinity by Rakestraw (1949), and later been redefined by Dickson (1981) as total alkalinity (TA) following:

$$TA = HCO_3^- + 2CO_3^{2-} + OH^- + B(OH)_4^- + HPO_4^{2-} + 2PO_4^{3-} + H_3SiO_4^- + 2H_2SiO_4^{2-} + NH_3 + HS^- + 2S^{2-} - H^+ - HF - HSO_4^- - 2H_2SO_4 - H_3PO_4 - HNO_2 - HNO_3 \quad (4)$$

This definition clarifies that in sum, reactions 1 – 3 do not change alkalinity. That also implies that an increase of alkalinity will lead to a chemical imbalance of these reactions, and the subsequent outbalancing will cause an uptake of CO_2 and subsequent conversion to HCO_3^-.

I.1.1. Ocean alkalinity enhancement and enhanced benthic weathering

OAE can be separated into two major groups: liquid-based and solid-based (Eisaman et al., 2023). For liquid-based solutions, the primary sources are either brines or minerals that have been dissolved in reactors (Caserini et al., 2021a; Eisaman et al., 2023; Rau et al., 2007; Rau and Caldeira, 1999). In both cases, the actual production of alkalinity consumes energy which either produces CO_2 directly or indirectly, as long as the energy mix is not entirely based on renewables. This excess CO_2 then either diminishes the efficiency or needs to be stored via CCS (if point-sourced). A further problematic aspect of liquid-based alkalization is the actual insertion into the ocean. Most commonly discussed options for this step are either distribution with ships, which could also be used to carry the reactor itself, or pipelines that disperse the alkalized liquid in the near-shore ocean (Caserini et al., 2021b; Eisaman et al., 2023). Either way, the formation of carbonate nuclei can lead to a 'runaway precipitation' of aragonite (Moras et al., 2022) in the reservoir in the direct proximity of the outlet either of the ship or the pipeline, which would diminish uptake efficiency, or in the worst case lead to an actual production of CO_2. To avoid this, the amount of alkalinity that is added and the dilution below critical TA concentrations must be well-constrained (Hartmann et al., 2023).

The materials used for solid-based solutions for OAE, again, can be divided into two groups: highly-reactive and low-reactive. Highly reactive materials such as lime (CaO), portlandite ($Ca(OH)_2$), periclase (MgO), however, do not occur naturally and thus need to be produced artificially, which again lowers the overall efficiency (Renforth and Henderson, 2017). Additionally, the precipitation of aragonite in the diffusive boundary layer around the grain, where very high oversaturation with respect to aragonite can occur, can lead to similar release of CO_2 as described for liquid based point sources of alkalinity (Bach et al., 2019; Moras et al., 2022). Using slower dissolving materials such as olivine, calcite would avoid these problems.

The dissolution reaction of these minerals can be described as:

Forsterite: $$Mg_2SiO_4 + 4H_2O + 4CO_2(aq) \rightarrow 2Mg^{2+} + H_4SiO_4 + 4HCO_3^- \quad (5)$$

Calcite: $$CaCO_3 + H_2O + CO_2(aq) \rightarrow Ca^{2+} + 2HCO_3^- \quad (6)$$

Where Forsterite is the magnesium rich endmember of the olivine mixing row.

Due to the lower reactivity, however, these materials would need to be ground to very small grainsizes to achieve the desired alkalization in the water column (Foteinis et al., 2023; Hangx and Spiers, 2009; Köhler et al., 2013; Strefler et al., 2018). For calcite, the bigger problem is that the surface oceans are oversaturated with respect to calcite, which means that it would not dissolve at all when added (Feely et al., 2023). This implies that these materials will eventually sink to the sea floor and, depending on the chemical conditions, dissolve in the sediment (Figure I 1). This idea of enhanced benthic weathering (EBW) has been promoted as a potentially effective way to achieve OAE as the "benthic weathering engine", a mix of micro- and macrofaunal activity, combined with oxidation processes, is supposed to foster the dissolution of added minerals (Meysman and Montserrat, 2017). The conceptual idea is that, firstly, larger invertebrates mix the sediment and by doing so pass mud – and likewise added minerals – through their guts several times a year (Meysman and Montserrat, 2017). These gut transits with high enzyme activity and additional abrasion then lead to enhanced dissolution of olivine, as the kinetics of the process increase with lower pH values (Rimstidt et al., 2012). Secondly, in surface sediments, organic matter is respired to CO_2, which lowers the pH (equations 1,3), fostering dissolution. Thirdly, the oxidation of sulfide (H_2S) via long distance electron transport has the potential to lower the pore water pH down to values of ~5 (Meysman et al., 2015), which is much lower than usually observed in organic rich sediments (Preisler et al., 2007). These low pH values not only fuel olivine dissolution, but also lead to undersaturation with respect to calcite and allow for its dissolution, even if overlaying bottom waters are oversaturated. Thus, the potential for intra-sedimentary weathering might be very high not only for olivine, but also for calcite. Despite the fact that 'metabolic calcite dissolution' driven by CO_2 respired from organic carbon is well established (Rao et al., 2012), to date, calcite has not gained much attention as a potential material for EBW.

I.1.1. EBW research, gaps in knowledge and scope of this thesis

Dedicated studies investigating EBW are scarce. Since Meysman and Montserrat (2017) suggested the concept and deepened their efforts in one follow-up study (Montserrat et al., 2017), only a few studies have investigated the possible effect of alkaline mineral addition to marine sediments (Bice et al., 2024). Still, there are several studies that tried to assess the potential, the efficiency and cost for coastal weathering, which, according to Meysman and Montserrat (2017), is largely comparable to EBW (Eisaman et al., 2023; Feng et al., 2017; Foteinis et al., 2023; Hangx and Spiers, 2009; Kanzaki et al., 2023; Tan et al., 2022; Wang et al., 2023). A major problem inherent with these studies is that they mainly rely on assumptions when it comes to the precise dissolution kinetics of the different minerals under in-situ conditions. For olivine, the dissolution kinetics in seawater have been investigated in only a handful of studies (Montserrat et al., 2017; Rigopoulos et al., 2018), which report different results for the precise weathering mechanism and possible side-effects under different conditions. This implies that a better understanding of dissolution kinetics of olivine in seawater is indispensable for further investigations towards EBW. For calcite, the situation is different due to its importance for ocean biogeochemistry. The dissolution kinetics have been well described under different saturation states and different temperatures (Naviaux et al., 2019a, 2019b). Still, these studies are based on laboratory experiments under conditions that are largely different compared to those prevailing during EBW. Porewater chemistry differs from idealized sea water, organic compounds could inhibit or foster dissolution, the grains on and in the sediment are exposed to the 'benthic weathering engine' and thus to low pH values and unknown interference with macro- and microbiological activity. These factors raise the question whether the current knowledge base is sufficient to allow for accurate estimates on the efficiency and economic feasibility of EBW. The aim of this thesis is to shed light on these unknowns and to clarify how (i) olivine (the major component of dunite) dissolves when exposed to

seawater, (ii) calcite and dunite react on and in organic rich sediments under controlled redox conditions, and (iii) these materials dissolve over the course of a year in a long-term experiment. Based on these new insights, this study further aims to assess the potential, the efficiency and the cost of enhanced benthic weathering using dunite and calcite.

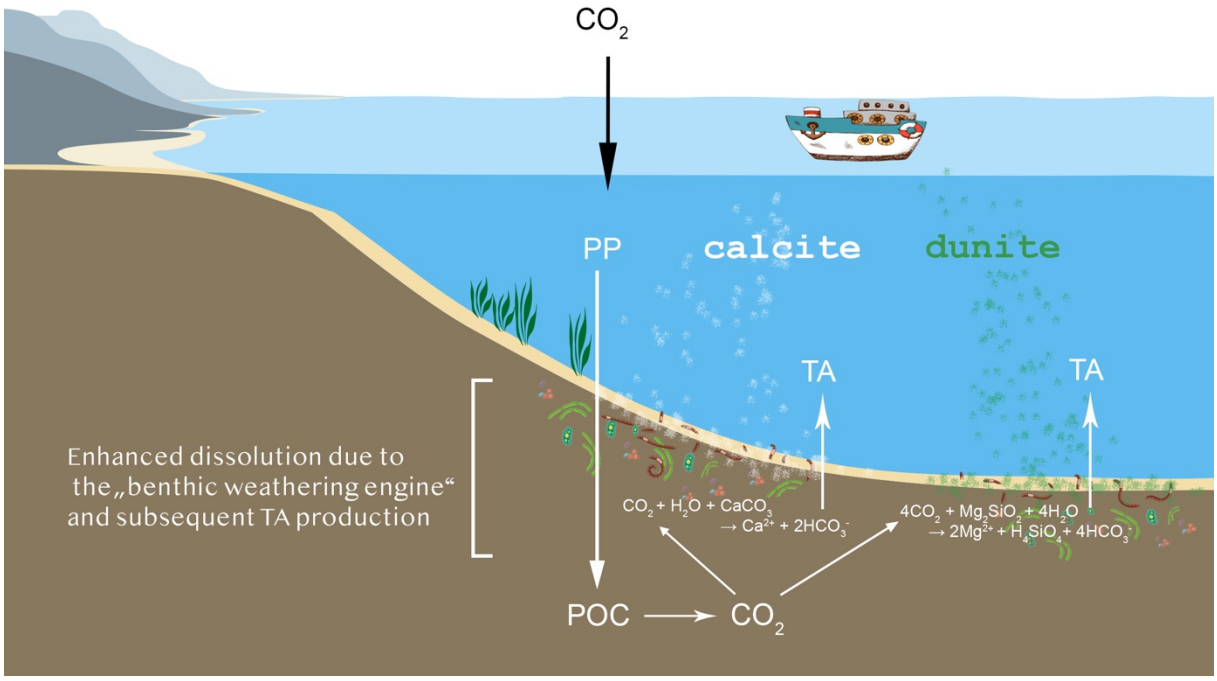

Figure I 1: Principle function of EBW: Primary production (PP) binds CO_2 in form of particulate organic carbon (POC), which is subsequently remineralized to metabolic CO_2 in the sediment. There, the CO_2 combined with the activity of the benthic weathering engine leads to the dissolution of alkaline materials (calcite and dunite).

I.2. Study area

In order to conduct the different experiments, sediments were retrieved from a shallow basin in the Eckernförde Bay in the south western Baltic Sea. The Baltic Sea features several unusual geochemical properties. The limited water exchange via the Danish Straits in combination with low evaporation and high freshwater input leads to a lateral salinity gradient that stretches from ~3 in the Gulf of Finland to ~18 in the Danish Straits, with the strongest gradient between the Danish Straits and the Arkona Sea (Feistel et al., 2010; Lass and Matthäus, 2008). Additionally, the Baltic Proper features a vertical salinity gradient that ultimately derives from the water exchange mechanism with the adjacent North Sea via the Kattegat and Skagerrak. This exchange predominantly occurs via outflow of fresher water at the surface and intrusion of saltier North Sea water at greater depths (Feistel et al., 2006; Lass and Matthäus, 2008; Schmidt et al., 1998, Figure 2). This leads to a strong stratification as dense inflowing waters accumulate in the deeper basins, creating a density gradient that inhibits mixing with overlaying waters and thus the ventilation of bottom waters, which fosters hypoxia and anoxia in deeper basins (Mohrholz et al., 2015). This anoxia is additionally increased by fluvial nutrient input, which causes enhanced primary production near the surface, and a subsequent deoxygenation of deeper waters due to the microbial consumption of detrital

organic material (Meier et al., 2017). The complex hydrography of the Baltic Sea has important implications for adjacent coastal bays.

The precise location, where the sediments were retrieved is Boknis Eck, a seasonally hypoxic, muddy basin in Eckernförde Bay with water depths of ~28 m. The entire inlet, is governed by a net quasi-upwelling which is induced by dense waters that invade the bottom layer of the adjacent Kiel Bight and subsequently of the inlet in spring and early summer (Figure I 2). These water masses displace the overlaying water and cause a near surface outflow and at the same time an initial stratification that is subsequently enhanced by the warming of surface waters and their refreshment via rain and groundwater. This leads to relatively stable barocline that develops in ~15 m water depth. In autumn and winter, storms mix the water column and oxygenate bottom waters (Dietze and Löptien, 2021). The transport of nutrient rich deeper waters to the surface fosters primary production (Balzer, 1984; Lennartz et al., 2014; Melzner et al., 2013). The subsequent accumulation of particulate organic carbon (POC) followed by its degradation lead to high CO_2 partial pressure (pCO_2) in bottom waters that lowers the saturation state with respect to calcite (Ω_{Cal}). The burial of approximately one fifth ~20 % of the POC that is exported from the surface layer to the deeper water body, combined with natural benthic TA flux partly derived from carbonate weathering and burial of sulfides (Wallmann et al., 2022), leads to a natural uptake of CO_2 (Balzer, 1984).

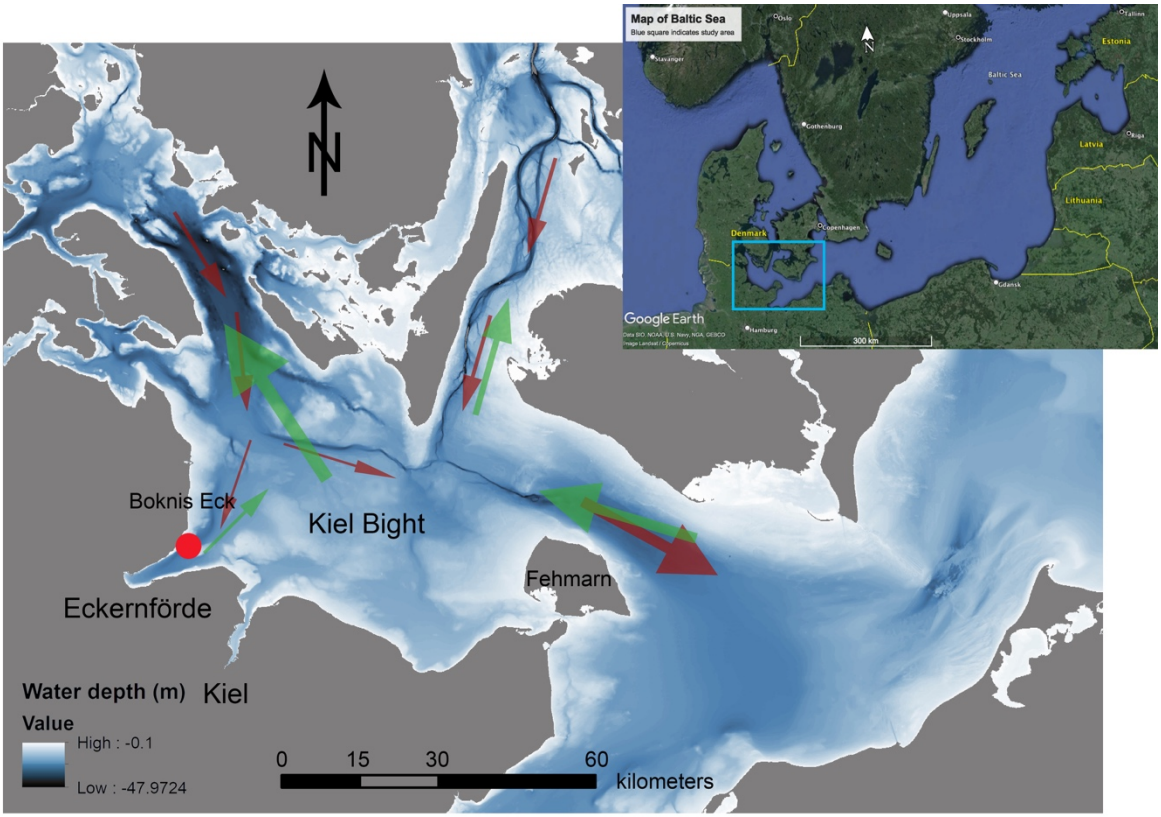

Figure I 2: Map of the study area. Red arrows indicate inflow path of salty bottom waters from the North Sea, Green arrows denote surface out-flow. Red dot shows the location where sediments for the studies in this thesis were obtained.

I.3. Chapter synopsis, connection and author contributions

I.3.1. Chapter 2

In a first set of experiments, dunite was exposed to artificial seawater to understand the precise dissolution kinetics and investigate possible side-effects (Fuhr et al., 2022). The results of these experiments made clear that, despite the relatively low reactivity of olivine, a set of secondary minerals precipitated presumably in the diffusive boundary layer around and on the grains, which reduces the CO_2 uptake efficiency. The fact that the major secondary mineral was aragonite suggested that dunite dissolution is most probably more efficient in environments where pore waters and bottom waters are undersaturated with respect to aragonite, again pointing towards EBW as a possible applications scenario.

A promising area featuring this specific demand are shallow depocenters of the Baltic Sea. Subsequently, a set of three experiments were conducted on organic rich sediments from the Baltic Sea, which are known to feature pore waters that are undersaturated with respect to calcite and aragonite (Preisler et al., 2007). This geochemical feature also led to the consideration of calcite as a potential source material for EBW in these environments and to the subsequent comparison of calcite and dunite with regards to their respective CO_2 sequestration efficiency.

I.3.2. Chapter 3

In the first of two incubation experiments conducted under controlled laboratory conditions, sediment cores from the Baltic Sea were amended with calcite and dunite in fully oxygenated and oversaturated ($\Omega_{Cal} > 1$) bottom waters (Fuhr et al., 2023). These redox conditions reflect the major states of the natural system in Boknis Eck during winter and spring. During these experiments, the added material was quickly worked into the sediment and subject to dissolution via the "benthic weathering engine". The results highlighted the importance of the microbial activity on pore water pH values that lead to very high dissolution rates of natural calcite. The associated background fluxes combined with a relatively low through-flow complicated the evaluation and interpretation of the results. Additionally, pore waters were altered due to the incubation over a longer period (85 days in total) which was subsequently considered for further incubation experiments.

I.3.3. Chapter 4

The second set of incubation experiments was performed under anoxic to hypoxic conditions and in undersaturated bottom waters ($\Omega_{Cal} < 1$), which reflects typical conditions in Boknis Eck during summer and autumn (Fuhr et al., 2024). Based on experiences from the first incubation (Chapter 3), the time of incubation was shortened (25 days) and a higher flow rate was applied. A first important finding of this study was that the added minerals were not worked into the sediment, but remained on top of it, over entire incubation due to a lack of bioturbation. Secondly, due to the improved set-up, the fluxes of weathering products of both materials could be quantified, and dissolution kinetics could be calculated. These were in good agreement with published literature values, which implies that literature values for dissolution kinetics in the water column are also valid under the respective chemical conditions.

The first two experiments shed light on the weathering behavior of calcite and dunite under controlled temperature and and redox conditions. The also made clear that EBW involves a variety of processes that eventually affect mineral dissolution rates. These again can vary spatially and temporally. This elucidated the need to investigate these processes over a longer period of time and on a larger spatial scale. Especially the impact of changing redox conditions and temperature is crucial to understand and was not reflected in the incubation experiments.

I.3.4. Chapter 5

In a final experiment, the dissolution of dunite and calcite was investigated in a benthocosms over the course of a year (Fuhr et al., submitted). For this purpose, sediment was transferred into large boxes with supernatant bottom waters from Kiel Fjord pumped through continuously. These sediments were amended with calcite and dunite respectively and the dissolution monitored over an entire annual September – September cycle. The results made clear that the dissolution under oxygenated conditions is primarily driven by temperature rather than pore water saturation state. The fact that the temperature sensitivity is higher than found in previous studies underpins that a variety of temperature-dependent processes is operating, which substantiates the principle function of the "weathering engine". These insights, combined with findings from Chapters 2 – 4 were used to model a possible mineral application scenario in Eckernförde Bay. The model calculated potential uptake of CO_2 and allowed for a first realistic assessment of efficiency and costs of EBW on organic sediments of the Baltic Sea. These results help to understand the global scalability of EBW for climate change mitigation.

I.3.5. Author contribution

Chapter 2: MF conducted the experiments, carried out most of the measurements, evaluated the results and wrote the manuscript.

Chapter 3: MF conducted the experiment, took the samples, evaluated the result and wrote the manuscript.

Chapter 4: MF conducted the experiment, took the samples, evaluated the result and wrote the manuscript.

Chapter 5: MF conducted the experiment, took most of the samples, evaluated the result and conceptualized the model. Additionally, MF helped with cost calculations and efficiency estimates for calcite based EBW.

I.3.6. Publications and outreach

I.3.6.1. Publications from this thesis:

Fuhr, M., Geilert, S., Schmidt, M., Liebetrau, V., Vogt, C., Ledwig, B., Wallmann, K., 2022. Kinetics of Olivine Weathering in Seawater: An Experimental Study. Front. Clim. 4:831587. https://doi.org/10.3389/fclim.2022.831587

Fuhr, M., Wallmann, K., Dale, A.W., Diercks, I., Kalapurakkal, H.T., Schmidt, M., Sommer, S., Böhnke, S., Perner, M., Geilert, S., 2023. Disentangling artificial and natural benthic weathering in organic rich Baltic Sea sediments. Front. Clim. https://doi.org/10.3389/fclim.2023.1245580

Fuhr, M., Wallmann, K., Dale, A.W., Kalapurakkal, H.T., Schmidt, M., Sommer, S., Deusner, C., Spiegel, T., Kowalski, J., Geilert, S., 2024. Alkaline mineral addition to anoxic to hypoxic Baltic Sea sediments as a potentially efficient CO2-removal technique. Front. Clim. https://doi.org/10.3389/fclim.2024.1338556

Chapter 5 is being submitted for publication in Nature Climate Change

I.3.6.2. Additional publications

Fuhr, M., Laukert, G., Yu, Y., Nürnberg, D., Frank, M., 2021. Tracing Water Mass Mixing From the Equatorial to the North Pacific Ocean With Dissolved Neodymium Isotopes and Concentrations. Front. Mar. Sci. 7, 1261. https://doi.org/10.3389/fmars.2020.603761

Wallmann, K., Diesing, M., Scholz, F., Rehder, G., Dale, A.W., Fuhr, M., Suess, E., 2022. Erosion of carbonate-bearing sedimentary rocks may close the alkalinity budget of the Baltic Sea and support atmospheric CO2 uptake in coastal seas. Front. Mar. Sci. 9:968069. https://doi.org/10.3389/fmars.2022.968069

Flipkens, G., Fuhr, M., Fiers, G., Meysman, F.J.R., Town, R.M., Blust, R., 2023. Enhanced olivine dissolution in seawater through continuous grain collisions. Geochim. Cosmochim. Acta 359, 84–99. https://doi.org/https://doi.org/10.1016/j.gca.2023.09.002

Spiegel, T., Diesing, M., Dale, A.W., Lenz, N., Schmidt, M., Sommer, S., Böttner, C., Fuhr, M., Kalapurakkal, H.T., Schulze, C.-S., Wallmann, K., 2024. Modelling mass accumulation rates and 210Pb rain rates in the Skagerrak: lateral sediment transport dominates the sediment input. Front. Mar. Sci. https://doi.org/10.3389/fmars.2024.1331102

I.3.6.3. Outreach

Lecture on CO_2 cycle and sink for "Climate School":

https://publicclimateschool.de/schulprogramm/stundenplan-mai-22/co2-senken/

Presentation on CO_2 cycles, sinks and anthropogenic CO_2 at the Young Climate Conference "LCOY":

https://lcoy.de/rueckblick/lcoy2022?2022=&tab=1

Presentation of mineral dissolution and EBW at the "GEOMAR science Day".

Podcast on "Littoral weathering and academic culture" with "Reviewer 2 does geoengineering":

https://open.spotify.com/episode/2KEVb0n0RgX3C9SHWTfKjC

References (I)

Amann, T., Hartmann, J., Struyf, E., De Oliveira Garcia, W., Fischer, E.K., Janssens, I., Meire, P., Schoelynck, J., 2020. Enhanced Weathering and related element fluxes - A cropland mesocosm approach. Biogeosciences 17, 103–119. https://doi.org/10.5194/bg-17-103-2020

Anderson, S., Newell, R., 2004. Prospects for carbon capture and storage technologies. Annu. Rev. Environ. Resour. 29, 109–142. https://doi.org/10.1146/annurev.energy.29.082703.145619

Arrhenius, S., 1896. XXXI. On the influence of carbonic acid in the air upon the temperature of the ground . London, Edinburgh, Dublin Philos. Mag. J. Sci. 41, 237–276. https://doi.org/10.1080/14786449608620846

Azar, C., Lindgren, K., Larson, E., Möllersten, K., 2006. Carbon Capture and Storage From Fossil Fuels and Biomass – Costs and Potential Role in Stabilizing the Atmosphere. Clim. Change 74, 47–79. https://doi.org/10.1007/s10584-005-3484-7

Bach, L.T., Gill, S.J., Rickaby, R.E.M., Gore, S., Renforth, P., 2019. CO2 Removal With Enhanced Weathering and Ocean Alkalinity Enhancement: Potential Risks and Co-benefits for Marine Pelagic Ecosystems . Front. Clim. .

Balzer, W., 1984. Organic matter degradation and biogenic element cycling in a nearshore sediment (Kiel Bight)1. Limnol. Oceanogr. 29, 1231–1246. https://doi.org/https://doi.org/10.4319/lo.1984.29.6.1231

Bice, K., Myers, T., Waldbusser, G., Meile, C., 2024. Countering the effect of ocean acidification in coastal sediments through carbonate mineral additions. EGUsphere 2024, 1–28. https://doi.org/10.5194/egusphere-2024-796

Bohr, C., 1899. Definition und Methode zur Bestimmung der Invasions- und Evasionscoefficienten bei der Auflösung von Gasen in Flüssigkeiten. Werthe der genannten Constanten sowie der Absorptionscoefficienten der Kohlensäure bei Auflösung in Wasser und in Chlornatriumlösu. Ann. Phys. 304, 500–525. https://doi.org/https://doi.org/10.1002/andp.18993040707

Buck, H.J., Carton, W., Lund, J.F., Markusson, N., 2023. Why residual emissions matter right now. Nat. Clim. Chang. 13, 351–358. https://doi.org/10.1038/s41558-022-01592-2

Budinis, S., Krevor, S., Dowell, N. Mac, Brandon, N., Hawkes, A., 2018. An assessment of CCS costs, barriers and potential. Energy Strateg. Rev. 22, 61–81. https://doi.org/https://doi.org/10.1016/j.esr.2018.08.003

Campbell, J.S., Foteinis, S., Furey, V., Hawrot, O., Pike, D., Aeschlimann, S., Maesano, C.N., Reginato, P.L., Goodwin, D.R., Looger, L.L., Boyden, E.S., Renforth, P., 2022. Geochemical Negative Emissions Technologies: Part I. Review. Front. Clim. 4:879133. https://doi.org/10.3389/fclim.2022.879133

Carton, W., Asiyanbi, A., Beck, S., Buck, H.J., Lund, J.F., 2020. Negative emissions and the long history of carbon removal. WIREs Clim. Chang. 11, e671. https://doi.org/https://doi.org/10.1002/wcc.671

Caserini, S., Cappello, G., Righi, D., Raos, G., Campo, F., De Marco, S., Renforth, P., Varliero, S., Grosso, M., 2021a. Buffered accelerated weathering of limestone for storing CO2: Chemical background. Int. J. Greenh. Gas Control 112, 103517. https://doi.org/10.1016/j.ijggc.2021.103517

Caserini, S., Pagano, D., Campo, F., Abbà, A., De Marco, S., Righi, D., Renforth, P., Grosso, M., 2021b. Potential of Maritime Transport for Ocean Liming and Atmospheric CO2 Removal . Front. Clim. .

Chenot, E., Deconinck, J.-F., Pucéat, E., Pellenard, P., Guiraud, M., Jaubert, M., Jarvis, I., Thibault, N., Cocquerez, T., Bruneau, L., Razmjooei, M.J., Boussaha, M., Richard, J., Sizun, J.-P., Stemmerik, L., 2018. Continental weathering as a driver of Late Cretaceous cooling: new insights from clay mineralogy of Campanian sediments from the southern Tethyan margin to the Boreal realm. Glob. Planet. Change 162, 292–312. https://doi.org/https://doi.org/10.1016/j.gloplacha.2018.01.016

Cirés, S., Ballot, A., 2016. A review of the phylogeny, ecology and toxin production of bloom-forming Aphanizomenon spp. and related species within the Nostocales (cyanobacteria). Harmful Algae. https://doi.org/10.1016/j.hal.2015.09.007

Cox, G.M., Halverson, G.P., Stevenson, R.K., Vokaty, M., Poirier, A., Kunzmann, M., Li, Z.-X., Denyszyn, S.W., Strauss, J. V, Macdonald, F.A., 2016. Continental flood basalt weathering as a trigger for

Neoproterozoic Snowball Earth. Earth Planet. Sci. Lett. 446, 89–99. https://doi.org/https://doi.org/10.1016/j.epsl.2016.04.016

Dahl, C., Hell, R., Leustek, T., Knaff, D., 2008. Introduction to Sulfur Metabolism in Phototrophic Organisms BT - Sulfur Metabolism in Phototrophic Organisms, in: Hell, R., Dahl, C., Knaff, D., Leustek, T. (Eds.), . Springer Netherlands, Dordrecht, pp. 1–14. https://doi.org/10.1007/978-1-4020-6863-8_1

De Nobel, W.T., Matthijs, H.C.P., Von Elert, E., Mur, L.R., 1998. Comparison of the light-limited growth of the nitrogen-fixing cyanobacteria Anabaena and Aphanizomenon. New Phytol. 138, 579–587. https://doi.org/10.1046/j.1469-8137.1998.00155.x

Dickson, A.G., 1981. An exact definition of total alkalinity and a procedure for the estimation of alkalinity and total inorganic carbon from titration data. Deep Sea Res. Part A. Oceanogr. Res. Pap. 28, 609–623. https://doi.org/https://doi.org/10.1016/0198-0149(81)90121-7

Dietze, H., Löptien, U., 2021. Retracing Hypoxia in Eckernförde Bight (Baltic Sea). Biogeosciences Discuss. 2021, 1–42. https://doi.org/10.5194/bg-2021-31

Doelman, J.C., Stehfest, E., van Vuuren, D.P., Tabeau, A., Hof, A.F., Braakhekke, M.C., Gernaat, D.E.H.J., van den Berg, M., van Zeist, W.-J., Daioglou, V., van Meijl, H., Lucas, P.L., 2020. Afforestation for climate change mitigation: Potentials, risks and trade-offs. Glob. Chang. Biol. 26, 1576–1591. https://doi.org/https://doi.org/10.1111/gcb.14887

Eisaman, M.D., Geilert, S., Renforth, P., Bastianini, L., Campbell, J., Dale, A.W., Foteinis, S., Grasse, P., Hawrot, O., Löscher, C.R., Rau, G.H., Rønning, J., 2023. Assessing the technical aspects of ocean-alkalinity-enhancement approaches. Guid. to Best Pract. Ocean Alkalinity Enhanc. Res. 2-oae2023, 3. https://doi.org/10.5194/sp-2-oae2023-3-2023

Feely, R.A., Jiang, L.-Q., Wanninkhof, R., Carter, B.R., Alin, S.R., Bednaršek, N., Cosca, C.E., 2023. ACIDIFICATION OF THE GLOBAL SURFACE OCEAN. Oceanography 36, 120–129.

Feistel, R., Nausch, G., Hagen, E., 2006. Unusual Baltic inflow activity in 2002-2003 and varying deep-water properties. Oceanologia 48, 21–35.

Feistel, R., Weinreben, S., Wolf, H., Seitz, S., Spitzer, P., Adel, B., Nausch, G., Schneider, B., Wright, D.G., 2010. Density and Absolute Salinity of the Baltic Sea 2006–2009. Ocean Sci. 6, 3–24. https://doi.org/10.5194/os-6-3-2010

Feng, E.Y., Koeve, W., Keller, D.P., Oschlies, A., 2017. Model-Based Assessment of the CO2 Sequestration Potential of Coastal Ocean Alkalinization. Earth's Futur. 5, 1252–1266. https://doi.org/10.1002/2017EF000659

Feng, L., Lei, G., Nie, Y., 2023. Exploring the eco-efficiency of cultivated land utilization and its influencing factors in black soil region of Northeast China under the goal of reducing non-point pollution and net carbon emission. Environ. Earth Sci. 82, 94. https://doi.org/10.1007/s12665-023-10770-0

Foteinis, S., Campbell, J.S., Renforth, P., 2023. Life Cycle Assessment of Coastal Enhanced Weathering for Carbon Dioxide Removal from Air. Environ. Sci. Technol. 57, 6169–6178. https://doi.org/10.1021/acs.est.2c08633

Friedlingstein, P., Solomon, S., Plattner, G.-K., Knutti, R., Ciais, P., Raupach, M.R., 2011. Long-term climate implications of twenty-first century options for carbon dioxide emission mitigation. Nat. Clim. Chang. 1, 457–461. https://doi.org/10.1038/nclimate1302

Fuhr, M., Geilert, S., Schmidt, M., Liebetrau, V., Vogt, C., Ledwig, B., Wallmann, K., 2022. Kinetics of Olivine Weathering in Seawater: An Experimental Study. Front. Clim. 4:831587. https://doi.org/10.3389/fclim.2022.831587

Fuhr, M., Wallmann, K., Dale, A.W., Diercks, I., Kalapurakkal, H.T., Schmidt, M., Sommer, S., Böhnke, S., Perner, M., Geilert, S., 2023. Disentangling artificial and natural benthic weathering in organic rich Baltic Sea sediments. Front. Clim. https://doi.org/10.3389/fclim.2023.1245580

Fuhr, M., Wallmann, K., Dale, A.W., Kalapurakkal, H.T., Schmidt, M., Sommer, S., Deusner, C., Spiegel, T., Kowalski, J., Geilert, S., 2024. Alkaline mineral addition to anoxic to hypoxic Baltic Sea sediments as a potentially efficient CO2-removal technique. Front. Clim. https://doi.org/10.3389/fclim.2024.1338556

Fuss, S., Lamb, W.F., Callaghan, M.W., Hilaire, J., Creutzig, F., Amann, T., Beringer, T., De Oliveira Garcia, W., Hartmann, J., Khanna, T., Luderer, G., Nemet, G.F., Rogelj, J., Smith, P., Vicente, J.V., Wilcox, J., Del Mar Zamora Dominguez, M., Minx, J.C., 2018. Negative emissions - Part 2: Costs, potentials and side effects. Environ. Res. Lett. 13. https://doi.org/10.1088/1748-9326/aabf9f

Gade, D., Gobom, J., Rabus, R., 2005. Proteomic analysis of carbohydrate catabolism and regulation in the marine bacterium Rhodopirellula baltica. Proteomics 5, 3672–3683. https://doi.org/https://doi.org/10.1002/pmic.200401200

Garrity, G.M., Bell, J.A., Lilburn, T., 2005. Family I. Thiotrichaceae fam. nov, in: Brenner DJ, Krieg NR, Staley JT, Garrity GM. New York, p. 131.

Hangx, S.J.T., Spiers, C.J., 2009. Coastal spreading of olivine to control atmospheric CO2 concentrations: A critical analysis of viability. Int. J. Greenh. Gas Control 3, 757–767. https://doi.org/10.1016/j.ijggc.2009.07.001

Hansen, G., Stone, D., 2016. Assessing the observed impact of anthropogenic climate change. Nat. Clim. Chang. 6, 532–537. https://doi.org/10.1038/nclimate2896

Hansen, J., Ruedy, R., Sato, M., Lo, K., 2010. GLOBAL SURFACE TEMPERATURE CHANGE. Rev. Geophys. 48. https://doi.org/https://doi.org/10.1029/2010RG000345

Harrington, K.J., Hilton, R.G., Henderson, G.M., 2023. Implications of the Riverine Response to Enhanced Weathering for CO2 removal in the UK. Appl. Geochemistry 152, 105643. https://doi.org/https://doi.org/10.1016/j.apgeochem.2023.105643

Hartmann, J., Kempe, S., 2008. What is the maximum potential for CO 2 sequestration by "stimulated" weathering on the global scale? Naturwissenschaften 95, 1159–1164. https://doi.org/10.1007/s00114-008-0434-4

Hartmann, J., Suitner, N., Lim, C., Schneider, J., Marín-Samper, L., Arístegui, J., Renforth, P., Taucher, J., Riebesell, U., 2023. Stability of alkalinity in ocean alkalinity enhancement (OAE) approaches – consequences for durability of CO2 storage. Biogeosciences 20, 781–802. https://doi.org/10.5194/bg-20-781-2023

Howe, J.P., 2015. This is nature; This is un-nature: Reading the keeling curve. Environ. Hist. Durh. N. C. https://doi.org/10.1093/envhis/emv005

Ignatusha, P., Lin, H., Kapuscinsky, N., Scoles, L., Ma, W., Patarachao, B., Du, N., 2024. Membrane Separation Technology in Direct Air Capture. Membranes (Basel). https://doi.org/10.3390/membranes14020030

Iizuka, A., Fujii, M., Yamasaki, A., Yanagisawa, Y., 2004. Development of a new CO2 sequestration process utilizing the carbonation of waste cement. Ind. Eng. Chem. Res. 43, 7880–7887. https://doi.org/10.1021/ie0496176

Imhoff, J.F., 2014. The Family Chromatiaceae BT - The Prokaryotes: Gammaproteobacteria, in: Rosenberg, E., DeLong, E.F., Lory, S., Stackebrandt, E., Thompson, F. (Eds.), . Springer Berlin Heidelberg, Berlin, Heidelberg, pp. 151–178. https://doi.org/10.1007/978-3-642-38922-1_295

IPCC, 2018. Summary for Policymakers. In: Global Warming of 1.5°C. An IPCC Special Report on the impacts of global warming of 1.5°C above pre-industrial levels and related global greenhouse gas emission pathways, in the context of strengthening the global response to. Cambridge Univ. Press 3–24. https://doi.org/10.1017/9781009157940.001

Kanwisher, J., 1960. pCO2 in Sea Water and its Effect on the Movement of CO2 in Nature12. Tellus 12, 209–215. https://doi.org/10.3402/tellusa.v12i2.9361

Kanzaki, Y., Planavsky, N.J., Reinhard, C.T., 2023. New estimates of the storage permanence and ocean co-benefits of enhanced rock weathering. PNAS Nexus 2, pgad059. https://doi.org/10.1093/pnasnexus/pgad059

Keeling, C.D., Stephen, C., Piper, S.C., Bacastow, R.B., Wahlen, M., Whorf, T.P., Heimann, M., Meijer, H. a., 2001. Exchanges of atmospheric CO2 and 13CO2 with the terrestrial biosphere and oceans from 1978 to 2000. Glob. Asp. SIO Ref. Ser. Scripps Inst. Ocean. San Diego 01–06. https://doi.org/10.1007/0-387-27048-5_5

Kemena, T.P., Matthes, K., Martin, T., Wahl, S., Oschlies, A., 2018. Atmospheric feedbacks in North Africa from an irrigated, afforested Sahara. Clim. Dyn. 50, 4561–4581.

https://doi.org/10.1007/s00382-017-3890-8

Kheshgi, H.S., 1995. Sequestering atmospheric carbon dioxide by increasing ocean alkalinity. Energy 20, 915–922. https://doi.org/https://doi.org/10.1016/0360-5442(95)00035-F

Köhler, P., Abrams, J.F., Völker, C., Hauck, J., Wolf-Gladrow, D.A., 2013. Geoengineering impact of open ocean dissolution of olivine on atmospheric CO2, surface ocean pH and marine biology. Environ. Res. Lett. 8. https://doi.org/10.1088/1748-9326/8/1/014009

Kriegler, E., Edenhofer, O., Reuster, L., Luderer, G., Klein, D., 2013. Is atmospheric carbon dioxide removal a game changer for climate change mitigation ? Clim. Change 118, 45–57. https://doi.org/10.1007/s10584-012-0681-4

Kriegler, E., Edmonds, J., Hallegatte, S., Ebi, K.L., Kram, T., Riahi, K., Winkler, H., van Vuuren, D.P., 2014. A new scenario framework for climate change research: the concept of shared climate policy assumptions. Clim. Change 122, 401–414. https://doi.org/10.1007/s10584-013-0971-5

Krupa, S. V, Kickert, R.N., 1989. The Greenhouse effect: Impacts of ultraviolet-B (UV-B) radiation, carbon dioxide (CO2), and ozone (O3) on vegetation. Environ. Pollut. 61, 263–393. https://doi.org/10.1016/0269-7491(89)90166-8

Lackner, K.S., 2003. A guide to CO2 sequestration. Science (80-.). 300, 1677–1678. https://doi.org/10.1126/science.1079033

Lal, R., 2004. Soil carbon sequestration to mitigate climate change. Geoderma. https://doi.org/10.1016/j.geoderma.2004.01.032

Lass, H.U., Matthäus, W., 2008. General Oceanography of the Baltic Sea. State Evol. Balt. Sea, 1952-2005 A Detail. 50-Year Surv. Meteorol. Clim. Physics, Chem. Biol. Mar. Environ. 5–43. https://doi.org/10.1002/9780470283134.ch2

Leeson, D., Mac Dowell, N., Shah, N., Petit, C., Fennell, P.S., 2017. A Techno-economic analysis and systematic review of carbon capture and storage (CCS) applied to the iron and steel, cement, oil refining and pulp and paper industries, as well as other high purity sources. Int. J. Greenh. Gas

Control 61, 71–84. https://doi.org/https://doi.org/10.1016/j.ijggc.2017.03.020

Lennartz, S.T., Lehmann, A., Herrford, J., Malien, F., Hansen, H.-P., Biester, H., Bange, H.W., 2014. Long-term trends at the Boknis Eck time series station (Baltic Sea), 1957–2013: does climate change counteract the decline in eutrophication? Biogeosciences 11, 6323–6339. https://doi.org/10.5194/bg-11-6323-2014

Lindzen, R.S., 2007. Taking Greenhouse Warming Seriously. Energy Environ. 18, 937–950. https://doi.org/10.1260/095830507782616823

Lu, K.-J., Chang, C.-W., Wang, C.-H., Chen, F.Y.-H., Huang, I.Y., Huang, P.-H., Yang, C.-H., Wu, H.-Y., Wu, W.-J., Hsu, K.-C., Ho, M.-C., Tsai, M.-D., Liao, J.C., 2023. An ATP-sensitive phosphoketolase regulates carbon fixation in cyanobacteria. Nat. Metab. 5, 1111–1126. https://doi.org/10.1038/s42255-023-00831-w

Luderer, G., Vrontisi, Z., Bertram, C., Edelenbosch, O.Y., Pietzcker, R.C., Rogelj, J., De Boer, H.S., Drouet, L., Emmerling, J., Fricko, O., Fujimori, S., Havlík, P., Iyer, G., Keramidas, K., Kitous, A., Pehl, M., Krey, V., Riahi, K., Saveyn, B., Tavoni, M., Van Vuuren, D.P., Kriegler, E., 2018. Residual fossil CO2 emissions in 1.5–2 °C pathways. Nat. Clim. Chang. 8, 626–633. https://doi.org/10.1038/s41558-018-0198-6

MacFarling Meure, C., Etheridge, D., Trudinger, C., Steele, P., Langenfelds, R., van Ommen, T., Smith, A., Elkins, J., 2006. Law Dome CO2, CH4 and N2O ice core records extended to 2000 years BP. Geophys. Res. Lett. 33. https://doi.org/10.1029/2006GL026152

Magnan, A.K., Pörtner, H.-O., Duvat, V.K.E., Garschagen, M., Guinder, V.A., Zommers, Z., Hoegh-Guldberg, O., Gattuso, J.-P., 2021. Estimating the global risk of anthropogenic climate change. Nat. Clim. Chang. 11, 879–885. https://doi.org/10.1038/s41558-021-01156-w

Martin, J.H., Gordon, R.M., Fitzwater, S.E., 1990. Iron in Antarctic waters. Nature 345, 156–158. https://doi.org/10.1038/345156a0

Meier, H.E.M., Höglund, A., Eilola, K., Almroth-Rosell, E., 2017. Impact of accelerated future global mean sea level rise on hypoxia in the Baltic Sea. Clim. Dyn. 49, 163–172.

https://doi.org/10.1007/s00382-016-3333-y

Melzner, F., Thomsen, J., Koeve, W., Oschlies, A., Gutowska, M.A., Bange, H.W., Hansen, H.P., Körtzinger, A., 2013. Future ocean acidification will be amplified by hypoxia in coastal habitats. Mar. Biol. 160, 1875–1888. https://doi.org/10.1007/s00227-012-1954-1

Meysman, F.J.R., Montserrat, F., 2017. Negative CO2 emissions via enhanced silicate weathering in coastal environments. Biol. Lett. https://doi.org/10.1098/rsbl.2016.0905

Meysman, F.J.R., Risgaard-Petersen, N., Malkin, S.Y., Nielsen, L.P., 2015. The geochemical fingerprint of microbial long-distance electron transport in the seafloor. Geochim. Cosmochim. Acta 152, 122–142. https://doi.org/https://doi.org/10.1016/j.gca.2014.12.014

Minx, J.C., Lamb, W.F., Callaghan, M.W., Fuss, S., Hilaire, J., Creutzig, F., Amann, T., Beringer, T., De Oliveira Garcia, W., Hartmann, J., Khanna, T., Lenzi, D., Luderer, G., Nemet, G.F., Rogelj, J., Smith, P., Vicente Vicente, J.L., Wilcox, J., Del Mar Zamora Dominguez, M., 2018. Negative emissions - Part 1: Research landscape and synthesis. Environ. Res. Lett. 13. https://doi.org/10.1088/1748-9326/aabf9b

Mohrholz, V., Naumann, M., Nausch, G., Krüger, S., Gräwe, U., 2015. Fresh oxygen for the Baltic Sea - An exceptional saline inflow after a decade of stagnation. J. Mar. Syst. 148, 152–166. https://doi.org/10.1016/j.jmarsys.2015.03.005

Montserrat, F., Renforth, P., Hartmann, J., Leermakers, M., Knops, P., Meysman, F.J.R., 2017. Olivine Dissolution in Seawater: Implications for CO2 Sequestration through Enhanced Weathering in Coastal Environments. Environ. Sci. Technol. 51, 3960–3972. https://doi.org/10.1021/acs.est.6b05942

Moras, C.A., Bach, L.T., Cyronak, T., Joannes-Boyau, R., Schulz, K.G., 2022. Ocean alkalinity enhancement – avoiding runaway CaCO3 precipitation during quick and hydrated lime dissolution. Biogeosciences 19, 3537–3557. https://doi.org/10.5194/bg-19-3537-2022

Mori, K., Suzuki, K.I., Yamaguchi, K., Urabe, T., Hanada, S., 2015. Thiogranum longum gen. nov., sp. nov., an obligately chemolithoautotrophic, sulfur-oxidizing bacterium of the family

Ectothiorhodospiraceaeisolated from a deep-sea hydrothermal field, and an emended description of the genus Thiohalomonas. Int. J. Syst. Evol. Microbiol. 65, 235–241. https://doi.org/10.1099/ijs.0.070599-0

Naviaux, J.D., Subhas, A. V, Dong, S., Rollins, N.E., Liu, X., Byrne, R.H., Berelson, W.M., Adkins, J.F., 2019a. Calcite dissolution rates in seawater: Lab vs. in-situ measurements and inhibition by organic matter. Mar. Chem. 215, 103684. https://doi.org/https://doi.org/10.1016/j.marchem.2019.103684

Naviaux, J.D., Subhas, A. V, Rollins, N.E., Dong, S., Berelson, W.M., Adkins, J.F., 2019b. Temperature dependence of calcite dissolution kinetics in seawater. Geochim. Cosmochim. Acta 246, 363–384. https://doi.org/https://doi.org/10.1016/j.gca.2018.11.037

Okesola, A.A., Oyedeji, A.A., Abdulhamid, A.F., Olowo, J., Ayodele, B.E., Alabi, T.W., 2018. Direct Air Capture: A Review of Carbon Dioxide Capture from the Air. IOP Conf. Ser. Mater. Sci. Eng. 413, 12077. https://doi.org/10.1088/1757-899X/413/1/012077

Oschlies, A., Koeve, W., Rickels, W., Rehdanz, K., 2010. Side effects and accounting aspects of hypothetical large-scale Southern Ocean iron fertilization. Biogeosciences 7, 4017–4035. https://doi.org/10.5194/bg-7-4017-2010

Parkhurst, D.L., Appelo, C.A.J., 1999. User's Guide to PHREEQC (Version 2): A Computer Program for Speciation, Batch-Reaction, One-Dimensional Transport, and Inverse Geochemical Calculations, Water-Resources Investigations Report 99-4259. https://doi.org/10.3133/wri994259

Petit, J.R., Jouzel, J., Raynaud, D., Barkov, N.I., Barnola, J.M., Basile, I., Bender, M., Chappellaz, J., Davis, M., Delaygue, G., Delmotte, M., Kotiyakov, V.M., Legrand, M., Lipenkov, V.Y., Lorius, C., Pépin, L., Ritz, C., Saltzman, E., Stievenard, M., 1999. Climate and atmospheric history of the past 420,000 years from the Vostok ice core, Antarctica. Nature. https://doi.org/10.1038/20859

Preisler, A., de Beer, D., Lichtschlag, A., Lavik, G., Boetius, A., Jørgensen, B.B., 2007. Biological and chemical sulfide oxidation in a Beggiatoa inhabited marine sediment. ISME J. 1, 341–353. https://doi.org/10.1038/ismej.2007.50

Puente-Sánchez, F., Arce-Rodríguez, A., Oggerin, M., García-Villadangos, M., Moreno-Paz, M., Blanco,

Y., Rodríguez, N., Bird, L., Lincoln, S.A., Tornos, F., Prieto-Ballesteros, O., Freeman, K.H., Pieper, D.H., Timmis, K.N., Amils, R., Parro, V., 2018. Viable cyanobacteria in the deep continental subsurface. Proc. Natl. Acad. Sci. U. S. A. 115, 10702–10707. https://doi.org/10.1073/pnas.1808176115

Rakestraw, N.W., 1949. The conception of alkalinity of excess base of sea water. J. Mar. Res. 8, 14–20.

Rao, A.M.F., Polerecky, L., Ionescu, D., Meysman, F.J.R., de Beer, D., 2012. The influence of pore-water advection, benthic photosynthesis, and respiration on calcium carbonate dynamics in reef sands. Limnol. Oceanogr. 57, 809–825. https://doi.org/https://doi.org/10.4319/lo.2012.57.3.0809

Rau, G.H., Caldeira, K., 1999. Enhanced carbonate dissolution:: a means of sequestering waste CO2 as ocean bicarbonate. Energy Convers. Manag. 40, 1803–1813. https://doi.org/https://doi.org/10.1016/S0196-8904(99)00071-0

Rau, G.H., Knauss, K.G., Langer, W.H., Caldeira, K., 2007. Reducing energy-related CO2 emissions using accelerated weathering of limestone. Energy 32, 1471–1477. https://doi.org/https://doi.org/10.1016/j.energy.2006.10.011

Renforth, P., 2012. The potential of enhanced weathering in the UK. Int. J. Greenh. Gas Control 10, 229–243. https://doi.org/https://doi.org/10.1016/j.ijggc.2012.06.011

Renforth, P., Henderson, G., 2017. Assessing ocean alkalinity for carbon sequestration. Rev. Geophys. 55, 636–674. https://doi.org/10.1002/2016RG000533

Renforth, P., Pogge von Strandmann, P.A.E., Henderson, G.M., 2015. The dissolution of olivine added to soil: Implications for enhanced weathering. Appl. Geochemistry 61, 109–118. https://doi.org/https://doi.org/10.1016/j.apgeochem.2015.05.016

Revelle, R., Suess, H.E., 1957. Carbon Dioxide Exchange Between Atmosphere and Ocean and the Question of an Increase of Atmospheric CO2 during the Past Decades. Tellus 9, 18–27. https://doi.org/https://doi.org/10.1111/j.2153-3490.1957.tb01849.x

Rhodes, C.J., 2016. The 2015 Paris climate change conference: COP21. Sci. Prog. 99, 97–104.

Rigopoulos, I., Harrison, A.L., Delimitis, A., Ioannou, I., Efstathiou, A.M., Kyratsi, T., Oelkers, E.H., 2018. Carbon sequestration via enhanced weathering of peridotites and basalts in seawater. Appl. Geochemistry 91, 197–207. https://doi.org/10.1016/j.apgeochem.2017.11.001

Rimstidt, J.D., Brantley, S.L., Olsen, A.A., 2012. Systematic review of forsterite dissolution rate data. Geochim. Cosmochim. Acta 99, 159–178. https://doi.org/10.1016/j.gca.2012.09.019

Santos, R.M., Verbeeck, W., Knops, P., Rijnsburger, K., Pontikes, Y., Van Gerven, T., 2013. Integrated Mineral Carbonation Reactor Technology for Sustainable Carbon Dioxide Sequestration: 'CO2 Energy Reactor.' Energy Procedia 37, 5884–5891. https://doi.org/https://doi.org/10.1016/j.egypro.2013.06.513

Saran, R.K., Kumar, R., Yadav, S., 2017. Climate change: mitigation strategyby various CO2 sequestration methods. pp. 227–236.

Schmidt, M., Seifert, T., Lass, H.U., Fennel, W., 1998. Patterns of salt propagation in the Southwestern Baltic Sea. Dtsch. Hydrogr. Zeitschrift 50, 345–364. https://doi.org/10.1007/BF02764229

Schoenberg, I.J., 1988. Contributions to the problem of approximation of equidistant data by analytic functions: Part A.—On the problem of smoothing or graduation. A first class of analytic approximation formulae. IJ Schoenb. Sel. Pap. 3–57. https://doi.org/10.1007/978-1-4899-0433-1_1

Schuiling, R.D., Krijgsman, P., 2006. Enhanced Weathering: An Effective and Cheap Tool to Sequester Co2. Clim. Change 74, 349–354. https://doi.org/10.1007/s10584-005-3485-y

Solomon, S., Plattner, G.-K., Knutti, R., Friedlingstein, P., 2009. Irreversible climate change due to carbon dioxide emissions. Proc. Natl. Acad. Sci. 106, 1704 LP – 1709. https://doi.org/10.1073/pnas.0812721106

Strefler, J., Amann, T., Bauer, N., Kriegler, E., Hartmann, J., 2018. Potential and costs of carbon dioxide removal by enhanced weathering of rocks. Environ. Res. Lett. 13. https://doi.org/10.1088/1748-9326/aaa9c4

Tan, R.R., Belmonte, B.A., Benjamin, M.F.D., Andiappan, V., Aviso, K.B., 2022. Optimization of

enhanced weathering networks with alternative transportation modes. Carbon Resour. Convers. 5, 167–176. https://doi.org/https://doi.org/10.1016/j.crcon.2022.04.002

Taylor, J.A., Lloyd, J., 1992. Sources and Sinks of Atmospheric CO2. Aust. J. Bot. 40, 407–418. https://doi.org/10.1071/BT9920407

Valipour, M., Bateni, S.M., Jun, C., 2021. Global Surface Temperature: A New Insight. Climate. https://doi.org/10.3390/cli9050081

van Vuuren, D.P., den Elzen, M.G.J., Lucas, P.L., Eickhout, B., Strengers, B.J., van Ruijven, B., Wonink, S., van Houdt, R., 2007. Stabilizing greenhouse gas concentrations at low levels: an assessment of reduction strategies and costs. Clim. Change 81, 119–159. https://doi.org/10.1007/s10584-006-9172-9

Wallmann, K., Diesing, M., Scholz, F., Rehder, G., Dale, A.W., Fuhr, M., Suess, E., 2022. Erosion of carbonate-bearing sedimentary rocks may close the alkalinity budget of the Baltic Sea and support atmospheric CO2 uptake in coastal seas. Front. Mar. Sci. 9:968069. https://doi.org/10.3389/fmars.2022.968069

Walve, J., Larsson, U., 2007. Blooms of Baltic Sea Aphanizomenon sp. (Cyanobacteria) collapse after internal phosphorus depletion . Aquat. Microb. Ecol. 49, 57–69.

Wang, H., Pilcher, D.J., Kearney, K.A., Cross, J.N., Shugart, O.M., Eisaman, M.D., Carter, B.R., 2023. Simulated Impact of Ocean Alkalinity Enhancement on Atmospheric CO2 Removal in the Bering Sea. Earth's Futur. 11, e2022EF002816. https://doi.org/10.1029/2022EF002816

Wegner, C.E., Richter-Heitmann, T., Klindworth, A., Klockow, C., Richter, M., Achstetter, T., Glöckner, F.O., Harder, J., 2013. Expression of sulfatases in Rhodopirellula baltica and the diversity of sulfatases in the genus Rhodopirellula. Mar. Genomics 9, 51–61. https://doi.org/10.1016/j.margen.2012.12.001

Wigley, T.M.L., Raper, S.C.B., 1990. Natural variability of the climate system and detection of the greenhouse effect. Nature 344, 324–327. https://doi.org/10.1038/344324a0

Wolf-Gladrow, D.A., Zeebe, R.E., Klaas, C., Körtzinger, A., Dickson, A.G., 2007. Total alkalinity: The explicit conservative expression and its application to biogeochemical processes. Mar. Chem. 106, 287–300. https://doi.org/10.1016/j.marchem.2007.01.006

Woodard, D., Branham, M., Buckingham, G., Hogue, S., Hutchins, M., Gosky, R., Marland, G., Marland, E., 2014. A spatial uncertainty metric for anthropogenic CO2 emissions. Greenh. Gas Meas. Manag. 4, 139–160. https://doi.org/10.1080/20430779.2014.1000793

Zeebe, R.E., Wolf-Gladrow, D. (Eds.), 2001a. Chapter 1 Equilibrium, in: CO2 in Seawater: Equilibrium, Kinetics, Isotopes, Elsevier Oceanography Series. Elsevier, pp. 1–84. https://doi.org/https://doi.org/10.1016/S0422-9894(01)80002-7

Zeebe, R.E., Wolf-Gladrow, D., 2001b. CO2 in seawater: equilibrium, kinetics, isotopes. Gulf Professional Publishing. https://doi.org/10.1016/s0422-9894(01)x8001-x

Zhang, J.-Z., 2023. Cyanobacteria blooms induced precipitation of calcium carbonate and dissolution of silica in a subtropical lagoon, Florida Bay, USA. Sci. Rep. 13, 4071. https://doi.org/10.1038/s41598-023-30905-4

Zomer, R.J., Trabucco, A., Bossio, D.A., Verchot, L. V, 2008. Climate change mitigation: A spatial analysis of global land suitability for clean development mechanism afforestation and reforestation. Agric. Ecosyst. Environ. 126, 67–80. https://doi.org/https://doi.org/10.1016/j.agee.2008.01.014

II. Kinetics of olivine weathering in seawater: an experimental study

Michael Fuhr [a*], Sonja Geilert [a], Mark Schmidt [a], Volker Liebetrau [a], Christoph Vogt [b], Brendan Ledwig [c] Klaus Wallmann [a]

[a] GEOMAR Helmholtz Centre for Ocean Research Kiel, Wischhofstr. 1-3, 24148 Kiel, Germany

[b] FB05 Geosciences and MARUM - Center for Marine Environmental Sciences, University of Bremen, Klagenfurter Straße 2-4, 28359 Bremen, Germany

[c] Christian-Albrechts-Universität zu Kiel, Ludewig-Meyn-Str. 10, 24118 Kiel, Germany

* Corresponding author at: GEOMAR Helmholtz Centre for Ocean Research Kiel, Wischhofstr. 1-3, 24148 Kiel, Germany.

Abstract

Enhanced weathering of mafic and ultra-mafic minerals has been suggested as a strategy for carbon dioxide removal (CDR) and a contribution to achieve a balance between global CO_2 sources and sinks (net zero emission). This study was designed to assess CDR by dissolution of ultramafic sand (UMS) in artificial seawater (ASW). Fine grained UMS with an olivine content of ~75% was reacted in ASW for up to 134 days at 1 bar and 21.5 – 23.9°C. A decline in total alkalinity (TA) was observed over the course of the experiments. This unexpected result indicates that TA removal via precipitation of cation-rich authigenic phases exceeded the production of TA induced by olivine dissolution. The TA decline was accompanied by a decrease in dissolved inorganic carbon and Ca concentrations presumably induced by $CaCO_3$ precipitation. Temporal changes in dissolved Si, Ca, Mg and TA concentrations observed during the experiments were evaluated by a numerical model to identify secondary mineral phases and quantify rates of authigenic phase formation. The modeling indicates that $CaCO_3$, FeOOH and a range of Mg-Si-phases were precipitated during the experiments. Chemical analysis of precipitates and reacted UMS surfaces confirmed that these authigenic phases accumulated in the batch reactors. Nickel released during olivine dissolution, a potential toxic element for certain organisms, was incorporated in the secondary phases and is thus not a suitable proxy for dissolution rates as proposed by earlier studies. The overall reaction stoichiometry derived from lab experiments was applied in a box model simulating atmospheric CO_2 uptake in a continental shelf setting induced by olivine addition. The model results indicate that CO_2 uptake is reduced by a factor of 5 due to secondary mineral formation and the buffering capacity of seawater. In comparable natural settings, olivine addition may thus be a less efficient CDR method than previously believed.

II.1. Introduction

The CO_2 content in the atmosphere has continuously increased over the last 120 years to a current maximum of 412 ppm (Howe, 2015; Keeling et al., 2001; MacFarling Meure et al., 2006). Since CO_2 acts as a greenhouse gas (Feldman et al., 2015), it is mainly responsible for the anthropogenic greenhouse effect (Lindzen, 2007; Solomon et al., 2009). The 2015 Paris Climate Change Conference COP21 agreed on limiting global warming to less than 2 °C compared to the preindustrial level. Furthermore, it was stated that reaching this goal can only be reached if zero net emissions of CO_2 are attained between 2030-2050 (Rhodes, 2016). The 2018 IPCC (Intergovernmental Panel on Climate Change) special report 'Global Warming of 1.5 °C' has made clear that this goal is only achievable if in addition to the reduction of CO_2 emissions, CO_2 is actively sequestered from the atmosphere in form of negative emissions (Friedlingstein et al., 2011; IPCC, 2021).

A vast variety of carbon dioxide removal (CDR) techniques has been proposed and critically reviewed over the last 20 years (Fuss et al., 2018; Iizuka et al., 2004; Lackner, 2003; Lal, 2004; Saran et al., 2018). Amongst other methods, CO_2 sequestration by alkalinity enhancement through silicate weathering has been highlighted as an affordable and effective CDR technique (Hartmann and Kempe, 2008; Montserrat et al., 2017; Oelkers, 2001; Renforth and Henderson, 2014). The general concept behind this technique is the chemical reaction of an idealized magnesium silicate, i.e. forsterite (Mg_2SiO_4), with water, following:

$$Mg_2SiO_4 + 4H_2O + 4CO_2 \rightarrow 2Mg^{2+} + H_4SiO_4 + 4HCO_3^- \quad \text{(I1)}$$

This reaction has been thoroughly studied in soils on land (Amann et al., 2020; Oelkers, 1999; Oelkers et al., 2015; Olsen and Rimstidt, 2008) but to a smaller extent in seawater, despite the fact that enhanced olivine weathering would have a triple positive effect if applied in the ocean: 1) CO_2 would be sequestered from the atmosphere into the ocean, 2) the acidification of the oceans would be reduced and 3) the supply of silica and iron, which are limiting nutrients in many parts of the ocean, would increase primary production and could lead to further CO_2 uptake (Hartmann et al., 2013; Montserrat et al., 2017). The idea behind this concept is to distribute fine grained olivine (Strefler et al., 2018) in coastal areas, along beaches and/or on shelf regions (Meysman and Montserrat, 2017; Montserrat et al., 2017). Subsequently, olivine dissolves following equation (1) and thus takes up CO_2 by contributing total alkalinity (TA) to the water column. A vast number of studies have investigated or reviewed the dissolution kinetics of olivine in aqueous solutions (Davis et al., 2009; Maher et al., 2016; Méheut and Schauble, 2014; Oelkers, 2001; Oelkers et al., 2018; Pokrovsky and Schott, 2000; Rimstidt et al., 2012) including filtered seawater (FSW) (Montserrat et al., 2017) and artificial seawater (ASW) (Montserrat et al., 2017; Rigopoulos et al., 2018). Montserrat et al. (2017) showed that during the dissolution of olivine in SW and ASW the amount of TA increase is up to ~80% lower than theoretically expected. This TA deficit was left unexplained but loosely related to the possible but not observed formation of secondary minerals. Other studies suggested that the low TA increase was caused by lower dissolution rates due to the formation of passivating surface layers that either consist of a deprotonated surface complex (Palandri and Kharaka, 2004; Pokrovsky and Schott, 2000) or repolymerized silicic acid (Maher et al., 2016) or the formation of secondary mineral phases on the olivine grains, which reduce the reactive surface (Béarat et al., 2006; E. King et al., 2010; Oelkers et al., 2018; Sissmann et al., 2013). These secondary minerals, including the formation of $CaCO_3$, have also been linked to direct TA loss and thus low TA increase observed in several studies (Béarat et al., 2006; Hangx and Spiers, 2009; Köhler et al., 2013; Meysman and Montserrat, 2017; Montserrat et al., 2017; Sissmann et al., 2013). However, the rates and mechanisms of their formation are poorly constrained especially in SW and ASW. Furthermore, the release of toxic elements such as nickel has been subject to speculations about a possible negative effect on the environment if olivine is applied in coastal ecosystems (Flipkens et al., 2021; Montserrat et al., 2017).

In this study, batch experiments were carried out in which ultramafic olivine sand was weathered in ASW. A special focus is laid on the formation of secondary phases and their impact on the CO_2 sequestration efficiency. The implications for the application of enhanced olivine weathering as a CDR measure for climate change mitigation are assessed. Furthermore, the release of potentially toxic elements such as nickel is investigated, which allows a better assessment of environmental risks associated with enhanced olivine weathering.

II.2. Materials and Methods

II.2.1. Materials

Commercially available ultra-mafic sand (UMS) was received from AdL Sandstrahltechnik, which, according to oral information from the company, ultimately derives from several quarries in northern Italy, presumably located in the mafic-ultramafic complex near Vidracco (Kremer et al., 2019). The olivine content of UMS was determined as 74.6 wt-%. For a detailed chemical composition see Tables 1 and 4S (supplement (suppl.)).

The UMS was milled and subsequently sieved to separate grains with a diameter of 100 – 125 µm , based on the recommendation by Strefler et al. (2018). The 100 - 125 µm fraction was then thoroughly washed with ASW until the supernatant was clear. Subsequently, the diluted salts were removed by at least three wash cycles with deionized water (18.2 MΩ-Milli-Q system, hereafter: MQe) until the supernatant was clear. The composition of ASW was calculated for a salinity of 35.0 (Millero et al., 2008). Additionally, 2.3 mmol/l $NaHCO_3$ were added to reach an alkalinity of ~2.3 mmol/l. All chemical components listed in Table 3S (suppl.) were dissolved in MQe. The initial Ca content was lower than listed (~320 mg/l instead of 422 mg/l). After day 50, the ASW used for replacement after sample taking contained the correct amount of Ca (422 mg/l). The lower initial Ca content was applied to keep the saturation state with respect to aragonite and calcite within natural ranges of the surface ocean (Feely et al., 2012) and to avoid strong oversaturation that can appear during the early stage of the experiment due to rapid dissolution of high-energy surface sites created during the milling process.

II.2.2. Experimental setup

The UMS was permitted to react with artificial seawater in 250 ml polyethylene (PE) batch reactors. Three different batches with variable amounts of UMS were prepared, each containing three replicates (n = 3) to verify the reproducibility of the experiments. The amount of ASW was 200 ml for all replicates and batches. 50 ml of ambient air were included to allow for equilibration with the atmosphere. The amount of UMS was varied from 20 g for Batch20 to 10 g for Batch10 and 5 g for Batch5 in order to investigate the effect of the solid/liquid ratio. The air was partly exchanged with the laboratory atmosphere every time samples were taken. All batch reactors with artificial seawater, UMS and gas phase were subjected to constant movement in Heidolph™ Reax2© over-head shakers at ~40 rpm. The experiment was conducted under controlled laboratory conditions (p = 1 bar, 21.5 °C < T < 23.9 °C).

II.2.3. Sampling procedure from batch reactors and water analysis

For each sample (23 in total), two aliquots (2 ml and 5 ml) were taken for further measurements and the same volume of artificial seawater was added to ensure a constant solid/liquid ratio. For the same reason it was made sure that no UMS grains were removed via sample taking. Sampling intervals increased from minutes to hours during day one to every two weeks between day 50 and day 134. The 5 ml aliquot was filtered through a 0.2 µm cellulose membrane filter and refrigerated in 5.2 ml Zinsser™ scintillation bottles. The 2 ml aliquot was used for direct pH measurements (see below) and not filtered to ensure a pristine chemical milieu. At the end of the experiments, the ASW in the batch reactors was carefully decanted over a 0.2 µm regenerated cellulose filter to recover the greyish suspended matter that had formed in the batch reactors during the experiment. Fine particles possibly stuck to the UMS grains were eluted by refilling the

batch reactor with fresh ASW, shaking and decanting it. This procedure was repeated until the supernatant was clear. Withal, it was made sure that all precipitates, which left the bottles, were recovered on the filters. Subsequently, the wet cake was rinsed with pH neutral MQe to elute dissolved species (e.g. salinity). Furthermore, the UMS used in Batch20 was recovered, very carefully rinsed with pH neutral MQe (to only elute salinity), and dried for scanning electron microscope energy-dispersive X-ray spectroscopy (SEM–EDX).

The water samples were analyzed for pH following Dickson (1993). TA was analyzed by titration with diluted HCl to an end point of pH = 4.5 (Stumm & Morgan, 1996; Gieskes et al., 1991) and element concentrations were determined using inductively coupled plasma optical emission spectrometry (ICP-OES).

II.2.4. Solid phase analysis

Pristine (unused and washed) and weathered UMS as well as the precipitates recovered from the batch reactors were digested after a modified alkali-fusion method of van den Boorn et al. (2006), in order to preserve Si, which is lost using conventional HF digestion methods. In contrast to van den Boorn et al. (2006), we used Teflon beakers on a hot plate instead of an oven. Between 20 and 40 mg of NaOH (Merck™ Suprapure®) and a drop of MQe were added and the sample set to reflux for 72 h at 120 °C. Afterwards the sample was diluted with 1ml MQe and transferred to a 1.5 ml save-lock tube and centrifuged at 11000 rpm. The supernatant was separately stored and the undissolved residues retransferred to the Teflon vial, together with 200µl of concentrated HNO_3 and set to reflux for 72 h at 120 °C. After the second reflux 1ml of MQe was added to the sample and the sample centrifuged and the supernatant removed, as described above. The entire procedure was then repeated. Subsequently, the dissolved samples (e.g. all aliquots of each sample) were retransferred to the Teflon beakers and measured with ICP-OES.

Additionally, major and trace elements were determined using the Panalytical Axios Plus X-ray spectrometer at the Institut für Chemie und Biologie des Meeres (ICBM) in Oldenburg. In brief, 700 mg of freeze-dried and homogenized ultra-mafic sand was mixed with 4200 mg lithiumtetraborate ($Li_2B_4O_7$ Spektromelt) and fused to glass beads. The accuracy and precision were determined by simultaneous runs of certified sediment standards BE-N and BIR-1 (IGGE; e.g. Govindaraju, 1994) and in-house standard (PSS) with better than 2.6 % RSD for major elements and 3.3 % RSD for trace elements.

In order to determine the precise composition of the single mineral phases, the UMS before and after the experiment was investigated using a JXA-8200 SuperProbe high resolution SEM and a WDX/EDX Combined Electron Probe Microanalyzer (EPMA) at GEOMAR. For this purpose, a small portion of reacted UMS (see section 2.3) and small portion of fresh UMS were poured on a self-sticking carbon plate. Thereby it was made sure that both samples did not mix and that the grains were placed solitarily. Furthermore, fresh UMS and reacted UMS were embedded in resin and the hardened samples were whetted to create a suitable surface for element analysis along a profile. Afterwards the samples were evaporated with carbon and placed in the EPMA. A large number of measuring points were evenly distributed along a profile with a distance between the measuring points of ~1.5 µm. The spatial resolution of each measuring point is ~5 µm. Hence, neighboring data points overlapped along the profile. The measured values were reported as atomic proportion normalized to 24 oxygen atoms with an RSD better than 0.7 % for simultaneously measured standards and better than 1.5 % for major elements. Finally, the element abundance was normalized to 100 wt.-% and the atomic proportion normalized to 24 oxygen. For

the analysis of carbonate grains, the carbon content was pre-set to 12.01 wt.-%. Apart from quantitative measurements, scanning electron microscope (SEM) images were taken with the same device.

In order to verify the mineral composition, the pristine UMS as well as the precipitates recovered from the batch reactors were measured on a Phillips X-ray diffractometer (XRD) equipped with an automatic divergency slit, monochromator and a Co-cube at 40kV and 35 mA. The samples were finely ground, pressed on an Si monocrystalline plate and measured with $2\theta = [4°; 75°]$ at 0.01° steps for one second at each step. The analysis of the XRD diffractograms was performed via the xPowder^{TM} software and the standard PDF2 database. The results and interpretations are shown in Figures 1S – 4S (suppl.).

II.2.5. Model setup

A dissolution-precipitation model was set up with Wolfram Mathematica to simulate the chemical reactions for each batch experiment. The kinetic box model considers dissolution of olivine after Rimstidt et al. (2012), precipitation of the secondary phases aragonite/calcite, sepiolite, crysotile, talc and $Fe(OH)_3$ based on saturation state calculations (Section S1, suppl.). The model also calculates the concentration of dissolved Mg, Si, Ca, Fe as well as TA and is used to infer the overall reaction stoichiometry.

For each species in solution, ordinary differential equations (ODEs) were formulated as:

$$\frac{dC}{dt} = \varphi_{ol} * r_{ol} - \sum_j \varphi_{m,j} * r_{m,j} - r_s * (C - C_{in}) \quad \text{(II2)}$$

where C is concentration of the considered species in the dissolved phase, t is time, φ_{ol} represents the abundance of the species in olivine (ol) and r_{ol} is the olivine dissolution rate. Precipitation of secondary mineral phases (j) is calculated by multiplying the respective precipitation rate ($r_{m,j}$) with a corresponding stoichiometric coefficient ($\varphi_{m,j}$) defining the content of the considered element in the respective mineral. Sampling and replacement by fresh ASW are considered by applying the sampling rate r_S and the concentration difference between sample (C) and unreacted ASW (C_{in}).

The model is solved using the solver for ordinary differential equations of MATHEMATICA (version 11.3).

The precipitation rate of secondary minerals depends on the corresponding saturation state ($\Omega_i(t)$):

$$r_{pre_i} = \varepsilon_{pre1_i} * UnitStep(\Omega_i(t) - 1) * |\Omega_i(t) - 1|^{\varepsilon_{pre2_i}} \quad \text{(II3)}$$

UnitStep expresses a function that returns 0 for arguments smaller than or equal to 0 and 1 for all arguments larger than 0. Hence, precipitation was assumed to take place only when the solutions were oversaturated with respect to the considered mineral ($\Omega_i(t) > 1$). ε_{pre2_i} defines the order of the reaction and ε_{pre1_i} is defined as

$$\varepsilon_{pre1_i} = k_{pre_i} * \left(1 - \frac{1}{1 + e^{\frac{t-\alpha_i}{\beta_i}}}\right) \quad \text{(II4)}$$

k_{pre_i} is a kinetic constant, α represents the time delay until the precipitation starts and β steers the speed with which the precipitation starts. ε_{pre1_i} was introduced because the solids used in our experiments did not contain seed material for the precipitation of secondary minerals. Hence, the precipitation did not start immediately after oversaturation was reached but with a delay expressed by ε_{pre1_i}. The kinetic constants k_{prei} (Equation II4) were employed to consider the fact that precipitation rates are not only determined by the degree of oversaturation but also by kinetic factors that may either slowdown or accelerate the precipitation reaction.

The oxidation of ferrous iron released during olivine dissolution was simulated applying the kinetic rate for abiotic iron oxidation (Millero et al., 1987).

The mineralogical composition of the UMS and the precipitates was determined with a simple mixing calculation. In a first step, element concentrations measured via ICP-OES were normalized to the measured Si content following:

$$C_{i,S} = conc_i / Si_S \tag{II5}$$

where $C_{i,S}$ $\left(\frac{mol_{element}}{mol_{Si_S}}\right)$ is the concentration of an element normalized to the Si concentration in the respective solid S (UMS or precipitates), $conc_i$ $\left(\frac{mol_{element}}{mg_S}\right)$ is the concentration of an element per milligram solid and Si_S $\left(\frac{mol_{Si_S}}{mg_S}\right)$ is the Si concentration in the solid.

In a second step, the composition was calculated following:

$$C_{i,bulk} = \sum_i \left(C_{i,min} * f_{bulk}\right) / Si_{bulk} \tag{II6}$$

$C_{i,bulk}$ $\left(\frac{mol_{element}}{mol_{Si_{bulk}}}\right)$ represents the molar fraction of an element i in the calculated composition normalized to mol of Si; $C_{i,min}$ $\left(\frac{mol_{element}}{mol_{mineral}}\right)$ is the molar content of the element in a certain mineral. f_{bulk} $\left(\frac{mol_{mineral}}{mol_{bulk}}\right)$ denotes the fraction of a certain mineral in the calculated composition and Si_{bulk} $\left(\frac{mol_{Si_{bulk}}}{mol_{bulk}}\right)$ represents the corresponding Si content (Table 1). The mineral phases used for this calculation were estimated from XRD and WDX measurements. The amount of each mineral (f_{bulk}) was then iterated until $C_{i,bulk}$ values for each element were acceptably close to the measured $C_{i,S}$ values. Normalization to Si was used to allow comparing concentrations (mol/mg) measured via ICP-OES to atomic proportions (normalized to 24 O) obtained via WDX and XRD.

II.3. Result

II.3.1. Composition of the ultra-mafic sand (UMS)

The major and trace element measurements (ICP-OES and XRF) of the UMS are mainly in good agreement with the oxide composition provided by the manufacturer (Table 6S). Furthermore, 5% of the UMS consisted of accessory oxides such as MnO, K_2O, CaO and Al_2O_3 which were not accounted for in

the manufacturer information. According to WDX measurements the olivine used consists of 90.3% forsterite and 9.7 % fayalite leading to the formula $(Mg_{0.90}Fe_{0.10})_2SiO_4$ (Fo90) and based on the simple mineral model accounts for 74.62% of the UMS (Table II 1). The second largest fraction is Orthopyroxene (Opx) with the simplified structural formula $(Mg_{0.9}Fe_{0.1})_2(Al_{0.15}Si_{0.85})_2O_6$ accounting for 15.92% followed by an amphibole (Amph., likely tremolite) with the structural formula $(Na_{0.36}K_{0.14})(Ca_{0.95}Mg_{0.05})_2(Cr_{0.014}Fe_{0.079}Mg_{0.79}Al_{0.087}Ti_{0.03})_5(Si_{7.4}Al_{0.6})O_{22}(OH)_2$ (5.41 %) and a Clinopyroxene (Cpx) with 3.5 % and the structural formula $(CaMg)_2(Si_{0.9}Al_{0.1})_2O_6$. Additionally, WDX measurements revealed the presence of accessory spinel and Ni and Fe sulfides. The abundance of these phases was estimated employing ICP-OES data and EDX observations.

Table II 1: Mineralogical model for UMS (bulk) combining XRD, WDX and ICP-OES data. Element concentrations in minerals are given as atomic proportion relative to 24 oxygen. Oxygen is not measured but set to 24. The mineral phases were determined based on XRD measurements, the elementary compositions of mineral phases are based on WDX measurements (Table 5S, suppl.). Opx: Orthopyroxene, Cpx: Clinopyroxene, Amph: Amphibole. $C_{i,bulk}\left(\frac{mol_{element}}{mol_{Si_{bulk}}}\right)$ represents the calculated bulk concentration of each element normalized to bulk Si, $C_{i,UMS}\left(\frac{mol_{element}}{mol_{Si_{UMS}}}\right)$ are measured element concentrations obtained by full digestion of UMS normalized to the measured Si content of the UMS.

Species	Al	Ca	Cr	Fe	K	Mg	Mn	Na	Ni	Ti	Si	O_2	% (wt.)
Phase													
Forsterite	0.002		0.002	1.182		11.02	0.018	0.003	0.036		5.868	24	74.62
Opx	0.663	0.093	0.034	0.767		7.032	0.019	0.055	0.007	0.010	7.504	24	15.92
Cpx	1.104	3.352	0.091	0.288		3.350		0.360	0.005	0.042	7.471	24	3.55
Amph.	1.454	1.905	0.071	0.393	0.174	4.518		0.369	0.008	0.096	7.242	24	5.40
Spinel	10.24		1.603	1.597		4.605	0.015		0.032	0.004		24	0.07
Sulfide				1.900					0.350				0.45
$C_{i,bulk}$	0.039	0.039	0.002	0.174	0.002	1.543	0.003	0.007	0.006	0.001	1.0	3.822	100
$C_{i,UMS}$	0.035	0.034	0.002	0.174	0.000	1.543	0.003	–	0.006	0.001	1.0	3.822	

II.3.2. Concentrations of dissolved species measured during the experiments

All experiments show a common trend of increasing TA in the early stage of the experiment and a decrease below initial values (2.36 ± 0.011 meq/l) after a certain period of time (Figure II 1a). The highest and lowest values (2.65 ± 0.011 meq/l; 1.266 ± 0.019 meq/l), were measured in Batch20 (solid/liquid = 1/10) after one day (highest) and at the very end of the experiment (lowest). Batch5 (solid/liquid = 1/40) shows the lowest overall temporal gradient. The peak values occur the latest for Batch5, which also shows the highest final TA values, even though associated with the largest errors. Dissolved silicon concentrations [Si] increase persistently over the entire experiment (Figure II 1b). The fastest increase is observed during the initial stage of the experiment (e.g. Tables 8S – 10S, suppl.). The rate of [Si] increase then stabilizes during the experiment to nearly constant values towards the end. An exception to that trend is visible in Batch5. Here, the rate increases abruptly around day 78 (Table 10S, suppl.) before a steady increase is attained. This rate change does not occur in all three replicates, which is reflected in high double standard deviation (2SD) values for [Si] towards the end of the experiment (Figure II 1b). The highest concentrations are observed at the end of the experiment with a final [Si] of 421.8 ± 1.3 µmol/l (Batch20), 286.6 ± 6.4 µmol/l (Batch10 (solid/liquid = 1/20)) and 190.3 ± 42.1 µmol/l (Batch5). Calcium concentrations [Ca] (Figure II 1c) show a common trend for all three batches: During the early stage of the

experiment, [Ca] stays relatively constant, before the concentrations start to drop. Towards the end of the experiment, [Ca] increases again. Similar to TA values, the initial decrease appears latest in Batch5 and earliest and strongest in Batch20. Interestingly, until day three [Ca] follows a pattern that is similar to Mg concentrations ([Mg]) values (Figure 5S, suppl.) with a well-pronounced peak in Batch20 after 115 minutes which, at the same time, represents the highest measured [Ca] value of all three batches ([Ca] = 8.26 ± 0.02 mmol/l). However, the temporal changes in [Mg] do not exceed the standard deviation of the three replicates due to the high [Mg] values in the ASW. In Batch20, [Ca] decreases constantly after one day from 8.10 ± 0.01 mmol/l to a minimum value of 6.58 ± 0.01 mmol/l at day 78. The decrease is weaker after day 50. For Batch10 and Batch5 the [Ca] decrease is less pronounced and occurs with a delay of 2 days in Batch10 and after 4 days in Batch5. After 50 days, the replenishment of ASW with high Ca concentrations (see section 2.1) caused an increase in [Ca] in all three batches.

Final experimental [Ca] is 6.83 ± 0.01 mmol/l for Batch20, 7.32 ± 0.01 mmol/l for Batch10 and 7.78 ± 0.01 mmol/l for Batch5. Overall, the behavior of [Si], [Ca] and TA reflects the amount of USM used in the experiments. Elevated solid/water ratios induce high [Si] and low [Ca] and TA values at the end of the experiments.

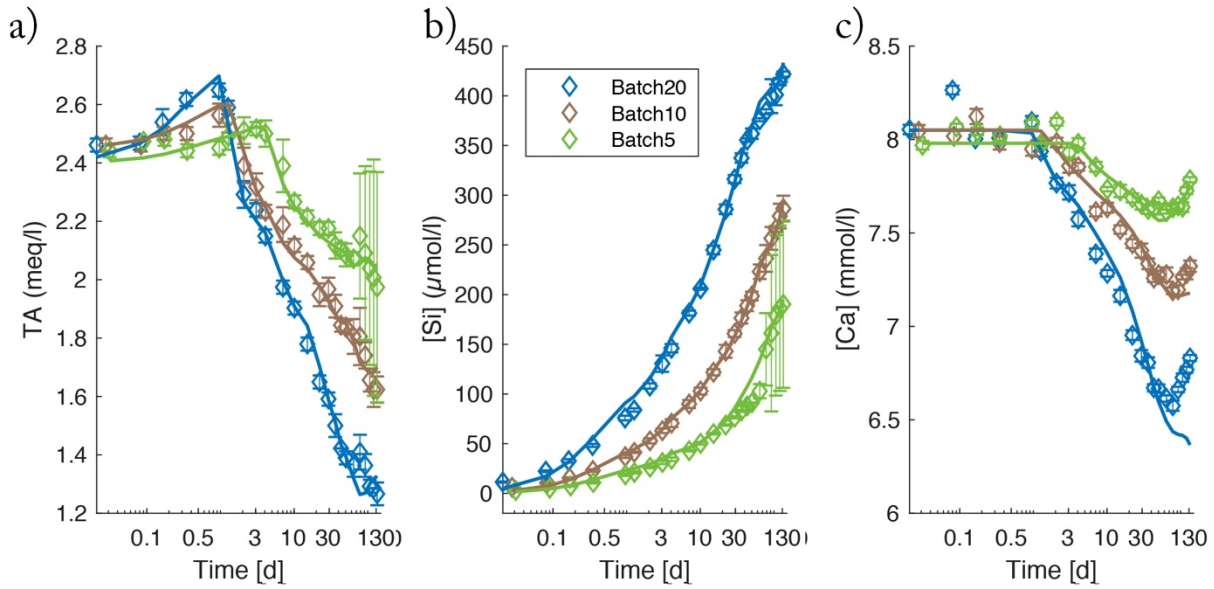

Figure II 1:TA (a), [Si] (b), and [Ca] (c) values measured during the experiments. Symbols indicate mean values of three replicates for each batch. Error bars are reported as ± 2SD of the mean values. Lines represent modelled concentrations (blue; Batch20, brown: Batch10, green; Batch5). A logarithmic scale is used for the time axis.

For all batches, the model used for the simulation was able to reproduce measured values very accurately (Figure II 1a – 1c). The sum of squared errors ranged between 0.03 and 0.52 with highest errors in Batch5. Additional data used in the modeling are provided and described in detail in the supplementary material, section S1.

II.3.3. Secondary mineral formation and precipitation rates

The change in water chemistry by dissolution of olivine and the subsequent accumulation of cations change the saturation state with respect to a variety of mineral phases containing these ions (Figure II 2). Saturation states (Ω_i) were calculated using PHREEQ (Parkhurst and Appelo, 1999) where values above 1 indicate oversaturation (suppl.). During all experiments, DIC calculated from measured TA and pH values follows the same trend as TA (Figure II 1a) and [Ca] (Figure II 1c). In contrast, pH values (Figure II 2b) follow a different trend. In all batches an initial increase in pH can be observed. This increase is strongest and appears earliest (until day 1) in Batch20. In Batch10 and Batch5 pH values rise less rapidly and highest values were measured latest in Batch5. Subsequently, the pH values decrease again in all batches. Again,

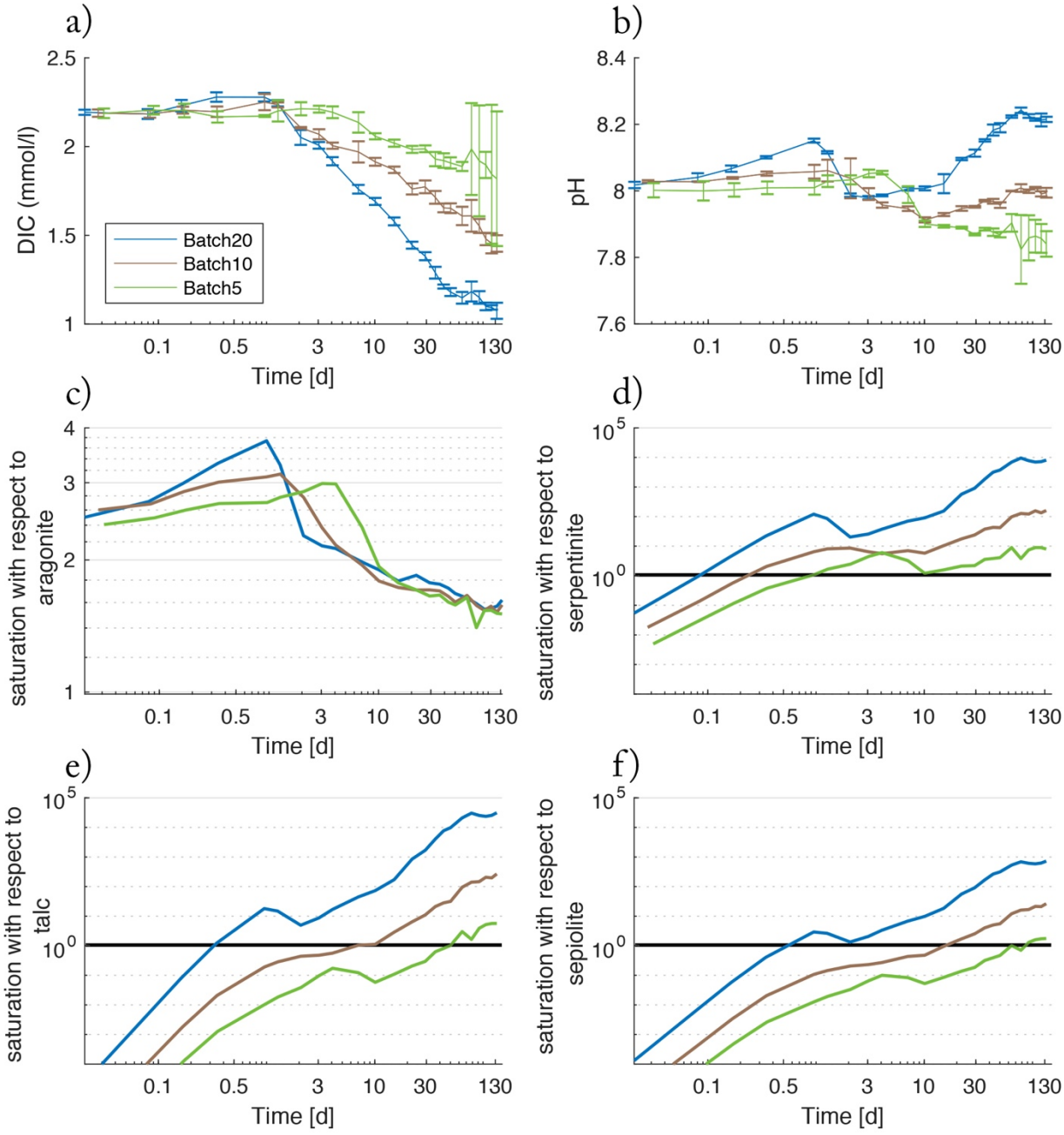

Figure II 2:DIC (a), pH (b) and saturation states with respect to aragonite (c), serpentine (d), talc (e) and sepiolite (f) as calculated for Batch20 (blue), Batch10 (brown) and Batch5 (green). Error bars in (a) reflect ± 2SD that are calculated form the standard deviations of measured pH and TA values.

this decrease ends first in Batch20 followed by Batch10 and is observed latest in Batch5. Contrary to the first increase, the subsequent drop has a similar magnitude in all batches which leads to lowest values in Batch5. After a well-pronounced peak, pH values decrease in Batch10 and Batch20 towards the end of the experiment. In Batch5 pH values plateau until day 78 before they slowly decrease towards the end. Note that the standard deviation of the three replicates in Batch5 becomes very large during the last days which leads to the assumption that an external input might have occurred in one of the Batch5 batch reactors.

In all three batches, the system is oversaturated with respect to aragonite (saturation state >1) over the entire course of the experiment (Figure II 2c). Following DIC (Figure II 2a) and TA, the saturation states increase towards an initial peak that occurs first in Batch20, then Batch10 and less pronounced in Batch5. During the subsequent decrease that persists until the end of the experiment, the saturation states in all three batches converge towards a common value of ~1.5.

For the phyllosilicate phases considered in this study (serpentinite, talc, sepiolite), the saturation states, which depend on [Si], [Mg] and pH, develop differently from saturation with respect to aragonite. Since Si and Mg concentrations increase persistently, saturations follow this trend which is, though, overlain by changes in pH values (Figures II 2d-f). The most striking features are the time after which the solution exceeds oversaturation with respect to the individual minerals (saturation values >1) and the extent of oversaturation attained at the end of the experiments. Whilst serpentine saturation (Figure II 2d) increases to a state of oversaturation very early in all batches (first Batch20 after ~0.1 days, latest Batch5 after ~1 day), saturations with respect to talc increase later and reveal higher differences between the batches (Figure II 2e). A similar trend but with overall lower oversaturation is visible for sepiolite (Figure II 2f). Thus, saturation with respect to both minerals (talc and sepiolite) rise above 1 in Batch5 only after day ~50 and day ~80 respectively.

II.3.4. Trace metal concentrations

Manganese concentrations [Mn] increase over the first 3 days during all experiments (Figure II 3a). A well-pronounced peak is clearly visible in all batches at day 3, followed by a minimum at day 4. Subsequently, [Mn] values increase again but do not follow a common trend anymore. Important features are the strong increase in Batch5 between day 46 and day 78 which coincides with a strong increase in [Si] (Figure II 1b) and the fact that lowest final values are observed in Batch20 (~0.3 µmol/l), whereas the concentrations in Btach10 and Batch5 are equal within the error (~0.5 µmol/l).

Despite the larger 2SD compared to [Mn], Ni concentrations show a clearly increasing trend throughout the experiment (Figure II 3b) with a tendency towards highest values for Batch20 until day 22. A strong final increase for Batch5, that coincides with the increase in [Si], leads to values that are equal within the error for all batches (Batch20: 1.23 ± 0.26 µmol/l, Batch10: 1.31±0.23, Batch5: 1.42 ±0.26 µmol/l).

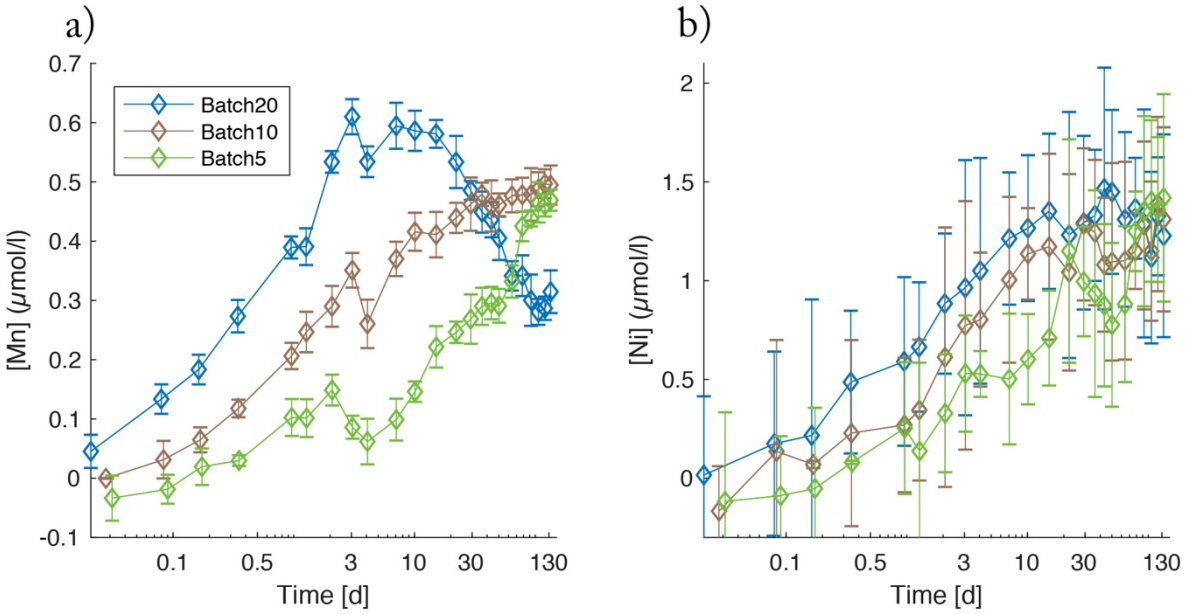

Figure II 3: Concentration of dissolved Mn (a) and Ni (b) for Batch20 (blue), Batch10 (brown) and Batch5 (green). Error bars are reported as ± 2SD.

II.3.5. Model results: composition of precipitates and overall stoichiometry

The kinetic rate law employed in the model allows for secondary mineral precipitation only after the solutions reach oversaturation with respect to the considered mineral (equations II3,II4). Precipitation does not start immediately after oversaturation is reached, since nucleation has to occur before precipitation can remove substantial amounts of solutes from solution. The time delay accounting for nucleation and the kinetic constants are derived by fitting the model to the measured dissolved species concentrations. The least deviation of modelled values from measured ones is reached with relatively low rates for talc and sepiolite precipitation compared to serpentine formation (Figures II 4b-d). It also becomes clear that apparently phyllosilicate formation is less dependent on the saturation state compared to aragonite precipitation (Figure II 4e; equations II3,II4, Table1S, suppl.). The fastest precipitation is applied for $Fe(OH)_3$ because dissolved ferrous Fe released from olivine is rapidly oxidized to ferric iron and precipitated as iron hydroxide. (Figures II 4a,f).

The time-integrated rates of olivine dissolution and secondary phase precipitation calculated in the model are employed to derive the overall reaction stoichiometry for each of the three batches:

Batch20:

$$0.77H_2O + (Mg_{0.90}Fe_{0.10})_2SiO_4 + 0.055O_2 + 0.89Ca^{2+} + 0.53CO_2 + 0.36HCO_3^- \rightarrow 0.18Fe(OH)_3 + 0.25Si(OH)_4 + 0.89CaCO_3 + 0.025Mg_2Si_3O_{7.5}(OH)(H_2O)_3 + 0.32Mg_3Si_2O_5(OH)_4 + 0.0090Mg_3Si_4O_{10}(OH)_2 + 0.016Fe^{3+} + 0.77Mg^{2+} \quad \text{(II7)}$$

Batch10:

$$0.79H_2O + (Mg_{0.90}Fe_{0.10})_2SiO_4 + 0.055O_2 + 0.98Ca^{2+} + 0.45CO_2 + 0.53HCO_3^- \rightarrow 0.18Fe(OH)_3 + 0.27Si(OH)_4 + 0.98CaCO_3 + 0.021Mg_2Si_3O_{7.5}(OH)(H_2O)_3 + 0.32Mg_3Si_2O_5(OH)_4 + 0.0061Mg_3Si_4O_{10}(OH)_2 + 0.012Fe^{3+} + 0.77Mg^{2+} \quad \text{(II8)}$$

Batch5:

$$0.79H_2O + (Mg_{0.90}Fe_{0.10})_2SiO_4 + 0.055O_2 + 0.98Ca^{2+} + 0.51CO_2 + 0.47HCO_3^- \rightarrow 0.19Fe(OH)_3 + 0.32Si(OH)_4 + 0.98CaCO_3 + 0.007Mg_2Si_3O_{7.5}(OH)(H_2O)_3 + 0.32Mg_3Si_2O_5(OH)_4 + 0.0025Mg_3Si_4O_{10}(OH)_2 + 0.013Fe^{3+} + 0.80Mg^{2+} \quad \text{(II9)}$$

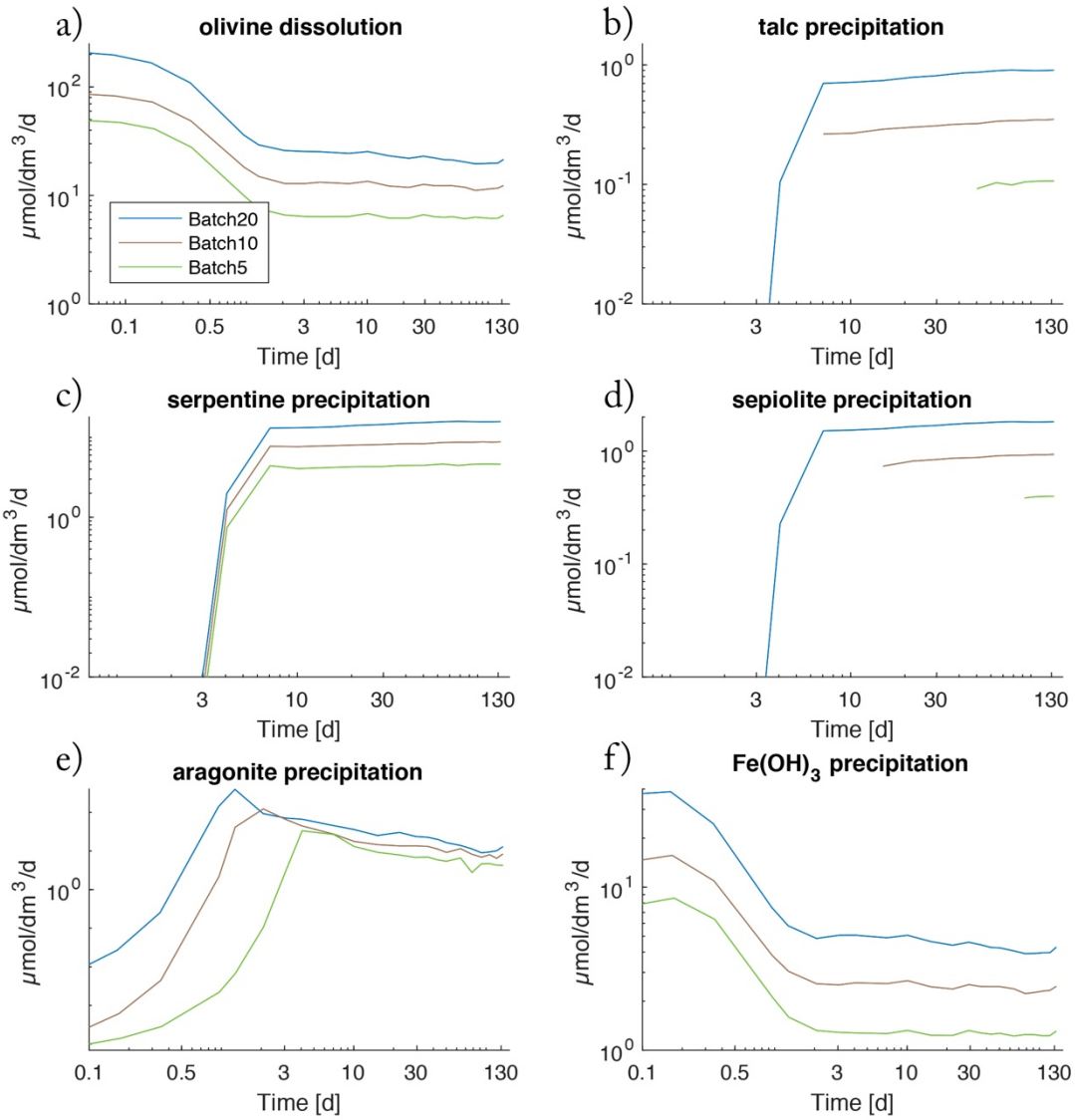

Figure II 4: Dissolution rate for olivine (a) and precipitation rates for secondary phases (b-f) as calculated via the model for all batches.

To verify these model results, the composition of the greyish suspended matter that had formed in the batch reactors was determined applying a simple mixing calculation (equations II3, II4). Especially the amount of fine-grained UMS in the suspended matter was scrutinized to subsequently estimate the composition of the actual precipitate. In contrast to the UMS procedure, no WDX measurements were

performed on the precipitate. Hence, the mixing calculations are only based on XRD scans (Figures 1S - 4S, suppl.) and full digestion, followed by ICP-OES measurements (Table 6S, suppl.). The results of the calculations are presented in Table II 2 and suggest a molar portion of UMS from 25% for Batch5 to 37.5% for Batch10. After the subtraction of these portions the result reveals very similar compositions for all batches with ~16-23 % sepiolite and >70 % aragonite as the major components. Minor phases are chrysotile (~3-4 %), $Fe(OH)_3$ (~3-4 %), and Al_2O_3. Even though Al_2O_3 is unlikely to have formed, it was included for the precipitates to match the measured compositions. It is most likely incorporated into the different partly amorphous Mg-Si-phases. Overall, the solid phase data and model results are broadly consistent as both indicate that $CaCO_3$ and a range of Mg-Si phases are the major secondary phases formed during the experiments.

II.3.6. EDX/WDX observations of weathered UMS

After 134 days of agitation in batch reactors, grains of UMS were distinctively rounded with secondary mineral phases grown in indentations and fissures (Figure II 5). The WDX measurement on the blank grain (Figure II 5a2) revealed that the Mg/Si ratio was elevated for the olivine grain (Mg/Si = 2.33) compared to the pristine value (Mg/Si = 1.78) (Table 5S suppl.). The secondary mineral phase measured in inundations clearly indicates calcium carbonate and a very small contribution of iron (Figure II 5a1).

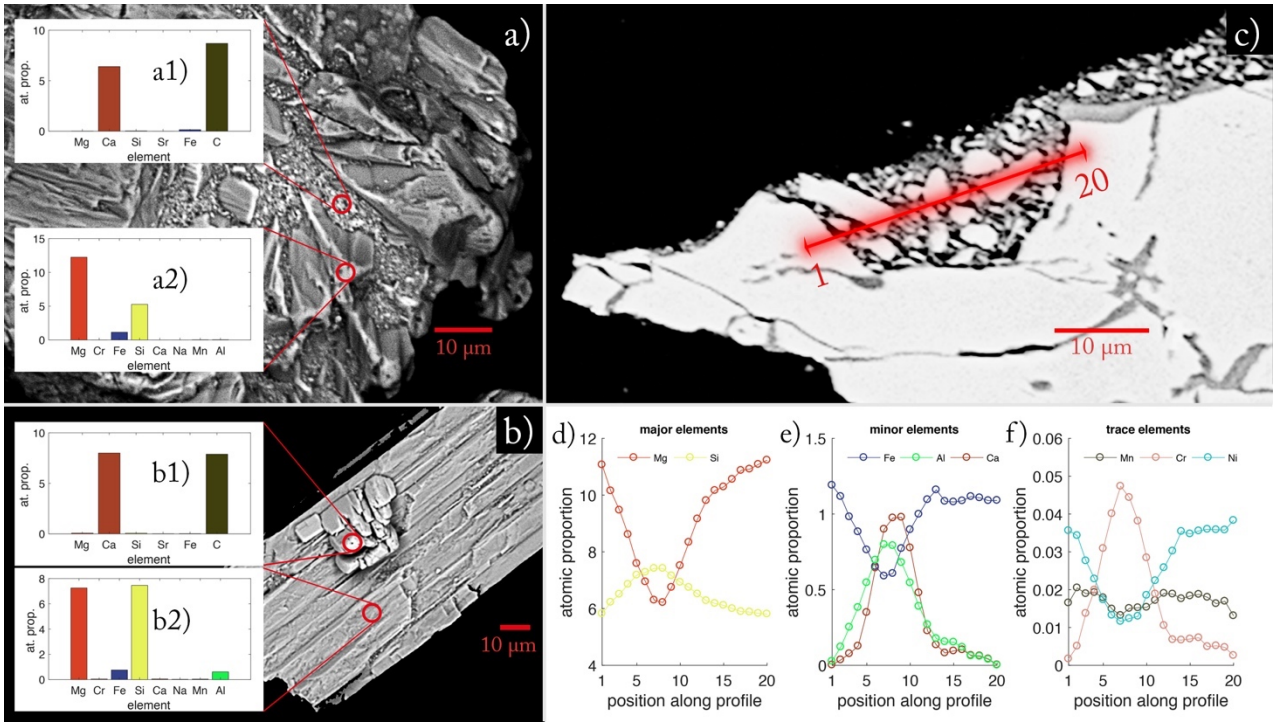

Figure II 5: EDX images of reacted UMS grains taken at the end of the experiments. a) Olivine grain with secondary mineral phases. a1) Atomic proportions in secondary minerals grown on olivine. a2) Atomic proportion of host mineral. b) Orthopyroxene grain with on-grown aragonite crystal. b1) Atomic proportion of secondary mineral grown on Orthopyroxene. b2) Atomic proportion of host mineral for secondary phase (b1). Red circles indicate areas of WDX composition measurements. c) illustrates the transect through secondary minerals on an olivine grain. The red line denotes the measured transect. d) shows the atomic proportion of major elements measured along the profile shown in 5c). e) shows the atomic proportion of minor elements measured along the profile shown in 5c). f) shows the atomic proportion of trace elements measured along the profile shown in 5c).

In Figure II 5b, the elementary distribution suggests orthopyroxene as host mineral for secondary mineral formation (Figure II 5b2). Here again, the data clearly indicate that the secondary phase is largely composed of calcium carbonate (Figure II 5b1). The cross-section measured on an altered olivine grain (Figure II 5c, Figures II 5d-e) illustrates that the material found on the grains not only consists of calcium carbonates. Instead, it is a heterogenous mixture of different phases with different densities (indicated by different shades of grey, Figure II 5c). The atomic proportion (relative to 24 oxygen atoms) along the profile (Figures II 5d-e) indicates a smooth transition from the host material olivine to different Mg-Si phases and back. The smoothness is an artefact of the measuring precision of the micro-probe indicated by the blurred area around the profile line. Hence the material is too fine grained to be examined in detail. Still, the asymmetric increase of Al and Ca indicates the presence of different phases along the profile which is underpinned by the jagged distribution of trace elements along the profile (Figure II 5f). Overall, the measurements revealed that the agglomerations are most likely a mix of fine-grained UMS remnants cemented with a mix of calcium carbonate and hardly determinable secondary Mg-Si-phases. The examples in Figure II 5 represent typical patterns obtained during a series of measurements. Table II 2: Calculated composition of suspended matter filtered from batch reactors. Values represent mean values of three replicates per batch. For the precise composition of the UMS, see Table II 1.

Table II 2: Calculated composition of suspended matter filtered from batch reactors. Values represent mean values of three replicates per batch. For the precise composition of the UMS, see Table II 1.

	Component	mol%	% (M)	mol on filter	mg on filter	mol % precipitate
Batch5	UMS	25.00	31.721	0.0258	3.735	
	Sepiolite	12.35	12.229	0.0127	1.440	16.73
	Serpentinite	2.60	3.167	0.0027	0.373	3.52
	Talc	1.10	0.917	0.0011	0.108	1.49
	$CaCO_3$	55.40	48.745	0.0572	5.739	75.07
	Fe(OH)3	2.35	2.146	0.0024	0.253	3.18
	Al2O3	1.20	1.076	0.0012	0.127	1.63
Batch10	UMS	37.05	45.762	0.0417	6.014	
	Sepiolite	14.40	13.304	0.0162	1.748	23.34
	Serpentinite	1.10	1.304	0.0012	0.171	1.78
	Talc	0.40	0.325	0.0005	0.043	0.65
	$CaCO_3$	43.40	37.172	0.0488	4.885	70.34
	Fe(OH)3	2.40	2.133	0.0027	0.280	3.89
	Al2O3	1.25	1.091	0.0014	0.143	2.03
Batch20	UMS	29.90	37.819	0.0675	9.733	
	Sepiolite	11.10	10.502	0.0190	2.703	16.04
	Serpentinite	2.00	2.428	0.0029	0.625	2.89
	Talc	0.40	0.332	0.0005	0.086	0.58
	$CaCO_3$	53.80	47.189	0.0610	12.145	77.75
	Fe(OH)3	1.90	1.729	0.0020	0.445	2.75
	Al2O3	0.90	0.804	0.0009	0.207	1.30

II.4. Discussion

II.4.1. Robustness of modelled and measured results

The consistency of measurements and model results suggests a step forward towards the precise understanding of the processes operating during olivine dissolution in seawater. For the interpretation of the results, however, it is necessary to shine a light on uncertainties. A crucial aspect is the surface area of the olivine grains. Rough edges that originate from the grinding process represent high energy sites which enhance the reactive surface of the grains but are worked off quickly during the early stage of the experiment. Even though, the initially enhanced reactive surface was considered in the kinetic model (Figure II 4a, equation 11S, suppl.), all calculations are based on the geometrical surface area for spherical grains with a diameter of ~100 µm. Hence, the actual reactive surface is most certainly larger than assumed in the kinetic model of olivine dissolution. It is thus possible that the dissolution rates were actually higher than those calculated in the model. Moreover, idealized mineral phases were used in the modeling of authigenic mineral precipitation whereas the solid phase analyses indicate the formation of amorphous phases with a poorly defined composition (Figure II 5).

Moreover, the model may not consider all processes occurring in the experiment. In general, olivine was assumed to be the only mineral phase that dissolves. Despite the considerably lower dissolution rates of other mineral phases (Gruber et al., 2019; Lerman et al., 1975; Wolff-Boenisch et al., 2011), their dissolution can play an important role at the beginning of the experiment due to the enhanced surface area. The admixture of very fine UMS particles that made up to 30 % of the recovered precipitates (Table 2) and enhanced surface roughness can lead to a large number of possibly fast initial dissolution-precipitation reactions that might explain fluctuations in elementary concentrations in the early stage of the experiment.

Despite these uncertainties, the model is able to reproduce the concentrations of dissolved species measured over the course of the experiments (Figure II 1). This and the fact that the same kinetic rate laws, functions and parameter values were used for all batches, suggests that the overall stoichiometries derived from the model are adequate.

II.4.2. Secondary mineral phases

The major goal of this study was to close the gaps in knowledge regarding the impact of secondary phases on the sequestration efficiency of enhanced silicate weathering. Thus, the experiments were designed to allow investigating the precipitation of secondary phases under the following premises:

- In order to reduce the number of unknown quantities, ASW was used instead of filtered seawater.
- Commercially available ultramafic sand was used since future large-scale applications of enhanced silicate weathering as CDR measure will rely on widely available rocks rather than purified olivine
- Different solid-phase/water ratios were applied to investigate the dependency of secondary mineral formation on saturation states.
- A kinetic model was specifically designed to provide a deeper understanding of the kinetics and overall stoichiometry of authigenic mineral formation.

The most striking feature in the data presented in this study are the counterintuitively decreasing TA values (Figure II 1a) as the weathering of olivine is supposed to lead to the exact opposite (Fuss et al., 2018; Köhler et al., 2013; Meysman and Montserrat, 2017; Montserrat et al., 2017; Oelkers et al., 2018; Renforth and Henderson, 2014; Rigopoulos et al., 2018; Rimstidt et al., 2012). The formation of secondary minerals has been invoked as a possible mechanism to reduce the net gain in TA during olivine weathering (Griffioen, 2017; Meysman and Montserrat, 2017; Montserrat et al., 2017; Oelkers et al., 2018; Torres et al., 2019) but to our knowledge have never been investigated in ASW in great detail. They appear in the form of phyllosilicates and carbonates. In seawater with a low rock/water ratio, the latter ones mainly exist in form of aragonite, calcite and Mg-calcite as these are the major authigenic carbonate phases that are formed in this chemical environment (Lein, 2004; Schrag et al., 2013; Torres et al., 2020; Wallmann et al., 2008). Mg-carbonates can be neglected as they only form under very special conditions mainly in highly alkaline facies with very high rock/water ratios, which do not match our experimental set-up (Dehouck et al., 2014; Entezari Zarandi et al., 2017; Ferrini et al., 2009; Moore et al., 2004; Power et al., 2013)

II.4.3. Precipitation of $CaCO_3$

The direct comparison of [Ca] and DIC (Figure II 1c, Figure II 2a) reveals that the decrease in [Ca] is accompanied by a corresponding decrease in DIC. Meanwhile, [Mg] concentrations increased (Figure II 5S suppl.). Combined with the low Mg/Si ratios in the recovered precipitates (Tables 6S, 7S, suppl.), the most likely explanation for these values is the formation of $CaCO_3$ either in the form of aragonite or calcite, as this process is the only one that has the potential to reduce both C and Ca to an equal amount. This is underlined by the composition of the precipitates (Table 2, Table 7S) that were calculated via equations II5 and II6. Stockmann et al. (2014) suggest that forsterite has the potential to foster the nucleation of calcite on its surface. The major difference in the experimental design of Stockmann et al. (2014) and this study is the reagent in which forsterite was dissolved. Whilst in this study ASW with a pH of ~8 was used, Stockmann et al. (2014) dissolved forsterite in Na-carbonate and Ca-chlorite solutions at a pH of ~9. XRD measurements of precipitates recovered from the batch reactors in this study revealed no significant calcite content but indicated the presence of aragonite (Figures 1S to 3S, suppl.). Despite the fact that these measurements have a very high noise/signal ratio and are therefore fraught with a very large error this is consistent with the findings of Rigopoulos et al. (2018), who found aragonite as the only $CaCO_3$ species in weathering experiments with dunite, and with the fact that aragonite is preferably precipitated in Mg rich solutions (De Choudens-Sánchez and González, 2009; Sun et al., 2015). Mixing calculations revealed that the precipitates recovered from the batch reactors consisted of ~72 % (molar) $CaCO_3$ averaged over all batches, which is very close to the modelled values of ~65 % (molar) as average for all batches. For natural seawater, Burton and Walter (1987) ascertained growth rates of aragonite 3 times higher compared to calcite at 25 °C with highest aragonite dominance for calcite saturations of ~5, which corresponds to the values during the early stage of the experiment of this study. These findings are supported by Zhong and Mucci (1989) who used a different rate equation but found very similar total rates. In order to match measured and modelled [Ca] and TA values, aragonite precipitation needed to be considered in the model used in this study (Figures II 4e, 6b). When comparing the rate parameters for aragonite precipitation which lead to the best model fit in this study, with the constants of Burton and Walter (1987), the values were higher compared to the values of Burton and Walter (1987) for Batch20 and Batch10 but matched for Batch5. The slightly higher values in this study indicate possible catalyzation of $CaCO_3$ precipitation on the surface of the UMS grains, as for the same saturation stronger precipitation takes place.

Our data clearly show that, contrary to findings of Montserrat et al. (2017), calcium carbonate is formed during the experiments and is responsible for most of the observed TA loss.

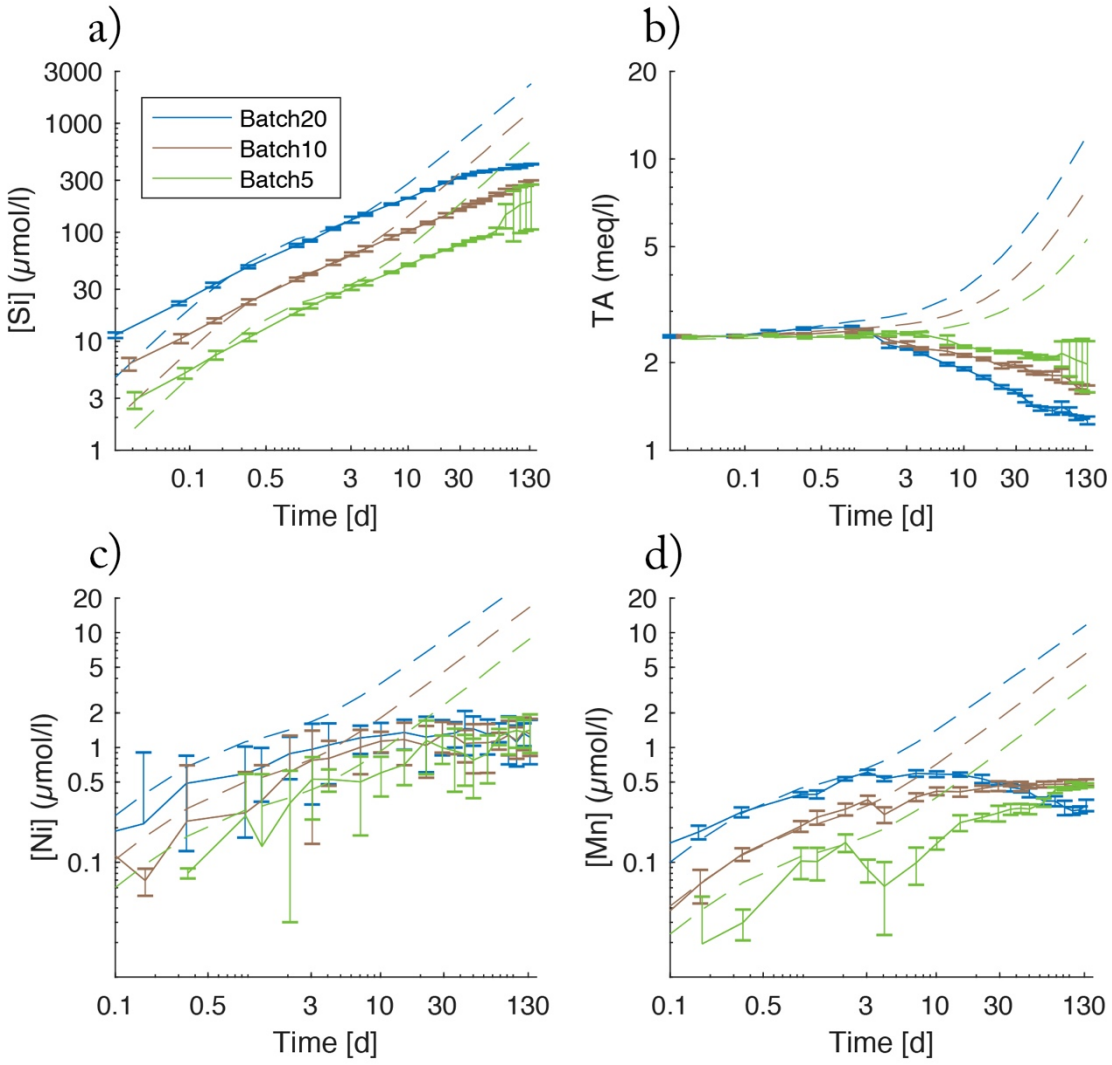

Figure II 6: Comparison of measured values (solid lines) for dissolved species and modelled concentrations that would result from congruent dissolution of UMS without formation of secondary minerals (dashed lines). a) silicon, b) TA, c) nickel, d) manganese.

II.4.4. Secondary phyllosilicate and $Fe(OH)_3$ phases

Next to calcium carbonate, phyllosilicates have the potential to form during olivine weathering (Buurman et al., 1988; Delvigne et al., 1979; Griffioen, 2017; Hellmann et al., 2012; Montserrat et al., 2017; Rigopoulos et al., 2018; Sissmann et al., 2013; Suárez et al., 2011). Hence, precipitation of serpentine, sepiolite and talc is investigated in this study (Figures II 4b-d). Calculated saturation states vary largely for the different minerals (Figure II 2). In the model, the precipitation of each mineral depends on the magnitude of oversaturation and a kinetic constant (Lasaga, 1998). The best fit to the Si, Mg and TA data was reached applying a very small rate constant for talc precipitation compared to rate constants for serpentine and sepiolite. Hence, talc is least represented in the model results (0.25 % (molar), averaged over all models). This is fairly congruent to the calculated composition of the recovered precipitates where the average content of talc was 0.89 % (molar) (Table 2). Large discrepancies between the model and the calculated mineral composition based on measurements occur with regard to the ratio of sepiolite to serpentine

$\left(\frac{sep}{serp}\right)$. The numerical model suggests a $\left(\frac{sep}{serp}\right)$ of ~0.066 (average of all batches) whereas the mineralogic model reveals a $\left(\frac{sep}{serp}\right)$ of 7.8. The saturation states (Figure II 2) clearly show that ASW was least oversaturated with respect to sepiolite in all batches and undersaturated in Batch10 and Batch5 for at least half the experimental period. Thus, sepiolite appears highly unlikely to be the major precipitated phase (Figure II 4d).

Hence, the remaining explanation is that a major portion of secondary phases with low Mg/Si ratios had stuck on the grains and was therefore not recovered. This is supported by EDS images (Figure II 5). Several grains were found that were covered with secondary phases. Next to $CaCO_3$ the WDX analysis of these secondary phases indicates a large variety of Mg-Si-phases. Via their composition, though, these phases could hardly be identified as any of the Si-phases considered in the model.

Also, XRD measurements do not indicate high amounts of the phyllosilicate phases that were considered in the model. It is thus likely that the Mg-Si bearing phases in this study show the same amorphous character as the phases found by Davis et al. (2009) who described a "deweylite assemblage" which stands for a mix of different Mg-silicates whose precise chemical composition can vary strongly (Hövelmann et al., 2011). Thus, the mixed composition of all Si-bearing precipitates could be understood as the composition of a Si-Mg-rich partly amorphous bulk phase, which is well represented by the noisy XRD diffractograms (Figures 1S -3S, suppl.).

Similarly to secondary phyllosilicates, $Fe(OH)_3$ seems to have attached to UMS grains, as the measured (and subsequently calculated) content of $Fe(OH)_3$ in the suspended matter recovered from the batch reactors was ~3 % on average and the model calculated ~13 % (averaged over all batches). This is evidenced by little dense flakes that were found on the weathered grains during EDX/WDX measurements that consisted mainly of Fe and is supported by the fact that less precipitate was recovered, than the suggested by the model. Like the precipitation of phyllosilicates and carbonates, the formation of $Fe(OH)_3$ releases protons. It is therefore important to consider this process with regards to the overall efficiency of enhanced silicate weathering.

II.4.5. Dissolution kinetics of olivine

Over the first 2-4 days of the experiments dissolved [Si] and TA values are close to those predicted by the kinetic rate law for olivine dissolution used in our model (Rimstidt et al. 2012). However, the measured concentrations are significantly lower than the predicted value over the following period (Figures II 6a, II 6b) This observation could in principle either be explained by a decline in the olivine dissolution rate due to surface passivation/occupation by secondary minerals, or by the removal of Si and TA from solution via precipitation of secondary minerals.

Montserrat et al. (2017), whose experiment A3 was very similar to the experiments of this study, proposed a dissolution rate for olivine in dependence of the changing saturation state with respect to olivine that was calculated after Palandri and Kharaka (2004). For the validation of this hypothesis, they fitted their model to the accumulation of Si in solution $\left(\frac{d[Si]}{dT}\right)$, regardless of Si removal by secondary phases. The outcome is a good approximation of the apparent dissolution rate.

A passivation of the surface as a result of incongruent weathering has previously been invoked as one explanation for the decrease in dissolution rate over time (Hellmann et al., 2012; Maher et al., 2016; Montserrat et al., 2017; Wolff-Boenisch et al., 2011). Apart from Mg isotopes (Hellmann et al., 2012), which

were not measured in this study, one indication for such processes is the cation depletion of the reactive surface of the olivine grains after the weathering process. Hellmann et al. (2012) as well as Maher et al. (2016) used HCl and NaCl solutions respectively which did not contain Mg. Likewise, Montserrat et al. (2017) reported highest Mg depletion on reactive surfaces for experiments with Mg-reduced ASW. Extensive WDX measurements applied in this study have not revealed such depletion. Instead, highest Mg/Fe ratios in olivine were measured on blank surfaces of weathered olivine that were not covered with secondary mineral phases (Figure II 5a2). Thus, the depletion and subsequent passivation of forsterite surfaces observed in other studies during dissolution seems to be a result of diffusive equilibration between a depleted reagent and the crystal surface. This effect did not occur in in our study, as the background activity of Mg is very high in ASW (Millero et al., 2008). Hence, following the idea of an equilibrated steady state for surface layers (Maher et al., 2016), olivine grains might as well be considered a temporary sink for Mg, assuming the diffusive replacement of Fe^{2+} with Mg^{2+} supplied from the ambient seawater, similar to the process of Mg-replacement by H^{+} described by Oelkers et al. (2018). Additionally, elevated (Mg+Fe)/Si ratios point towards the results of Pokrovsky and Schott (2000), who described the preferential release of Si during the early stage of dissolution (100 days in their experiment) for non-acidic solutions.

Further passivation of the grain surface due to occupation with secondary minerals (Béarat et al., 2006; E. King et al., 2010; Sissmann et al., 2013; Oelkers et al., 2018) appears unlikely as the portion of reactive surface covered by authigenic phases was relatively small in this study (data not shown). Considering these observations and the solid phase data that were obtained in our experimental set-up, it is likely that most of the Si and TA deficit (Figures II6a, II6b) in the dissolved phase is induced by the precipitation of secondary phases rather than a decline in dissolution rate.

II.4.6. Fate of Nickle and its usability as a dissolution proxy

Ni concentrations were suggested as a possible proxy for olivine dissolution by Montserrat et al. (2017). The comparison of [Ni] values (Figures II3b, II6c), though, clearly shows that the accumulation of Ni is not proportional to the amount of dissolved olivine calculated by the model (Tables 11S – 13S, suppl.) and not even proportional to the accumulation of [Si] in solution (Figures II 1b, II 6a). Incongruent weathering of olivine (Montserrat et al., 2017) can be excluded as, during the early stage of the experiment and thus before the precipitation of secondary minerals started, the accumulation of dissolved Si and Mn (which have a satisfyingly small 2SD) are proportional to the amount of olivine used in the experiments. Now under the assumption of congruent weathering, the expected [Ni] values would be 5.70 µmol/l for Batch20, 4.28 µmol/l for Batch10 and 2.26 µmol/l for Batch5. The measured values were significantly lower (Figure II 3b). Therefore, some removal process must be operating, that is apparently strongest in Batch20 and weakest in Batch5, leading to values that are identical within the error in all batches at the end of the experiment. Ni and Mn can be adsorbed on the surface of phyllosilicate phases, FeOOH and $CaCO_3$ and incorporated in the crystal lattice of calcite and aragonite during carbonate precipitation (Alvarez et al., 2021; Castillo Alvarez et al., 2020; Hoffmann and Stipp, 2001; Lakshtanov and Stipp, 2007; Lazarević et al., 2010). Carré et al. (2017) even proposed aragonite precipitation as a way to remove dissolved Ni from seawater. Therefore, it is likely that the Ni and Mn deficits (Figures II 6c, II 6d) observed at the end of the experiments are due to uptake of these trace elements in authigenic $CaCO_3$, Mg-Si and FeOOH phases.

As a conclusion, it becomes clear that the variety of processes affecting Ni and Mn concentrations in batch experiments excludes both as a reliable proxy for olivine dissolution rate determination. However,

the proposed strong Ni uptake in authigenic phases reduces toxic metal release that would limit the applicability of olivine weathering for CO_2 sequestration (Blewett and Leonard, 2017).

II.4.7. Sequestration efficiency

In a first approach the CO_2 conversion observed in the experiments (R_{ex}) can be expressed as a function of total inorganic carbon (TIC) following:

$$R_{ex} = \Delta TIC = (DIC_{final} + PIC_{final}) - (DIC_{ini} + \sum_j (DIC_{ini} * 0.007 - DIC(t) * 0.007)) \quad \text{(II10)}$$

where DIC_{final} is the DIC at the end of the experiment, PIC_{final} is the amount of particulate inorganic carbon in form of $CaCO_3$ at the end of the experiment and DIC_{ini} is the initial DIC at the beginning of the experiment. $\sum_j (DIC_{ini} * 0.007 - DIC(t) * 0.007)$ represents the amount of DIC added during sample taking (0.007 l per sample). PIC_{final} was calculated via the entire [Ca] loss during the experiment following,

$$PIC_{final} = [Ca]_{ini} - [Ca]_{final} + \sum_j ([Ca]_{in}(t) * 0.007 - [Ca](t) * 0.007) \quad \text{(II11)}$$

where $[Ca]_{ini}$ is the initial Ca concentration, $[Ca]_{final}$ is the final concentration and $[Ca]_{in}(t)$ is the function of the Ca input derived on sample taking that changes over time. The calculated net uptake was 0.21 mmol (Batch20), 0.166 mmol (Batch10) and 0.143 mmol (Batch5). Still, these values derive from a quasi-closed system with very limited CO_2 supply.

Hence, the efficiency of CO_2 uptake was investigated using a 1-box model where olivine with a grain diameter of 100 µm is dissolved in a 50 m deep water layer representative for the coastal ocean. The model box defines the seafloor at 50 m water depth. Hence, settling olivine grains that are rapidly deposited at the seafloor (Köhler et al., 2013) are kept within the system and continuously take part in the dissolution process. Hence, all olivine grains contribute equally to the overall dissolution rate whether they are kept in suspension or deposited at the seabed (Feng et al., 2017). Concentration and grain size of olivine were kept constant over the simulation period, for simplicity reasons. It is, thus, assumed that new olivine is added to the system to compensate for any olivine loss induced by dissolution. The concentration of olivine in the model box was set to a constant value of 10 mg dm^{-3} and the box was equilibrated with the atmosphere by applying a constant atmospheric pCO_2 of 400 µatm.

Mass balance equations (ordinary differential equations) for TA and DIC were set up and solved numerically to simulate temporal changes in DIC and TA. The TA mass balance considers TA production via olivine dissolution (4 x olivine dissolution rate) with the olivine dissolution rate depending on olivine concentration, grain size, temperature and pH (Rimstidt et al., 2012). TA consumption via authigenic mineral formation is considered applying the stoichiometry derived from dissolution experiments (Batch10, equation II8). Rates of mineral precipitation were calculated from olivine dissolution rates applying the corresponding stoichiometric coefficient. The DIC mass balance considers DIC removal via $CaCO_3$ precipitation and DIC gain induced by CO_2 uptake from the atmosphere.

Initial values applied in the model (salinity: 34.77, temperature: 17.88°C, pressure: 1 bar, total alkalinity: 2308 µmol kg^{-1}, total boron: 415 µmol kg^{-1}) correspond to the mean composition of surface water in the global ocean (Sarmiento and Gruber, 2006; Spivack and Edmond, 1987). The initial DIC concentration was set to 2053 µmol kg^{-1} to obtain an initial pCO_2 of 400 µatm in surface water. Equilibrium calculations were conducted using stability constants valid for seawater (Zeebe and Wolf-Gladrow, 2001). Total alkalinity (TA) was defined as:

$$TA = HCO_3^- + 2CO_3^- + B(OH)_4^- + OH^- - H^+ \quad \text{(II12)}$$

while CO_2 uptake from the atmosphere was calculated as:

$$FCO_2 = v_p(CO_2(eq) - CO_2) \quad \text{(II13)}$$

where v_P is the piston velocity (20 cm h^{-1} (Sarmiento, J.L. Gruber, 2006)), $CO_2(eq)$ is the concentration of dissolved CO_2 at equilibrium with the atmosphere and CO_2 is the time-dependent concentration calculated from TA and DIC (Sarmiento and Gruber, 2006).

In a first model run, olivine dissolution was simulated without secondary mineral formation to constrain the loss in CO_2 uptake efficiency induced by the buffer capacity of seawater (Middelburg et al., 2020). The efficiency (eff) is calculated as the ratio of the CO_2 uptake flux (FCO_2) and the depth-integrated rate of CO_2 consumption (RCO_2) induced by olivine dissolution (RCO_2 = 4 x olivine dissolution rate, eff = FCO_2/RCO_2). The model was run over a period of 10 years to equilibrate the water column with the overlying atmosphere (Figure II 7). The shift in acid-base equilibria induced by olivine-driven CO_2 consumption (e.g. $2HCO_3^- \rightarrow CO_2 + CO_3^{2-} + H_2O$) reduces the efficiency by about 42 % at the end of the simulation period. TA and DIC increase continuously due to alkalinity release by olivine dissolution and CO_2 uptake from the atmosphere, respectively, while the CO_2 uptake flux approaches a plateau after the water column is equilibrated with the atmosphere. The depth-integrated rate of olivine dissolution was almost constant over the model run. The small increase in pH from 8.035 at the start to 8.075 at the end of simulation (data not shown) induced a small decrease in RCO_2 from an initial value of 147 mmol m^{-2} yr^{-1} to a final value of 145 mmol m^{-2} yr^{-1}.

In a second model run, precipitation of ferric iron oxides and Si-Mg-phases was implemented employing the stoichiometry derived from batch experiments (batch10, equation II8). Precipitation of ferric iron oxides and Si-Mg-phases strongly affects the model results. The increase in TA and DIC is reduced, whereas CO_2 uptake and CO_2 efficiency are strongly diminished since protons are released during the precipitation reactions. The efficiency at the end of the model period decreased from 0.58 in the model run without secondary mineral formation to only 0.25. Most of the efficiency loss is caused by the precipitation of Mg-

Si-phases that consumes large amounts of alkalinity due to the strong proton release induced by these reactions (6 mol H^+ per mol of serpentinite/talc, 4 mol H^+ per mol of sepiolite).

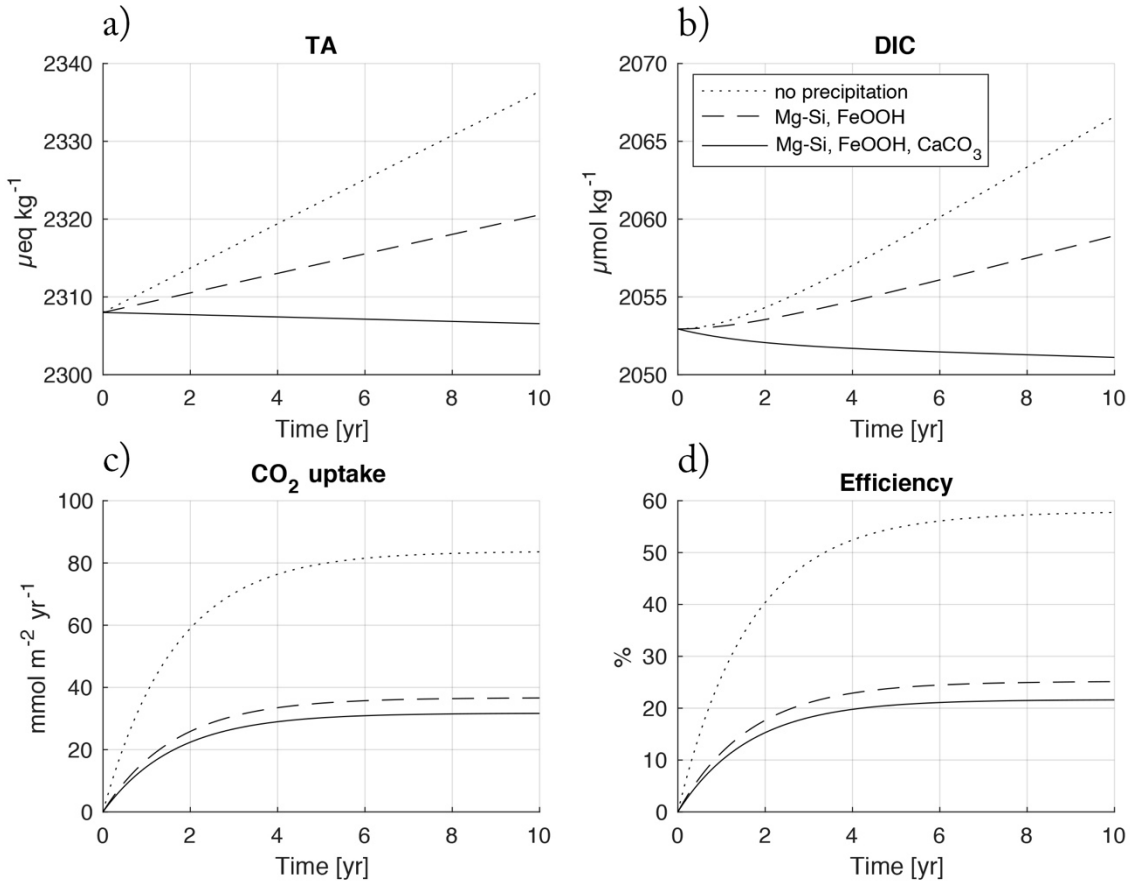

Figure II 7: Model experiments simulating the effect of olivine dissolution on seawater composition and CO_2 uptake from the atmosphere. Dotted lines show results for a model run without secondary mineral formation. Broken lines represent model results for the precipitation of ferric iron oxides (FeOOH) and Mg-Si-phases (serpentinite, talc, sepiolite). Solid lines indicate the results for a model run where all authigenic phases (FeOOH, Mg-Si-phases, $CaCO_3$) precipitate according to the stoichiometry observed in our lab experiments. a. Total alkalinity. b. Dissolved inorganic carbon. c. CO_2 uptake from the atmosphere (FCO_2). d. Efficiency of CO_2 uptake is defined as FCO_2 /RCO_2 where RCO_2 is the depth-integrated rate of CO_2 consumption induced by olivine dissolution (= 4 x olivine dissolution rate).

In a final model run, all secondary phases including $CaCO_3$ are allowed to precipitate. $CaCO_3$ formation has a strong effect on solution composition and induces a decline in both TA and DIC. The CO_2 uptake is further reduced such that the efficiency drops to 0.21 after 10 years. $CaCO_3$ formation has a smaller effect on CO_2 fluxes than Mg-Si-phase precipitation even though $CaCO_3$ is the major secondary phase formed during the experiments. This somewhat surprising model result is related to the acid-base stoichiometry of carbonate precipitation where only two moles of alkalinity are removed per mol of $CaCO_3$, while the coeval DIC loss promotes CO_2 uptake from the atmosphere.

Additional model runs were conducted to explore the effects of olivine concentration (1 – 1000 mg dm^{-3}) and grain size (10 – 100 µM) on CO_2 uptake efficiency (data not shown). The experiments showed that olivine dissolution rates and CO_2 uptake fluxes strongly increase when higher concentrations and smaller grain sizes are applied. However, the CO_2 uptake efficiency was constant (0.21) over the explored parameter space when the stoichiometry derived from our lab experiments was applied. Hence, the low efficiency

obtained in the box model simulations seems to be a robust result, if the overall stoichiometry that we observed in our lab experiments is also valid in the field. There are, however, a number of factors that may induce a change in the rates of olivine dissolution and secondary mineral precipitation. Hence, the solid/liquid ratio and the rates of water replacement, CO_2 uptake from the atmosphere and biological activity may affect the ratios between dissolution and precipitation reactions. These factors should be investigated in future lab and field experiments.

II.4.8. Implications for field application

The experimental results of this study show that precipitation of secondary minerals ($CaCO_3$, Mg-Si-phases, FeOOH) compromises the efficiency of CO_2 uptake by olivine dissolution. It should, however be noted that the stoichiometry that we observed in our lab experiments may not be valid for all field conditions. Moreover, we found higher rates of alkalinity removal than previous studies with pure olivine that were conducted under comparable experimental conditions (Montserrat et al., 2017). This observation may be due to the high solid/solution ratios applied in our experiments and could be related to the fact that we used commercially available olivine (UMS) that was not pure but contained a number of accessory minerals. Our use of ultramafic sand rather than pure olivine may be justified since large-scale CDR will probably not be conducted with pure olivine but with rocks containing other minerals and impurities. The range of dissolved Si concentrations attained in our experiments (Figure II 1) is similar to the concentrations observed in bioturbated surface sediments (Dale et al., 2021). Since grains added to seawater will rapidly sink to the seafloor where they are mixed into surface sediments by benthic biota, the experimental conditions may be close to those in benthic habitats where most of the dissolution is expected to occur.

Precipitation rates of authigenic Mg-Si-phases may be lower than observed in our experiments, though, when olivine is applied to highly dynamic environments such as the coastal zone (beaches, surf zones), where dissolution products are rapidly removed (Hangx and Spiers, 2009; Meysman and Montserrat, 2017; Montserrat et al., 2017). It is, however, possible that $CaCO_3$ precipitation may also occur in these coastal environments since our data imply that carbonate precipitation is catalyzed by olivine surfaces even at low degrees of aragonite oversaturation. Further work is needed to scrutinize whether the abrasive effects of wave action may suppress $CaCO_3$ precipitation (Meysman and Montserrat, 2017).

Anyhow, fine-grained olivine added to the shelf environment will ultimately be transported by bottom currents to local depo-centers where low bottom current velocities allow for the permanent burial of sediments. These environments are marked by high accumulation rates of both sediments and organic matter (De Haas et al., 2002). The low pH values induced by the release of metabolic CO_2 during organic matter degradation largely inhibit $CaCO_3$ precipitation in these sedimentary environments while FeOOH formation is limited to surface sediments due to the reducing conditions prevailing in these deposits (Silburn et al., 2017; Van Cappellen and Wang, 1996). However, authigenic Mg-Si- phases and clays are formed in these benthic environments (Michalopoulos and Aller, 1995). Since the formation of cation-rich phases induces CO_2 release, the overall efficiency of CO_2 uptake might be strongly diminished as observed in our experiments. It is, hence, possible that, when applied in the field, olivine weathering is less efficient than previously believed. On the other hand, adverse environmental effects may be smaller than previously anticipated since data obtained during the experiments in this study indicate that Ni and other toxic metals will largely be fixed in authigenic phases. However, more work needs to be done to explore how variable conditions in pelagic and benthic environments may affect the ratio between olivine dissolution and

authigenic mineral precipitation and, hence, the efficiency of CO_2 uptake from the atmosphere and the rate of toxic metal release.

II.5. Summary, conclusion and outlook

This study presents a first dedicated attempt to investigate the formation of secondary mineral phases in artificial seawater (ASW) during olivine weathering. For this purpose, ultra-mafic sand (UMS) was brought to reaction with ASW applying different solid/liquid ratios. The results strongly suggest the formation of $CaCO_3$, as evidenced by the congruent loss of Ca and DIC observed over the course of the experiments. XRD measurements suggest, that aragonite is the major $CaCO_3$ species precipitated which is underlined by the fact that this variation is more likely to be precipitated in Mg-rich solutions. This is further supported by WDX measurements that showed pure $CaCO_3$ crystals on the surface of weathered olivine grains. These observations are confirmed by the results of a numerical model that simulated the dissolution of olivine and the precipitation of several secondary mineral phases including aragonite. Moreover, the model results allowed estimating the overall stoichiometry of the combined dissolution-precipitation reaction. The thorough analysis of ASW and precipitates recovered from the batch reactors underline that Si-bearing phases must also have formed during the experiment. The precise character (amorphous or crystalline) and chemical composition of these phases, though, afford further dedicated studies. Via the different accumulation rates of Ni in the different batches, this study revealed that these secondary mineral phases most likely are a major sink for this toxic element, excluding it as a proxy for olivine dissolution rates. This makes the precise knowledge of secondary phase formation and characteristics crucial for the feasibility of enhanced olivine weathering on the one hand and for the understanding of the dissolution kinetics of olivine on the other. Experimental combined with modelling results suggest that the formation of secondary phases lowers the overall sequestration efficiency to ~20% during the application of enhanced olivine weathering in a shallow shelf sea. This bears implications for possible application sites, as not only physical parameters, but, more importantly, chemical parameters in the field steer secondary mineral formation and thus the overall efficiency.

Sandy shelf sediments and specifically the surf zone may be appropriate sites for enhanced olivine dissolution since the flushing of surface sediments by ambient bottom waters may mitigate the accumulation of dissolution products and the formation of secondary silicate and carbonate minerals in these permeable and physically dynamic deposits. Alternatively, application sites where pore and or bottom waters are undersaturated with respect to the major secondary phases would be a promising target for enhanced coastal weathering of olivine.

Our experimental and modelling results hence indicate that it may be promising to also investigate $CaCO_3$ as alkaline mineral for CO_2 removal since secondary mineral formation is usually not observed during $CaCO_3$ dissolution. $CaCO_3$ could be added to sediment depo-centers on the shelf where large amounts of metabolic CO_2 are formed (about 3 Pg yr^{-1} at global scale) that can be converted into bicarbonate by $CaCO_3$ dissolution (Dunne et al., 2007). This process would accelerate the CO_2 shelf pump (Bozec et al., 2005) and promote further CO_2 uptake from the atmosphere. This approach may be most successful in marine environments where bottom waters are enriched in CO_2 and undersaturated with respect to calcite and aragonite. These conditions occur e.g. in oxygen minimum zones and partly anoxic marginal basins such as the Baltic Sea (Tyrrell et al., 2008). The CO_2 release from Baltic Sea sediments

amounts to 80 Tg yr^{-1} (Nilsson et al., 2019). The addition of a corresponding amount of $CaCO_3$ may thus dramatically enhance CO_2 uptake from the atmosphere. Moreover, $CaCO_3$ addition may support the formation of authigenic carbonate fluorapatite and could thereby reduce benthic phosphate fluxes (Ruttenberg and Berner, 1993). Hence, $CaCO_3$ addition may mitigate eutrophication, which is a major problem in many shelf regions, while olivine addition would promote Si and Fe release and potentially amplify eutrophication. Further lab studies, field experiments and numerical modeling also focusing on the biological impact are needed to better constrain the efficiency and environmental effects of these CDR approaches and their large-scale applicability.

Data availability statement (II)

The original contributions presented in the study are included in the article and supplementary files Further inquiries can be directed to the corresponding author.

Author Contributions (II)

MF carried out the experiments, processed most of the samples in the laboratory and wrote the manuscript. SG helped with sample preparation in the clean-lab and contributed with discussions. MS supervised XRD interpretation and contributed with discussions. VL initiated and supervised EDX/WDX measurements and contributed with discussions. CV supported XRD interpretation. BL carried out additional XRD measurements and helped with XRD interpretation. KW designed the numerical models used in this study and contributed with discussions. All authors contributed to the article and approved the submitted version.

Funding (II)

This study was funded by the Bundesministerium für Bildung und Forschung (BMBF) (Project RETAKE, granted to SG) in the framework of the Deutsche Allianz für Meeresforschung (DAM) mission "CDRmare".

Acknowledgements (II)

We would like to thank Philipp Böning (ICBM, Oldenburg) for carrying out XRF measurements and interpretation. We also acknowledge Anke Bleyer (GEOMAR), Bettina Domeyer (GEOMAR) and Regina Surberg (GEOMAR) for their help with technical and analytical procedures in the clean laboratory, respectively. Additionally, we thank Mario Thöner (GEOMAR) for his great support during EDX/WDX measurements. In deep mourning we commemorate our dear friend and highly respected and regarded colleague Dr. Volker Liebetrau who deceased short before the publication of this study. Our thoughts are with his family and beloved ones.

References (II)

Alvarez, C.C., Quitté, G., Schott, J., Oelkers, E.H., 2021. Nickel isotope fractionation as a function of carbonate growth rate during Ni coprecipitation with calcite. Geochim. Cosmochim. Acta 299, 184–198. https://doi.org/10.1016/j.gca.2021.02.019

Amann, T., Hartmann, J., Struyf, E., De Oliveira Garcia, W., Fischer, E.K., Janssens, I., Meire, P., Schoelynck, J., 2020. Enhanced Weathering and related element fluxes - A cropland mesocosm approach. Biogeosciences 17, 103–119. https://doi.org/10.5194/bg-17-103-2020

Béarat, H., J. McKelvy, M., V. G. Chizmeshya, A., Gormley, D., Nunez, R., W. Carpenter, R., Squires, K., H. Wolf, G., 2006. Carbon Sequestration via Aqueous Olivine Mineral Carbonation: Role of Passivating Layer Formation. Environ. Sci. & Technol. 40, 4802–4808. https://doi.org/10.1021/es0523340

Blewett, T.A., Leonard, E.M., 2017. Mechanisms of nickel toxicity to fish and invertebrates in marine and estuarine waters. Environ. Pollut. 223, 311–322. https://doi.org/10.1016/j.envpol.2017.01.028

Bozec, Y., Thomas, H., Elkalay, K., De Baar, H.J.W., 2005. The continental shelf pump for CO2 in the North Sea—evidence from summer observation. Mar. Chem. 93, 131–147. https://doi.org/10.1016/J.MARCHEM.2004.07.006

Burton, E.A., Walter, L.M., 1987. Relative precipitation rates of aragonite and Mg calcite from seawater: Temperature or carbonate ion control? Geology 15, 111–114. https://doi.org/10.1130/0091-7613(1987)15<111:RPROAA>2.0.CO;2

Buurman, P., Meijer, E.L., Wijck, J.H.V., 1988. Weathering of chlorite and vermiculite in ultramafic rocks of Cabo Ortegal, northwestern Spain. Clays Clay Miner. 36, 263–269. https://doi.org/10.1346/ccmn.1988.0360308

Carré, C., Gunkel-Grillon, P., Serres, A., Jeannin, M., Sabot, R., Quiniou, T., 2017. Calcareous electrochemical precipitation, a new method to trap nickel in seawater. Environ. Chem. Lett. 15, 151–156. https://doi.org/10.1007/s10311-016-0602-2

Castillo Alvarez, C., Quitté, G., Schott, J., Oelkers, E.H., 2020. Experimental determination of Ni isotope fractionation during Ni adsorption from an aqueous fluid onto calcite surfaces. Geochim. Cosmochim. Acta 273, 26–36. https://doi.org/10.1016/j.gca.2020.01.010

Dale, A.W., Paul, K.M., Clemens, D., Scholz, F., Schroller-Lomnitz, U., Wallmann, K., Geilert, S., Hensen, C., Plass, A., Liebetrau, V., Grasse, P., Sommer, S., 2021. Recycling and Burial of Biogenic Silica in an Open Margin Oxygen Minimum Zone. Global Biogeochem. Cycles 35, e2020GB006583. https://doi.org/10.1029/2020GB006583

Davis, M.C., Brouwer, W.J., Wesolowski, D.J., Anovitz, L.M., Lipton, A.S., Mueller, K.T., 2009. Magnesium silicate dissolution investigated by 29Si MAS, 1H–29Si CPMAS, 25Mg QCPMG, and 1H–25Mg CP QCPMG NMR. Phys. Chem. Chem. Phys. 11, 7013–7021. https://doi.org/10.1039/B907494E

De Choudens-Sánchez, V., González, L.A., 2009. Calcite and Aragonite Precipitation Under Controlled Instantaneous Supersaturation: Elucidating the Role of CaCO3 Saturation State and Mg/Ca Ratio on Calcium Carbonate Polymorphism. J. Sediment. Res. 79, 363–376. https://doi.org/10.2110/jsr.2009.043

De Haas, H., Van Weering, T.C.E., De Stigter, H., 2002. Organic carbon in shelf seas: sinks or sources, processes and products. Cont. Shelf Res. 22, 691–717. https://doi.org/10.1016/S0278-4343(01)00093-0

Dehouck, E., Gaudin, A., Mangold, N., Lajaunie, L., Dauzères, A., Grauby, O., Le Menn, E., 2014. Weathering of olivine under CO2 atmosphere: A martian perspective. Geochim. Cosmochim. Acta 135, 170–189. https://doi.org/https://doi.org/10.1016/j.gca.2014.03.032

Delvigne, J., Bisdom, E.B.A., Sleeman, J., Stoops, G., 1979. Olivines, their pseudomorphs and secondary products. Pedologie 29, 247–309.

Dickson, A.G., 1993. pH buffers for sea water media based on the total hydrogen ion concentration scale. Deep Sea Res. Part I Oceanogr. Res. Pap. 40, 107–118. https://doi.org/10.1016/0967-0637(93)90055-8

Dunne, J.P., Sarmiento, J.L., Gnanadesikan, A., 2007. A synthesis of global particle export from the surface ocean and cycling through the ocean interior and on the seafloor. Global Biogeochem. Cycles 21, GB4006. https://doi.org/10.1029/2006GB002907

E. King, H., Plümper, O., Putnis, A., 2010. Effect of Secondary Phase Formation on the Carbonation of Olivine. Environ. Sci. & Technol. 44, 6503–6509. https://doi.org/10.1021/es9038193

Entezari Zarandi, A., Larachi, F., Beaudoin, G., Plante, B., Sciortino, M., 2017. Nesquehonite as a carbon sink in ambient mineral carbonation of ultramafic mining wastes. Chem. Eng. J. 314, 160–168. https://doi.org/https://doi.org/10.1016/j.cej.2017.01.003

Feely, R.A., Sabine, C.L., Byrne, R.H., Millero, F.J., Dickson, A.G., Wanninkhof, R., Murata, A., Miller, L.A., Greeley, D., 2012. Decadal changes in the aragonite and calcite saturation state of the Pacific Ocean. Global Biogeochem. Cycles 26(3), GB3001. https://doi.org/10.1029/2011GB004157

Feldman, D.R., Collins, W.D., Gero, P.J., Torn, M.S., Mlawer, E.J., Shippert, T.R., 2015. Observational determination of surface radiative forcing by CO2 from 2000 to 2010. Nature 519, 339–343. https://doi.org/10.1038/nature14240

Feng, E.Y., Koeve, W., Keller, D.P., Oschlies, A., 2017. Model-Based Assessment of the CO2 Sequestration Potential of Coastal Ocean Alkalinization. Earth's Futur. 5, 1252–1266. https://doi.org/10.1002/2017EF000659

Ferrini, V., De Vito, C., Mignardi, S., 2009. Synthesis of nesquehonite by reaction of gaseous CO2 with Mg chloride solution: Its potential role in the sequestration of carbon dioxide. J. Hazard. Mater. 168, 832–837. https://doi.org/https://doi.org/10.1016/j.jhazmat.2009.02.103

Flipkens, G., Blust, R., Town, R.M., 2021. Deriving Nickel (Ni(II)) and Chromium (Cr(III)) Based Environmentally Safe Olivine Guidelines for Coastal Enhanced Silicate Weathering. Environ. Sci. Technol. 55, 12362–12371. https://doi.org/10.1021/ACS.EST.1C02974/SUPPL_FILE/ES1C02974_SI_001.PDF

Friedlingstein, P., Solomon, S., Plattner, G.-K., Knutti, R., Ciais, P., Raupach, M.R., 2011. Long-term climate implications of twenty-first century options for carbon dioxide emission mitigation. Nat. Clim. Chang. 1, 457–461. https://doi.org/10.1038/nclimate1302

Fuss, S., Lamb, W.F., Callaghan, M.W., Hilaire, J., Creutzig, F., Amann, T., Beringer, T., De Oliveira Garcia, W., Hartmann, J., Khanna, T., Luderer, G., Nemet, G.F., Rogelj, J., Smith, P., Vicente, J.V., Wilcox, J., Del Mar Zamora Dominguez, M., Minx, J.C., 2018. Negative emissions - Part 2: Costs, potentials and side effects. Environ. Res. Lett. 13(6) 063002. https://doi.org/10.1088/1748-9326/aabf9f

Gieskes, J., Gamo, T., Brumsack, H., 1991. Chemical methods for interstitial water analysis aboard JOIDES Resolution. O D P Tech Note 15. https://doi.org/10.2973/odp.tn.15.1991

Govindaraju, K., 1994. 1994 COMPILATION OF WORKING VALUES AND SAMPLE DESCRIPTION FOR 383 GEOSTANDARDS. Geostand. Newsl. 18, 1–158. https://doi.org/10.1046/j.1365-2494.1998.53202081.x-i1

Griffioen, J., 2017. Enhanced weathering of olivine in seawater: The efficiency as revealed by thermodynamic scenario analysis. Sci. Total Environ. 575, 536–544. https://doi.org/10.1016/j.scitotenv.2016.09.008

Gruber, C., Harlavan, Y., Pousty, D., Winkler, D., Ganor, J., 2019. Enhanced chemical weathering of albite under seawater conditions and its potential effect on the Sr ocean budget. Geochim. Cosmochim. Acta 261, 20–34. https://doi.org/10.1016/j.gca.2019.06.049

Hangx, S.J.T., Spiers, C.J., 2009. Coastal spreading of olivine to control atmospheric CO2 concentrations: A critical analysis of viability. Int. J. Greenh. Gas Control 3, 757–767. https://doi.org/10.1016/j.ijggc.2009.07.001

Hartmann, J., Kempe, S., 2008. What is the maximum potential for CO 2 sequestration by "stimulated" weathering on the global scale? Naturwissenschaften 95, 1159–1164. https://doi.org/10.1007/s00114-008-0434-4

Hartmann, J., West, A.J., Renforth, P., Köhler, P., De La Rocha, C.L., Wolf-Gladrow, D.A., Dürr, H.H., Scheffran, J., 2013. Enhanced chemical weathering as a geoengineering strategy to reduce atmospheric carbon dioxide, supply nutrients, and mitigate ocean acidification. Rev. Geophys. 51, 113–149. https://doi.org/10.1002/rog.20004

Hellmann, R., Wirth, R., Daval, D., Barnes, J.P., Penisson, J.M., Tisserand, D., Epicier, T., Florin, B., Hervig, R.L., 2012. Unifying natural and laboratory chemical weathering with interfacial dissolution-reprecipitation: A study based on the nanometer-scale chemistry of fluid-silicate interfaces. Chem. Geol. 294–295, 203–216. https://doi.org/10.1016/j.chemgeo.2011.12.002

Hoffmann, U., Stipp, S.L.S., 2001. The behavior of Ni2+ on calcite surfaces. Geochim. Cosmochim. Acta 65, 4131–4139. https://doi.org/10.1016/S0016-7037(01)00691-3

Hövelmann, J., Austrheim, H., Beinlich, A., Anne Munz, I., 2011. Experimental study of the carbonation of partially serpentinized and weathered peridotites. Geochim. Cosmochim. Acta 75, 6760–6779. https://doi.org/10.1016/j.gca.2011.08.032

Howe, J.P., 2015. This is nature; This is un-nature: Reading the keeling curve. Environ. Hist. Durh. N. C 20:2, 286-293. https://doi.org/10.1093/envhis/emv005

Iizuka, A., Fujii, M., Yamasaki, A., Yanagisawa, Y., 2004. Development of a new CO2 sequestration process utilizing the carbonation of waste cement. Ind. Eng. Chem. Res. 43, 7880–7887. https://doi.org/10.1021/ie0496176

IPCC, 2021: *Climate Change 2021: The Physical Science Basis. Contribution of Working Group I to the Sixth Assessment Report of the Intergovernmental Panel on Climate Change* [Masson-Delmotte, V., P. Zhai, A. Pirani, S.L. Connors, C. Péan, S. Berger, N. Caud, Y. Chen, L. Goldfarb, M.I. Gomis, M. Huang, K. Leitzell, E. Lonnoy, J.B.R. Matthews, T.K. Maycock, T. Waterfield, O. Yelekçi, R. Yu, and B. Zhou (eds.)]. Cambridge University Press, Cambridge, In Press.

Keeling, C.D., Stephen, C., Piper, S.C., Bacastow, R.B., Wahlen, M., Whorf, T.P., Heimann, M., Meijer, H. a., 2001. Exchanges of atmospheric CO2 and 13CO2 with the terrestrial biosphere and oceans from 1978 to 2000. Glob. Asp. SIO Ref. Ser. Scripps Inst. Ocean. San Diego 01–06. https://doi.org/10.1007/0-387-27048-5_5

Köhler, P., Abrams, J.F., Völker, C., Hauck, J., Wolf-Gladrow, D.A., 2013. Geoengineering impact of open ocean dissolution of olivine on atmospheric CO2, surface ocean pH and marine biology. Environ. Res. Lett. 8(1), 014009. https://doi.org/10.1088/1748-9326/8/1/014009

Kremer, D., Etzold, S., Boldt, J., Blaum, P., Hahn, K.M., Wotruba, H., Telle, R., 2019. Geological mapping and characterization of possible primary input materials for the mineral sequestration of carbon dioxide in Europe. Minerals 9(8), 485. https://doi.org/10.3390/min9080485

Lackner, K.S., 2003. A guide to CO2 sequestration. Science, 300(6526), 1677–1678. https://doi.org/10.1126/science.1079033

Lakshtanov, L.Z., Stipp, S.L.S., 2007. Experimental study of nickel(II) interaction with calcite: Adsorption and coprecipitation. Geochim. Cosmochim. Acta 71, 3686–3697. https://doi.org/10.1016/j.gca.2007.04.006

Lal, R., 2004. Soil carbon sequestration to mitigate climate change. Geoderma, 123(1-2), 1-22. https://doi.org/10.1016/j.geoderma.2004.01.032

Lasaga, A.C., 1998. Kinetic theory in the earth sciences. Princeton University Press, Princeton. https://doi.org/10.1515/9781400864874

Lazarević, S., Janković-Častvan, I., Djokić, V., Radovanović, Z., Janaćković, D., Petrović, R., 2010. Iron-Modified Sepiolite for Ni2+ Sorption from Aqueous Solution: An Equilibrium, Kinetic, and Thermodynamic Study. J. Chem. & Eng. Data 55, 5681–5689. https://doi.org/10.1021/je100639k

Lein, A.Y., 2004. Authigenic Carbonate Formation in the Ocean. Lithol. Miner. Resour. 39, 1–30. https://doi.org/10.1023/B:LIMI.0000010767.52720.8f

Lerman, A., Mackenzie, F.T., Bricker, O.P., 1975. Rates of dissolution of aluminosilicates in seawater. Earth Planet. Sci. Lett. 25, 82–88. https://doi.org/10.1016/0012-821X(75)90213-7

Lindzen, R.S., 2007. Taking Greenhouse Warming Seriously. Energy Environ. 18, 937–950. https://doi.org/10.1260/095830507782616823

MacFarling Meure, C., Etheridge, D., Trudinger, C., Steele, P., Langenfelds, R., van Ommen, T., Smith, A., Elkins, J., 2006. Law Dome CO2, CH4 and N2O ice core records extended to 2000 years BP. Geophys. Res. Lett. 33(14), L14810. https://doi.org/10.1029/2006GL026152

Maher, K., Johnson, N.C., Jackson, A., Lammers, L.N., Torchinsky, A.B., Weaver, K.L., Bird, D.K., Brown, G.E., 2016. A spatially resolved surface kinetic model for forsterite dissolution. Geochim. Cosmochim. Acta 174, 313–334. https://doi.org/10.1016/j.gca.2015.11.019

Méheut, M., Schauble, E.A., 2014. Silicon isotope fractionation in silicate minerals: Insights from first-principles models of phyllosilicates, albite and pyrope. Geochim. Cosmochim. Acta 134, 137–154. https://doi.org/10.1016/j.gca.2014.02.014

Meysman, F.J.R., Montserrat, F., 2017. Negative CO2 emissions via enhanced silicate weathering in coastal environments. Biol. Lett. 13(4), 20160905. https://doi.org/10.1098/rsbl.2016.0905

Michalopoulos, P., Aller, R.C., 1995. Rapid Clay Mineral Formation in Amazon Delta Sediments: Reverse Weathering and Oceanic Elemental Cycles. Science (80-.). 270, 614–617. https://doi.org/10.1126/science.270.5236.614

Middelburg, J.J., Soetaert, K., Hagens, M., 2020. Ocean Alkalinity, Buffering and Biogeochemical Processes. Rev. Geophys. 58, e2019RG000681. https://doi.org/10.1029/2019RG000681

Millero, F.J., Feistel, R., Wright, D.G., McDougall, T.J., 2008. The composition of Standard Seawater and the definition of the Reference-Composition Salinity Scale. Deep. Res. Part I Oceanogr. Res. Pap. 55, 50–72. https://doi.org/10.1016/j.dsr.2007.10.001

Millero, F.J., Sotolongo, S., Izaguirre, M., 1987. The oxidation kinetics of Fe(II) in seawater. Geochim. Cosmochim. Acta 51, 793–801. https://doi.org/10.1016/0016-7037(87)90093-7

Montserrat, F., Renforth, P., Hartmann, J., Leermakers, M., Knops, P., Meysman, F.J.R., 2017. Olivine Dissolution in Seawater: Implications for CO2 Sequestration through Enhanced Weathering in Coastal Environments. Environ. Sci. Technol 51(7), 3960-3972. https://doi.org/10.1021/acs.est.6b05942

Moore, T.S., Murray, R.W., Kurtz, A.C., Schrag, D.P., 2004. Anaerobic methane oxidation and the formation of dolomite. Earth Planet. Sci. Lett. 229, 141–154. https://doi.org/https://doi.org/10.1016/j.epsl.2004.10.015

Nilsson, M.M., Kononets, M., Ekeroth, N., Viktorsson, L., Hylén, A., Sommer, S., Pfannkuche, O., Almroth-Rosell, E., Atamanchuk, D., Andersson, J.H., Roos, P., Tengberg, A., Hall, P.O.J., 2019. Organic carbon recycling in Baltic Sea sediments – An integrated estimate on the system scale based on in situ measurements. Mar. Chem. 209, 81–93. https://doi.org/10.1016/J.MARCHEM.2018.11.004

Oelkers, E.H., 2001. An experimental study of forsterite dissolution rates as a function of temperature and aqueous Mg and Si concentrations. Chem. Geol. 175, 485–494. https://doi.org/10.1016/S0009-2541(00)00352-1

Oelkers, E.H., 1999. A comparison of forsterite and enstatite dissolution rates and mechanisms, in: Growth, Dissolution and Pattern Formation in Geosystems. In: Jamtveit B., Meakin P. (eds), Springer, Dordrecht, 253–267. https://doi.org/10.1007/978-94-015-9179-9_12

Oelkers, E.H., Benning, L.G., Lutz, S., Mavromatis, V., Pearce, C.R., Plümper, O., 2015. The efficient long-term inhibition of forsterite dissolution by common soil bacteria and fungi at Earth surface conditions. Geochim. Cosmochim. Acta 168, 222–235. https://doi.org/10.1016/j.gca.2015.06.004

Oelkers, E.H., Declercq, J., Saldi, G.D., Gislason, S.R., Schott, J., 2018. Olivine dissolution rates: A critical review. Chem. Geol. 500, 1–19. https://doi.org/10.1016/j.chemgeo.2018.10.008

Olsen, A.A., Rimstidt, J.D., 2008. Oxalate-promoted forsterite dissolution at low pH. Geochim. Cosmochim. Acta 72, 1758–1766. https://doi.org/10.1016/j.gca.2007.12.026

Palandri, J.L., Kharaka, Y.K., 2004. A compilation of rate parameters of water-mineral interaction kinetics for application to geochemical modeling, USGS Open File Report 2004-1068. https://doi.org/10.3133/ofr20041068

Parkhurst, D.L., Appelo, C.A.J., 1999. User's Guide to PHREEQC (Version 2): A Computer Program for Speciation, Batch-Reaction, One-Dimensional Transport, and Inverse Geochemical Calculations, Water-Resources Investigations Report 99-4259. https://doi.org/10.3133/wri994259

Pokrovsky, O.S., Schott, J., 2000. Kinetics and mechanism of forsterite dissolution at 25°C and pH from 1 to 12. Geochim. Cosmochim. Acta 64, 3313–3325. https://doi.org/10.1016/S0016-7037(00)00434-8

Power, I.M., Wilson, S.A., Dipple, G.M., 2013. Serpentinite Carbonation for CO2 Sequestration. Elements 9, 115–121. https://doi.org/10.2113/gselements.9.2.115

Renforth, P., Henderson, G., 2014. Assessing ocean alkalinity for carbon sequestration. *Rev. Geophys.*, 55, 636– 674. https://doi.org/10.1002/2016RG000533

Rhodes, C.J., 2016. The 2015 Paris climate change conference: COP21. Sci. Prog. 99, 97–104.

Rigopoulos, I., Harrison, A.L., Delimitis, A., Ioannou, I., Efstathiou, A.M., Kyratsi, T., Oelkers, E.H., 2018. Carbon sequestration via enhanced weathering of peridotites and basalts in seawater. Appl. Geochemistry 91, 197–207. https://doi.org/10.1016/j.apgeochem.2017.11.001

Rimstidt, J.D., Brantley, S.L., Olsen, A.A., 2012. Systematic review of forsterite dissolution rate data. Geochim. Cosmochim. Acta 99, 159–178. https://doi.org/10.1016/j.gca.2012.09.019

Ruttenberg, K.C., Berner, R.A., 1993. Authigenic apatite formation and burial in sediments from non-upwelling, continental margin environments. Geochim. Cosmochim. Acta 57, 991–1007. https://doi.org/10.1016/0016-7037(93)90035-U

Saran, R.K., Arora, V., Yadav, S., 2018. CO2 sequestration by mineral carbonation: a review. Glob. Nest J 20, 497–503. https://doi.org/10.30955/gnj.002597

Sarmiento, J.L. Gruber, N., 2006. J. L. Sarmiento & N. Gruber 2006. Ocean Biogeochemical Dynamics. xiii + 503 pp. Princeton, Woodstock: Princeton University Press. 0 691 01707 7. Geol. Mag. 144, 1034. https://doi.org/10.1017/S0016756807003755

Schrag, D.P., Higgins, J.A., Macdonald, F.A., Johnston, D.T., 2013. Authigenic Carbonate and the History of the Global Carbon Cycle. Science (80-.). 339, 540–543. https://doi.org/10.1126/science.1229578

Silburn, B., Kröger, S., Parker, E.R., Sivyer, D.B., Hicks, N., Powell, C.F., Johnson, M., Greenwood, N., 2017. Benthic pH gradients across a range of shelf sea sediment types linked to sediment characteristics and seasonal variability. Biogeochemistry 135, 69–88. https://doi.org/10.1007/s10533-017-0323-z

Sissmann, O., Daval, D., Brunet, F., Guyot, F., Verlaguet, A., Pinquier, Y., Findling, N., Martinez, I., 2013. The deleterious effect of secondary phases on olivine carbonation yield: Insight from time-resolved aqueous-fluid sampling and FIB-TEM characterization. Chem. Geol. 357, 186–202. https://doi.org/10.1016/j.chemgeo.2013.08.031

Solomon, S., Plattner, G.-K., Knutti, R., Friedlingstein, P., 2009. Irreversible climate change due to carbon dioxide emissions. Proc. Natl. Acad. Sci. 106, 1704 LP – 1709. https://doi.org/10.1073/pnas.0812721106

Spivack, A.J., Edmond, J.M., 1987. Boron isotope exchange between seawater and the oceanic crust. Geochim. Cosmochim. Acta 51, 1033–1043. https://doi.org/https://doi.org/10.1016/0016-7037(87)90198-0

Stockmann, G.J., Wolff-Boenisch, D., Bovet, N., Gislason, S.R., Oelkers, E.H., 2014. The role of silicate surfaces on calcite precipitation kinetics. Geochim. Cosmochim. Acta 135, 231–250. https://doi.org/10.1016/j.gca.2014.03.015

Strefler, J., Amann, T., Bauer, N., Kriegler, E., Hartmann, J., 2018. Potential and costs of carbon dioxide removal by enhanced weathering of rocks. Environ. Res. Lett. 13(3), 034101. https://doi.org/10.1088/1748-9326/aaa9c4

Stumm & Morgan, 1996. Aquatic chemistry: chemical equilibria and rates in natural waters. Choice Rev. Online 33, 171-229. https://doi.org/10.5860/choice.33-6312

Suárez, S., Nieto, F., Velasco, F., Martín, F.J., 2011. Serpentine and chlorite as effective Ni-Cu sinks during weathering of the Aguablanca sulphide deposit (SW Spain). TEM evidence for metal-retention mechanisms in sheet silicates. Eur. J. Mineral. 23, 179–196. https://doi.org/10.1127/0935-1221/2011/0023-2084

Sun, W., Jayaraman, S., Chen, W., Persson, K.A., Ceder, G., 2015. Nucleation of metastable aragonite CaCO₃ in seawater. Proc. Natl. Acad. Sci. 112, 3199 LP – 3204. https://doi.org/10.1073/pnas.1423898112

Torres, M.A., Dong, S., Nealson, K.H., West, A.J., 2019. The kinetics of siderophore-mediated olivine dissolution. Geobiology 17, 401–416. https://doi.org/10.1111/gbi.12332

Torres, M.E., Hong, W.-L., Solomon, E.A., Milliken, K., Kim, J.-H., Sample, J.C., Teichert, B.M.A., Wallmann, K., 2020. Silicate weathering in anoxic marine sediment as a requirement for authigenic carbonate burial. Earth-Science Rev. 200, 102960. https://doi.org/https://doi.org/10.1016/j.earscirev.2019.102960

Tyrrell, T., Schneider, B., Charalampopoulou, A., Riebesell, U., 2008. Coccolithophores and calcite saturation state in the Baltic and Black Seas. Biogeosciences 5, 485–494. https://doi.org/10.5194/bg-5-485-2008

Van Cappellen, P., Wang, Y., 1996. Cycling of iron and manganese in surface sediments; a general theory for the coupled transport and reaction of carbon, oxygen, nitrogen, sulfur, iron, and manganese. Am. J. Sci. 296, 197 LP – 243. https://doi.org/10.2475/ajs.296.3.197

van den Boorn, S.H.J.M., Vroon, P.Z., van Belle, C.C., van der Wagt, B., Schwieters, J., van Bergen, M.J., 2006. Determination of silicon isotope ratios in silicate materials by high-resolution MC-ICP-MS using a sodium hydroxide sample digestion method. J. Anal. At. Spectrom. 21, 734–742. https://doi.org/10.1039/B600933F

Wallmann, K., Aloisi, G., Haeckel, M., Tishchenko, P., Pavlova, G., Greinert, J., Kutterolf, S., Eisenhauer, A., 2008. Silicate weathering in anoxic marine sediments. Geochim. Cosmochim. Acta 72, 2895–2918. https://doi.org/https://doi.org/10.1016/j.gca.2008.03.026

Wolff-Boenisch, D., Wenau, S., Gislason, S.R., Oelkers, E.H., 2011. Dissolution of basalts and peridotite in seawater, in the presence of ligands, and CO2: Implications for mineral sequestration of carbon dioxide. Geochim. Cosmochim. Acta 75, 5510–5525. https://doi.org/10.1016/j.gca.2011.07.004

Zeebe, R.E., Wolf-Gladrow, D., 2001. CO2 in seawater: equilibrium, kinetics, isotopes. Gulf Professional Publishing 65, 85-140. https://doi.org/10.1016/s0422-9894(01)x8001-x

Zhong, S., Mucci, A., 1989. Calcite and aragonite precipitation from seawater solutions of various salinities: Precipitation rates and overgrowth compositions. Chem. Geol. 78, 283–299. https://doi.org/10.1016/0009-2541(89)90064-8

III. Disentangling artificial and natural benthic weathering in organic rich Baltic Sea sediments

Michael Fuhr [a*], Klaus Wallmann [a], Andrew W. Dale [a], Isabel Diercks [a], Habeeb Thanveer Kalapurakkal [a], Mark Schmidt [a], Stefan Sommer[a], Stefanie Böhnke[a], Mirjam Perner[a], Sonja Geilert [a,b]

[a]GEOMAR Helmholtz Centre for Ocean Research Kiel, Wischhofstr. 1-3, 24148 Kiel, Germany
[b] Department of Earth Sciences, Utrecht University, Utrecht, The Netherlands

* Corresponding author at: GEOMAR Helmholtz Centre for Ocean Research Kiel, Wischhofstr. 1-3, 24148 Kiel, Germany.

Abstract

Enhanced mineral dissolution in the benthic environment is currently discussed as a potential technique for ocean alkalinity enhancement (OAE) to reduce atmospheric CO_2 levels. This study explores how biogeochemical processes affect the dissolution of alkaline minerals in surface sediments during laboratory incubation experiments. These involved introducing dunite and calcite to organic-rich sediments from the Baltic Sea under controlled conditions in an oxic environment. The sediment cores were incubated with Baltic Sea bottom water. Findings reveal that the addition of calcite increased the benthic alkalinity release from 0.4 μmol cm^{-2} d^{-1} (control) to 1.4 μmol cm^{-2} d^{-1} (calcite) as well as other weathering products such as calcium. However, these enhanced fluxes returned to lower fluxes after approximately four weeks yet still higher than the unamended controls. Microbial activity appeared to be the primary driver for lowering pore water pH and thus enhanced weathering.

In several sediment cores, pH profiles taken at the start of the experiments indicated activity of sulfur oxidizing *Beggiatoa* spp, which was verified by RNA-profiling of 16S rRNA genes. The pH profiles transitioned to those commonly associated with the activity of cable bacteria as the experiments progressed. The metabolic activity of cable bacteria would explain the significantly lower pH values (~5.6) at sediment depths of 1-3 cm, which would favor substantial calcite dissolution. However, a high abundance of cable bacteria was not reflected in 16S rRNA sequence data. Total alkalinity (TA) fluxes in these cores increased by a factor of ~3, with excess TA/calcium ratios indicating that the enhanced flux originated from calcite dissolution. The dissolution of dunite or the potential formation of secondary minerals could not be identified due to the strong natural flux of silicic acid, likely due to biogenic silica dissolution. Furthermore, no accumulation of potentially harmful metals such as nickel was observed, as highlighted as a potential risk in other studies concerning OAE.

Given the complexity of sediment chemistry and changes of the benthic conditions induced by the incubation, it remains challenging to distinguish between natural and enhanced mineral weathering. Further investigation, including the identification of suitable tracers for mineral dissolution, are necessary to assess the feasibility of benthic weathering as a practical approach for OAE and climate change mitigation.

III.1. Introduction

The 2018 IPCC (Intergovernmental Panel on Climate Change) special report 'Global Warming of 1.5 °C' and following reports clearly state that negative emissions will be necessary to keep global warming below 2 °C compared to preindustrial levels (IPCC, 2021, 2018). Thus, many studies have tried to assess and evaluate different strategies to achieve these negative emissions via carbon dioxide removal (CDR)

(Beuttler et al., 2019; Campbell et al., 2022; Feng et al., 2017; Fuss et al., 2018; Iizuka et al., 2004; Lackner, 2003; Lal, 2004). Among these methods, ocean alkalinity enhancement (OAE) via enhanced weathering (EW) of silicate and carbonate minerals was proposed, leading to an envisioned increase of CO_2-uptake into the surface ocean and thus serving as an affordable and effective CDR method (Campbell et al., 2022; Caserini et al., 2021; Hartmann and Kempe, 2008; Montserrat et al., 2017; Oelkers, 2001; Renforth and Henderson, 2017).

For example, the dissolution of an idealized magnesium silicate mineral such as forsterite (Mg_2SiO_4) and carbonate ($CaCO_3$) can be summarized as:

Forsterite: $$Mg_2SiO_4 + 4H_2O + 4CO_2 \rightarrow 2Mg^{2+} + H_4SiO_4 + 4HCO_3^- \quad \text{(III1)}$$

$CaCO_3$: $$CaCO_3 + H_2O + CO_2 \rightarrow Ca^{2+} + 2HCO_3^- \quad \text{(III2)}$$

These equations demonstrate that CO_2 uptake via forsterite, the Mg-endmember of olivine, is theoretically four times higher compared to $CaCO_3$. Both reactions have been scrutinized with regards to their kinetics mainly in aqueous solutions, with only a few in seawater (Flipkens et al., 2023; Fuhr et al., 2022; Montserrat et al., 2017; Rigopoulos et al., 2018; Rimstidt et al., 2012; Subhas et al., 2015; Walter and Morse, 1985). During the dissolution of olivine, the release of nickel has been proposed as a potential toxicant (Flipkens et al., 2021) and as a potential proxy for olivine dissolution (Montserrat et al., 2017). Furthermore, the formation of secondary minerals such as $CaCO_3$ and phyllosilicates has been described by Fuhr et al. (2022) and Rigopoulos et al. (2018). Their formation depends on the saturation state of the aqueous solution with respect to these minerals and diminishes the CO_2 uptake (Béarat et al., 2006; Burton and Walter, 1987; E. King et al., 2010; Fuhr et al., 2022; Hartmann et al., 2023; Lein, 2004; Moras et al., 2022; Sternbeck and Sohlenius, 1997). Fuhr et al. (2022) subsequently proposed environments where bottom waters are undersaturated with respect to secondary minerals to avoid this negative effect. Since the dissolution of $CaCO_3$, one of the major secondary phases, is driven by undersaturation, it appears sensible to also investigate the possible application of this material in such environments.

The Baltic Sea, where organic rich sediments release up to 80 Tg yr^{-1} of CO_2 (Nilsson et al., 2019), might offer potential sites for benthic OAE research. Natural CO_2 production results in high CO_2 partial pressure (pCO_2) and subsequently seasonally undersaturation with respect to calcite in bottom waters ($\Omega_{Cal} < 1$) (Melzner et al., 2013) making parts of the Baltic Sea sediments a potential alkaline mineral application site for enhanced benthic weathering. Additionally, bioturbation might entrain added alkaline substrates into the surface sediments where microbial activity can lead to very low pH and subsequently low Ω_{Cal} values, which may enhance dissolution of both olivine and calcite (Meysman et al., 2015; Meysman and Montserrat, 2017; Montserrat et al., 2017). However, the shallow sedimentary depocenters in the Baltic Sea display strong biogeochemical and physical seasonality, which leads to a highly complex chemical system governed by variable oxygen availability, bottom water temperatures, microbial activities, and organic matter degradation rates (Dale et al., 2011; Melzner et al., 2013; Perner et al., 2022). Moreover, the large benthic background fluxes induced by natural $CaCO_3$ input via continental erosion and diatom dissolution (Borawska et al., 2022; Gasiūnaitė et al., 2005; Wallmann et al., 2022) constitute further challenges for disentangling natural and enhanced weathering, as they might overprint potential fluxes induced by enhanced benthic weathering.

This experimental study examines the geochemical processes affecting enhanced benthic weathering of calcite and olivine, the major component of dunite, in intact sediment cores derived from Boknis Eck, a shallow depocenter (~28 m water depth) in Eckernförde Bay (southwestern Baltic Sea) under controlled

laboratory conditions. The bottom waters of this region are subject to a strong seasonality. During winter, the entire water column is mixed leading to weak chemical and physical gradients. During summer and autumn, warm and brackish surface waters over-flow colder and saltier bottom waters. The increasing stratification induces continuous deoxygenation with depth leading to hypoxic to anoxic conditions with lower pH values and high pCO2 in late summer and early autumn (Lennartz et al., 2014; Melzner et al., 2013). In order to understand mineral dissolution processes and to quantify alkalinity enhancement via enhanced benthic weathering, bottom water and pore water chemistry combined with micro-profiling and microbial 16S rRNA gene data are used in this study to disentangle natural and enhanced weathering under predominantly aerobic winter conditions.

III.2. Materials and Methods

III.2.1. Materials

Ten sediment cores (50 cm multi-corer) and 120 l of bottom water were recovered from 27 m water depth (below the euphotic zone) at Boknis Eck, Eckernförde Bay, with FK Littorina on January 13th 2022. These cores contained 20 - 24 cm of sediment and between 1.5 l and 2 l of bottom water. After recovery, the cores containing mainly fine-grained sediments of the clay to fine sand fraction, were sealed top and bottom with rubber plugs, held in upright position, and taken to a cool laboratory (12.5 °C). One core was sliced for pore water and sediment analyses and one core was subsampled for bacterial 16S rRNA amplicon sequencing immediately after recovery. They served to provide data characteristic of the initial sediment conditions. Eight cores were kept for the incubation experiments. Dunite and calcite were used as alkaline materials to investigate their efficiency with respect to OAE. Dunite (Olivine AFS 80) was obtained from Sibelco^{TM} that ultimately derives from several quarries in Årheim (Norway). Via sieving, the 20µm – 30µm fraction was extracted. For the mineralogical composition see Table 1S(supplement). Since the dunite used in this study contains 88.8% olivine (Table 1S, supplement) and this mineral dissolves much faster than the other components (Pokrovsky and Schott, 2000), it was assumed that olivine is the major dissolving silicate phase. For correct nomenclature, though, dunite will be used to describe the added material, whereas olivine will be used to describe the dissolution kinetics and stoichiometry of this mineral. Ground limestone ($CaCO_3$ > 99%, Jurassic, grain size < 0.1mm) obtained from the German limestone association (Table 2S, supplement) was first rinsed with deionized water (18.2 MΩ cm^{-1}-Milli-Q system). In order to avoid an unknown fine fraction remaining in suspension during the experiment, the material was first mixed with deionized water in a settling column (height 20 cm), and particles that remained in suspension after 20 seconds were decanted. This procedure was repeated until the supernatant water was clear after 20 seconds to ensure that after adding the material to the sediment cores, all particles sink to the sediment surface after several minutes. Due to the high calcite content, this material will henceforth be referred to as calcite.

III.2.2. Determination of reactive surface

For dunite grains, the reactive surface was calculated as the surface of spherical grains as the majority of studies report dissolution kinetics based on this assumption (Rimstidt et al., 2012).

For calcite grains, the reactive surface was determined via gas adsorption using the Brunauer-Emmett-Teller (BET) method following Brunauer et al. (1938) on a Stöhlein^{TM} AREA-Meter II. For this method two equally sized vessels one containing the sample and the other empty, are filled with nitrogen at atmospheric pressure at room temperature. Subsequently, both adsorption flasks are immersed in liquid nitrogen,

cooling them to the boiling point of liquid nitrogen. At this temperature, the sample adsorbs nitrogen, resulting in a pressure difference between the adsorption flask and the reference flask, which is measured using a differential manometer. The specific surface area is calculated from this pressure difference, the initial pressure, and the sample weight. Results of the measurements and calculations are summarized in Table 1.

Table III 3: Overview over different cores, including bottom water (BW) volumes, treatments (Cal = calcite, Dun = dunite, C = control), BET surface area of calcite (measured) and geometrical surface area of dunite grains assuming an average grain size of 25 µm.

Core name	Cal1	Cal2	Cal3	Dun1	Dun2	Dun3	C1	C2
Volume BW	2l	2l	2l	2l	2l	2l	1.5l	2l
Mineral/rock:	Calcite	Calcite	Calcite	Dunite	Dunite	Dunite	-	-
Mass (g):	7.8618	7.8618	7.8618	4.4781	4.4781	4.4781	-	-
Grain size (µm)	-	-	-	20-30	20-30	20-30		
BET-surf. ($m^2\ g^{-1}$)	0.45±0.06	0.45±0.06	0.45±0.06	-	-	-	-	-
Geom. surf. ($m^2\ g^{-1}$)	-	-	-	0.073±0.004	0.073±0.004	0.073±0.004	-	-

III.2.3. Experimental setup

The eight sediment cores were placed in a rack in an upright position. The bottom water was carefully removed via suction and replaced with a known volume (1.5 l – 2.0 l) of filtered (0.2 µm) Baltic Sea bottom water in order to remove pelagic auto- and heterotrophs and suspended particles. The volume of water added depended on the height of sediment in each core which varied slightly due to the recovery method. After this procedure, a gaseous headspace of ca. 10 cm was left in each core. Furthermore, the cores were equipped with adjustable stirring heads that contained ports for inserting optodes to continuously record pH and O_2 concentrations in the overlying water (for details see section 2.4). In order to prevent anoxic conditions developing, ambient air was bubbled into the water column. The water column in each core was slowly and continuously flushed with a constant throughflow of 40 µl min^{-1} from a single reservoir of bottom water. The residence time of the water inside the cores was thus about 4 to 5 weeks.

The cores were kept untreated for three weeks prior to mineral addition in order to equilibrate with the laboratory environment and to obtain a quasi-steady state natural background for each core. After this period, calcite (Cal1 – Cal3) and dunite (Dun1 – Dun3) were carefully spread on the sediment surface with three replicates for each treatment. Two control cores were left untreated (C1, C2). A precise description of each core is given in Table III 1. The incubation was carried out in darkness for approximately three months at 12.5 °C.

III.2.4. Sampling procedure and analysis

Bottom water samples were taken from the outflow of each core over a time period of several hours. Thus, samples represent the average outflow over the respective time period. Sampling intervals increased from daily during the first two weeks to every three to four days and weekly towards the end of the experiment. All samples were filtered through a 0.2 µm cellulose membrane filter and refrigerated in 25 ml Zinsser™

scintillation vials. A 5 ml aliquot was frozen directly after the sampling procedure for later nutrient analysis. Nutrient measurements were performed either via manual photometric measurement (NH_4) or using a Seal – Analytical™ QuAAtro autoanalyzer (PO_4^{3-}, NO_2^-, NO_3^-). Samples for TA were analyzed directly after sampling by titration of 1 ml of bottom/pore water with 0.02N HCl following Ivanenkov and Lyakhin (1978). Titration was ended when a stable purple color appeared. During titration, the sample was degassed by continuous bubbling with nitrogen to remove any generated CO_2 and H_2S. The acid was standardized using an IAPSO seawater standard. Anion element concentrations (SO_4^{2-}, Cl^-, Br^-) were determined using ion chromatography (IC, METROHM 761 Compact, conductivity mode). Acidified sub-samples (30 µl suprapure HNO_3^- + 3 ml sample) were prepared for analyses of major and trace elements (Si, Na, K, Li, B, Mg, Ca, Sr, Mn, Ni and Fe) by inductively coupled plasma optical emission spectroscopy (ICP-OES, Varian 720-ES).

At the end of the experiments, the bottom water was removed via suction and the cores were sliced for pore water, solid phase and bacterial 16S rRNA analysis. The pore waters were recovered by centrifuging each respective sediment layer in 50 ml falcon tubes at 3000 rpm for 10 minutes. Afterwards, the supernatant water was transferred to polyethylene (PE) vials in an Ar-filled glove bag to minimize contact with oxygen. In addition to the parameters listed above, pore waters were analyzed for H_2S and Fe^{2+}. For the analysis of dissolved Fe^{2+} concentrations, sub-samples of 1 ml were taken within the glove bag, immediately stabilized with ascorbic acid and analyzed within 30 minutes after complexation with 20 µl of Ferrozin. For H_2S, an aliquot of pore water was diluted with appropriate amounts of oxygen-free artificial seawater and the H_2S was fixed by immediate addition of zinc acetate gelatin solution. Further details are described by Dale et al. (2014) and Dale et al. (2016).

Subsamples for bacterial community analyses were collected from surface sediments (0-2 cm) of all treatments and controls at the beginning of the experiment, after 42 days and at the end of the incubation (72 days, t6). At the end of the experiment (91 days, t7), not only the surface sediment but the entire core of one control (C1) was subsampled, with a resolution of 1 cm in the first 4 cm, followed by 2 cm sampling below the 4 cm horizon. The same resolution was used for the above-mentioned environmental start core that was also subsampled in a whole. All microbiological samples were immediately frozen at -80°C until further processing.

Bottom water pH and O_2 were continuously measured using logging devices (Pyroscience™ PHROBSC-PK8 and OXROB3, respectively) calibrated following the instructions as provided by the manufacturer. Three TRIS-buffers were used to calibrate the pH probe for brackish bottom water conditions (Müller et al., 2018; Pratt, 2014). pH is reported on the total scale.

III.2.5. Solid phase analysis

Total carbon (TC) and total organic carbon (TOC) as well as total nitrogen (TN) and total sulfur (TS) were measured in freeze-dried and ground sediment samples by flash combustion using the Carlo Erba Element Analyzer (NA-1500). Total inorganic carbon (TIC) was calculated by subtracting TOC from TC. The accuracy of the method was tested by method blanks and two reference standards (2.5-Bis(5-tert-butyl-2-benzo-oxazol-2-yl)thiophene (BBOT, HEKAteck™) and one internal sediment standard). For more details see Bohlen et al. (2011) and Dale et al. (2011).

III.2.6. Micro profiling

Sediment micro profiling was performed using a motorized Unisense™ micromanipulator (MMS). Oxygen, pH and H_2S profiles were measured with Unisense™ sensors Ox-50, pH-100 and SULPH-100, respectively. Vertical step sizes were adjusted to the respective sensor (minimum size was twice the needle diameter) and desired measuring resolution to keep the time for profiling as short as possible (100 µm for all O_2 profiles, 250µm for first pH and H_2S profiles, later 300 µm). All sensors were calibrated in accordance with manufacturer recommendations for saline solutions (Unisens™ calibration kit for SULPH-100 with a calibration concentration of 109 µmol l^{-1}). Additionally to WTW™ standard pH buffers (4.01, 7.00 and 10.01), the pH sensitivity of the pH-100 in brackish waters and the off-set was determined using three TRIS-buffers (Müller et al., 2018; Pratt, 2014). After obtaining H_2S and pH profiles, the total dissolved sulfur concentration was calculated according to the Unisense™ guidelines based on Millero et al. (1988) and Jeroschewski et al. (1996). Unless otherwise stated, H_2S henceforth refers to total dissolved hydrogen sulfide ($H_2S + HS^-$).

III.2.7. Flux calculations from bottom water concentrations and oxygen profiles

Solute fluxes were calculated based on concentrations in the inflow and the outflow following:

$$F_e = \left(\left(\frac{dC_e}{dt} + k_w \times C_{out} - k_w \times C_{in}\right) \times V_{MUC}\right) / A_{sed} \quad \text{(III3)}$$

where F_e is the flux of any component (e) over the entire sediment surface (mol cm^{-2} d^{-1}), $\frac{dC_e}{dt}$ is the measured concentration change of the respective element over a specific time (mol l^{-1} d^{-1}) assuming that the concentration of this element is not affected by any process in the water column. k_w is the water exchange rate in d^{-1}, C_{out} is the outflow concentration (mol l^{-1}), C_{in} is the inflow concentration (mol l^{-1}), V_{MUC} is the bottom water volume (l) in each core and A_{sed} (cm^2) is the sediment surface area of each core.

These calculations were performed for all measured solutes except oxygen and H_2S. Additionally, diffusive fluxes were calculated based on pore water profiles following:

$$F_{sed} = -\phi \times D_s \times \frac{dC}{dz} \quad \text{(III4)}$$

where F_{sed} is the flux of a respective solute (µmol cm^{-2} d^{-1}), ϕ is the porosity, D_s is the molecular diffusion coefficient in the sediment and dC/dz is the concentration gradient where the flux is determined. D_s was calculated as:

$$D_s = \frac{D_M}{\phi^{1-m}} \quad \text{(III5)}$$

where D_M is the molecular diffusion coefficient in seawater and m is an empirical factor (here m = 3) (Boudreau, 1997). The D_M values were calculated following Boudreau (1997).

For a clearer visualization, the flux data were smoothened using a moving average. For further calculations, raw flux data were used (S1.1, Figure 1S, supplement).

III.2.8. Temporal segmentation of experimental data

In order to compare results from the different cores, the experiment was segmented into different time intervals. These time intervals were defined individually for each core in a way that each interval started intermediate between the times that microsensor profiles were obtained. The time intervals for each core are listed in Table III 2 and reported as starting time to end time in days after addition of substrates.

Table III 4: Pore water properties of all cores in the upper 6cm of the sediment during different time intervals (t1 to t7). Time intervals were defined around each time a microsensor profile was measured and are reported as starting time (d) - end time (d). O_2 depth describes the depth when oxygen concentrations reached 0 µmol l^{-1}, $Diss_{pot}$ is the depth integrated undersaturation with respect to calcite (section 4.4), the average (av.) pH is the mean value in the upper 6 cm of sediment, H_2S budget is the H_2S inventory in the upper 6 cm of sediment, and H_2S flux is the flux of H_2S from deeper sediments towards the surface based on H_2S micro profiles. H_2S depth defines the depth below the sediment surface where concentrations exceeded 1 µmol l^{-1}. TA, Ca and Si fluxes were calculated based on bottom water concentrations.

	time interval (days of experiment)	O_2 depth (mm)	$Diss_{pot}$ (cm)	av. pH	H_2S budget (µmol cm^{-2})	H_2S flux (µmol cm^{-2} d^{-1})	H_2S depth mm	TA flux (µmol cm^{-2} d^{-1})	Ca flux (µmol cm^{-2} d^{-1})	Si flux (µmol cm^{-2} d^{-1})
Cal1										
t1	"-3 - 1"	1.6	0.24	7.82	0.00	0.07	53.50	0.35	-0.80	0.48
t2	"2 - 5"	2.1	0.01	7.91	0.05	0.39	53.10	2.65	2.73	0.31
t3	"6 - 14"	1.4	0.04	7.84	0.32	0.69	48.00	1.00	0.81	0.23
t4	"15 - 28"	2.7	0.02	7.89	0.37	0.28	45.00	0.93	0.27	0.30
t5	"29 - 42"	2.4	0.60	7.51	0.90	0.23	27.60	0.80	0.21	0.28
t6	"43 - 56"	3	1.25	7.38	0.73	0.15	25.20	0.91	0.07	0.24
t7	"57 - 69"	3.9	1.43	7.15	0.54	0.14	26.40	0.92	0.19	0.24
Cal2										
t1	"-3 - 0"	2.3	0.60	7.62	0.80	0.73	38.00	0.20	-0.74	0.38
t2	"1 -4"	1.8	0.12	7.68	2.61	2.72	37.00	2.56	1.65	0.15
t3	"5 - 13"	1.7	0.00	7.69	2.13	0.53	28.50	0.96	0.80	0.16
t4	"14-27"	2.1	0.02	7.63	2.17	0.32	22.20	0.51	0.42	0.19
t5	"28 - 41"	2.9	0.32	7.44	3.01	0.34	16.50	0.45	0.24	0.16
t6	"42 - 56"	2.6	0.75	7.38	4.23	0.47	12.60	1.13	0.20	0.15
t7	"57 - 69"	3.2	1.43	7.18	2.35	0.39	22.20	2.07	0.54	0.17
Cal3										
t1	"-3 - 2"	1.4	0.45	7.36	2.18	0.41	28.50	1.37	-0.85	0.37
t2	"3 - 6"	2.1	0.17	7.48	3.35	0.55	26.00	1.79	1.23	0.30
t3	"7 - 15"	2.1	0.41	7.48	2.60	0.37	23.10	1.38	0.30	0.28
t4	"16 - 29"	2.9	0.34	7.34	2.48	0.40	26.70	0.57	0.30	0.30
t5	"30 - 43"	3.1	2.22	7.34	2.47	0.37	18.60	1.16	0.31	0.27
t6	"44 - 57"	3.6	1.43	7.24	1.91	0.31	23.70	1.09	-0.01	0.15
t7	"58 - 69"	4.6	2.06	7.08	1.31	0.26	23.10	1.13	0.70	0.24
Dun1										
t1	"-3 - 2"	1.5	0.44	7.81	0.86	2.19	44.50	0.11	0.40	0.42
t2	"3 - 6"	2.2	0.16	7.89	0.79	0.88	44.60	1.06	0.61	0.31
t3	"7 - 15"	1.5	0.14	7.94	1.03	0.51	43.50	0.32	0.58	0.26
t4	"16 - 29"	1.6	0.30	7.86	0.99	0.61	39.90	0.86	0.25	0.26
t5	"30 - 43"	3	0.36	7.75	0.93	0.93	35.40	0.45	0.09	0.23
t6	"44 - 57"	3.3	0.20	7.74	1.74	0.27	24.00	0.66	0.14	0.21
t7	"58 - 69"	3.5	1.17	7.38	1.43	0.21	18.60	0.99	0.04	0.22

	time interval (days of experiment)	Oxy depth (mm)	$Diss_{pot}$ (cm)	av. pH	H_2S budget (µmol cm^{-2})	H2S flux (µmol cm^{-2} d^{-1})	H_2S depth µm	TA flux (µmol cm^{-2} d^{-1})	Ca flux (µmol cm^{-2} d^{-1})	Si flux (µmol cm^{-2} d^{-1})
Dun2										
t1	"-3 - 0"	1.8	0.43	7.89	0.62	0.92	42.50	-0.13	-0.81	0.52
t2	"1 -4"	1.4	0.27	7.81	1.88	2.15	37.20	1.47	0.28	0.24
t3	"5 - 13"	2.7	0.18	7.83	2.31	0.31	28.50	0.28	0.66	0.26
t4	"14 - 27"	2.2	0.19	7.80	1.39	0.56	33.60	0.85	0.74	0.26
t5	"28 - 41"	2.5	1.00	7.38	1.47	0.35	26.70	1.03	0.24	0.23
t6	"42 - 56"	3	1.77	7.16	1.19	0.32	25.20	1.30	0.26	0.24
t7	"57 - 69"	3.1	1.81	7.16	1.03	0.26	20.40	0.96	0.42	0.25
Dun3										
t1	"-3 - 1"	1.3	1.99	6.97	2.14	0.82	30.50	2.06	1.09	0.32
t2	"2 - 5"	1	2.15	6.97	1.98	0.42	29.40	3.58	1.36	0.28
t3	"6 - 14"	1.6	2.25	6.93	2.36	0.51	27.60	3.26	2.07	0.19
t4	"15 - 28"	2.2	2.09	6.94	2.10	0.41	22.80	0.64	0.75	0.28
t5	"29 - 42"	2	0.43	7.19	2.61	0.30	12.00	-0.07	0.37	0.32
t6	"43 - 56"	2.7	0.29	7.28	2.88	0.35	12.90	0.39	0.05	0.27
t7	"57 - 69"	4	0.69	7.19	2.32	0.30	11.00	0.78	0.25	0.24
C1										
t1	"-3 - 0"	1.7	0.37	7.69	0.68	1.76	47.50	0.49	-0.27	0.63
t2	"1 - 3"	1.3	0.23	7.78	0.83	1.04	43.50	0.04	1.07	0.30
t3	"4 - 6"	1.6	0.27	7.75	0.80	0.43	46.10	0.85	0.05	0.23
t4	"7 - 13"	1.6	0.61	7.60	0.76	0.51	41.10	0.23	0.97	0.27
t5	"14 - 27"	2.5	0.65	7.65	0.27	0.46	47.70	0.45	0.48	0.23
t6	"28 - 43"	2.6	1.32	7.42	0.14	0.28	47.10	0.91	0.35	0.27
t7	"44 -56"	3.3	1.12	7.41	0.67	0.28	36.90	1.15	0.32	0.22
t8	"57 - 69"	3.6	1.50	7.25	0.43	0.15	31.50	1.47	0.56	0.27
C2										
t1	"-3 - 0"	1.2	2.41	6.87	2.50	0.77	24.50	2.60	1.58	0.39
t2	"1 - 4"	1.1	2.39	6.94	2.02	0.24	22.20	6.22	3.07	0.21
t3	"5 - 8"	2.2	2.99	6.76	2.31	0.48	21.00	5.75	0.95	0.17
t4	"9 - 15"	1.4	3.32	6.65	1.89	0.52	20.10	4.78	2.70	0.19
t5	"16 -27"	2	3.89	6.51	1.69	0.37	21.60	2.18	1.20	0.16
t6	"28 - 42"	2.7	3.39	6.74	0.28	0.10	19.50	1.41	1.21	0.17
t7	"43 - 56"	4.6	3.43	6.78	0.86	0.39	19.50	0.90	0.92	0.17
t8	"57 - 69"	5.8	3.89	6.74	0.60	0.43	14.70	0.13	0.77	0.20

The pore water O_2, H_2S and pH were assumed to be constant in each time interval. Subsequently the fluxes for O_2 and H_2S calculated from the microsensor data were averaged over the respective time interval to provide values in µmol cm^{-2} d^{-1} (Table III 2). The oxygen penetration depth was defined as the depth where the oxygen concentration reached detection limit (~0.2 µM). pH values are reported as an average over the entire depth where each profile was obtained. The depth where H_2S first appeared below the sediment surface was defined as the depth where measured H_2S exceeded the analytical precision (~2 µmol l^{-1}). H_2S inventory for each time period were calculated by integrating bulk sediment concentrations over the upper 6 cm height and are reported as µmol cm^{-2}.

III.2.9. Sequencing and sequence processing of 16S amplicon data

For studying the composition of the microbial community, a 16S amplicon library compatible with the Illumina MiSeq System was prepared as described previously (Böhnke et al., 2019; Perner et al., 2022). Briefly, RNA was extracted from around 300 mg sediment sample using the NucleoBond RNA Soil Mini

kit (Macherey-Nagel, Düren, Germany) followed by subsequent DNaseI digestion using the RapidOut DNA Removal kit (Thermo Fisher Scientific GmbH, Waltham, Massachusetts, USA). Total environmental RNA was transcribed into cDNA with Invitrogen's SuperScript® VILO™ cDNA Synthesis Kit (Life Technologies™, Darmstadt, Germany). Purified cDNA (Zymo Clean & Concentrator-5, Irvine, CA, USA) was then used to generate 16S ribosomal amplicons for the bacterial hypervariable V3 and V4 regions using the primer pairs S-D-Bac-0341-b-S-17 and S-D-Bac-0785-a-A-21 as described by Klindworth et al., (2013). Sequencing was done in collaboration with the Competence Centre for Genomic Analysis (CCGA) of the Institute of Clinical Molecular Biology (IKMB, CAU Kiel, Germany) in a 2x300 bp paired-end sequencing run on the Illumina MiSeq platform (Illumina, St. Diego, USA).

For sequence processing the Qiime2 workflow was applied (Bolyen et al., 2019). Here, filtering and merging of demultiplexed raw reads were performed using the dada2-plugin with default settings and removal of the primer sequences (Callahan et al., 2016). For taxonomic assignments, the SILVA database release 138 (99% OTUs full-length sequences) (Quast et al., 2013) was pretrained with the respective primer pairs for bacteria (Bokulich et al., 2018; Pedregosa et al., 2011). The assignments were computed using the feature-classifier plugin (classify sklearn) with default settings and the pre-trained SILVA classifier (Bokulich et al., 2018). The phylogeny was calculated using the "align-to-tree-maffft-fasttree" pipeline (Price et al., 2010). Statistical analyses and plots were performed using R software (R Foundation for Statistical Computing, Vienna, Austria. URL https://www.R-project.org/) using the 'microeco' package (Liu et al., 2021).

III.3. Results

III.3.1. Geochemical changes in pore water over time

Pore water analysis of one core was performed at the beginning of the experiment, and in all cores at the end of the experiment (Figure III 1a). In all cores, SO_4^{2-} concentrations decreased with depth. In the initial core, SO_4^{2-} decreased to < 1 mM. Concentrations and penetration depths increased significantly in all cores over the course of the experiment, whereas the bottom water concentration increased only slightly from ~17 mmol l^{-1} to ~18 mmol l^{-1} (Figure III 1a). In deeper sediment layers, the concentration increase was much larger, varying from 3 mmol l^{-1} in Dun3 to 6 mmol l^{-1} in Dun2 at 20 cm depth.

This downcore decrease in SO_4^{2-} was mirrored by a downcore increase in H_2S (Figure III 1b). At the end of the incubation, H_2S concentrations in all cores were lower compared to initial values. The H_2S loss relative to the initial values was slightly smaller than the SO_4^{2-} increase with large variations between the different cores (~800 µmol l^{-1} in Dun2 to ~2000 µmol l^{-1} in C2 at the end of the experiment compared to ~4000 µmol l^{-1} at the beginning in 20 cm depth). In the initially sampled core, the H_2S front (i.e. the depth where H_2S increases sharply) was about 3 cm. By the end of the experiment, this depth horizon had shifted downwards to ~5 cm and to ~7 cm in the cores Dun2 and C1, respectively. Exceptions to this trend are Cal2 and Dun3, where no change in the H_2S depth horizon from the initial value was observed.

In all cores, TA increased with depth (Figure III 1c), but decreased in each depth layer over the course of the experiment by 10 mmol l^{-1} (C2) to 15 mmol l^{-1} (Cal2) compared to the initial values.

A different behavior was observed for NH_4^+. Compared to the initially sampled core, lower concentrations were measured in the upper sediment sections (0 cm – 7 cm) towards the end of the experiment in all cores. However, the concentrations in deeper layers did not decrease and fluctuated around initial values (Figure III 1d).

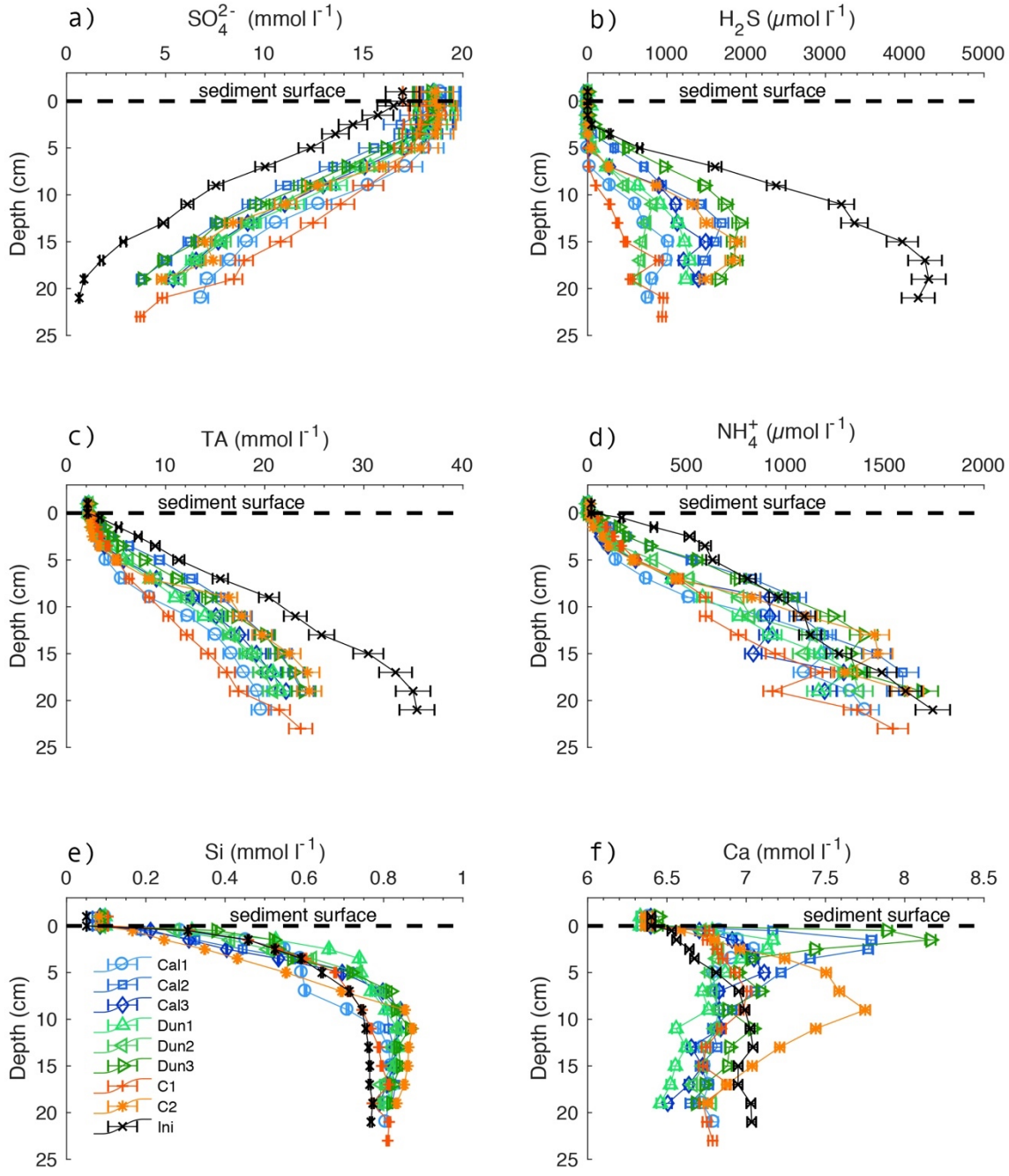

Figure III 1: SO_4^{2-}, b) H_2S, c) TA d) NH_4^+ e) Si and f) Ca concentrations in all sediment cores. Colored markers indicate concentrations in each core at the end of the experiment. Black crosses indicate the concentrations in the initial core. Horizontal dashed line represents the sediment surface. Data above the sediment surface are bottom waters. Error bars report analytical precision.

Initial Si concentrations (Figure III 1e) increased sharply in the upper 5 – 7 centimeters. This concentration gradient weakened with depth and reached asymptotic values of about 750 µmol l^{-1} below 15 cm depth. In the cores sampled after the experiment, concentrations in all cores increased to ~850 to

~950 µmol l^{-1} at ~10 cm depth. In the upper 5 cm, concentrations were mostly lower compared to initial values.

Initial Ca concentrations increased linearly from ~6.4 to ~7.0 mmol l^{-1} at 7 cm depth, and then fluctuated around these values in deeper layers. Final concentrations in the upper sediment were markedly higher than initial ones, and up to ~6.8 mmol l^{-1} (C1) and ~8.2 mmol l^{-1} (Dun3). In most incubated cores, Ca concentrations showed peaks between 2.5 cm and 5 cm. An exception to this was core C2 with highest values (~7.8 mmol l^{-1}) observed at 10 cm depth. Below the peak, Ca concentrations decreased in all cores to values between ~6.4 mmol l^{-1} (Dun1) and ~6.8 mmol l^{-1} in C1.

III.3.2. Fate of added material and solid phase composition

After the addition of calcite and dunite, the substrates initially covered the sediment surface as an approximately 0.5 mm thick layer. Within the first two weeks the grains had been entrained into the sediment and were continuously transported further downwards until they reached a depth of 1-2 cm after about six weeks. By the experiment, the substrates were visible as a brighter layer in the sediment through the walls of the cores clearly distinguishable from the matrix (Figure 4S, supplement).

In the initially sampled core, TIC content varied between 0 and ~ 4.5 wt.% with a slight increase downcore (Figure III 2). In calcite-treated cores, TIC content at the surface at the end of the experiment was up to 16 % in the uppermost sample. C1 also showed values of ~6% in the upper 3 cm. After the experiment, TIC contents in all cores below 3 cm were in the same range, except in Dun3 where TIC contents up to 10% were measured at 15 cm depth. This core showed overall higher concentrations compared to the other treatments.

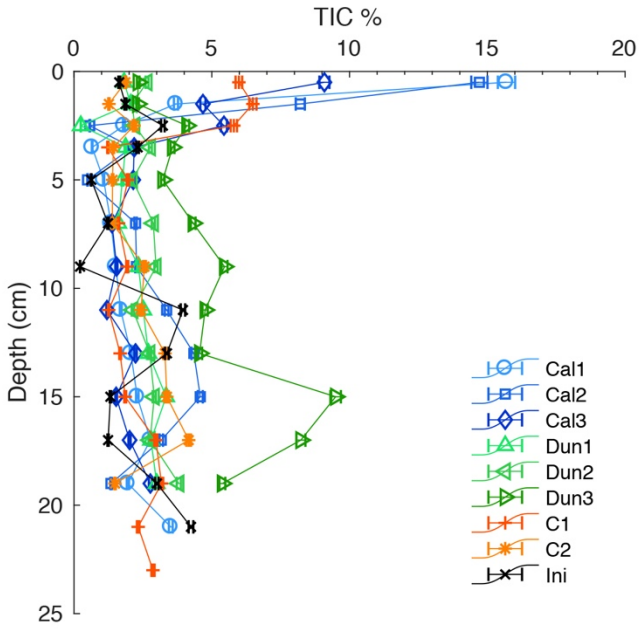

Figure III 2: TIC content in the solid phase of all cores. Colored markers indicate contents in each core at the end of the experiment. Black crosses indicate the contents in the initial core. Error bars report analytical precision.

III.3.3. pH shift in pore waters as observed by micro profiling

The pH distribution in pore water profiles was highly dynamic (Figure III 3) with two major regimes that occurred at different times in nearly all cores (exceptions are Dun3 and C2). Initially, pH decreased by around 0.5 units in the oxic surface layer (~1– 2 mm, Table III 2) and then increased in deeper sediments by up to 1.4 units (peaking around 4 cm) before decreasing again below 5 cm. Lowest surface pH (~7.0) was observed in Dun1 and Dun2 (Figure III 3), along with highest values in deeper sediments (~8.4). Over the course of the experiment, this distribution gradually shifted to the second major regime that was initially observed in Dun3 and C2, that is, a clear pH peak with values up to 8.5 (Dun3) just below the surface. With increasing depth, pH decreased down to values of ~5.6 (C2).

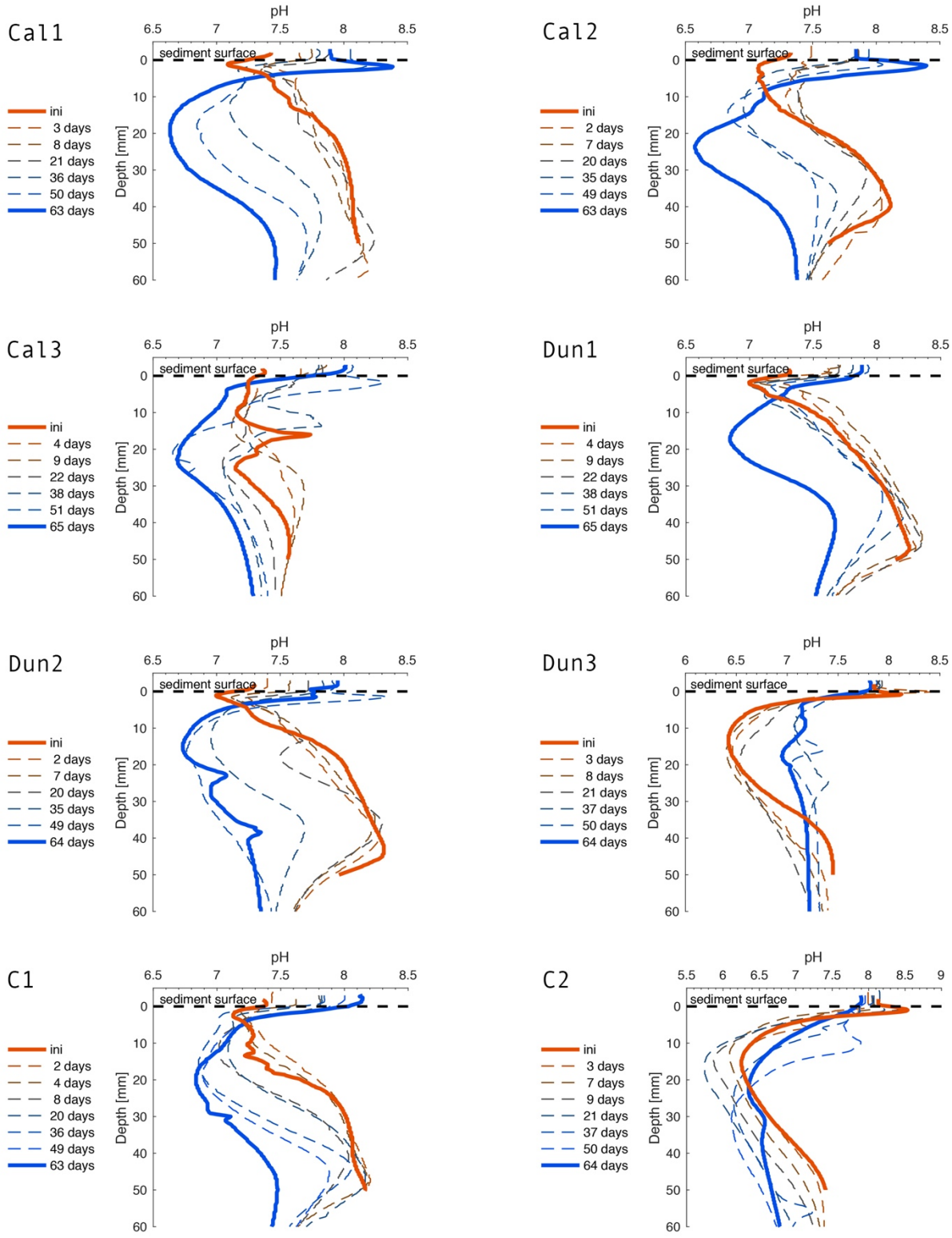

Figure III 3: pH-profiles over the course of the experiment. Solid red and blue lines indicate the initial (one day before addition of substrates) and final profiles, respectively. Dashed lines represent the profiles measured in days after addition of alkaline min

III.3.4. Bottom water chemistry and fluxes across the sediment/water interface

TA concentrations in bottom waters increased over time in all cores over the first month of the experiments (Figure III 4a). These changes are mirrored by corresponding TA fluxes (Figure III 4b). Addition of alkaline minerals led to an almost immediate increase in TA fluxes for all calcite and dunite-treated cores. The reference core (C2) and dunite-treated core (Dun3) initially showed a very rapid TA increase to peak values of 4 mmol l^{-1} (Dun3) to 5.5 mmol l^{-1} (C2). Towards the end of the experiment, TA fluxes generally declined to about 1 - 2 µmol cm^{-2} d^{-1} for all cores treated with alkaline minerals. The two reference cores (C1, C2) covered a surprisingly large range in TA concentrations and fluxes despite no minerals being added.

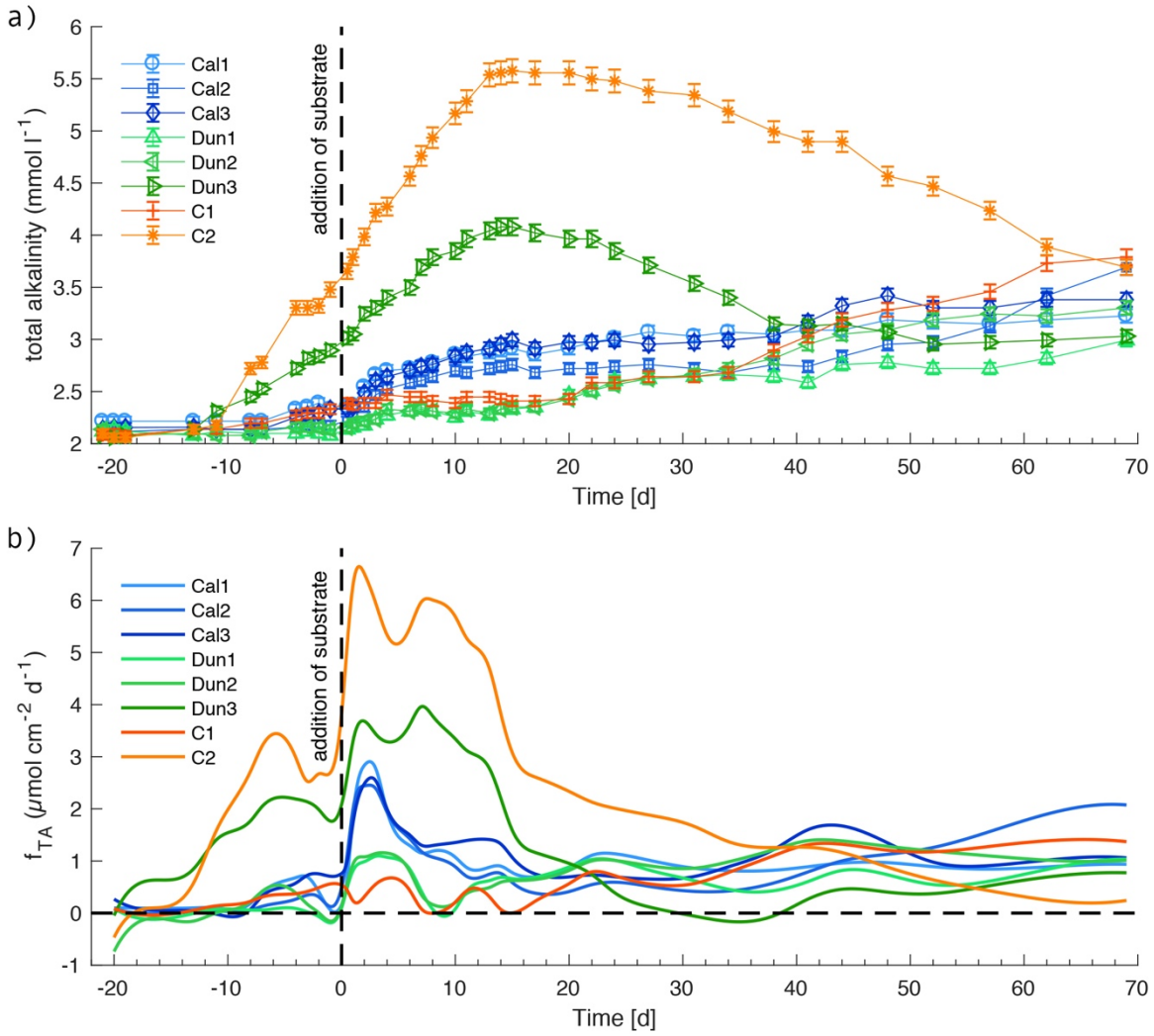

Figure III 4: TA concentrations in bottom waters (a) and fluxes at the sediment surface (b) in all sediment cores. Positive fluxes denote a flux from the sediment to the bottom water and negative fluxes vice versa. Dashed lines indicate the addition of substrates. Time is given in days relative to mineral addition. Error bars on the concentrations denote analytical precision. Fluxes were calculated from bottom water concentrations (Eq. III3). For clarity, flux data were filtered as described in the supplement (S1). Note that filtered data is only used for visualization and not for any further calculations.

Dissolved silicon concentrations (Figure III 5a) increased in all cores during the early stage of the experiment to peak values between ~190 µM (Dun3) and ~375 µM (Cal1). The corresponding fluxes (Figure III 5b) averaged between 0.28 µmol cm^{-2} d^{-1} and 0.65 µmol cm^{-2} d^{-1} in the respective cores during this period. During the eight days prior to addition of substrates, the concentrations in all cores slightly decreased, as reflected in decreasing fluxes. An increase in Si concentrations between day -1 and day 0 was associated with elevated fluxes just prior to mineral addition. A strong decrease in average fluxes around day 0 led to a slight decrease in Si concentrations. Afterwards the increasing trend in concentrations was a common feature for all cores with no significant trend ascribable to a specific treatment. Over the course of the experiment, the fluxes smoothened out and varied between 0.16 µmol cm^{-2} d^{-1} (Cal1) and 0.3 µmol cm^{-2} d^{-1} (C1).

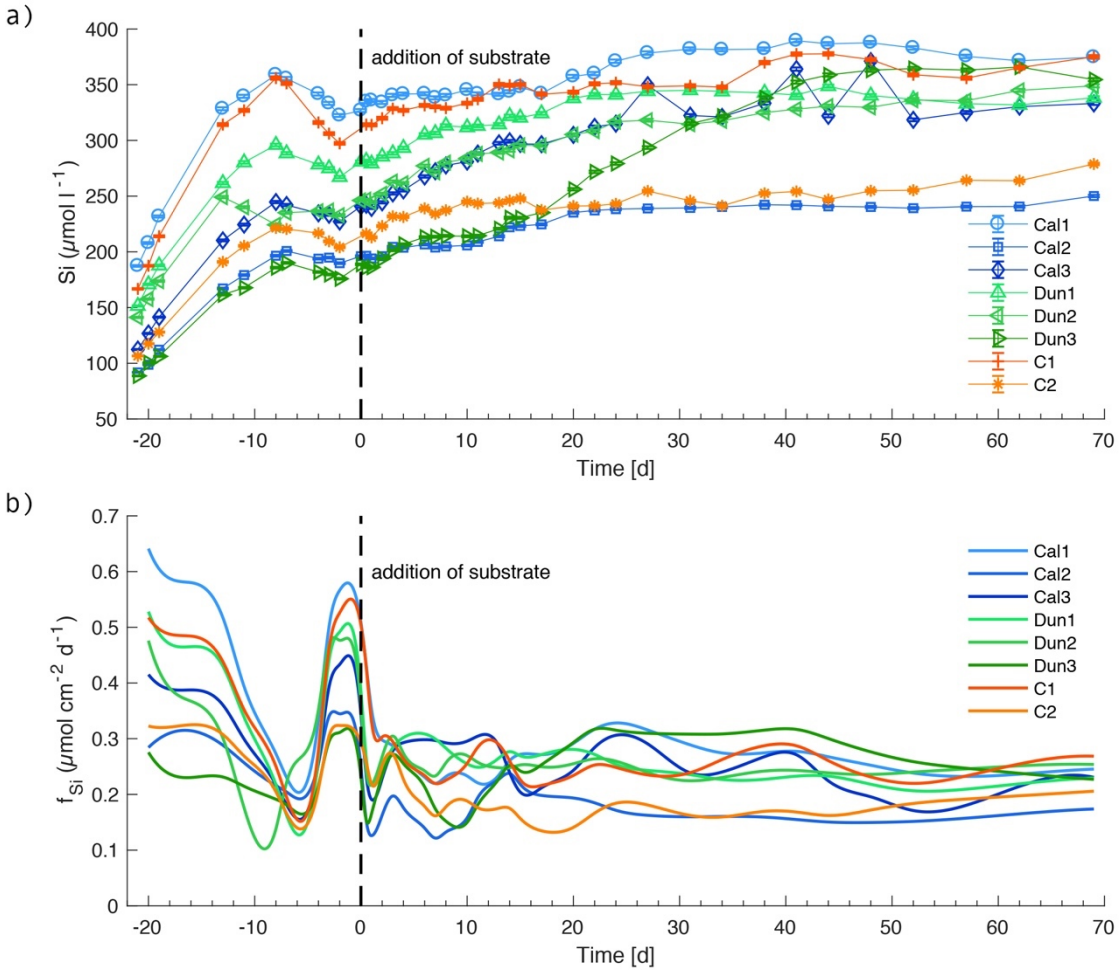

Figure III 5: Si concentrations in bottom waters (a) and fluxes at the sediment surface (b) in all sediment cores. See Fig. III 4 for further information.

Dissolved calcium (Ca) concentrations showed more muted trends than TA fluxes, yet clearer trends than Si concentrations (Figure III 6a). Ca concentrations decreased in all cores shortly before mineral addition and then showed an overall increase in all cores over the course of the experiment. The highest Ca concentrations were observed in those cores that also reached anomalously high TA values (C2, Dun3, Figure III 4a, Figure III 6a) The addition of calcite led to an almost immediate increase in dissolved Ca fluxes (Figure III 6b, Cal1 – Cal3). Ca fluxes decreased after a few days and reached values in the range of 0.3 – 0.8 µmol cm^{-2} d^{-1} towards the end of the experiments for all calcite-treated cores. Interestingly a similar development of fluxes was observed in dunite treated cores.

Throughout the experiment, nickel concentrations stayed below detection limit (~0.2 µmol l^{-1}) both in pore waters and in bottom waters (data not shown).

Oxygen concentrations in bottom waters (Figure 2S, supplement) varied widely during the early stage of the experiment when oxygen was only supplied by diffusion across the air/water interface. The lowest concentrations were measured between day 2 and 3 in Cal2 and C1 (~90 µmol l^{-1}). After bubbling the water column with ambient air directly in the liners, oxygen concentrations increased and stabilized around full saturation (~292 µmol l^{-1}) in all cores. Higher values probably result from small gas bubbles stuck to the tip of the optode. Temporarily lower values occurred in Dun3 (~120 µmol l^{-1}, day 69), Cal2 (day 1) and C2 (~90 µmol l^{-1}, day 2).

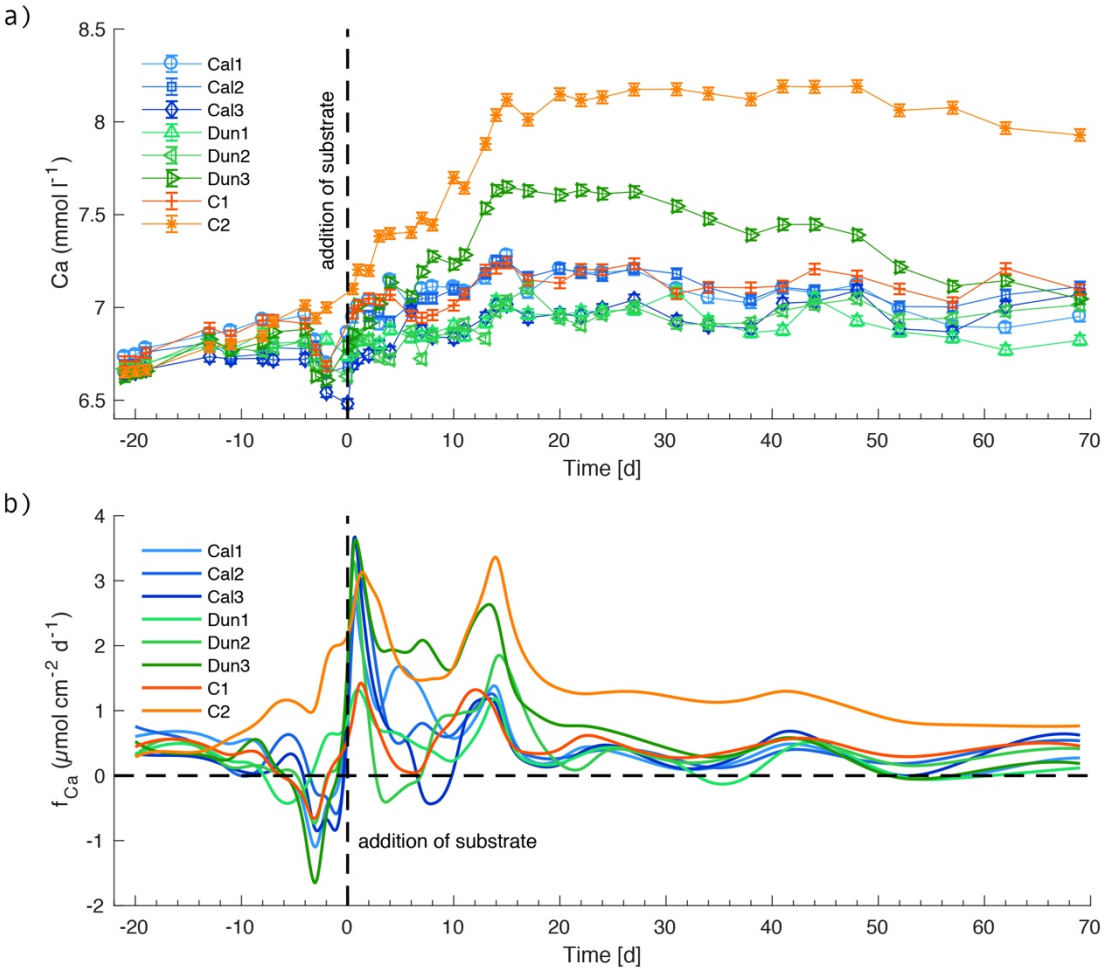

Figure III 6: Ca concentrations in bottom waters (a) and fluxes at the sediment surface (b) in all sediment cores. See Fig. III 4 for further information.

Bottom water pH increased in all cores over the course of the experiment (Figure 3S, supplement). The earliest and strongest increase occurred in C2 (pH 8.2 on day 15) and Dun3, in accordance with the high TA fluxes observed in these cores. Although pH remained at a high level in C2 (~8.15), it decreased in Dun3 after day 15 to values around 7.7. In the other cores, pH values fluctuated around 7.2 – 7.4 until the addition of substrates and the beginning of the bubbling of bottom waters. Subsequently, a strong increase to values around 7.9 was observed until day 15 that was most pronounced in the calcite treated cores and C1. The weakest increase was observed in Dun2 where pH reached values of ~7.75. After day 25, all cores (except C2 and Dun3) followed a rather similar trend of a slow pH increase. Final values ranged from 7.9 (Dun1) to 8.2 (C1).

III.3.5. Calculated properties of sediment cores over discrete time intervals

The assessment of the time intervals in each core reveals common trends in all cores except Dun3. Highest calcite dissolution potentials ($Diss_{pot}$, defined in section 4.4) were observed towards the end of the experiment. The overall range of these values was between 0.0017 cm (Cal2, t3) and 3.8898 cm (C2, t8). pH values decreased in all cores over the course of the experiment, yet again with the exception of Dun3. Another common feature is the shallowing of the H_2S front between 53.5 mm (Cal1, t1) and 11.0 mm (Dun3, t7). This decrease is not clear in all cores, however. The H_2S fluxes varied over the course of the experiment, with a slight tendency towards lower values at the end of the experiment. TA and Ca fluxes varied with highest values around t2 in most cores. Si fluxes did not show any obvious time dependency.

III.3.6. Bacterial community compositions and bacterial shifts in treatments

Based on RNA-profiling of 16S rRNA genes, the active parts of the microbial communities of the different incubations were dominated by (i) phylogenetically distinct chemolithoautotrophic, sulfide oxidizing Gammaproteobacteria, primarily related to *Beggiatoaceae (*mostly *Candidatus* Parabeggiatoa and *Candidatus* Isobeggiatoa*)*, *Thiotrichaceae* (uncultured)*, Ectothiorhodospiraceae* (mostly *Thiogranum*) and *Chromatiaceae*, (ii) sulfate-reducing Desulfobacterota of the *Desulfosarcinaceae* and *Desulfobulbaceae*, (iii) members of the Planctomycetes, mostly heterotrophic *Pirellulaceae* (*Rhodopirellula, Blastopirellula*) and the Pla4 lineage as well as Cyanobacteria affiliated with *Nostocaceae* (*Aphanizomenon*) and *Cyanobiaceae* (Figure III 7). *Sulfurimonas* sp. (Campylobacterota), hallmarked by versatile metabolisms (hydrogen, sulfur and nitrogen cycling) (Han and Perner, 2015), and the uncultured Sva0081 (*Desulfobacteraceae*), which has been suggested as important H_2-scavenger in marine sediments (Dyksma et al., 2018), were abundant throughout the treatments (Figure III 7). Cable bacteria associated with *Candidatus* Electrothrix were found in all incubations, albeit in low numbers (Figure III 7). Maximum values at the beginning of the incubations were found in Cal1 (1.8%), Cal2 (3.6%), Dun2 (2.3%) and Dun3 (1.4%), and after 72 days of incubation in C2 (1.8%), Cal3 (2.2%), Dun1 (3.0%), Dun2 (1.8%) and Dun3 (1.6%) (Figure III 7). Abundances of *Candidatus* Electrothrix in other cores were below 1%.

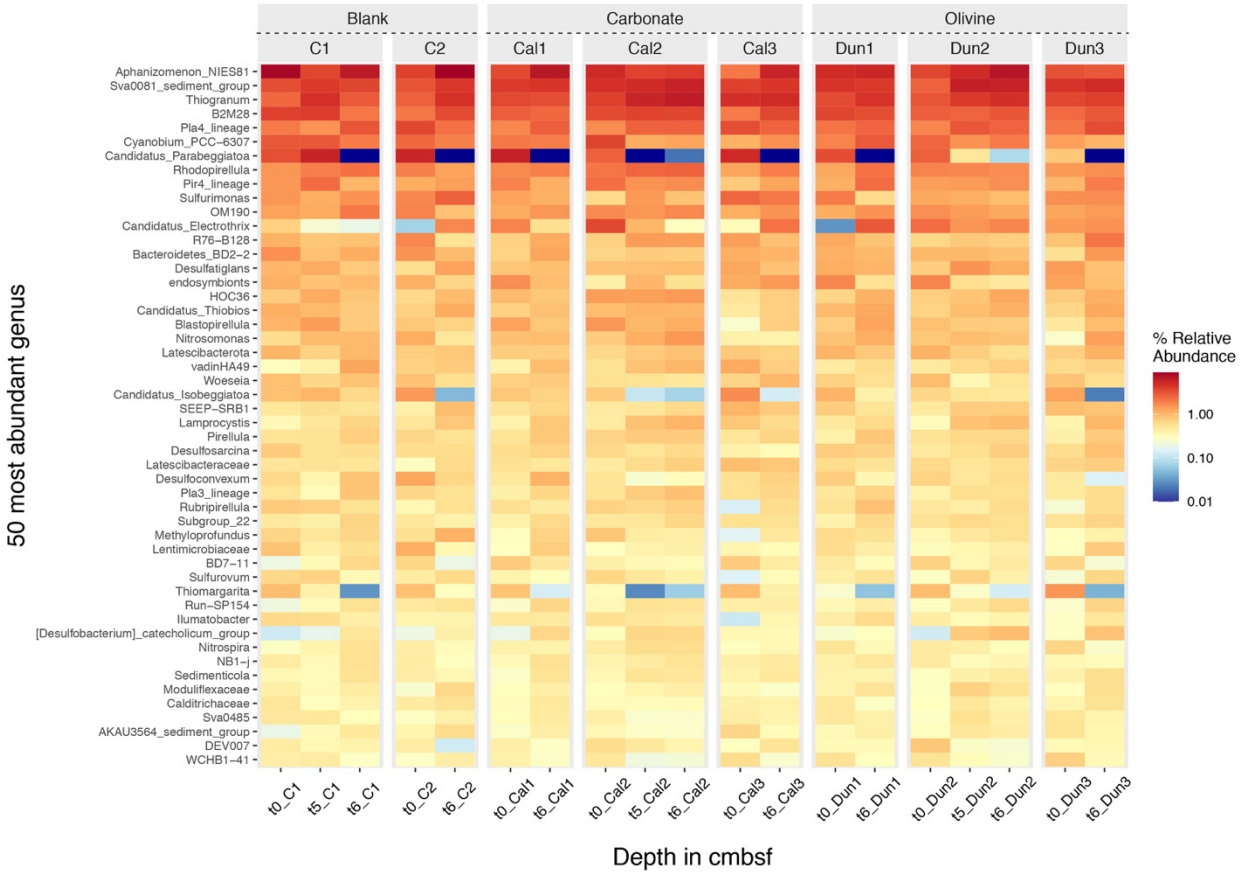

Figure III 7: Heatmap of species abundances for the 50 most abundant genera. The name of the genus is shown on the left, the subsample time-point is shown at the bottom and the facet above indicates the treatment including controls (C1 and C2), carbonate (Cal1, Cal2, and Cal3) and olivine addition (Dun1, Dun2, and Dun3). The intensity of the color in the heatmap represents the abundance of each genus ranging from dark red to dark blue for high and low abundances, respectively.

III.4. Discussion

III.4.1. Robustness of experimental set-up and data

When interpreting results from laboratory experiments, it is instructive to scrutinize the set-up of the experiment for deviations from the natural system. Key considerations of potential importance for interpreting the results of this study include the following:

- The cores were recovered in January 2022 with bottom water temperatures of 6.9 °C. For technical reasons, the laboratory temperature was 12.5 °C. This temperature change accelerates chemical and biological processes and might lead to an overestimation of weathering rates and a rapid change in the biochemistry.
- During core recovery, the sediments are likely to be slightly disturbed, which is obviously highly important for assessing benthic weathering. An initially uneven sediment surface may later settle in the core liner due to gravity and bioturbation. This can lead to a spatial shift in the oxidation horizons and alter the oxygen exposer or availability in surface sediments. Acidification by oxidation and altered dissolution of minerals as well as a change in particulate organic matter (POM) degradation and microbial activity might be a consequence.
- After recovery, the cores were sealed with a rubber plug at the bottom. This cuts off geochemical gradients and fluxes from deeper sediment which will impact the chemical inventory of the sediment core over time and change availabilities of substrates educts for energy-yielding redox reactions and thus the microbial community.
- A low water through flow rate was applied in order to detect temporal changes in bottom water TA and other solutes that have a large seawater background. Accumulation or depletion of solutes in the bottom water will lead to artificial alteration of diffusive fluxes across the sediment-water interface and thus an underestimation of mineral dissolution rates.
- As a response to the large decrease in oxygen levels shortly after the beginning of the experiment, the bottom water was carefully bubbled with air. This reduced the calculated initial pCO_2 from around 2000 µatm at the beginning of the experiment to ~700 µatm after bubbling. Although 700 µatm is realistic for the natural system at certain times of year (Melzner et al., 2013), this led, combined with the accumulation of TA, to stronger oversaturation of bottom waters with respect to calcite than expected in the natural setting (Figure 5S, supplement). In a natural system mineral dissolution might thus be higher.
- The last geochemical data point was obtained on day 69 after addition of substrates, whereas the final sampling of the cores took place on days 90 to 92. During this time, the fluxes and temperature varied largely due to technical problems. Thus, the final pore water data in the very upper centimeters might have been slightly altered over this period. The effect of this alteration is difficult to assess, but most likely relatively small.
- The pore water chemistry (except from micro profiles) for each core could only be examined at the end of the experiment. Thus, the comparison with initial conditions obtained from one reference core needs to be treated with caution.

- Maintaining near to in-situ bottom water conditions in the laboratory over the course of the experiment proved to be extremely challenging. Biogeochemical and physical alteration and artifacts could thus not be avoided.

A careful discussion of pore water alteration is essential when interpreting the results of laboratory experiments. In this study, several key considerations highlight the importance of assessing the potential deviations from the natural system. Despite these complexities, it is important to acknowledge that these challenges are inherent to studies involving such kind of laboratory experiments, and the data obtained from such experiments thus remain valuable and informative for understanding benthic weathering processes under experimental conditions.

III.4.2. Pore water nutrient shifts due to incubation and the impact on TA

The most striking change in pore water solutes was the loss of H_2S and a concomitant increase of SO_4^{2-} concentrations between the initially sampled core and the final sampling (Figures III 1a,b). H_2S production is mainly driven by the anaerobic oxidation of methane (AOM) and particulate organic carbon oxidation via SO_4^{2-} reduction (POCSR) (Barnes and Goldberg, 1976; Froelich et al., 1979; Mark Jensen et al., 2003; Torres et al., 2020):

AOM:

$$CH_4 + SO_4^{2-} + H^+ \rightarrow H_2S + HCO_3^- \quad \text{(III6)}$$

POCSR:

$$(CH_2O)_{106}(NH_3)_{16}(H_3PO_4) + 53SO_4^{2-} + 14H^+ \rightarrow 106HCO_3^- + 16NH_4^+ + 53H_2S + HPO_4^{2-} \quad \text{(III7)}$$

Thus, both processes convert SO_4^{2-} to H_2S with the formation of 2 moles (AOM) and 2.28 moles (POCSR) of TA per mole of SO_4^{2-}.

Since the concentration gradients of SO_4^{2-} and H_2S at the bottom of the initial core were close to zero (Figures III 1a, b), a reduced H_2S flux from deeper sediments as a consequence of plugging the bottom of the cores can be ruled out as an explanation for the lower final H_2S concentrations compared to the initially sampled core. Towards the end of the experiment, the constant SO_4^{2-} concentrations down to ~3 cm below the sediment surface point towards reduced POCSR, which is also observed in the lower NH_4^+ concentrations (Figure III 1d). This decrease is likely a consequence of a lack of supply of fresh POM during the incubation. The deeper penetration of SO_4^{2-} and the lower H_2S and TA concentrations below 3-5 cm could point towards lower POCSR, but the NH_4^+ rather indicate little change from the initial POCSR. Thus, it appears that the production of H_2S independently from SO_4^{2-} was limited during the experiment. The most likely explanation is that the plug introduced at the bottom of the cores shut down the upward transport of methane (CH_4) from deeper layers as described for Boknis Eck sediment e.g. by Maltby et al. (2018). This cutoff from CH_4 supply would result in a decline in AOM rates below 20 cm where the AOM zone was likely situated. Considering the stoichiometry of AOM (Equation III7), this change allowed for a decrease in SO_4^{2-} consumption and deeper SO_4^{2-} penetration and a decline in dissolved H_2S and TA production rates and concentrations at depth (Equation III7).

The apparently stronger decrease of H_2S over time compared to the increase in SO_4^{2-} may be a consequence of shifted Fe-H_2S balance and a possibly stronger formation of FeS. Also, the elevated

laboratory temperatures compared to initial in situ conditions can foster the formation of pyrite (Thiel et al., 2019). The decrease in H_2S concentrations and flux to the upper layers of the sediment may have affected the microbial community and thus the experimental results.

In addition to reduced AOM, the lower TA values in deeper sediment can point towards authigenic formation of $CaCO_3$. This is in line with lower Ca^{2+} concentrations in deeper sediments towards the end of the experiment (Figure III 1f). This formation does not appear to be influenced by the treatment of the different cores, but is most likely a consequence of the increase in temperature during the incubation since $CaCO_3$ solubility decreases with increasing temperature (Zeebe and Wolf-Gladrow, 2001).

III.4.3. Changes in pore water pH and possible explanations

Overall, the pH profiles of most sediment cores looked very similar at the start of the experiment and then evolved over time (Figure III 3). Pore water pH is driven by a variety of oxidation and reduction processes which either release or consume protons. These processes are mainly driven by microbes that utilize the respective Gibbs free energy that the different chemical reactions yield (Fenchel and Jørgensen, 1977; Froelich et al., 1979).

Previous work has demonstrated that the pH profiles in the organic rich sediments of Boknis Eck are dominated by Fe^{3+} reduction coupled to H_2S oxidation and subsequent Fe^{2+} oxidation via manganese oxide (MnO_2) (Preisler et al., 2007). A suboxic zone between the H_2S horizon and the maximum oxygen penetration depth (Table III 2) is commonly observed in sediments inhabited by the filamentous H_2S - oxidizing bacteria of the family *Beggiatoacea* that use nitrate to oxidize H_2S via Dissimilatory Nitrate Reduction to Ammonium (DNRA) (Preisler et al., 2007; Schulz and Jørgensen, 2001):

$$H_2S + NO_3^- + H_2O \rightarrow SO_4^{2-} + NH_4^+ \quad \text{(III8)}$$

These bacteria can store nitrate within their intracellular vacuoles and transport it down into the sediment, leading to the formation of a suboxic zone (Jørgensen and Nelson, 2004). H_2S oxidation by *Beggiatoa* spp. is typically characterized by low pH values in the oxic zone and a clear peak around the H_2S horizon (Jørgensen and Revsbech, 1983; Sayama et al., 2005). In most cores (except Dun3 and C1), this situation is reflected in the initial pH conditions at the beginning of the experiment (Figure III 3) and the presence of *Beggiatoa* spp. is supported by bacterial 16S rRNA amplicon sequencing data (Figure III 7 and Discussion S3.1, supplement).

Over time, though, in all cores except Dun3 and C2, the pH profile shifted towards a shape that was observed initially in Dun3 and C2, indicating a change in the predominant H_2S oxidation pathway. Instead of decreasing, pH values increased in the upper millimeter of the sediment, peaking at around the maximum oxygen penetration depth (Figure III 3, Table III 2). These maxima were situated above a very strong decrease in pH towards the lowest measured values of ~5.7 in core C2. The pH minima were observed slightly above the H_2S horizon. The latter type of profile shape has previously been associated with the activity of cable bacteria (Malkin et al., 2014; Meysman et al., 2015; Nielsen et al., 2010). Like *Beggiatoa* spp., these bacteria oxidize H_2S to SO_4^{2-}, but in two spatially separated reactions, termed long-distance electron transfer (Meysman et al., 2015; Nielsen et al., 2010; Risgaard-Petersen et al., 2012):

Step one: $$H_2S + 4H_2O \rightarrow SO_4^{2-} + 8e^- + 10H^+ \quad \text{(III9)}$$

Step two: $$2O_2 + 8e^- + 8H^+ \rightarrow 4H_2O \quad \text{(III10)}$$

Step one takes place around the H_2S horizon. The electrons released are then transported upwards within the bacterial filaments to the oxic layer where step two takes place. Thus, per mole of H_2S oxidized, 10 moles of protons are released in deeper sediments and 8 moles of protons are consumed in the oxic surface layer. The combination of these two processes would explain the pH peak at the surface and low pH values around the H_2S horizon (Figure III 3, Table III 2) (Malkin et al., 2014; Meysman et al., 2015, 2019). Thus, the pH profiles in cores Dun3 and C2 resemble profiles that would be generated by cable bacteria activity, but over time this activity appeared to cease, which is shown by the less pronounced surface peak and increasing pH values in pore waters. This hypothesis stands in contrast to the RNA-profiling data where, according to 16S rRNA gene proportions, cable bacteria, namely *Candidatus* Electrothrix increased in C2 and remained unchanged in Dun3 over time (Figure III 7). Although the pH profiles of most incubations support increasing activity of cable bacteria over time of the experiments, we could not verify this by identifying increasing proportions of 16S rRNA genes from known cable bacteria. A detailed discussion on the microbial development is provided in the supplement (S3.1). With regards to the aims of this study, it is important to highlight that it cannot be resolved conclusively whether the changes in pore water pH are a naturally occurring feature or were induced by the laboratory incubation conditions. This will be considered for the evaluation of enhanced weathering in the further discussion.

III.4.4. Evaluation of enhanced and natural calcite weathering

The easiest approach to evaluate calcite dissolution is the assessment of bottom water concentrations of the weathering products (TA and Ca) and the respective fluxes via the sediment surface. Figures III 4a and b indicate a slightly increased TA accumulation and elevated fluxes in cores Cal1 – Cal3 directly after the addition of calcite. These fluxes combined with elevated Ca concentrations and fluxes (Figures III 6a,b) point towards dissolution in bottom waters during addition. Still, with regards to the overall experiment, there is no clear trend in Ca fluxes, or in TA fluxes or corresponding bottom water concentrations that could be attributed to a certain treatment. The reason for this observation is obviously the large inhomogeneity of the different cores with regards to pH values which are a major driver for calcite dissolution (Walter and Morse, 1985). In order to reliably quantify weathering processes in the different cores it is necessary to evaluate them under the geochemical conditions that foster or inhibit calcite dissolution during different time intervals (Table III 2).

The rate of calcite dissolution is driven by saturation state with respect to calcite (Ω_{cal}; Walter and Morse, 1985 and references therein). In this study, CO_3^{2-} concentrations were calculated using measured pH and TA pore water values, leading to estimations of Ω_{cal}:

$$\Omega_{cal} = \frac{[Ca] \times [CO_3^{2-}]}{Ks_{cal}} \quad \text{(III11)}$$

where [Ca] and $[CO_3^{2-}]$ are the concentrations of calcium and carbonate, respectively, and Ks_{cal} is the solubility product of calcite at the respective salinity, temperature and pressure (Zeebe and Wolf-Gladrow, 2001). To provide temporal estimates of Ω_{cal}, the initial and final values of TA and Ca were interpolated linearly for each depth layer We recognize the obvious uncertainty associated with this approach and the following results should be interpreted with this in mind.

The total amount of calcite that can be dissolved is driven by the degree of undersaturation over the whole core. Since calcite only dissolves when ambient pore waters are undersaturated with respect to this mineral ($\Omega_{cal} < 1$), a dissolution potential ($Diss_{pot}$ (cm)) was defined by integrating Ω_{cal} over the region where undersaturation was observed:

$$Diss_{pot} = \int_{z(\Omega<1)}^{z(\Omega>1)} (1 - \Omega_{cal}(z))\, dz \qquad \text{(III12)}$$

where $\Omega_{cal}(z)$ is the saturation state at depth z (cm) in the sediment. $z(\Omega<1)$ and $z(\Omega>1)$ refer to depths where Ω_{cal} values fall below 1 and above 1, respectively. Thus, $Diss_{pot}$ combines the degree of undersaturation and the depth interval where undersaturation occurs (Figure III 8).

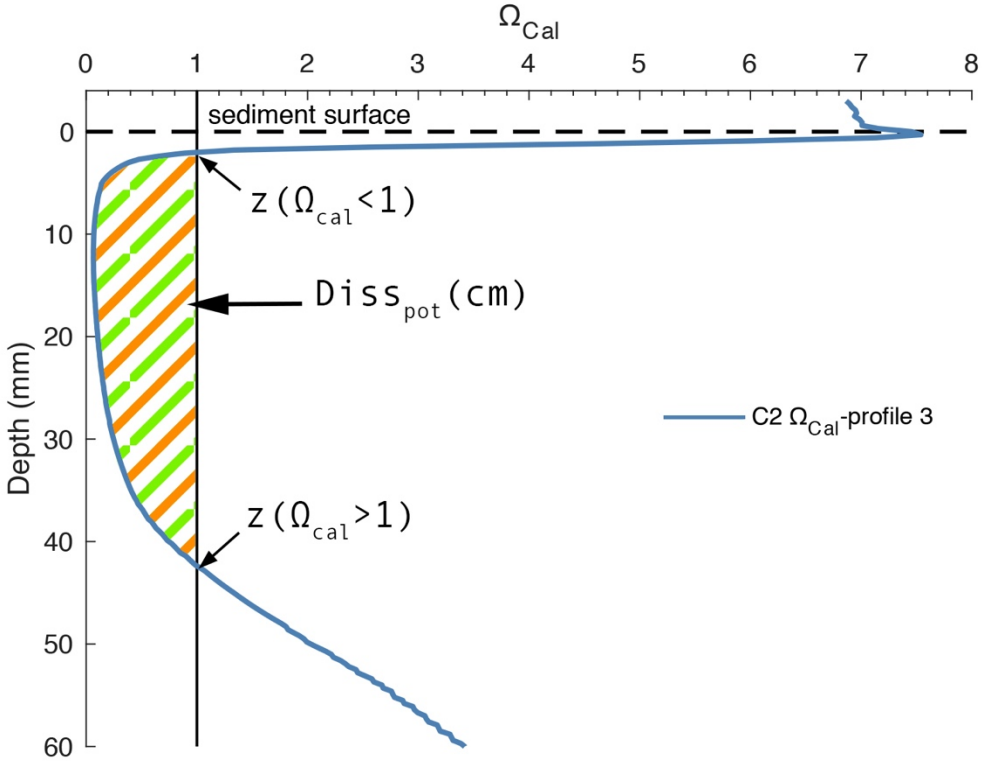

Figure III 8: Illustrative example for calculation of Disspot on one representative profile (Profile 3, C2). Horizontal dashed line indicates sediment surface. Vertical solid line demarks ΩCal<1. Hatched area depicts the sediment depths where calcite can dissolve.

$Diss_{pot}$ values depend on the dynamic interplay between pH and calcite dissolution. When $CaCO_3$ dissolves in pore waters, the saturation state with respect to $CaCO_3$ increases due the accumulation of weathering products. This has the effect of lowering $Diss_{pot}$. At the same time, a higher sedimentary flux of the weathering products to the bottom water should be observed. Consequently, Ca and TA fluxes together with $Diss_{pot}$ values at a given time indicate how much calcite is being dissolved compared to how much calcite could be dissolved. The higher the calcite content of a sediment that bears a source of protons, the higher the ratio of Ca and TA fluxes to $Diss_{pot}$, the more effective is the dissolution process. The maximum dissolvable calcite content would then be indicated by high fluxes combined with $Diss_{pot}$ values close to 0.

Highest $Diss_{pot}$ values are associated with elevated TA and Ca fluxes during the discrete time intervals in cores C2 and Dun3 (Figures III 9a,b). This clearly indicates that the natural inventory of calcium carbonate in the form of either calcite or aragonite (Figure III 2) is being dissolved in corrosive pore waters. To disentangle these natural fluxes from enhanced fluxes induced by the addition of calcite, the pH profiles were compared to profiles obtained at Boknis Eck in situ under natural conditions (Preisler et al., 2007). At the time of sampling, these sediments were dominated by the activity of *Beggiatoa* spp. and were more similar to the initial profiles in e.g. Dun1 and Cal1. Therefore, based on these in situ profiles and Dun1 and Cal1 profiles, a realistic maximum value for $Diss_{pot}$ was defined (dashed line in Figures III 9a,b). This approach was chosen for because it only considers naturally observed and thus unambiguously realistic

weathering regimes. In addition, not all cores showed extreme $Diss_{pot}$ values. By considering time intervals with similar $Diss_{pot}$ values, comparisons between different treatments are more justified.

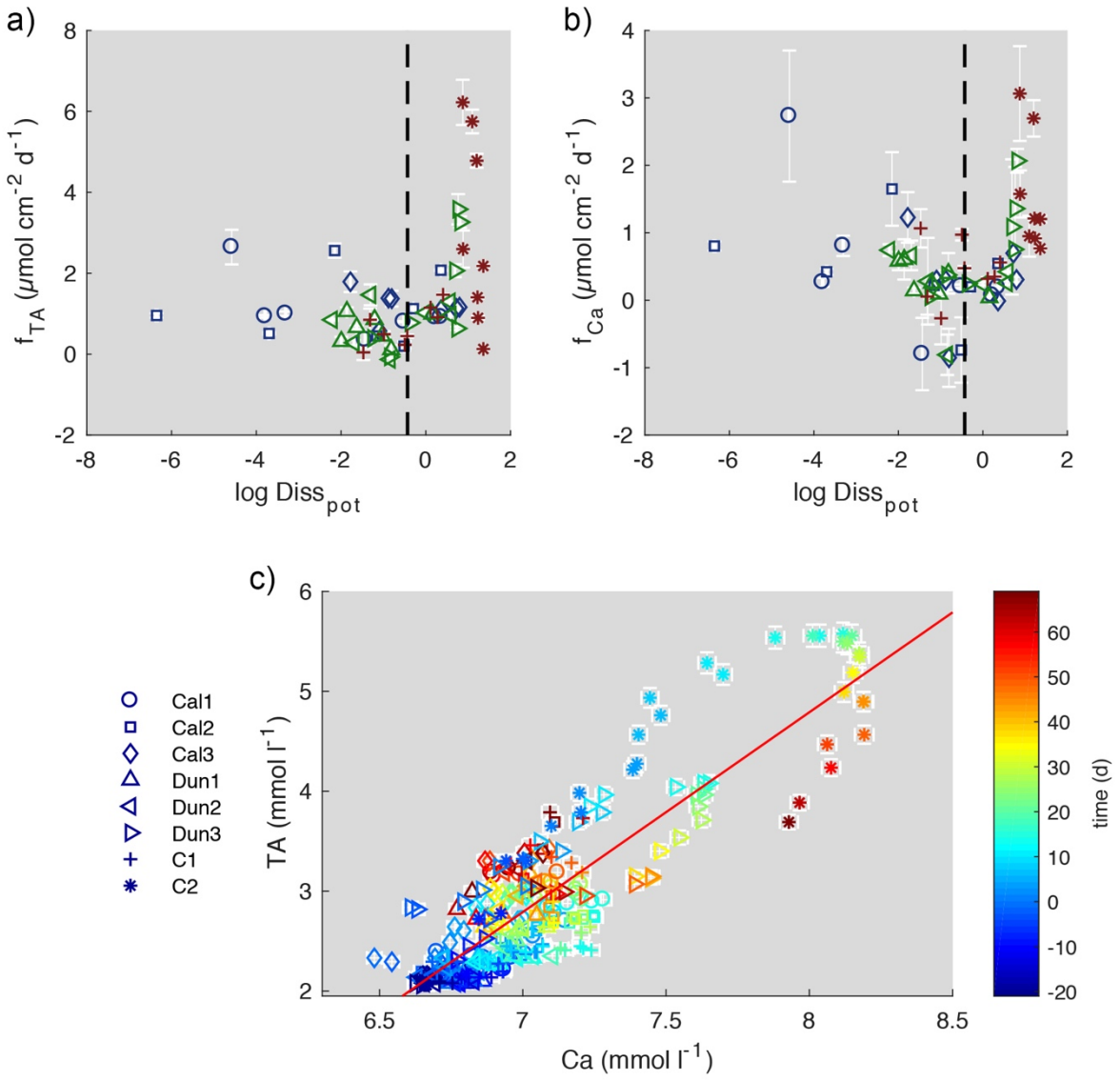

Figure III 9: Comparison of $Diss_{pot}$ to TA fluxes (a) and Ca fluxes (b) during discrete time intervals and Ca concentration to TA values over entire course of the experiment (c). Dashed lines in (a) and (b)indicate highest natural $Diss_{tot}$ values. Red solid line (c) indicates a TA/Ca ratio of 2. Blue markers in (a) and (b) show values from calcite treated cores, green labels show dunite treated cores and red labels show control cores. Color coding in c) indicates the time at which each sample was taken relative to addition of substrates. Error bars report 2SD.

For the evaluation of enhanced carbonate weathering, the fluxes of the different cores during time periods where $Diss_{pot}$ was below this value were then averaged and compared (Table III 3). This procedure excludes values obtained in C2, as in this core pH was very low over the entire course of the experiment. The results of the comparison show that TA fluxes were 0.961±0.096 µmol cm^{-2} d^{-1} higher in calcite treated cores than in the control experiment. The ratio of F_{TA}/F_{Ca} of 1.45 (Table III 3) in the calcite treated cores is lower than the theoretical value of 2 (Equation III2), which points towards a loss of alkalinity which is not associated with Ca. We suggest that TA derived from $CaCO_3$ dissolution was diminished by the oxidation of reduced species in the oxic surface sediment (Dale et al., 2021, 2011; Perner et al., 2022; Rassmann et al., 2020; Wallmann et al., 2008). The $\Delta F_{TA}/\Delta F_{Ca}$ values which represent the ratio of enhanced fluxes compared to

the control experiment, though, are close to 2 (1.99), which would be the ratio expected for calcite dissolution. Hence, the additional fluxes were most likely induced by the addition of calcite to the sediment. Overall, it is important to acknowledge that the accumulation of weathering products in bottom waters and the low pCO_2 have led to higher Ω_{cal} values than expected in the natural system (Melzner et al., 2013). In more corrosive bottom waters the dissolution of calcite might be higher than observed in this study.

Table III 5: TA, Ca and Si fluxes in different cores averaged over different treatments during comparable time intervals. Note that RSD for calcite and dunite treated cores represent relative standard deviation (RSD) between averages of each core. RSD for control experiments derives from only one core (Table 2) and is thus larger. $\Delta F_{TA}/\Delta F_{Ca}$ ratios indicate ratios between difference in flux between treatments and the control experiment.

Treatment	F_{TA} µmol cm^{-2} d^{-1}	RSD %	F_{Ca} µmol cm^{-2} d^{-1}	RSD %	F_{Si} µmol cm^{-2} d^{-1}	RSD %	F_{TA}/F_{Ca}	$\Delta F_{TA}/\Delta F_{Ca}$
Calcite:	1.373	10.31	0.944	34.97	0.247	28.04	1.45	1.99
Dunite:	0.634	39.59	0.373	46.34	0.261	4.09	1.70	-2.55
Control:	0.412	73.48	0.460	125.18	0.329	51.14	0.90	

To assess the suitability of weathering products as a proxy for mineral dissolution, TA and Ca concentrations in bottom waters were directly compared over the entire experiment (Figure III 9c). The data clearly show that the ratio of TA/Ca is not always 2 (indicated by the thin red line, Figure III 9c), as expected from equation 2. Instead, TA appears to increase before Ca concentrations. This is an especially well pronounced feature in C2 and Dun3, in which highest TA concentrations were observed during the early stage of the experiment. In the other cores this enhanced TA/Ca ratio was observed towards the end of the experiment (color coding in Figure III 9c).

When comparing the different pH profiles in C2 and Dun3 (Figure III 3), it is clear that very low values and subsequently high $Diss_{pot}$ values dominated during the early stage of the experiment. During this time, the TA:Ca ratio in bottom waters is clearly higher than 2:1 (blue to green symbols in Figure III 9c). In the other cores, similar conditions appeared later in the experiment (yellow to red symbols in Figure III 9c). Since the low pH values presumably result from cable bacteria, their metabolism (Equations III9, III10) might lead to an altered TA/Ca ratio. The different diffusive coefficients of Ca^{2+} and HCO_3^-, which is the main contributor to TA, might alternatively be responsible for this effect, as $D_{Ca} < D_{HCO3}$ (Boudreau, 1997). This might also explain why the ratio of TA/Ca decreased in C2 and Dun3 towards the end of the experiment. Along with the higher consistency of measured TA values and calculated fluxes, this suggests that a combination of TA and Ca may be the best way to assess weathering efforts, even though TA is the main driver for CO_2 uptake in the surface ocean (Wolf-Gladrow et al., 2007) and thus of more relevance with respect to CDR studies.

III.4.5. Strong background fluxes disguise olivine dissolution

Dunite is an igneous rock with an olivine content of over 90% (Hochstetter, 1859) and displays rapid dissolution rates in seawater (Fuhr et al., 2022; Rigopoulos et al., 2018; Rimstidt et al., 2012; Wolff-Boenisch et al., 2006). Assuming that dunite dissolution represents olivine dissolution, the rate can be described as a function of temperature and pH (Rimstidt et al., 2012):

$$\log(r_{ol}) = 4.07 - 0.256 \times pH - \frac{3465}{T} \quad \text{(III13)}$$

where r_{ol} is the dissolution rate given in mol m^{-2} s^{-1}, T is temperature in K. In the temperature and pH range of this study, a pH increase from 7 to 8 would lead to an identical 55 % decrease in rate as a theoretical temperature change from 12.5 to 6.59 °C. Thus, the pH changes observed in our experiment (Figure III 3) must play an important role for olivine dissolution.

The chemical process of olivine dissolution ought to lead to an accumulation of magnesium (Mg^{2+}), Si and TA (Equation III1). The high Mg background of ~32 mmol l^{-1} in seawater at Boknis Eck prevents detection of the additional Mg due to analytical precision (± 2%). Hence, the candidate proxies for detecting olivine dissolution are Si and TA concentrations. However, Si concentrations and fluxes over entire course of the experiment showed no trends between the differently treated cores (Figure III 5). TA concentrations and fluxes (Figures III 4a,b) slightly increased directly after the addition of dunite in Dun1 and Dun2, pointing towards olivine dissolution (Fuhr et al., 2022). Since Dun3 was dominated by $CaCO_3$ dissolution in the early stage of the experiment, the TA fluxes from olivine dissolution in this core were strongly overprinted.

Pore water pH values were compared to Si fluxes averaged for each time step (Figure III 10). A slightly lower gradient of the linear regression between pH and Si fluxes in cores treated with dunite might be interpreted as increased contribution from olivine dissolution for lower pH values. Still, the correlation for all cores is weak (R^2 values between 0.241 and 0.072). Overall, the increase in Si flux with higher pH values in all cores points towards dissolution of either siliceous detrital material or biogenic debris such as diatomaceous frustules that are highly abundant in Baltic Sea sediments (Gasiūnaitė et al., 2005; Lewin, 1961). These processes result in a high background signal that overprinted Si contribution by olivine weathering at lower pH values.

When comparing the different treatments during comparable time intervals (Table III 3), cores treated with dunite showed slightly enhanced TA fluxes (0.634 µmol $cm^{-1.}$ d^{-1}) compared to the control experiment (0.412 µmol $cm^{-1.}$ d^{-1}). The very large standard deviations of 40 % and 73 %, though, diminish the significance of these data. Overall, the data does not allow for olivine dissolution to be evaluated in the experiment neither qualitatively nor quantitatively using these proxies.

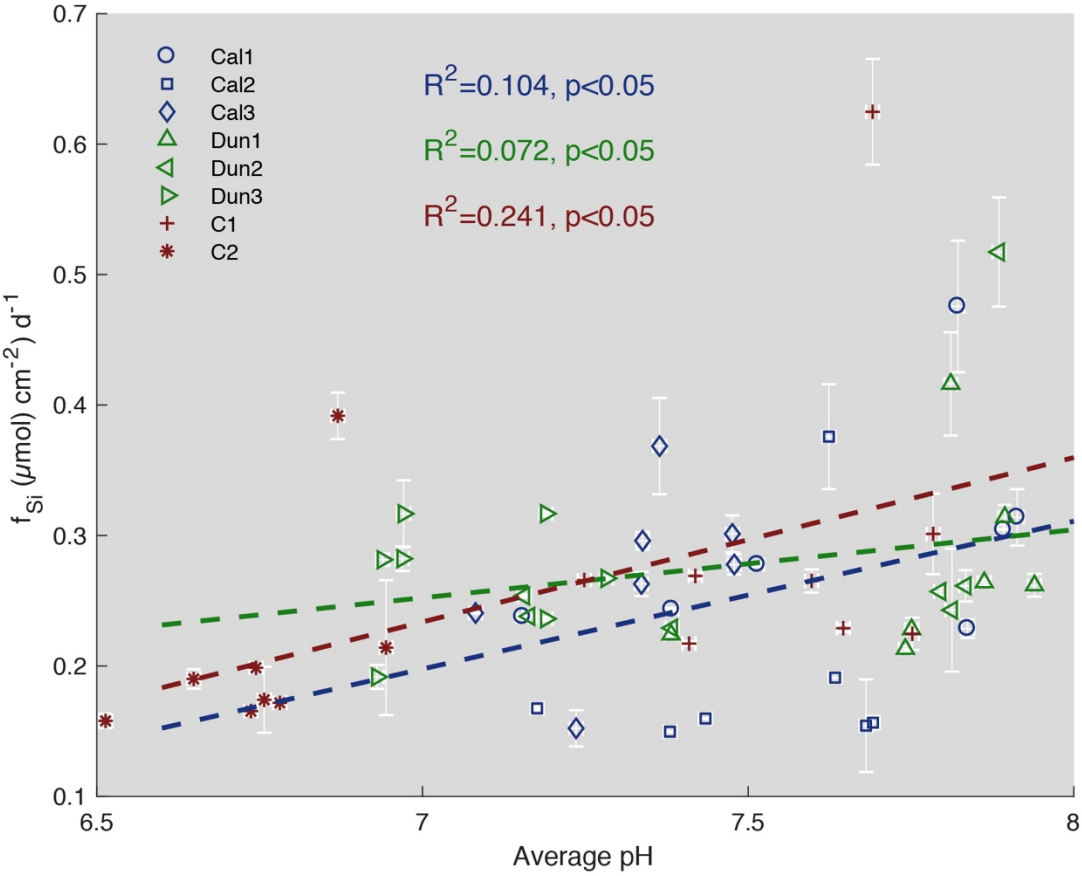

Figure III 10: Cumulated Si fluxes via the sediment surface for each time step defined in Table III 3 versus pH in pore waters. Blue symbols represent calcite treated cores, green symbols show dunite treated cores and red symbols represent controls. Dashed lines show linear correlations for each treatment. R2 values represent the fit of each correlation. Error bars represent SD.

Dissolved nickel, which was proposed as a dissolution proxy by Montserrat et al. (2017), was below detection limit (~0.2 µmol l^{-1}) in all samples. Consequently, although it cannot serve as a dunite dissolution tracer, it can likely be excluded as a possible toxic threat to fauna (Flipkens et al., 2021) in the current benthic environment. Likewise, the formation of secondary mineral formation associated with olivine weathering (Fuhr et al., 2022) cannot be resolved based on the present data set.

III.4.6. Challenges for attribution

Marine alkalinity enhancement via enhanced weathering at the seabed requires monitoring to quantify rates of mineral dissolution and alkalinity production and ultimately the uptake flux of atmospheric CO_2 in the ocean induced by deliberate mineral addition. To this end, a methodology needs to be established and suitable tracers have to be defined that allow for a reliable quantification of mineral dissolution rates.

Dissolved Si would be a suitable tracer to quantify dissolution rates of olivine and other reactive silicate minerals added to the seabed. However, our experimental data clearly show that benthic Si fluxes are dominated by the dissolution of biogenic opal and other sedimentary Si phases such that olivine dissolution rates could not be quantified using this tracer. Since biogenic opal produced by diatoms and other siliceous plankton is deposited and dissolved in almost all coastal and shelf sediments (Tréguer et al., 2021), the

attribution problems that were encountered during this study will very likely also emerge during field experiments and large-scale application of benthic marine alkalinity enhancement. It may be possible to solve this attribution problem using stable Si isotopes ($\delta^{30}Si$) since biogenic opal and detrital silicate minerals have distinct isotopic compositions such that benthic fluxes induced by the dissolution of these separate phases can be differentiated (Geilert et al., 2020). Future work should, hence, test whether $\delta^{30}Si$ may be a suitable tracer of the dissolution of deliberately added silicate minerals.

Dissolved Ca could be used to quantify dissolution rates of carbonates (calcite, aragonite) added to the seabed. Data obtained in this study indicate that this may be possible but that the interpretation of benthic Ca flux data is complicated by the dissolution of calcite delivered by coastal and seabed erosion in the study area (Wallmann et al., 2022). Similar problems may arise in other coastal and shelf settings where carbonate minerals produced by erosion and calcareous plankton are deposited and dissolved at the seabed. Since the stable isotopic composition of Ca and Sr bound in natural and deliberately added carbonate minerals may differ (Teng et al., 2021), employing these isotope tracers (e.g. $\delta^{44/40}Ca$, $\delta^{88/86}Sr$) might improve attribution.

According to our experimental results, TA may be the most suitable tracer to quantify the dissolution of alkaline minerals (olivine, calcite) added to the seabed. However, large TA fluxes were not only induced by the dissolution of added minerals but also by the dissolution of naturally-occurring carbonate minerals. Moreover, observed TA was likely consumed via H_2S and iron oxidation. The resulting benthic TA fluxes were, hence, strongly modulated by microbially catalyzed redox reactions and very sensitive to shifts in the microbial community (primarily *Beggiatoa* spp. vs. other microbes including cable bacteria). Since these TA-producing and consuming microbial metabolisms occur in all coastal and shelf sediments (Boudreau, 1997), attribution problems will also arise in field experiments and applications. Attribution of TA fluxes to the dissolution of added alkaline mineral will, therefore, only be possible after accounting for highly dynamic natural TA background fluxes that can change on seasonal and shorter time scales in most benthic environments (Dale et al., 2013). Overall, the difficulties encountered with attribution will subsequently complicate monitoring, reporting and verification (MRV) in a possible field application scenario.

III.5. Summary, conclusion and outlook

This study presents results from an incubation of organic-rich sediment cores recovered from Boknis Eck in Eckernförde Bay where dunite and calcite were added to assess the potential for benthic alkalinity enhancement. The incubation of the cores and lack of methane flux from deeper sediments led to a reduction of AOM, which altered the H_2S inventory in pore waters. Additionally, the precipitation of authigenic carbonates was indicated by reduced TA and Ca concentrations in pore waters towards the end of the experiment. These alterations and the decline in upward H_2S fluxes may have led to a shift of pH profiles formed by the activity of *Beggiatoa* spp. to profiles associated with the activity of cable bacteria. The altered pH values in pore waters changed the saturation state with respect to calcite (Ω_{cal}). In order to evaluate the enhanced weathering in dunite (olivine) and calcite treated cores, the experimental results were split into several time steps. The comparison of time intervals with similar chemical conditions suggests that TA fluxes were significantly increased by the addition of calcite and that TA currently appears to be the best proxy for evaluating enhanced weathering of calcite, and the most relevant variable for understanding CO_2 uptake from the atmosphere. The increase in TA fluxes following the addition of dunite was too small to be resolved with available proxies due to high background fluxes. The possible formation of secondary minerals induced by olivine weathering could not be resolved.

The experiments were conducted in the laboratory under conditions that were as similar as possible to those in the field during the time of sampling (winter season). However, temperature, oxygen levels and the pCO_2 of bottom water can vary largely over the annual cycle in Boknis Eck (Melzner et al., 2013). In order to understand the weathering behavior of both calcite and dunite (olivine) under natural conditions, it would thus be necessary to conduct further experiments, such as incubations under anoxic to hypoxic conditions and long-term experiments that reflect the weathering behavior under more natural conditions. Experiments in benthocosms might have the potential to reflect natural conditions at least with regards to temperature, bottom water pH, sediment heterogeneity and POC availability. Still, the fluxes from deeper sediments would still be difficult to capture realistically. Field experiments and stable isotope tracers may help to better understand the effect and the impact of enhanced benthic weathering as a CDR measure for climate change mitigation.

Data availability statement (III)

The original contributions presented in the study are included in the article and supplementary files. Further inquiries can be directed to the corresponding author. The data presented in the study are deposited at the Sequence Read Archive (SRA) of the National Center for Biotechnology Information (NCBI) under the BioProject PRJNA988924 repository, accession number SAMN36035013 to SAMN36035020 and SAMN37271069 to SAMN37271133. (Table 3S, supplement).

Author Contributions (III)

SG designed the study, MF and ID conducted the experiment, HK helped with pH measurements, SS supervised micro profiling and data logging, AD advised and supported lab procedures, KW helped with discussions, MS helped with the experimental set-up and sensoring, MP supervised molecular biology work and interpreted 16S sequencing data, SB performed bioinformatics analyses and helped with interpreting 16S sequencing data, MF wrote the manuscript. All authors contributed to editing the manuscript.

Funding (III)

This study was funded by the Bundesministerium für Bildung und Forschung (BMBF) (Project RETAKE, awarded to SG) in the framework of the Deutsche Allianz für Meeresforschung (DAM) mission "CDRmare".

Acknowledgements (III)

We would like to thank Anke Bleyer (GEOMAR), Bettina Domeyer (GEOMAR), Gabriele Schüßler (GEOMAR) Regina Surberg (GEOMAR) and Ronny Baaske (GEOMAR) for their help with technical and analytical procedures in the laboratory. Furthermore, we thank Antje Beck for her tremendous support during the experimental set-up and Diana Vasquez Gardenas for fruitful discussions. Additionally, we thank the crew of FK Littorina for their support during recovery of sediment cores and the technical support from the Technik- und Logistikzentrum (TLZ) at GEOMAR.

References (III)

Barnes, R.O., Goldberg, E.D., 1976. Methane production and consumption in anoxic marine sediments. Geology 4, 297–300. https://doi.org/10.1130/0091-7613(1976)4<297:MPACIA>2.0.CO;2

Béarat, H., J. McKelvy, M., V. G. Chizmeshya, A., Gormley, D., Nunez, R., W. Carpenter, R., Squires, K., H. Wolf, G., 2006. Carbon Sequestration via Aqueous Olivine Mineral Carbonation: Role of Passivating Layer Formation. Environ. Sci. & Technol. 40, 4802–4808. https://doi.org/10.1021/es0523340

Beuttler, C., Charles, L., Wurzbacher, J., 2019. The Role of Direct Air Capture in Mitigation of Anthropogenic Greenhouse Gas Emissions. Front. Clim. https://doi.org/10.3389/fclim.2019.00010

Bohlen, L., Dale, A.W., Sommer, S., Mosch, T., Hensen, C., Noffke, A., Scholz, F., Wallmann, K., 2011. Benthic nitrogen cycling traversing the Peruvian oxygen minimum zone. Geochim. Cosmochim. Acta 75, 6094–6111. https://doi.org/https://doi.org/10.1016/j.gca.2011.08.010

Böhnke, S., Sass, K., Gonnella, G., Diehl, A., Kleint, C., Bach, W., Zitoun, R., Koschinsky, A., Indenbirken, D., Sander, S.G., Kurtz, S., Perner, M., 2019. Parameters Governing the Community Structure and Element Turnover in Kermadec Volcanic Ash and Hydrothermal Fluids as Monitored by Inorganic Electron Donor Consumption, Autotrophic CO2 Fixation and 16S Tags of the Transcriptome in Incubation Experiments. Front. Microbiol. https://doi.org/10.3389/fmicb.2019.02296

Bokulich, N.A., Kaehler, B.D., Rideout, J.R., Dillon, M., Bolyen, E., Knight, R., Huttley, G.A., Gregory Caporaso, J., 2018. Optimizing taxonomic classification of marker-gene amplicon sequences with QIIME 2's q2-feature-classifier plugin. Microbiome 6, 90. https://doi.org/10.1186/s40168-018-0470-z

Bolyen, E., Rideout, J.R., Dillon, M.R., Bokulich, N.A., Abnet, C.C., Al-Ghalith, G.A., Alexander, H., Alm, E.J., Arumugam, M., Asnicar, F., Bai, Y., Bisanz, J.E., Bittinger, K., Brejnrod, A., Brislawn, C.J., Brown, C.T., Callahan, B.J., Caraballo-Rodríguez, A.M., Chase, J., Cope, E.K., Da Silva, R., Diener, C., Dorrestein, P.C., Douglas, G.M., Durall, D.M., Duvallet, C., Edwardson, C.F., Ernst, M., Estaki, M., Fouquier, J., Gauglitz, J.M., Gibbons, S.M., Gibson, D.L., Gonzalez, A., Gorlick, K., Guo, J., Hillmann, B., Holmes, S., Holste, H., Huttenhower, C., Huttley, G.A., Janssen, S., Jarmusch, A.K., Jiang, L., Kaehler, B.D., Kang, K. Bin, Keefe, C.R., Keim, P., Kelley, S.T., Knights, D., Koester, I., Kosciolek, T., Kreps, J., Langille, M.G.I., Lee, J., Ley, R., Liu, Y.-X., Loftfield, E., Lozupone, C., Maher, M., Marotz, C., Martin, B.D., McDonald, D., McIver, L.J., Melnik, A. V, Metcalf, J.L., Morgan, S.C., Morton, J.T., Naimey, A.T., Navas-Molina, J.A., Nothias, L.F., Orchanian, S.B., Pearson, T., Peoples, S.L., Petras, D., Preuss, M.L., Pruesse, E., Rasmussen, L.B., Rivers, A., Robeson, M.S., Rosenthal, P., Segata, N., Shaffer, M., Shiffer, A., Sinha, R., Song, S.J., Spear, J.R., Swafford, A.D., Thompson, L.R., Torres, P.J., Trinh, P., Tripathi, A., Turnbaugh, P.J., Ul-Hasan, S., van der Hooft, J.J.J., Vargas, F., Vázquez-Baeza, Y., Vogtmann, E., von Hippel, M., Walters, W., Wan, Y., Wang, M., Warren, J., Weber, K.C., Williamson, C.H.D., Willis, A.D., Xu, Z.Z., Zaneveld, J.R., Zhang, Y., Zhu, Q., Knight, R., Caporaso, J.G., 2019. Reproducible, interactive, scalable and extensible microbiome data science using QIIME 2. Nat. Biotechnol. 37, 852–857. https://doi.org/10.1038/s41587-019-0209-9

Borawska, Z., Szymczycha, B., Silberberger, M.J., Koziorowska-Makuch, K., Szczepanek, M., Kędra, M., 2022. Benthic fluxes of dissolved silica are an important component of the marine Si cycle in the coastal zone. Estuar. Coast. Shelf Sci. 273, 107880. https://doi.org/https://doi.org/10.1016/j.ecss.2022.107880

Boudreau, B.P., 1997. Diagenetic models and their implementation.Springer, Berlin, Germany.

Brunauer, S., Emmett, P.H., Teller, E., 1938. Adsorption of Gases in Multimolecular Layers. J. Am. Chem. Soc. 60, 309–319. https://doi.org/10.1021/ja01269a023

Burton, E.A., Walter, L.M., 1987. Relative precipitation rates of aragonite and Mg calcite from seawater: Temperature or carbonate ion control? Geology 15, 111–114. https://doi.org/10.1130/0091-7613(1987)15<111:RPROAA>2.0.CO;2

Callahan, B.J., McMurdie, P.J., Rosen, M.J., Han, A.W., Johnson, A.J.A., Holmes, S.P., 2016. DADA2: High-resolution sample inference from Illumina amplicon data. Nat. Methods 13, 581–583. https://doi.org/10.1038/nmeth.3869

Campbell, J.S., Foteinis, S., Furey, V., Hawrot, O., Pike, D., Aeschlimann, S., Maesano, C.N., Reginato, P.L., Goodwin, D.R., Looger, L.L., Boyden, E.S., Renforth, P., 2022. Geochemical Negative Emissions Technologies: Part I. Review. Front. Clim. 4:879133. https://doi.org/10.3389/fclim.2022.879133

Caserini, S., Cappello, G., Righi, D., Raos, G., Campo, F., De Marco, S., Renforth, P., Varliero, S., Grosso, M., 2021. Buffered accelerated weathering of limestone for storing CO2: Chemical background. Int. J. Greenh. Gas Control 112, 103517. https://doi.org/10.1016/j.ijggc.2021.103517

Dale, A.W., Bertics, V.J., Treude, T., Sommer, S., Wallmann, K., 2013. Modeling benthic–pelagic nutrient exchange processes and porewater distributions in a seasonally hypoxic sediment: evidence for massive phosphate release by *Beggiatoa*? Biogeosciences 10, 629–651. https://doi.org/10.5194/bg-10-629-2013

Dale, A.W., Paul, K.M., Clemens, D., Scholz, F., Schroller-Lomnitz, U., Wallmann, K., Geilert, S., Hensen, C., Plass, A., Liebetrau, V., Grasse, P., Sommer, S., 2021. Recycling and Burial of Biogenic Silica in an Open Margin Oxygen Minimum Zone. Global Biogeochem. Cycles 35, e2020GB006583. https://doi.org/10.1029/2020GB006583

Dale, A.W., Sommer, S., Bohlen, L., Treude, T., Bertics, V.J., Bange, H.W., Pfannkuche, O., Schorp, T., Mattsdotter, M., Wallmann, K., 2011. Rates and regulation of nitrogen cycling in seasonally hypoxic sediments during winter (Boknis Eck, SW Baltic Sea): Sensitivity to environmental variables. Estuar. Coast. Shelf Sci. 95, 14–28. https://doi.org/https://doi.org/10.1016/j.ecss.2011.05.016

Dale, A.W., Sommer, S., Lomnitz, U., Bourbonnais, A., Wallmann, K., 2016. Biological nitrate transport in sediments on the Peruvian margin mitigates benthic sulfide emissions and drives pelagic N loss during stagnation events. Deep. Res. Part I Oceanogr. Res. Pap. 112, 123–136. https://doi.org/10.1016/j.dsr.2016.02.013

Dale, A.W., Sommer, S., Ryabenko, E., Noffke, A., Bohlen, L., Wallmann, K., Stolpovsky, K., Greinert, J., Pfannkuche, O., 2014. Benthic nitrogen fluxes and fractionation of nitrate in the Mauritanian oxygen minimum zone (Eastern Tropical North Atlantic). Geochim. Cosmochim. Acta 134, 234–256. https://doi.org/10.1016/j.gca.2014.02.026

Dyksma, S., Pjevac, P., Ovanesov, K., Mussmann, M., 2018. Evidence for H2 consumption by uncultured Desulfobacterales in coastal sediments. Environ. Microbiol. 20, 450–461. https://doi.org/10.1111/1462-2920.13880

E. King, H., Plümper, O., Putnis, A., 2010. Effect of Secondary Phase Formation on the Carbonation of Olivine. Environ. Sci. & Technol. 44, 6503–6509. https://doi.org/10.1021/es9038193

Fenchel, T.M., Jørgensen, B.B., 1977. Detritus Food Chains of Aquatic Ecosystems: The Role of Bacteria BT - Advances in Microbial Ecology, in: Alexander, M. (Ed.), . Springer US, Boston, MA, pp. 1–58. https://doi.org/10.1007/978-1-4615-8219-9_1

Feng, E.Y., Koeve, W., Keller, D.P., Oschlies, A., 2017. Model-Based Assessment of the CO2 Sequestration Potential of Coastal Ocean Alkalinization. Earth's Futur. 5, 1252–1266. https://doi.org/10.1002/2017EF000659

Flipkens, G., Blust, R., Town, R.M., 2021. Deriving Nickel (Ni(II)) and Chromium (Cr(III)) Based Environmentally Safe Olivine Guidelines for Coastal Enhanced Silicate Weathering. Environ. Sci. Technol. 55, 12362–12371. https://doi.org/10.1021/ACS.EST.1C02974/SUPPL_FILE/ES1C02974_SI_001.PDF

Flipkens, G., Fuhr, M., Fiers, G., Meysman, F.J.R., Town, R.M., Blust, R., 2023. Enhanced olivine dissolution in seawater through continuous grain collisions. Geochim. Cosmochim. Acta 359, 84–99. https://doi.org/https://doi.org/10.1016/j.gca.2023.09.002

Froelich, P.N., Klinkhammer, G.P., Bender, M.L., Luedtke, N.A., Heath, G.R., Cullen, D., Dauphin, P., Hammond, D., Hartman, B., Maynard, V., 1979. Early oxidation of organic matter in pelagic sediments of the eastern equatorial Atlantic: suboxic diagenesis. Geochim. Cosmochim. Acta 43, 1075–1090. https://doi.org/https://doi.org/10.1016/0016-7037(79)90095-4

Fuhr, M., Geilert, S., Schmidt, M., Liebetrau, V., Vogt, C., Ledwig, B., Wallmann, K., 2022. Kinetics of Olivine Weathering in Seawater: An Experimental Study. Front. Clim. 4:831587. https://doi.org/10.3389/fclim.2022.831587

Fuss, S., Lamb, W.F., Callaghan, M.W., Hilaire, J., Creutzig, F., Amann, T., Beringer, T., De Oliveira Garcia, W., Hartmann, J., Khanna, T., Luderer, G., Nemet, G.F., Rogelj, J., Smith, P., Vicente, J.V., Wilcox, J., Del Mar Zamora Dominguez, M., Minx, J.C., 2018. Negative emissions - Part 2: Costs, potentials and side effects. Environ. Res. Lett. 13. https://doi.org/10.1088/1748-9326/aabf9f

Gasiūnaitė, Z.R., Cardoso, A.C., Heiskanen, A.-S., Henriksen, P., Kauppila, P., Olenina, I., Pilkaitytė, R., Purina, I., Razinkovas, A., Sagert, S., Schubert, H., Wasmund, N., 2005. Seasonality of coastal phytoplankton in the Baltic Sea: Influence of salinity and eutrophication. Estuar. Coast. Shelf Sci. 65, 239–252. https://doi.org/https://doi.org/10.1016/j.ecss.2005.05.018

Geilert, S., Grasse, P., Doering, K., Wallmann, K., Ehlert, C., Scholz, F., Frank, M., Schmidt, M., Hensen, C., 2020. Impact of ambient conditions on the Si isotope fractionation in marine pore fluids during early diagenesis. Biogeosciences 17, 1745–1763. https://doi.org/10.5194/bg-17-1745-2020

Han, Y., Perner, M., 2015. The globally widespread genus Sulfurimonas: versatile energy metabolisms and adaptations to redox clines . Front. Microbiol. .

Hartmann, J., Kempe, S., 2008. What is the maximum potential for CO 2 sequestration by "stimulated" weathering on the global scale? Naturwissenschaften 95, 1159–1164. https://doi.org/10.1007/s00114-008-0434-4

Hartmann, J., Suitner, N., Lim, C., Schneider, J., Marín-Samper, L., Arístegui, J., Renforth, P., Taucher, J., Riebesell, U., 2023. Stability of alkalinity in ocean alkalinity enhancement (OAE) approaches – consequences for durability of CO2 storage. Biogeosciences 20, 781–802. https://doi.org/10.5194/bg-20-781-2023

Hochstetter, F. von, 1859. Lecture on the Geology of the Province of Nelson. New Zeal. Governemt Gaz. (Province Nelson) 7, 90–102.

Iizuka, A., Fujii, M., Yamasaki, A., Yanagisawa, Y., 2004. Development of a new CO2 sequestration process utilizing the carbonation of waste cement. Ind. Eng. Chem. Res. 43, 7880–7887. https://doi.org/10.1021/ie0496176

IPCC, 2021. Climate Change 2021: The Physical Science Basis. Contribution of Working Group I to the Sixth Assessment Report of the Intergovernmental Panel on Climate Change [Masson-Delmotte, V., P. Zhai, A. Pirani, S.L. Connors, C. Péan, S. Berger, N. Caud, Y. Chen, Cambridge University Press.

IPCC, 2018. Summary for Policymakers. In: Global Warming of 1.5°C. An IPCC Special Report on the impacts of global warming of 1.5°C above pre-industrial levels and related global greenhouse gas emission pathways, in the context of strengthening the global response to. Cambridge Univ. Press 3–24. https://doi.org/10.1017/9781009157940.001

Ivanenkov, V.N., Lyakhin, Y.I., 1978. Determination of the alkalinity of seawater. Methods Hydrochem. Stud. Ocean 110–115.

Jeroschewski, P., Steuckart, C., Kühl, M., 1996. An Amperometric Microsensor for the Determination of H2S in Aquatic Environments. Anal. Chem. 68, 4351–4357. https://doi.org/10.1021/ac960091b

Jørgensen, B., Revsbech, N., 1983. Colorless Sulfur Bacteria, Beggiatoa spp. and Thiovulum spp., in O2 and H2S Microgradients. Appl. Environ. Microbiol. 45, 1261–1270. https://doi.org/10.1128/aem.45.4.1261-1270.1983

Jørgensen, B.B., Nelson, D.C., 2004. Sulfide oxidation in marine sediments: Geochemistry meets microbiology, in: Amend, J.P., Edwards, K.J., Lyons, T.W. (Eds.), Sulfur Biogeochemistry - Past and Present. Geological Society of America, p. 0. https://doi.org/10.1130/0-8137-2379-5.63

Klindworth, A., Pruesse, E., Schweer, T., Peplies, J., Quast, C., Horn, M., Glöckner, F.O., 2013. Evaluation of general 16S ribosomal RNA gene PCR primers for classical and next-generation sequencing-based diversity studies. Nucleic Acids Res. 41, e1–e1. https://doi.org/10.1093/nar/gks808

Lackner, K.S., 2003. A guide to CO2 sequestration. Science (80-.). 300, 1677–1678. https://doi.org/10.1126/science.1079033

Lal, R., 2004. Soil carbon sequestration to mitigate climate change. Geoderma. https://doi.org/10.1016/j.geoderma.2004.01.032

Lein, A.Y., 2004. Authigenic Carbonate Formation in the Ocean. Lithol. Miner. Resour. 39, 1–30. https://doi.org/10.1023/B:LIMI.0000010767.52720.8f

Lennartz, S.T., Lehmann, A., Herrford, J., Malien, F., Hansen, H.-P., Biester, H., Bange, H.W., 2014. Long-term trends at the Boknis Eck time series station (Baltic Sea), 1957–2013: does climate change counteract the decline in eutrophication? Biogeosciences 11, 6323–6339. https://doi.org/10.5194/bg-11-6323-2014

Lewin, J.C., 1961. The dissolution of silica from diatom walls. Geochim. Cosmochim. Acta 21, 182–198. https://doi.org/https://doi.org/10.1016/S0016-7037(61)80054-9

Liu, C., Cui, Y., Li, X., Yao, M., 2021. microeco: an R package for data mining in microbial community ecology. FEMS Microbiol. Ecol. 97, 255. https://doi.org/10.1093/femsec/fiaa255

Malkin, S.Y., Rao, A.M.F., Seitaj, D., Vasquez-Cardenas, D., Zetsche, E.-M., Hidalgo-Martinez, S., Boschker, H.T.S., Meysman, F.J.R., 2014. Natural occurrence of microbial sulphur oxidation by long-range electron transport in the seafloor. ISME J. 8, 1843–1854. https://doi.org/10.1038/ismej.2014.41

Maltby, J., Steinle, L., Löscher, C.R., Bange, H.W., Fischer, M.A., Schmidt, M., Treude, T., 2018. Microbial methanogenesis in the sulfate-reducing zone of sediments in the Eckernförde Bay, SW Baltic Sea. Biogeosciences 15, 137–157. https://doi.org/10.5194/bg-15-137-2018

Mark Jensen, M., Thamdrup, B., Rysgaard, S., Holmer, M., Fossing, H., 2003. Rates and regulation of microbial iron reduction in sediments of the Baltic-North Sea transition. Biogeochemistry 65, 295–317. https://doi.org/10.1023/A:1026261303494

Melzner, F., Thomsen, J., Koeve, W., Oschlies, A., Gutowska, M.A., Bange, H.W., Hansen, H.P., Körtzinger, A., 2013. Future ocean acidification will be amplified by hypoxia in coastal habitats. Mar. Biol. 160, 1875–1888. https://doi.org/10.1007/s00227-012-1954-1

Meysman, F.J.R., Cornelissen, R., Trashin, S., Bonné, R., Martinez, S.H., van der Veen, J., Blom, C.J., Karman, C., Hou, J.-L., Eachambadi, R.T., Geelhoed, J.S., Wael, K. De, Beaumont, H.J.E., Cleuren, B., Valcke, R., van der Zant, H.S.J., Boschker, H.T.S., Manca, J. V, 2019. A highly conductive fibre network enables centimetre-scale electron transport in multicellular cable bacteria. Nat. Commun. 10, 4120. https://doi.org/10.1038/s41467-019-12115-7

Meysman, F.J.R., Montserrat, F., 2017. Negative CO2 emissions via enhanced silicate weathering in coastal environments. Biol. Lett. https://doi.org/10.1098/rsbl.2016.0905

Meysman, F.J.R., Risgaard-Petersen, N., Malkin, S.Y., Nielsen, L.P., 2015. The geochemical fingerprint of microbial long-distance electron transport in the seafloor. Geochim. Cosmochim. Acta 152, 122–142. https://doi.org/https://doi.org/10.1016/j.gca.2014.12.014

Millero, F.J., Plese, T., Fernandez, M., 1988. The dissociation of hydrogen sulfide in seawater. Limnol. Oceanogr. 33, 269–274. https://doi.org/10.4319/lo.1988.33.2.0269

Montserrat, F., Renforth, P., Hartmann, J., Leermakers, M., Knops, P., Meysman, F.J.R., 2017. Olivine Dissolution in Seawater: Implications for CO2 Sequestration through Enhanced Weathering in Coastal Environments. Environ. Sci. Technol. https://doi.org/10.1021/acs.est.6b05942

Moras, C.A., Bach, L.T., Cyronak, T., Joannes-Boyau, R., Schulz, K.G., 2022. Ocean alkalinity enhancement – avoiding runaway CaCO3 precipitation during quick and hydrated lime dissolution. Biogeosciences 19, 3537–3557. https://doi.org/10.5194/bg-19-3537-2022

Müller, J.D., Bastkowski, F., Sander, B., Seitz, S., Turner, D.R., Dickson, A.G., Rehder, G., 2018. Metrology for pH measurements in brackish waters-part 1: Extending electrochemical pHT measurements of TRIS buffers to salinities 5-20. Front. Mar. Sci. 5, 1–12. https://doi.org/10.3389/fmars.2018.00176

Nielsen, L.P., Risgaard-Petersen, N., Fossing, H., Christensen, P.B., Sayama, M., 2010. Electric currents couple spatially separated biogeochemical processes in marine sediment. Nature 463, 1071–1074. https://doi.org/10.1038/nature08790

Nilsson, M.M., Kononets, M., Ekeroth, N., Viktorsson, L., Hylén, A., Sommer, S., Pfannkuche, O., Almroth-Rosell, E., Atamanchuk, D., Andersson, J.H., Roos, P., Tengberg, A., Hall, P.O.J., 2019. Organic carbon recycling in Baltic Sea sediments – An integrated estimate on the system scale based on in situ measurements. Mar. Chem. 209, 81–93. https://doi.org/10.1016/j.marchem.2018.11.004

Oelkers, E.H., 2001. An experimental study of forsterite dissolution rates as a function of temperature and aqueous Mg and Si concentrations. Chem. Geol. 175, 485–494. https://doi.org/10.1016/S0009-2541(00)00352-1

Pedregosa, F., Varoquaux, G., Gramfort, A., Michel, V., Thirion, B., Grisel, O., Blondel, M., Prettenhofer, P., Weiss, R., Dubourg, V., Vanderplas, J., Passos, A., Cournapeau, D., Brucher, M., Perrot, M., Duchesnay, É., 2011. Scikit-learn: Machine learning in Python. J. Mach. Learn. Res. 12, 2825–2830.

Perner, M., Wallmann, K., Adam-Beyer, N., Hepach, H., Laufer-Meiser, K., Böhnke, S., Diercks, I., Bange, H.W., Indenbirken, D., Nikeleit, V., Bryce, C., Kappler, A., Engel, A., Scholz, F., 2022. Environmental changes affect the microbial release of hydrogen sulfide and methane from sediments at Boknis Eck (SW Baltic Sea). Front. Microbiol. https://doi.org/10.3389/fmicb.2022.1096062

Pokrovsky, O.S., Schott, J., 2000. Kinetics and mechanism of forsterite dissolution at 25°C and pH from 1 to 12. Geochim. Cosmochim. Acta 64, 3313–3325. https://doi.org/10.1016/S0016-7037(00)00434-8

Pratt, K.W., 2014. Measurement of pHT values of Tris buffers in artificial seawater at varying mole ratios of Tris: Tris·HCl. Mar. Chem. 162, 89–95. https://doi.org/10.1016/j.marchem.2014.03.003

Preisler, A., de Beer, D., Lichtschlag, A., Lavik, G., Boetius, A., Jørgensen, B.B., 2007. Biological and chemical sulfide oxidation in a Beggiatoa inhabited marine sediment. ISME J. 1, 341–353. https://doi.org/10.1038/ismej.2007.50

Price, M.N., Dehal, P.S., Arkin, A.P., 2010. FastTree 2 – Approximately Maximum-Likelihood Trees for Large Alignments. PLoS One 5, e9490.

Quast, C., Pruesse, E., Yilmaz, P., Gerken, J., Schweer, T., Yarza, P., Peplies, J., Glöckner, F.O., 2013. The SILVA ribosomal RNA gene database project: Improved data processing and web-based tools. Nucleic Acids Res. 41. https://doi.org/10.1093/nar/gks1219

Rassmann, J., Eitel, E.M., Lansard, B., Cathalot, C., Brandily, C., Taillefert, M., Rabouille, C., 2020. Benthic alkalinity and dissolved inorganic carbon fluxes in the Rhône River prodelta generated by decoupled aerobic and anaerobic processes. Biogeosciences 17, 13–33. https://doi.org/10.5194/bg-17-13-2020

Renforth, P., Henderson, G., 2017. Assessing ocean alkalinity for carbon sequestration. Rev. Geophys. 55, 636–674. https://doi.org/10.1002/2016RG000533

Rigopoulos, I., Harrison, A.L., Delimitis, A., Ioannou, I., Efstathiou, A.M., Kyratsi, T., Oelkers, E.H., 2018. Carbon sequestration via enhanced weathering of peridotites and basalts in seawater. Appl. Geochemistry 91, 197–207. https://doi.org/10.1016/j.apgeochem.2017.11.001

Rimstidt, J.D., Brantley, S.L., Olsen, A.A., 2012. Systematic review of forsterite dissolution rate data. Geochim. Cosmochim. Acta 99, 159–178. https://doi.org/10.1016/j.gca.2012.09.019

Risgaard-Petersen, N., Revil, A., Meister, P., Nielsen, L.P., 2012. Sulfur, iron-, and calcium cycling associated with natural electric currents running through marine sediment. Geochim. Cosmochim. Acta 92, 1–13. https://doi.org/https://doi.org/10.1016/j.gca.2012.05.036

Sayama, M., Risgaard-Petersen, N., Nielsen, L.P., Fossing, H., Christensen, P.B., 2005. Impact of Bacterial NO3− Transport on Sediment Biogeochemistry. Appl. Environ. Microbiol. 71, 7575–7577. https://doi.org/10.1128/AEM.71.11.7575-7577.2005

Schulz, H.N., Jørgensen, B.B., 2001. Big Bacteria. Annu. Rev. Microbiol. 55, 105–137. https://doi.org/10.1146/annurev.micro.55.1.105

Sternbeck, J., Sohlenius, G., 1997. Authigenic sulfide and carbonate mineral formation in holocene sediments of the baltic sea. Chem. Geol. 135, 55–73. https://doi.org/10.1016/S0009-2541(96)00104-0

Subhas, A. V, Rollins, N.E., Berelson, W.M., Dong, S., Erez, J., Adkins, J.F., 2015. A novel determination of calcite dissolution kinetics in seawater. Geochim. Cosmochim. Acta 170, 51–68. https://doi.org/https://doi.org/10.1016/j.gca.2015.08.011

Teng, F.Z., Watkins, J. and Dauphas, N., 2021. Non-Traditional Stable Isotopes. De Gruyter, Chantilly. https://doi.org/doi:10.1515/9783110545630

Thiel, J., Byrne, J.M., Kappler, A., Schink, B., Pester, M., 2019. Pyrite formation from FeS and H2S is mediated through microbial redox activity. Proc. Natl. Acad. Sci. 116, 6897–6902. https://doi.org/10.1073/pnas.1814412116

Torres, M.E., Hong, W.-L., Solomon, E.A., Milliken, K., Kim, J.-H., Sample, J.C., Teichert, B.M.A., Wallmann, K., 2020. Silicate weathering in anoxic marine sediment as a requirement for authigenic carbonate burial. Earth-Science Rev. 200, 102960. https://doi.org/https://doi.org/10.1016/j.earscirev.2019.102960

Tréguer, P.J., Sutton, J.N., Brzezinski, M., Charette, M.A., Devries, T., Dutkiewicz, S., Ehlert, C., Hawkings, J., Leynaert, A., Liu, S.M., Llopis Monferrer, N., López-Acosta, M., Maldonado, M., Rahman, S., Ran, L., Rouxel, O., 2021. Reviews and syntheses: The biogeochemical cycle of silicon in the modern ocean. Biogeosciences 18, 1269–1289. https://doi.org/10.5194/bg-18-1269-2021

Wallmann, K., Aloisi, G., Haeckel, M., Tishchenko, P., Pavlova, G., Greinert, J., Kutterolf, S., Eisenhauer, A., 2008. Silicate weathering in anoxic marine sediments. Geochim. Cosmochim. Acta 72, 2895–2918. https://doi.org/https://doi.org/10.1016/j.gca.2008.03.026

Wallmann, K., Diesing, M., Scholz, F., Rehder, G., Dale, A.W., Fuhr, M., Suess, E., 2022. Erosion of carbonate-bearing sedimentary rocks may close the alkalinity budget of the Baltic Sea and support atmospheric CO2 uptake in coastal seas. Front. Mar. Sci. 9:968069. https://doi.org/10.3389/fmars.2022.968069

Walter, L.M., Morse, J.W., 1985. The dissolution kinetics of shallow marine carbonates in seawater: A laboratory study. Geochim. Cosmochim. Acta 49, 1503–1513. https://doi.org/https://doi.org/10.1016/0016-7037(85)90255-8

Wolf-Gladrow, D.A., Zeebe, R.E., Klaas, C., Körtzinger, A., Dickson, A.G., 2007. Total alkalinity: The explicit conservative expression and its application to biogeochemical processes. Mar. Chem. 106, 287–300. https://doi.org/10.1016/j.marchem.2007.01.006

Wolff-Boenisch, D., Gislason, S.R., Oelkers, E.H., 2006. The effect of crystallinity on dissolution rates and CO2 consumption capacity of silicates. Geochim. Cosmochim. Acta 70, 858–870. https://doi.org/https://doi.org/10.1016/j.gca.2005.10.016

Zeebe, R.E., Wolf-Gladrow, D. (Eds.), 2001. Chapter 1 Equilibrium, in: CO2 in Seawater: Equilibrium, Kinetics, Isotopes, Elsevier Oceanography Series. Elsevier, pp. 1–84. https://doi.org/https://doi.org/10.1016/S0422-9894(01)80002-7

IV. Alkaline mineral addition to anoxic to hypoxic Baltic Sea sediments as a potentially efficient CO_2-removal technique

Michael Fuhr [a*], Klaus Wallmann [a], Andrew W. Dale [a], Habeeb Thanveer Kalapurakkal [a], Mark Schmidt [a], Stefan Sommer [a], Christian Deusner [a], Timo Spiegel [a], Jannes Kowalski [c] Sonja Geilert [a,b]

[a] GEOMAR Helmholtz Centre for Ocean Research Kiel, Wischhofstr. 1-3, 24148 Kiel, Germany
[b] Department of Earth Sciences, Utrecht University, Utrecht, The Netherlands
[c] Institut für Geowissenschaften, Christian-Albrechts-Universität zu Kiel, Ludewig-Meyn-Str. 10, 24118 Kiel, Germany

* Corresponding author at: GEOMAR Helmholtz Centre for Ocean Research Kiel, Wischhofstr. 1-3, 24148 Kiel, Germany. Tel.: ++49 431 600 2888

Abstract

Recent studies have begun to explore the potential of enhanced benthic weathering (EBW) in the Baltic Sea as a measure for climate change mitigation. To augment the understanding of EBW under seasonally changing conditions, this study aims to investigate weathering processes under anoxia to hypoxia in corrosive bottom waters, which reflect late summer conditions in the Baltic Sea. Dunite and calcite were added to sediment cores retrieved from Eckernförde Bay (Western Baltic Sea) with a constant flow-through of deoxygenated, CO_2-enriched Baltic Sea bottom water. The addition of both materials increased benthic alkalinity release by 2.94 µmol cm^{-2} d^{-1} (calcite) and 1.12 µmol cm^{-2} d^{-1} (dunite), compared to the unamended control experiment. These excess fluxes are significantly higher than those obtained under winter conditions.

The comparison with bottom water oxygen concentrations emphasizes that highest fluxes of alkalinity were associated with anoxic phases of the experiment. An increase in Ca and Si fluxes showed that the enhanced alkalinity fluxes could be attributed to calcite and dunite weathering. First order rate constants calculated based on these data were close to rates published in previous studies conducted under different conditions. This highlights the suitability of these proxies for mineral dissolution and justifies the use of these rate constants in modelling studies investigating EBW in the Baltic Sea and areas with similar chemical conditions. Generally stable pH profiles over the course of the experiment, together with the fact that the added minerals remained on the sediment surface, suggest that corrosive bottom waters were the main driving factor for the dissolution of the added minerals. These factors have important implications for the choice of mineral and timing for EBW as a possible marine carbon dioxide removal method in seasonally hypoxic to anoxic regions of the Baltic Sea.

IV.1. Introduction

In recent years, the pressing need to limit global warming to levels below 2°C compared to preindustrial times has prompted extensive discussions about the imperative role of Carbon Dioxide Removal (CDR) strategies (Beuttler et al., 2019; Campbell et al., 2022; Feng et al., 2017; Foteinis et al., 2023; Fuss et al., 2018; IPCC, 2021). In the pursuit of innovative strategies to mitigate the profound consequences of rising atmospheric carbon dioxide (CO_2) levels and the imminent climate crisis, Ocean Alkalinity Enhancement (OAE) through enhanced weathering has emerged as a promising avenue. This strategy aims to enhance CO_2 storage capacity within the surface ocean, possibly presenting an economical and efficient pathway for

CDR (Campbell et al., 2022; Caserini et al., 2021; Hartmann and Kempe, 2008; Montserrat et al., 2017; Oelkers, 2001; Renforth and Henderson, 2017).

Materials used for this approach on the one hand need to consume protons upon dissolution and on the other hand must dissolve rapidly under the conditions found in the environment where OAE is applied. Two promising minerals are olivine ($(Mg,Fe)_2SiO_4$), a fast dissolving nesosilicate, with the two endmembers forsterite (Mg_2SiO_4) and fayalite (Fe_2SiO_4), and calcite, a highly abundant calcium carbonate ($CaCO_3$) (Kremer et al., 2019; Renforth and Henderson, 2017; Rimstidt et al., 2012; Subhas et al., 2015). Since olivine is the major component of dunite, an ultramafic, igneous rock, and the purification of the mineral is cost intense, dunite instead of olivine would be used in an application scenario (Fuhr et al., 2023; Hochstetter, 1859; Rigopoulos et al., 2018). Still, olivine is the fastest dissolving component of dunite, which is why for the efficiency and efficacy of enhanced dunite weathering, olivine dissolution is the key process (Palandri and Kharaka, 2004; Rimstidt et al., 2012). Understanding the kinetics of the dissolution reactions of forsterite, the most abundant variety of olivine, and calcite is central to the effectiveness of Enhanced Benthic Weathering (EBW). These reactions can be summarized as follows:

Forsterite: $$Mg_2SiO_4 + 4H_2O + 4CO_2(aq) \rightarrow 2Mg^{2+} + H_4SiO_4 + 4HCO_3^- \quad \text{(IV1)}$$

Calcite: $$CaCO_3 + H_2O + CO_2(aq) \rightarrow Ca^{2+} + 2HCO_3^- \quad \text{(IV2)}$$

To date, much of the research on OAE and mineral dissolution in sea water has mainly focused on laboratory environments with well-defined chemical and hydrological characteristics (Flipkens et al., 2023; Fuhr et al., 2022; Montserrat et al., 2017; Naviaux et al., 2019; Rimstidt et al., 2012; Subhas et al., 2015; Walter and Morse, 1985). These studies have revealed complexities, including the potential release of toxicants like nickel during olivine dissolution (Flipkens et al., 2021; Montserrat et al., 2017) and the formation of secondary minerals such as $CaCO_3$ and phyllosilicates, which can hinder CO_2 uptake (Béarat et al., 2006; Burton and Walter, 1987; E. King et al., 2010; Fuhr et al., 2022; Hartmann et al., 2023; Lein, 2004; Moras et al., 2022; Rigopoulos et al., 2018; Sternbeck and Sohlenius, 1997). Importantly, these secondary minerals can alter the overall stoichiometry of the dissolution process, leading to disparities between calculated and actual dissolution kinetics (Fuhr et al., 2022). Furthermore, recent studies using sediments from the Baltic Sea have illuminated the distinctive challenges that arise under conditions closer to the natural system (Fuhr et al., 2023).

In the Baltic Sea, distinguishing between natural and EBW is difficult, given the substantial benthic background fluxes driven by natural $CaCO_3$ input from continental erosion for calcium and diatom dissolution for silica that can overshadow potential fluxes induced by enhanced benthic weathering (Borawska et al., 2022; Fuhr et al., 2023; Gasiūnaitė et al., 2005; Wallmann et al., 2022). Furthermore, the dissolution kinetics of both calcite and olivine remain largely unexplored in the brackish waters of the Baltic Sea, introducing uncertainty whether dissolution rates assumed in modeling studies based on standard seawater (Fakhraee et al., 2023; Feng et al., 2017; Griffioen, 2017) can be applied in this specific region. Despite these challenges, the high organic-rich sediments releasing up to 80 Tg yr^{-1} of dissolved inorganic carbon (DIC) in the Baltic Sea make it an intriguing setting for EBW studies (Nilsson et al., 2019).

Modeling plays a pivotal role in assessing the feasibility and impact of OAE through EBW as a marine carbon dioxide removal (mCDR) strategy. Currently existing models rely on dissolution kinetics derived from studies conducted in marine environments that do not align with the unique chemical and hydrological properties of the Baltic Sea, where the partly seasonal, partly perennial seasonal stratification of the brackish water body, combined with limited deep water renewal leads to very low pH values in bottom waters (Meier et al., 2019; Melzner et al., 2013). This disconnect between the assumptions underlying many modeling efforts and the specific conditions of the Baltic Sea creates a critical need for empirical investigations of mineral dissolution kinetics, which can, in turn, inform more accurate and regionally tailored modeling efforts.

By investigating the efficiency of EBW under conditions of hypoxia to anoxia as well as CO_2 enrichment, this study complements a previous study, where calcite and dunite were added to Baltic Sea sediments exposed to oxic, calcite-oversaturated bottom waters (Fuhr et al., 2023). To this end, sediment cores were retrieved from Boknis Eck, a shallow, seasonally hypoxic to anoxic depocenter in Eckernförde Bay in the southwestern Baltic Sea, amended with calcite and dunite and exposed to calcite-undersaturated bottom waters under controlled laboratory conditions with the aim to simulate conditions prevailing during late summer in this part of the Baltic Sea (Melzner et al., 2013). The study not only contributes to our understanding of benthic weathering in the Baltic Sea but also enhances the accuracy and reliability of modeling approaches for assessing the potential of EBW as a mCDR strategy.

IV.2. Materials and Methods

IV.2.1. Materials

On 26 October, 2022, a total of nine sediment cores (60 cm long) were retrieved from Boknis Eck with a multiple-corer from a water depth of 27m with the research vessel FK Littorina. Alongside the sediment cores, 500 liters of bottom water were also collected. The sediment cores contained 20-24 cm of surface sediment. Immediately after recovery, the cores were sealed at the top and bottom with rubber bungs, maintained in an upright position, and transported to a temperature-controlled laboratory at 12.5 °C, which reflects natural summer conditions in the study area (Melzner et al., 2013). One of the cores was sliced for subsequent pore water and sediment analyses to determine initial natural background conditions. The results of these measurements are reported in Figure S4 in the supplement.

For the incubation experiments, a total of eight cores were selected. Two different alkaline materials, dunite and calcite, were added to assess their effectiveness in OAE. The dunite (olivine AFS 80) used was sourced from quarries in Årheim, Norway, and the 20µm – 30µm fraction was isolated through sieving. The mineralogical composition of the dunite is reported in Table 1S (supplement). The calcite used was ground limestone provided by the German Limestone Association, with a calcium carbonate content exceeding 99% (Table 2S, supplement) and grain sizes below 0.12 mm. Prior to the experiment, the calcite was rinsed with deionized water with a conductivity of 18.2 $M\Omega\ cm^{-1}$. To eliminate the fine fraction of the material, the calcite was mixed with deionized water in a settling column (20 cm height), and particles that remained in suspension after 20 seconds were decanted. This process was repeated until the supernatant water became clear after 20 seconds. As a result, all particles were expected to settle on the sediment surface within a few minutes after adding the calcite to the sediment cores. Grain size distribution and median grain size after washing are reported in Table IV 1 and Figure S1 (supplement).

IV.2.2. Determination of reactive surface area

Since the majority of studies used the geometrical surface assuming spherical grains to determine olivine dissolution (Rimstidt et al., 2012), the surface of dunite grains was determined likewise, assuming a grain size of 25 µm (Table IV 1).

The reactive surface of calcite grains was determined via gas adsorption following the Brunauer-Emmett-Teller (BET) method after Brunauer et al. (1938) on a Stöhlein^{TM} AREA-Meter II.

The findings from the measurements and calculations are presented in Table IV 1.

Table IV 1: Overview on materials used in the experiment, including bottom water (BW) volumes, treatments (Cal = calcite, Dun = dunite, C = control), BET surface area of calcite (measured) and geometrical surface area of dunite grains, calculated for an average grain size of 25µm.

Core name	Cal1	Cal2	Cal3	Dun1	Dun2	Dun3	C1	C2
Volume BW (dm^3)	2.083	2.052	1.942	2.021	2.178	2.060	1.824	2.099
Mineral:	Calcite	Calcite	Calcite	Dunite	Dunite	Dunite	-	-
Mass (g):	7.8618	7.8618	7.8618	4.4781	4.4781	4.4781	-	-
Grain size (µm)	D_{50}=87	D_{50}=87	D_{50}=87	20-30	20-30	20-30		
BET-surf. ($m^2\ g^{-1}$)	0.45±0.06	0.45±0.06	0.45±0.06	-	-	-	-	-
Geom. surf. ($m^2\ g^{-1}$)	-	-	-	0.073±0.004	0.073±0.004	0.073±0.004	-	-

IV.2.3. Experimental setup

Eight sediment cores were positioned vertically in a rack. Since the sediment surface was slightly oxidized by the bottom water (~125 µmol l^{-1} upon recovery), the cores were left plugged on the top for 13 days to settle after recovery until the sediment surface was anoxic. To achieve chemical conditions that are expected in the natural system (Melzner et al., 2013), 500 l of retrieved sea water were degassed via bubbling with pure dinitrogen gas in batches of 100 l. Afterwards, between 50 and 60 l were transferred into an evacuated gas tight bag. After the transfer, pH and total alkalinity (TA) were measured to determine the DIC of the water. Afterwards the DIC was increased via adding pure CO_2 until a CO_2 partial pressure (pCO_2) of ~2300 - ~3300 µatm was established mimicking conditions prevailing in Boknis Eck during summer (Melzner et al., 2013). This mixture is hereafter referred to as modified bottom water. The pCO_2 was slightly increased in the reservoir over time to compensate for alkalinity increases in the water overlying the cores due to benthic anaerobic degradation of organic matter and maintain calcite undersaturation.

Stirring heads were installed on the cores, allowing for the insertion of optodes for continuous measurements of bottom water pH and oxygen (Pyroscience^{TM} PHROBSC-PK8 and OXROB3-SUB, respectively). The logging was done on a self-constructed 16 channel device for O_2 and pH (each parameter 8 channels). For the measurement of O_2 and pH for each channel, the underwater OEM O2 meter PICO-O2-SUB (Pyroscience) and the underwater OEM pH meter PICO-PH-SUB (Pyroscience) were used, respectively. Calibration was carried out according to the manufacturer's instructions. For brackish bottom water conditions, all pH probes including micro-sensors (section 2.6) were calibrated using three TRIS-

buffers (Müller et al., 2018; Pratt, 2014). Thus, pH values reported in this study refer to the total pH scale (pH_T, Dickson, 1993). The equilibrium constants for further calculations were chosen accordingly.

To prevent the development of oxic conditions, it was ensured that as little gas phase as possible was left in the cores. Elimination of pelagic autotrophs, heterotrophs, and suspended particles was achieved by flushing the cores with modified bottom water for 2 days with a flow rate of 1.5 mml min^{-1}. Afterwards, a continuous throughflow of 700 µl min^{-1} from the reservoir of modified bottom water was applied, leading to a residence time of approximately 2.1 days inside the cores.

For the experimental incubations, six cores received additions of alkaline materials, three with calcite (Cal1 - Cal3) and three cores with dunite (Dun1 - Dun3), leading to three replicates per treatment. Two control cores remained untreated (C1, C2). The amount of added substrate was based on the rain rate of particulate organic carbon observed in Boknis Eck (0.5 mmol cm^{-2} a^{-1}, Dale et al., 2011), the proton consumption of each substrate (Equations IV1,IV2) and then doubled to achieve a resolvable weathering signal. A detailed parameter description of each experiment can be found in Table IV 1. Prior to mineral addition, the cores were monitored untreated for six days to establish a natural baseline. The incubation lasted for 25 days. The volume of water in each core was determined at the end of the experiment via measuring the height of the water column after removing the stirring heads.

IV.2.4. Sampling procedure and analysis

Bottom water samples (12 ml) were collected from the outflow of each core, over several minutes. Sampling was conducted daily for the first two weeks and then every two days till the end of the experiment. All samples were filtered using a 0.2 µm cellulose membrane filter and stored refrigerated in Exetainer® 12ml Vials. TA samples (1 ml) were titrated with 0.02N HCl following the method described by Ivanenkov and Lyakhin (1978), with titration ending upon the appearance of a stable purple color. During titration, continuous nitrogen bubbling degassed the sample to eliminate any generated CO_2 and H_2S. The procedure was calibrated using an IAPSO seawater standard. Anion element concentrations (SO_4^{2-}, Cl^-, Br^-) were determined using ion chromatography (IC, METROHM 761 Compact, conductivity mode). Acidified sub-samples (3 ml sample and 30 µl suprapure HNO_3^-) were prepared for major and trace element analyses (Si, Na, K, Li, B, Mg, Ca, Sr, Mn, Ni, and Fe) using inductively coupled plasma optical emission spectroscopy (ICP-OES, Varian 720-ES).

At the end of the experiments, bottom water was removed via suction, and the cores were sliced for analysis of pore water and solid phases. Pore waters were obtained by centrifuging each sediment layer in 50 ml Falcon tubes at 3000 rpm for 10 minutes. The resulting supernatant water was filtered (0.2 µm regenerated cellulose syringe filters) and transferred to polyethylene vials within an oxygen-free glove bag environment. Additional parameters, such as H_2S and Fe^{2+}, were analyzed in the pore waters. For dissolved Fe^{2+} analysis, 1 ml sub-samples (1 ml) were stabilized with ascorbic acid and complexed with Ferrozin within 30 minutes inside the glove bag. H_2S measurements involved diluting an aliquot of pore water with oxygen-free artificial seawater and fixing of H_2S through immediate addition of zinc acetate gelatin solution. Further details on these procedures can be found in Dale et al. (2014, 2016). Bottom water solute concentrations are reported in the supplement.

IV.2.5. Solid phase analysis

Freeze-dried and ground sediment samples were subjected to flash combustion using the EuroEA 3000 element analyzer (EuroVector, Pavia, Italy) to measure total carbon (TC), total organic carbon (TOC), total nitrogen (TN), and total sulfur (TS). The total inorganic carbon (TIC) content was determined by subtracting the TOC value from the TC measurement. Method blanks and two reference standards, namely 2.5-Bis(5-tert-butyl-2-benzo-oxazol-2-yl)thiophene (BBOT, HEKAteck^{TM}), and an internal sediment standard, were employed to evaluate the accuracy of the analytical method.

IV.2.6. Micro-profiling

To conduct sediment micro-profiling, a motorized Unisense^{TM} micromanipulator (MMS) was employed. Oxygen, pH, and H_2S profiles were measured using Unisense^{TM} micro-sensors Ox-50, pH-100, and SULPH-100, respectively. The vertical step sizes were adjusted based on the sensor specifications (at least twice the needle diameter) and the desired measurement resolution to minimize profiling time (100 µm for O_2 profiles, 300µm for pH and H_2S profiles). Sensor calibration followed the manufacturer's recommendations, with the Unisense^{TM} calibration kit used for SULPH-100 at a calibration concentration of 109 µmol l^{-1}.

Following the acquisition of H_2S and pH profiles, the total dissolved sulfide concentration was calculated according to Unisense^{TM} guidelines based on the work of Millero et al. (1988) and Jeroschewski et al. (1996). Unless specified otherwise, the term H_2S refers to the total dissolved sulfide concentration ($\approx H_2S + HS^-$). Micro-profiles were obtained at the beginning of the experiment (t = -6 d), directly before the addition of substrates (t = 0 d) and at the end of the experiment (t = 19 d). Results of these measurements are presented in the supplement.

IV.2.7. Flux calculations from bottom water concentrations and oxygen profiles

Solute fluxes across the sediment surface were determined by applying the following calculations, which consider the concentrations of an element in the inflow and outflow:

$$F_e = \left(\left(\frac{dC_e}{dt} + k_w \times C_{out} - k_w \times C_{in}\right) \times V_{MUC}\right) / A_{sed} \quad \text{(IV3)}$$

F_e represents the element flux across the entire sediment surface (mol cm^{-2} d^{-1}), $\frac{dC_e}{dt}$ denotes the rate of concentration change of the specific element over a defined time (mol l^{-1} d^{-1}), k_w represents the water exchange rate in d^{-1}, C_{out} signifies the concentration in the outflow (mol l^{-1}), C_{in} represents the concentration in the inflow (mol l^{-1}), V_{MUC} denotes the volume of bottom water (l) in each core, and A_{sed} (cm^2) signifies the surface area of the incubated sediment cores.

Calculation of the carbonate system and saturation states

The rate of calcite dissolution, R, is dependent on its saturation state (Ω_{cal}; Walter and Morse, 1985 and references therein) following:

$$R = k(1 - \Omega_{cal})^n \quad \text{(IV4)}$$

where k is an empirical rate constant (μmol g^{-1} hr^{-1}) and n is the reaction order. The Ω_{cal} values are a function of Ca^{2+} and CO_3^{2-} concentrations, where the latter is a function of the carbonate system equilibria (Zeebe and Wolf-Gladrow, 2001). In this study, CO_3^{2-} and hence Ω_{cal} were calculated using measured pH and TA pore and bottom water values, following:

$$\Omega_{cal} = \frac{[Ca] \times [CO_3^{2-}]}{Ks_{cal}} \quad \text{(IV5)}$$

where $[Ca]$ and $[CO_3^{2-}]$ are the concentrations of dissolved calcium and carbonate, respectively, and Ks_{cal} is the solubility product of calcite at the respective salinity, temperature and pressure (Zeebe and Wolf-Gladrow, 2001). Due to the experimental set-up, TA and Ca^{2+} concentrations in pore waters could not be measured over time. Therefore, only initial and final values for both parameters were used and interpolated linearly for each depth layer between the initial and final concentrations. We recognize the uncertainty associated with this approach.

Further properties of the carbonate system (pCO_2, DIC) were calculated as described by Zeebe and Wolf-Gladrow (2001).

IV.3. Results

IV.3.1. Bottom water chemistry and fluxes across the sediment-water interface

Bottom water TA concentrations averaged over each treatment remained relatively stable around the reservoir value (2.08 mmol l^{-1}) in all treatments before the addition of alkaline materials (Figure IV 1a). After mineral addition, TA increased in all cores to values between 2.35 ± 0.1 mmol l^{-1} (control cores (C)) and 2.45 ± 0.1 mmol l^{-1} (dunite treated cores (Dun)). After 5 days, TA values were equal within error in all treatments. After day five, values dropped to ~2.25 ± 0.1 mmol l^{-1} in dunite treated cores and to ~2.15 ± 0.1 mmol l^{-1} in the control experiments while they remained elevated in calcite treated cores. For the rest of the experiment, TA concentrations remained relatively stable at values of ~2.39 ± 0.05 mmol l^{-1} (calcite treated cores(Cal)), ~2.27 ± 0.06 mmol l^{-1} (dun) and 2.16 ± 0.03 mmol l^{-1} (C).

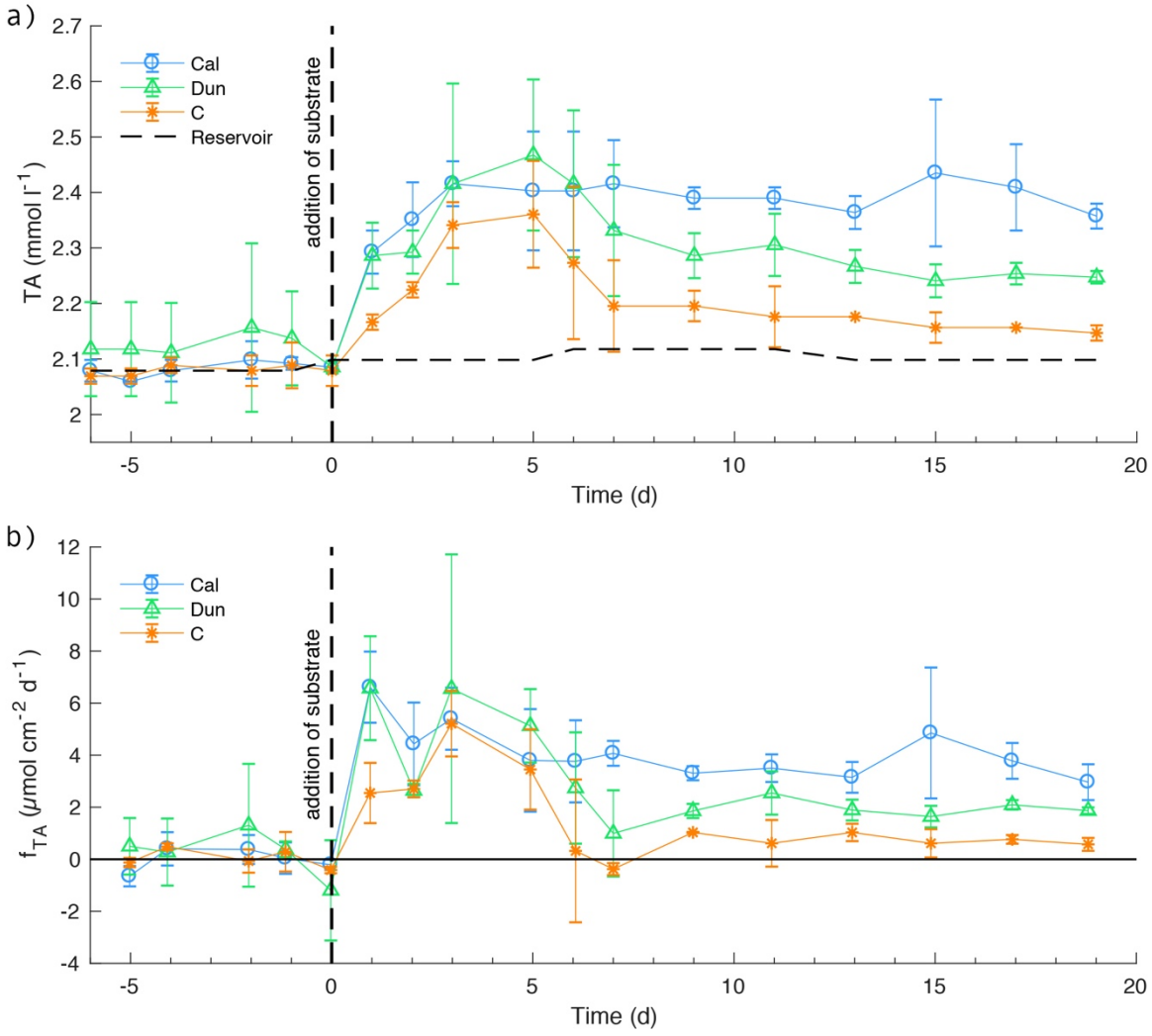

Figure IV 1: TA concentrations in bottom waters (a) and fluxes at the sediment surface (b) averaged over the different treatments. Positive fluxes denote a flux from the sediment to the bottom water and negative fluxes vice versa. Horizontal dashed line in a) shows concentration in the reservoir. Dashed vertical lines indicate the addition of substrates. Changes in the reservoir concentration denote the times a new reservoir was used. Time is given in days relative to mineral addition. Solid horizontal line denotes f_{TA} = 0. Error bars denote one standard deviation (SD) from the average of the replicates. Fluxes were calculated from bottom water concentrations (Eq. IV3).

These changes are reflected in corresponding TA fluxes (Figure IV 1b). Before the addition of alkaline minerals, fluxes varied around ~0.3 ± 1 µmol cm^{-2} d^{-1} within error in all treatments. The addition of alkaline minerals led to an immediate increase in TA fluxes for the calcite- and dunite-treated cores to values around 6 ± 2 µmol cm^{-2} d^{-1} on day one. In the reference cores, fluxes also increased at the time of addition and peaked at values of ~5 ± 1 µmol cm^{-2} d^{-1} on day 3. Towards the end of the experiment, the system approached a steady state with relatively constant fluxes for each set of the equally treated cores. The highest values (~3.8 ± 0.5 µmol cm^{-2} d^{-1}) at that point in time were observed in calcite treated cores followed by dunite treated cores (~1.9 ± 0.1 µmol cm^{-2} d^{-1}). Lowest final values were observed in the control experiment with ~0.6 ± 0.1 µmol cm^{-2} d^{-1}.

Dissolved silicon (Si) concentrations (Figure IV 2a) increased in all treatments during the early stage of the experiment to peak values between ~65 ± 10 µmol l^{-1} (Cal) and ~77 ± 15 µmol l^{-1} (Dun). Just before the

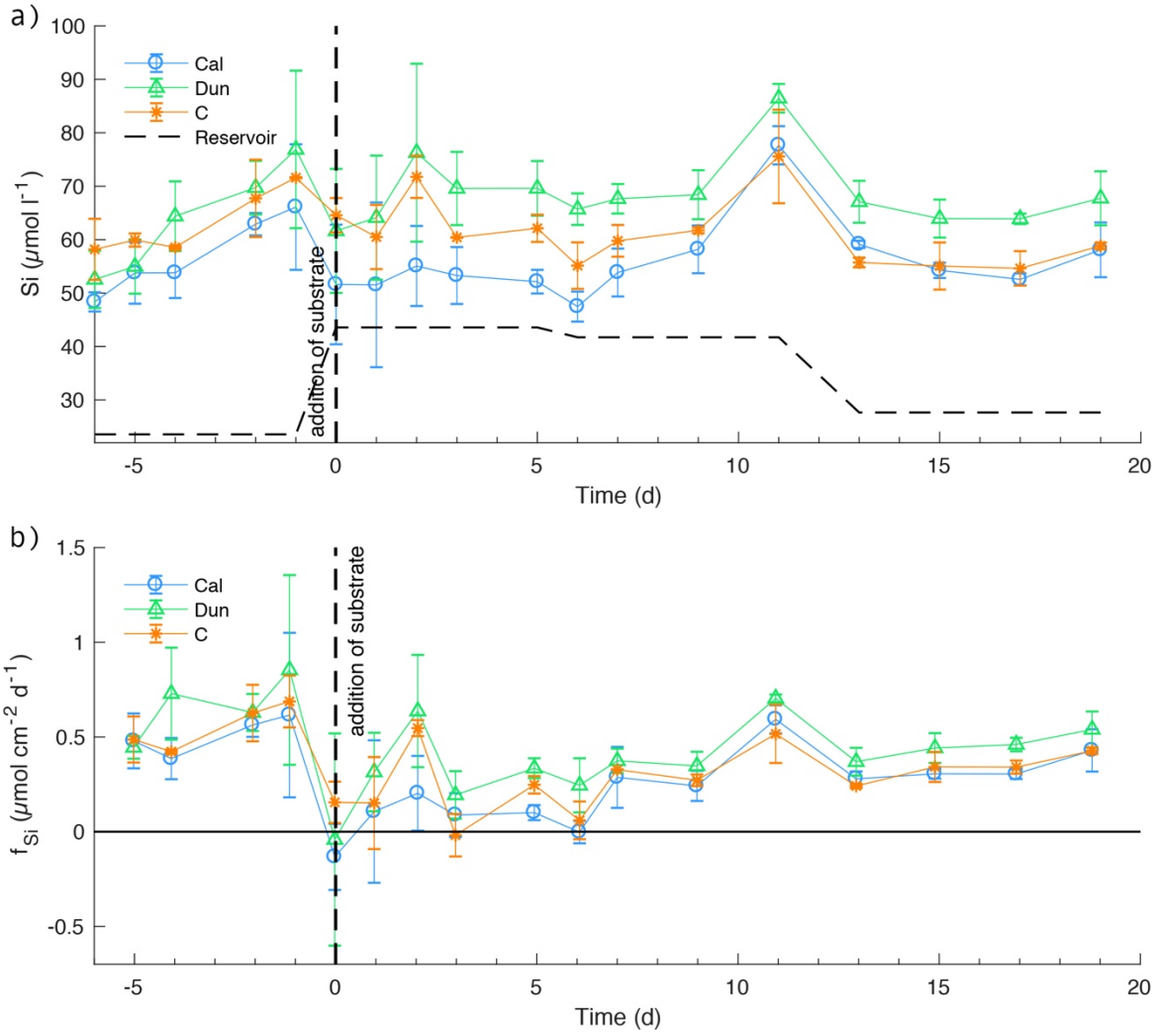

Figure IV 2: Si concentrations in bottom waters (a) and fluxes at the sediment surface (b) averaged over the different treatments. See Figure IV 1 for further information.

addition, Si levels decreased to ~52 ± 12 µmol l^{-1} (Cal) and ~65 ± 3 µmol l^{-1} (C). After the addition of alkaline substrates, concentrations increased to slightly higher values in dunite treated cores compared to the other treatments. Overall, large error bars indicate strong variability within the different treatments, obscuring clear trends. Over the course of the experiment, bottom water concentrations varied slightly between ~50 ± 3 µmol l^{-1} (Cal) and ~70 ± 5 µmol l^{-1} (Dun) with one clear peak in all treatments around day 11. During the entire experiment, highest Si concentrations were observed in dunite treated cores. This

difference became clearer towards the end of the experiment. The corresponding fluxes (Figure IV 2b) averaged between 0.45 ± 0.1 µmol cm^{-2} d^{-1} and 0.75 ± 0.6 µmol cm^{-2} d^{-1} before addition of substrates. Afterwards, fluxes were overall lower, ranging between 0 ± 0.1 µmol l^{-1} and 0.55 ± 0.3 µmol l^{-1}, with decreasing fluctuations and error bars towards the end of the experiment. Again, highest values at a given time were observed in dunite treated cores with clearly higher values compared to the other treatments towards the end of the experiment.

Dissolved calcium (Ca) concentrations averaged over each treatment (Figure IV 3a) showed clearer trends than Si concentrations. Ca concentrations remained fairly constant around ~7.1 ± 0.5 mmol l^{-1} and thus slightly above reservoir concentrations before the addition of substrates. After the addition, values significantly increased in calcite treated cores to concentrations around ~7.17 ± 0.05 mmol l^{-1} whereas in the other treatments, values dropped slightly and tracked the concentrations in the reservoir. After day 5

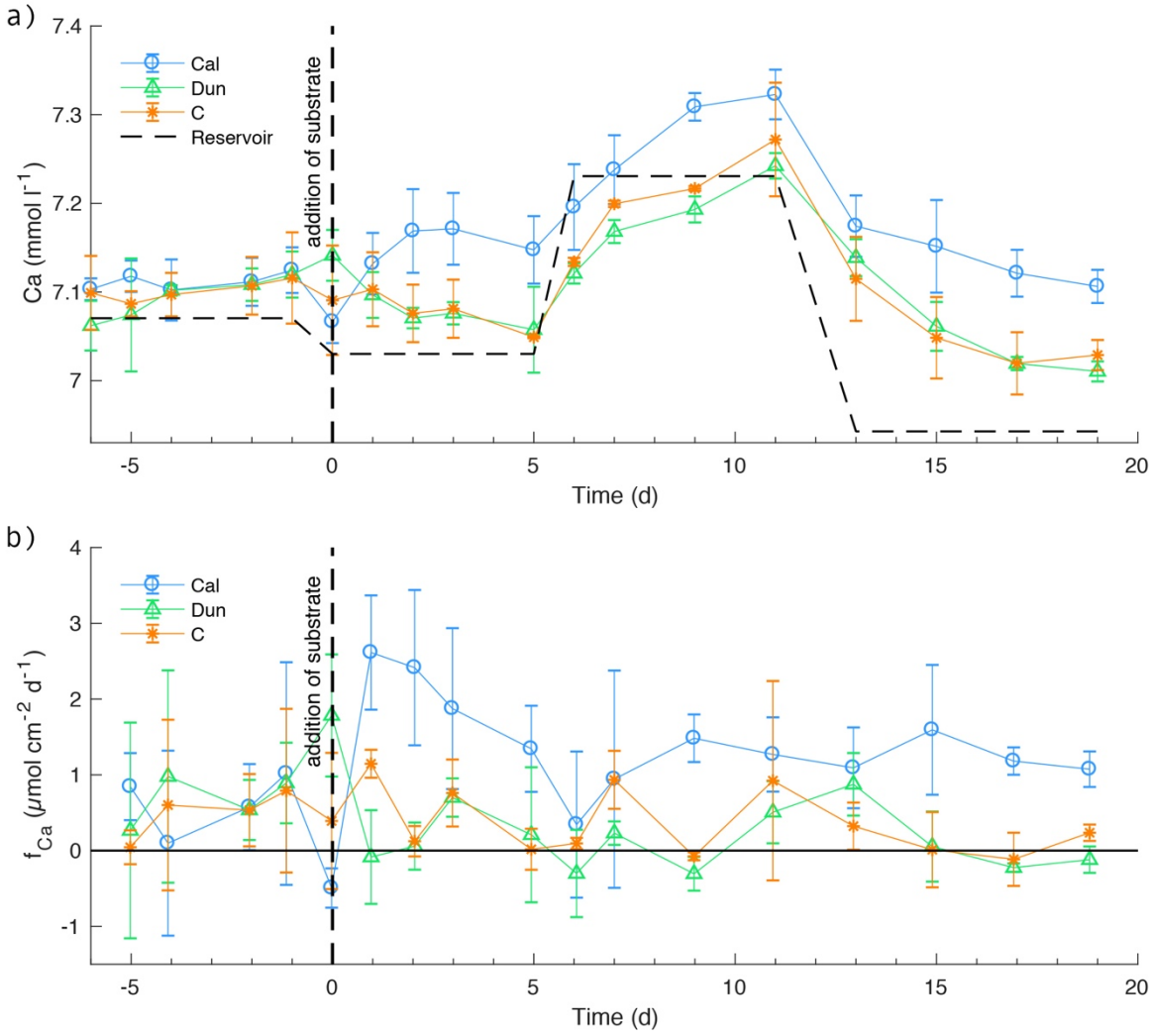

Figure IV 3: Ca concentrations in bottom waters (a) and fluxes at the sediment surface (b) averaged over the different treatments. See Figure IV 1 for further information.

the reservoir concentrations increased to 7.23 mmol l^{-1}. This increase is also visible in bottom water concentrations in all treatments. On day 11, concentrations in dunite treated cores and the control cores averaged around ~7.24 ± 0.06 mmol l^{-1} while concentrations in calcite treated cores reached up to ~7.32 ± 0.02 mmol l^{-1}. Towards the end of the experiment lower reservoir concentrations of 6.94 mmol l^{-1}

led to lower bottom water concentrations that stabilized at ~7.11 ± 0.01 mmol l^{-1} in calcite treated cores compared to ~7.02 ± 0.01 mmol l^{-1} in the other two treatments.

This development is reflected in Ca fluxes. Between day -5 and day 0, values averaged around ~0.5 ± 1.5 µmol cm^{-2} d^{-1}, but remained fairly stable within error. Directly after the addition, the fluxes in calcite treated cores peaked at values around ~2.7 ± 0.8 µmol cm^{-2} d^{-1}. Until day 6 values then decreased to 0.2 ± 0.9 cm^{-2} d^{-1} to stabilize around 1.2 ± 0.2 µmol cm^{-2} d^{-1} towards the end of the experiment. In the other two treatments, values fluctuated between -0.1 ± 0.05 and 1.1 ± 1.0 µmol cm^{-2} d^{-1} with final values around 0 ± 0.2 µmol cm^{-2} d^{-1} with a tendency towards slightly negative values in dunite treated cores.

Throughout the experiment, nickel concentrations stayed below detection limit (~0.2 µmol l^{-1}) both in pore waters and in bottom waters.

Oxygen concentrations in bottom waters (Figure IV 4) stayed at ~0 µmol l^{-1} in cores Cal1, Dun3 and C1 over the course of the experiment. They varied widely in the other cores. At the beginning of the incubation, oxygen concentrations were ~0 µmol l^{-1} in all cores except C1 where concentrations were close to the reservoir concentration of 20 µmol l^{-1}, but increased to values between 120 µmol l^{-1} (Dun1) and 23 µmol l^{-1} (Cal2). Between day 0 and day 3 in Cal3 concentrations peaked at ~25 µmol l^{-1} on day two and at 140 µmol l^{-1} in Cal2 around day 5. Between day 6 and day 11, reservoir concentrations of 40 µmol l^{-1} were accompanied by overall higher bottom water concentration of up to 150 µmol l^{-1} in Dun1. Until day 15, concentrations decreased back to ~0 µmol l^{-1} in C1, Dun1 and Dun2 but remained between 120 µmol l^{-1} and 130 µmol l^{-1} in Cal2 and Cal 3. Towards the end of the experiment concentrations had decreased back to values below 2 µmol l^{-1} in all cores except from C1, where for the only time during the experiment concentrations had increased to ~80 µmol l^{-1} during the last day of the incubation.

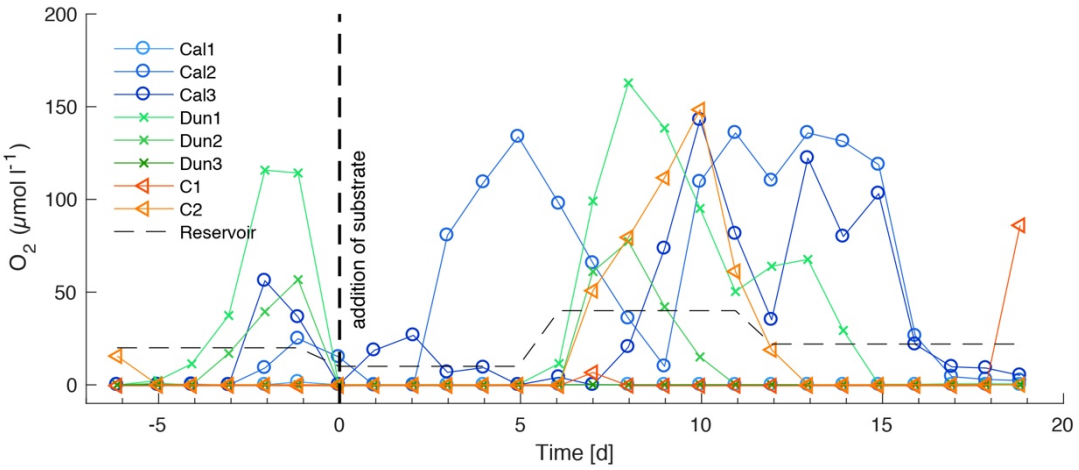

Figure IV 4: Oxygen concentrations in bottom waters over the entire time of the experiment for calcite treated cores (blue circles), dunite treated cores (green crosses) and control experiments (orange triangles). Measuring accuracy is 0.3 µmol l^{-1}, resolution is 0.15 µmol l^{-1} (according to manufacturer). Vertical dashed line indicates time of addition of alkaline substrates. Thin dashed, horizontal line denotes oxygen concentrations in the reservoir tank. Changes in the reservoir concentration denote the times a new reservoir was used

Due to a failure of the pH logging system, bottom water pH values are only available each time a micro-profile was obtained. To calculate the bottom water carbonate system properties, these pH values were interpolated linearly between the three obtained data points in each core. Before the addition of substrates, the calculated pCO_2 values in all cores fluctuated around the reservoir value (~2350 µatm) with a decreasing trend in all cores (Figure IV 5a). Lowest values just before the addition were observed in dunite treated

cores (~2000 µatm), with highest values (~2400 µatm) in the two control cores. At the time the substrates were added, the new reservoir pCO_2 was higher (~2950 µatm) than the first batch. Subsequently, pCO_2 in all cores increased with highest values of ~2800 µatm in the two control cores, ~2400 µatm in dunite and calcite treated cores. After the reservoir was changed, they decreased again to ~2300 µatm such that the values in dunite and calcite treated cores were the same after ~5 days. For the rest of the experiment pCO_2 remained relatively stable in dunite treated cores at ~2100 µatm while values in calcite treated cores continuously decreased to ~1850 µatm on day 19. The highest pCO_2 at the end of the experiment was observed in control cores (~2500 µatm).

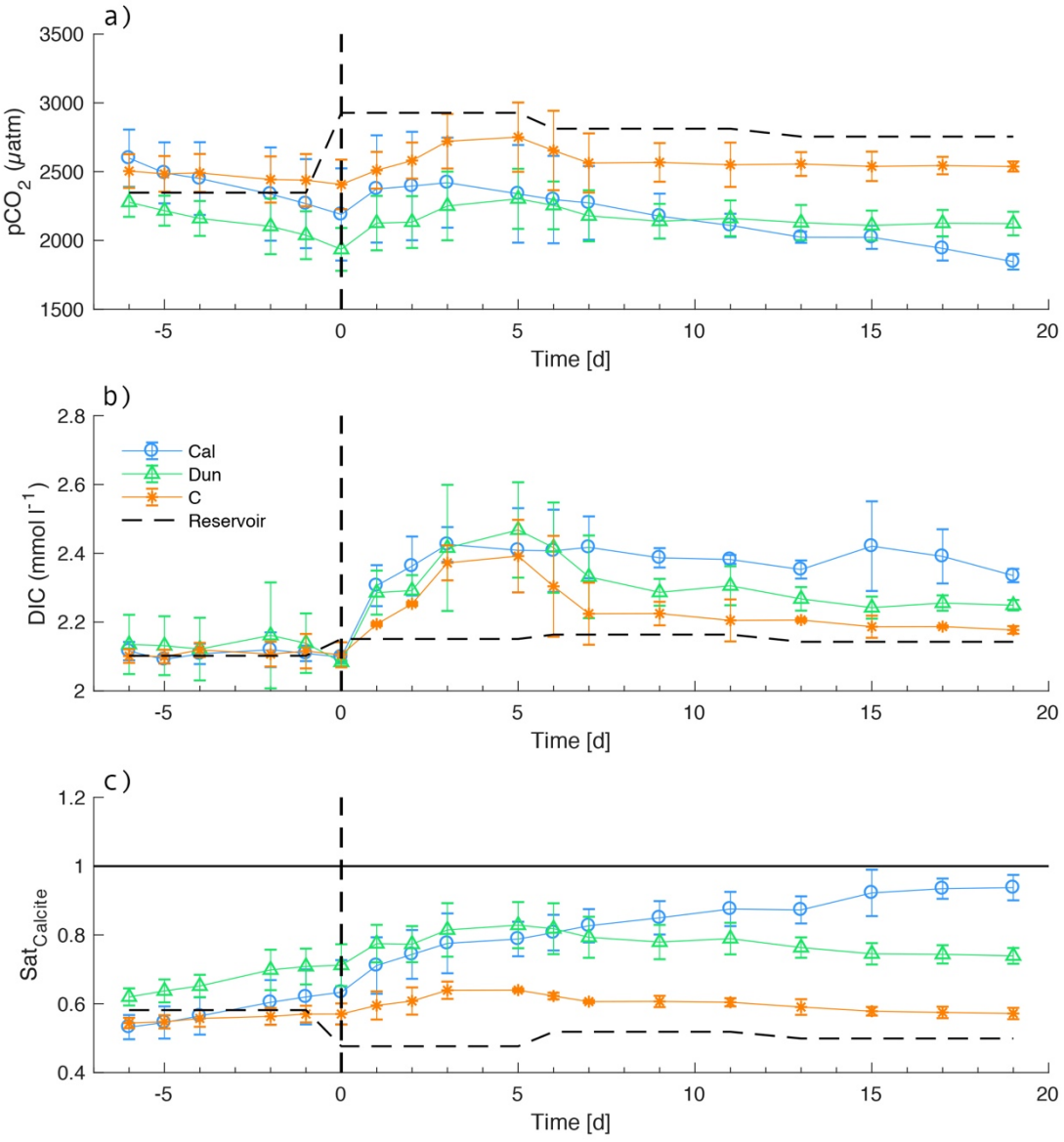

Figure IV 5: pCO_2 (a), DIC (b) and $Sat_{Calcite}$ (c) values in bottom waters over the entire course of the experiment. Values are reported as average of each treatment. Error bars report 1 SD of the averaged values. Vertical dashed lines denote the time of addition of substrates. The horizontal line in c denotes the saturation with respect to calcite.

Before the addition of substrates, calculated DIC values remained stable within the error around the reservoir value of ~2.1 mmol l^{-1} (Figure IV 5b). After the addition, values increased in all cores until day 5

to values of ~2.4 mmol l^{-1}. After the reservoir was changed between days 5 and 6, DIC decreased to 2.2 mmol l^{-1} in control cores and 2.3 mmol l^{-1} in dunite treated cores. In calcite treated cores, values remained significantly higher around ~2.4 mmol l^{-1}. Towards the end of the experiment, reservoir values of around ~2.15 mmol l^{-1} led to final values of ~2.16 mmol l^{-1} in the control cores, ~2.25 mmol l^{-1} in dunite treated cores and ~2.35 mmol l^{-1} in calcite treated cores.

Saturation with respect to calcite remained below 1, implying corrosive bottom waters in all cores over the entire course of the experiment (Figure IV 5c). Overall these values mirrored the pCO_2 values. Before addition of substrates they were close to the reservoir value of ~0.6. Until the second reservoir change between day 5 and 6, they increased to values around ~0.8 in calcite and dunite treated cores and ~0.63 in the control cores. After day 6 in calcite treated cores, values increased continuously to ~0.93. In all other treatments (dunite and controls) values decreased to ~0.76 in dunite treated cores and 0.6 in control cores, thus only slightly above the reservoir value of ~0.5.

IV.3.2. Solid phase TIC content and distribution of added material

After mineral addition, calcite and dunite covered the sediment surface as an approximately 0.5 mm thick layer. This layer remained at the surface throughout the experiment with only very minor visible changes (Figure S2, supplement).

In the initially sampled core (black line and crosses in Figure IV 6), TIC content varied between ~0.3 and ~ 3.2 wt.% in depths below 2.5 cm. Above this depth to the sediment surface, values increased progressively to ~9.7 wt.%. In calcite-treated cores, TIC content at the surface was increased up to 28 % in the uppermost sample (0.5 cm). Directly below this depth (1.5 cm) and further downcore the TIC content varied between ~0 and ~8 wt.% in all cores. At the surface, TIC levels in dunite-treated and control cores were significantly lower compared to the initially sampled core and ranged between ~0 and ~4 wt.%.

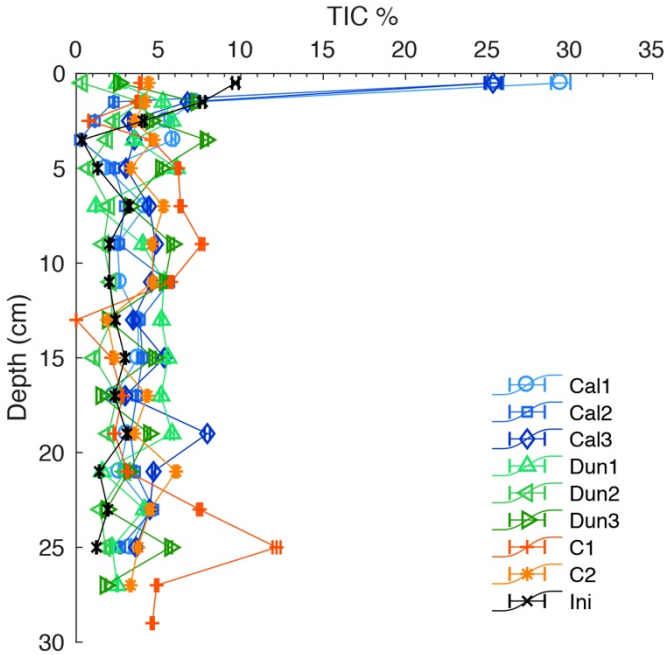

Figure IV 6: TIC content in the solid phase of all cores. Colored markers indicate contents in each core at the end of the experiment. Black crosses indicate the contents in the initial core. Error bars report analytical precision.

IV.4. Discussion

IV.4.1. Changes in bottom water and porewater composition over the course of the experiments

The data showed a consistent trend between all sediment cores. The cores behaved very similarly, until the addition of substrates, followed by a phase with more dynamic developments in bottom water chemistry. Afterwards, the different cores approached a quasi-steady state with similar trends between equally treated cores. The pore water solute concentrations, as well as the pore water pH profiles (Figures S3, S4, supplement), did not change significantly over the course of the experiment, which indicates that sediments were not significantly altered by the incubation. Slightly enhanced Ca concentrations in the upper sediment of Cal2 and Cal3, compared to all other cores, point either towards diffusion into the sediment or towards entrainment of calcite grains into the surface sediment and subsequent sedimentary dissolution in the corrosive porewaters in the upper millimeters, especially in Cal2 (Figure S5, supplement). The uniformity of pore water solute concentrations in most cores with the initially sampled core suggests that deviations observed in C1 and Dun1 reflect the spatial inhomogeneity of the sediment composition, despite the close proximity of coring locations. In previous experiments conducted under oxic conditions, drastic changes were observed in porewater composition over the course of the experiments (Fuhr et al. 2023). These changes did not occur in the experiments in the present study which is most likely a consequence of the shorter incubation time and the fact that the cores were recovered at an ambient temperature of 10.2 °C, thus closer to the laboratory conditions (12.5 °C), compared to 6.9 °C in the former experiment. The shift in the pore water pH profiles in Cal2 and Cal3, however, appears very similar to changes observed in sediments from the same location under oxic conditions (Fuhr et al., 2023). In general, pH shifts in all cores were low and had a comparably minor impact on sedimentary fluxes and bottom water chemistry. The stable pore waters combined with the steady state attained at the end of the experiment, allows for a straightforward interpretation of the data.

IV.4.2. Correlation between oxygen concentrations and TA in bottom waters

For the assessment of TA that derives from EBW, it is necessary to consider the oxidation state of bottom waters, which controls the benthic release of reduced substances such as H_2S, NH_4^+, Fe^{2+}, Mn^{2+} and PO_4^{3-} generated during anaerobic organic matter degradation including denitrification (Hiscock and Millero, 2006).

In order to assess the correlation between oxygen and TA concentrations in bottom waters, TA measured in individual cores (Figure S6, supplement) was plotted as function of the respective oxygen concentrations (Figure IV 7). Oxygen concentrations in all cores varied between 0 µmol l^{-1} (C1 and Dun3) and 150 µmol l^{-1} in Dun1 on day 8. These variations are driven by the supply of oxygen from the reservoir via the throughflow, invasion of oxygen into the cores along the joints of the stirring heads and oxygen consumption in bottom waters as well as in the sediments. The reservoir oxygen concentrations slightly varied as a complete deoxygenation was technically not possible, and minor oxygen invasion during the transfer into the gastight reservoir bag was inevitable. H_2S was not measured in bottom waters or the reservoir over time. Nevertheless, a sulfidic smell in collected samples indicated its presence in several cores during phases with very low oxygen concentrations. Furthermore, H_2S was detected in bottom waters of

Dun3 during the initial micro-profiling and in Cal2 during the profile obtained just before the addition of substrates (Figure S7, supplement).

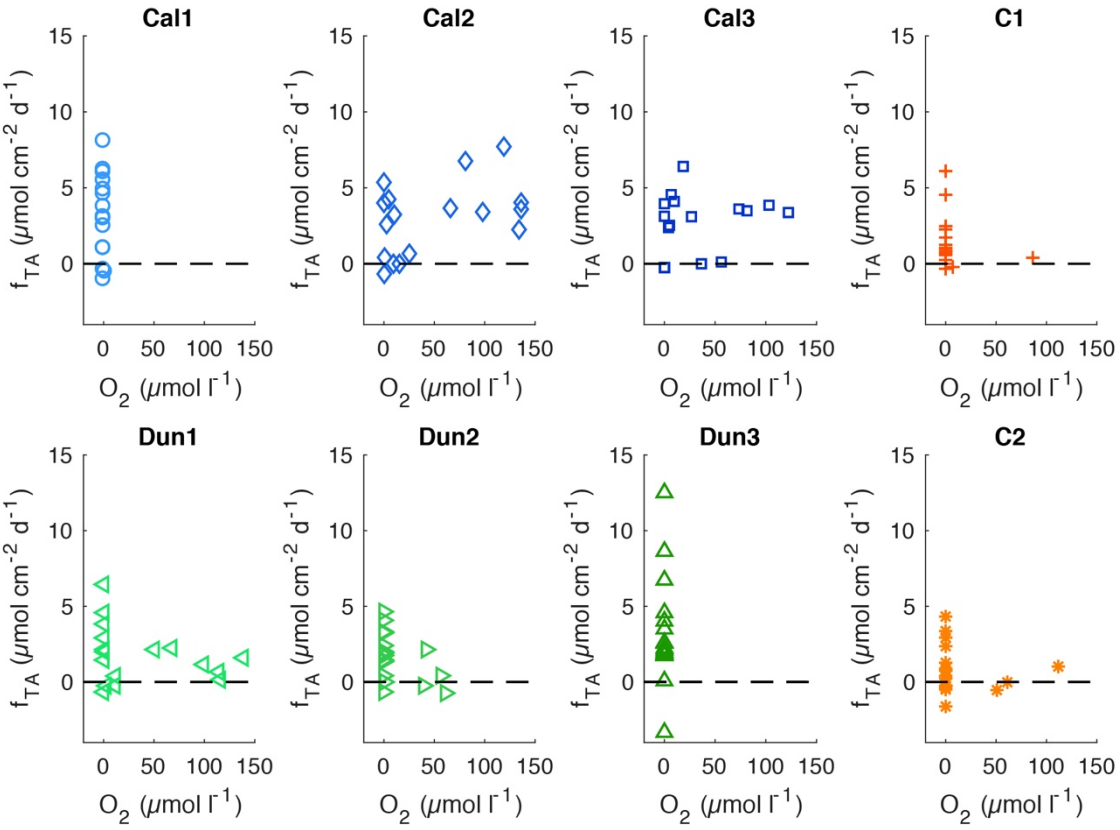

Figure IV 7: TA fluxes (fTA) over oxygen concentrations in bottom waters. Horizontal dashed line denotes fTA=0. Analytical precision (~0.5 µmol cm-2 d-1 for fTA and ~2µmol l-1 for O2) are not shown for clarity.

Additionally, a control measurement on day 5 revealed H_2S in the overlying water in cores Cal1, Dun2, Dun3 and C1 during a phase with very low oxygen concentrations in the reservoir and bottom waters (Figure IV 4). Increased TA fluxes during this anoxic phase together with the increased TA concentrations in Dun3 before addition of substrates suggests that during anoxic phases, as soon as the available oxygen had been completely consumed, reduced species such as H_2S were released into the bottom waters, and thus contributed to TA. The reoxidation of these species during phases with higher oxygen availability subsequently consumed TA (Figure IV 7). During phases with higher oxygen content in bottom waters, considerable TA fluxes were only observed in calcite and to a lesser degree in dunite amended cores. In most other cores, higher fluxes only occurred during anoxia.

IV.4.3. Usability of the carbonate system for assessment of enhanced weathering

The most important limitation for interpreting the bottom water carbonate system is the interpolation of pH values between the three obtained pH profiles (see section 3.1). The consequence is that possible pH changes due to temporal TA changes (Figure IV 1) are not considered. It is, hence, possible that the pCO_2 and DIC values (Figures IV 5a,b) were lower between day 0 and day 5 in cores where TA was presumably released from the sediment due to very low oxygen concentrations, whereas Ω_{Cal} values were higher (Figure IV 5c). This hypothesis is underpinned by the fact that the calculated DIC values increased in all cores

during that phase and remained elevated on that higher level in calcite treated cores whereas they decreased in the dunite treated and control cores. The decrease of DIC in dunite treated cores is difficult to reasonably explain by known chemical processes, since the reservoir as well as the cores were very limited in exchange with ambient air. Therefore, the phase between day 0 and day 7 will not be considered in further discussions. In contrast, the calculated bottom water carbonate system properties are more reliable towards the end of the experiment and less influenced by errors induced due to interpolated pH values. Furthermore, in a steady state situation, as reflected in TA concentrations and fluxes (Figure IV 1b), the entire carbonate system should be relatively constant as the reservoir and sedimentary fluxes are the only sources for DIC.

The low bottom water pCO_2 (Figure IV 5a) and the corresponding elevated DIC in calcite treated cores suggest contribution of DIC via $CaCO_3$ dissolution and a subsequent conversion of dissolved CO_2 to HCO_3^-. The most important indicator for calcite dissolution is the Ω_{Cal}, especially in the calcite treated cores. Despite the fact that the interpolated pH values might lead to an underestimation of Ω_{Cal} values between day 0 to day 5, the final values of ~0.94 (Figure IV 5c) suggest that in these cores the bottom waters remained corrosive throughout the experiment, which is important for evaluating the dissolution kinetics and mechanisms in this study.

IV.4.4. Evaluation of enhanced and natural $CaCO_3$ weathering

Despite the aforementioned uncertainties associated with the calculated carbonate system properties over time, the development of a steady state in the cores towards the end of the experiment implies that it is reasonable to focus on the last five days of the experiment to disentangle natural and enhanced weathering. For these days, sedimentary fluxes of corresponding weathering products (TA, Ca and Si) were averaged and compared (Table IV 2).

Table IV 6: TA, Ca and Si fluxes in different cores averaged for different treatments over the last 5 days of the experiment. Errors for dunite and calcite represent standard deviation (SD) between averages of each treatment. Since for the control experiment, only two cores were used, errors indicate the deviation of each core from the average. $\Delta F_{TA}/\Delta F_i$ ratios indicate ratios between flux differences between treatments and the control experiment.

	F_{TA}	F_{Ca}	F_{Si}	$\Delta F_{TA}/\Delta F_{Ca}$	$\Delta F_{TA}/\Delta F_{Si}$
Treatment	**µmol cm^{-2} d^{-1}**	**µmol cm^{-2} d^{-1}**	**µmol cm^{-2} d^{-1}**		
Calcite:	3.69±1.15	1.24±0.36	0.33±0.08	2.60	-294.1
Dunite:	1.87±0.26	0.15±0.54	0.45±0.09	28.1	10.2
Control:	0.75±0.34	0.11±0.22	0.34±0.08		

If TA is generated via $CaCO_3$ dissolution, the ratio of F_{TA}:F_{Ca} is expected to be 2:1 (Equation IV2). In the calcite treated cores the uncorrected ratio was ~2.97:1 (not shown in Table IV 2). This ratio is higher than the expected ratio, since it results from a combination of natural and enhanced weathering as well as TA fluxes that derive from metabolic processes. The natural background fluxes were considered by subtracting TA and Ca fluxes of the untreated control cores from the cores with mineral addition (ΔF_{TA} = F_{TA} treated core – F_{TA} (control), ΔF_{Ca} = F_{Ca} (treated core) – F_{Ca} (control), likewise for ΔF_{Si}), resulting in a corrected ratio of $\Delta F_{TA}/\Delta F_{Ca}$ = 2.60:1 (Tab. 2). The remaining excess TA indicates that an additional TA flux of ~1.21 µmol d^{-1} cm^{-2} was possibly not directly driven by $CaCO_3$ dissolution. Thus, it is important to understand

potential mechanisms that can lead to these elevated TA fluxes. In a previous study investigating weathering on sediments from the same location under fully oxic conditions (Fuhr et al. 2023), similar excess TA fluxes were possibly driven by microbial metabolism, which could, in principle, also explain additional TA fluxes from the sediment in cores Cal2 and Cal3. At the same time, these two cores also showed enhanced Ca^{2+} pore water concentrations in the upper 3 – 4 cm of the sediment (Figure S4, supplement). This elevation is not visible in pore water TA values of the same cores (Figure S4, supplement). It may be possible that the higher diffusion coefficient of HCO_3^- compared to Ca^{2+} (Boudreau, 1997), caused HCO_3^- to diffuse out of the very upper sediment before Ca^{2+}, as proposed by Fuhr et al. (2023). The difference between the excess TA flux observed in controls (~0.53 μmol d^{-1} cm^{-2}) and calcite treated cores (~1.21 μmol d^{-1} cm^{-2}) is ~0.68 μmol d^{-1} cm^{-2}. The depth-integrated excess dissolved Ca^{2+} in the upper pore water of these cores (Figure S4, supplement) is ~1.1 μmol cm^{-2}, which would be an equivalent of ~2.2 μmol cm^{-2} of TA. Given that these values were obtained over the last five days of the experiment, this diffusive time lag would explain an additional ~0.43 μmol d^{-1} cm^{-2} TA flux and therefore a significant fraction of the elevated TA:Ca ratio.

With regards to Ω_{Cal} profiles (Figure S5, supplement), the upper millimeters of the incubated cores were much less undersaturated with respect to calcite than those previously incubated under oxic conditions (Fuhr et al. 2023). Hence, dissolution within the sediment is unlikely to significantly contribute to calcite weathering. This, together with Ω_{cal} values in bottom waters (Figure IV 5c), implies that the driver for calcite dissolution under hypoxic to anoxic conditions is the corrosive bottom water. This hypothesis is corroborated by the very low Ca^{2+} fluxes in dunite treated and control cores (Figure IV 3b, Table IV 2), despite TIC contents of 3 – 5 % in the sediment solid phase (Figure IV 6).

With this weathering mechanism in mind, it is reasonable to use only Ca^{2+} concentrations and fluxes to quantify enhanced $CaCO_3$ dissolution and not both TA and Ca^{2+} as proposed by Fuhr et al. (2023) for oxic conditions. This approach avoids uncertainties induced by potential natural benthic weathering and other processes that may have induced additional TA fluxes. The enhanced Ca^{2+} flux and thus the rate of enhanced weathering (R_{ew}) can then be described as:

$$R_{ew} = (F_{Ca(Cal)} - F_{Ca(C)}) \quad \text{(IV6)}$$

where $F_{Ca(Cal)}$ is the calculated average flux in the calcite treated core and $F_{Ca(C)}$ is the calculated average flux in the control cores.

This calculation leads to an enhanced Ca flux and R_{ew} of 1.12±0.40 μmol cm^{-2} d^{-1} in the calcite treated cores. Based on this number and the amount of $CaCO_3$, it is now possible to estimate a first order dissolution rate constant (k_r) following:

$$k_{rCa} = \frac{R_{diss}}{A_{Cal}} \quad \text{(IV7)}$$

where R_{diss} is the dissolution rate over the entire surface of the sediment of one core ($R_{Diss} = R_{ew} \times$ sediment surface area) and A_{Cal} is the reactive surface of the calcite added on the sediment (BET-surf., Table1).

This leads to a rate constant k_{rCa} of 0.0025±0.0008 μmol cm^2 d^{-1} and subsequently to a $Log_{10}(k_{rCa})$ of -13.54±0.12 mol cm^{-2} s^{-1} for a mean Ω_{Cal} value of 0.9 (Fig. 5C). These values are in line with values reported by Naviaux et al. (2019) of -13.5±0.4 for $0.8<\Omega_{Cal}<1$ for in situ dissolution in the North Pacific Ocean. The conformity of these rate constants estimates implies that the kinetic constant and rate law for calcite

dissolution assessed in previous studies can be employed to calculate and simulate the dissolution rates of calcite added to Baltic Sea surface sediments that are exposed to undersaturated bottom waters.

IV.4.5. Assessment of olivine dissolution rates and kinetics

The high olivine content of over 90% in dunite (Hochstetter, 1859), justifies the assumption that olivine dissolution is representative for dunite dissolution. The dunite dissolution rate can be described as a function of temperature and pH (Rimstidt et al., 2012).

The high Mg^{2+} content in Baltic Sea water (~36±0.72 mmol l^{-1}) excludes its use as a proxy for olivine dissolution due to the analytical resolution. Thus, excess TA and/or dissolved Si might be reasonable proxies.

In all cores, background fluxes of Si were observed, which are presumably induced by diatom dissolution (Dale et al., 2021; Fuhr et al., 2023; Gasiūnaitė et al., 2005; Rickert, 2000). As performed for calcite treated cores, these background fluxes for both TA and Si were subtracted from the average fluxes in the dunite treated cores (Table IV 2). Additionally, the TA flux induced by $CaCO_3$ dissolution was subtracted (twice F_{Ca}). This led to a residual F_{TA}:F_{Si} ratio of 7.52. Following Equation IV1, this ratio should be 4 if the olivine dissolution was the only source of excess TA in dunite treated cores. This suggests that either ~0.39 µmol d^{-1} cm^{-2} of additional TA was released from the sediments, or that the overall stoichiometry of the dissolution process was altered due to either secondary mineral formation (Fuhr et al., 2022) or incongruent weathering (e.g. preferential release of Si over Mg or vice versa; Montserrat et al., 2017). The latter cannot be assessed in the frame of this study and will therefore be accepted as a possible explanation, but not discussed further. The formation of secondary minerals would explain lower dissolved Si fluxes, but at the same time also diminished TA fluxes (Fuhr et al., 2022). Additionally, results from studies on olivine dissolution in an open system (Flipkens et al., 2023) suggest that even when grains are not in suspension, as in the present study, and in higher saline water, the formation of secondary minerals is very unlikely to occur. Hence, it can be assumed that the altered F_{TA}:F_{Si} ratios derived from additional sedimentary TA fluxes are not linked to olivine weathering or $CaCO_3$ dissolution, but rather sedimentary fluxes of reduced species (see section IV.4.2)

With these assumptions in mind, the dissolution kinetics of olivine can be estimated following equations 6 and 7, with Si as a candidate proxy, assuming congruent weathering. Considering the amount and geometric surface area of the added dunite (Table IV 1), the first order rate constant for olivine dissolution can be calculated by normalizing the mean observed Si release rate over the last 5 days of the incubations (R_{Diss} = 7.17x10^{-11} to 1.48x10^{-10} mol s^{-1}) with the available dunite surface area (0.574 m^2, Equation IV7). The result is a k_{rSi} of 1.822·10^{-10} mol m^{-2} s^{-1} and subsequent $Log_{10}(k_{rSi})$ of -9.76±0.16 (-9.90 < $Log_{10}(k_{rSi})$ < -9.59). This value is close to values suggested by Rimstidt et al. (2012) whose rate law yields $Log_{10}(k_{rSi})$ = -9.96 for the temperature and pH values prevailing during our experiments (12.5°C, pH = 7.44). The slightly higher observed values may result from the calculations of the reactive surface or enhanced dissolution along highly reactive sights on the grains (Fuhr et al., 2022). Alternatively, the non-dunite related Si fluxes might have been slightly higher in dunite treated cores than in the control cores that were employed to calculate excess fluxes. Still, the conformity of k_{rSi} values suggests that the sedimentary excess Si flux largely derives from dunite (olivine) dissolution and that the kinetic constant and rate law for dunite dissolution assessed in previous studies (Rimstidt et al. 2012) can be employed to calculate and simulate the dissolution rates of dunite added to Baltic Sea surface sediments.

IV.4.6. Comparison of different dissolution mechanisms and materials

The evaluation of enhanced fluxes and the fate of the added substrates in this study has revealed that during anoxic to hypoxic phases the added alkaline minerals remained directly on the sediment surface due to minimal bioturbation and are dissolved by undersaturated bottom waters. Under oxic conditions (Fuhr et al. 2023), the substrates were quickly worked into the sediment by bioturbation such that dissolution was

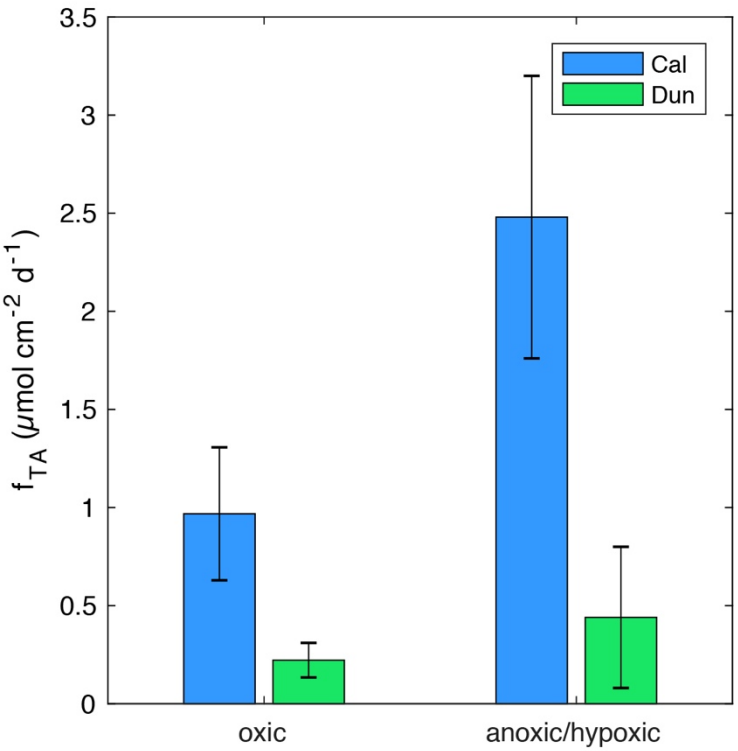

Figure IV 8: Comparison of enhanced fluxes under oxic (Fuhr et al., 2023) and anoxic to hypoxic conditions (this study) in calcite (blue) and dunite (green) treated cores. Fluxes under anoxic/hypoxic conditions were calculated based on excess Ca and Si fluxes. For

governed by intra-sedimentary processes and the resulting chemical conditions of the pore waters. Dissolution under oxic conditions appears to be slower as the transport of weathering products is driven by diffusion, whereas dissolution on the sediment implies a fast removal of weathering products directly to the bottom water. Furthermore, intra-sedimentary dissolution is only possible in the zone where Ω_{Cal} values fall below 1 (Fuhr et al., 2023). When the added material is worked into the sediment, it might not be completely exposed to corrosive pore waters. In contrast, the presented results suggest that minerals located on top of the sediment and exposed to corrosive bottom waters are more likely to completely dissolve. These differences lead to excess TA fluxes (Figure IV 8) that were ~2.5 times higher under anoxic to hypoxic conditions (2.48 ± 1.15 µmol cm^{-2}d^{-1}) compared to oxic bottom waters (0.968 ± 0.096 µmol cm^{-2}d^{-1}, Fuhr et al., 2023) in calcite treated cores.

At the same time, the enhanced TA fluxes induced by the materials are different. Despite the fact that olivine weathering is 4 times more efficient with regards to TA release compared to calcite weathering (Equations 1,2), the actual TA fluxes were 4.4 (oxic) to 5.6 (anoxic/hypoxic) times higher in calcite treated

cores than those in the dunite treatments. The reason for these large differences is based on the different dissolution kinetics of both materials. Given that the average grainsize of the applied dunite was much smaller than that of the added calcite (Table IV 1) and that the temperature of 12.5 °C constitutes the uppermost temperature that can be expected in the natural system at Boknis Eck (Melzner et al., 2013), this raises the question whether usage of olivine as a material for EBW is sensible in the Baltic Sea. It is possible, though, that under the confined laboratory conditions the benthic "weathering engine" (Meysman and Montserrat, 2017) was not as efficient as it might be under natural conditions. Nevertheless, these differences in condition and material-based efficiency are crucial findings of this study. They suggest that calcite addition is a more efficient method of EBW than dunite amendment for most seafloor areas in the Baltic Sea.

IV.4.7. Implications for field and modeling applications

In combination with recently investigated EBW under oxic conditions (Fuhr et al., 2023), it becomes apparent that in the relatively cold Baltic Sea, calcite addition leads to significant excess TA fluxes which makes it the candidate material for OAE in this region.

Based on the assessment of different weathering mechanisms and the subsequently much higher excess TA fluxes under anoxic to hypoxic conditions, the ideal timing for addition of substrates for enhanced weathering in Boknis Eck would probably be at the beginning of anoxic to hypoxic phases. This would maximize the time that the added material is exposed to corrosive bottom waters and maximize weathering. Based on long-term observations in Boknis Eck (Melzner et al., 2013) the best time for addition would therefore be between June and early September, depending on the onset of anoxia.

Furthermore, the results of the present study reveal that under anoxic to hypoxic conditions the weathering of calcite and dunite can be traced and quantified based on dissolved Ca and Si, respectively. The concentration increase for both species was high enough to be detected and distinguishable from the background flux despite the higher flow rate in this experiment compared to the previous experiments carried out by Fuhr et al. (2023). This is also due to the fact that under anoxic to hypoxic conditions, limited macrofaunal activity allows natural and enhanced fluxes of weathering products to be more easily distinguished. As a consequence, these conditions would facilitate the monitoring during a field application for example via benthic flux chambers.

The highest TA fluxes were observed during highly anoxic periods of the experiment but were not accompanied by Ca or Si fluxes which suggests that during these strictly anoxic phases high TA background fluxes may increase pH values and thus reduce or, in the case of calcite, possibly inhibit dissolution. At the same, in an open natural system, the dilution and dispersal of the released TA is likely much larger than in laboratory incubations. Combined with the high concentrations of metabolically formed CO_2, this may lead to seasonal and possibly persistent undersaturation with respect to calcite in strictly anoxic basins (Lass and Matthäus, 2008, Lencina Avila and Rehder, pers. communication). This would enhance the total area of sediments suitable for enhanced benthic weathering in the Baltic Sea (Carman and Cederwall, 2001).

An important finding of this study is the fact that the first order rate constants derived from sedimentary fluxes of dissolved Ca and Si were very close to values that were obtained in other laboratory and field studies (Naviaux et al., 2019; Rimstidt et al., 2012). This implies that these kinetic constants and the corresponding rate laws can be employed to simulate EBW and investigate the uptake of atmospheric CO_2 induced by OAE in the Baltic Sea and presumably other anoxic to hypoxic ocean basins.

IV.5. Summary, conclusion and outlook

The present study investigates EBW of calcite and dunite on organic rich sediments from Boknis Eck in the Eckernförde Bay covered by CO_2 enriched and de-oxygenated bottom waters, to assess the potential of these minerals for alkalinity enhancement and thus mCDR. For this purpose, sediment cores were amended with calcite and dunite and subsequently incubated for 19 days. The bottom water in the cores was subjected to a constant throughflow from a gas tight reservoir with deoxygenated Baltic Sea water with a defined pCO_2. The addition of both materials led to an increase on weathering products such as TA, dissolved Ca and dissolved Si compared to untreated control experiments. These fluxes could be attributed to different sedimentary processes and thus the enhanced fluxes identified and quantified. The first order rate constants that were calculated based on these enhanced fluxes fit very well to the rate constants and corresponding rate laws previously published for calcite and olivine dissolution which underlines the inference that the enhanced fluxes derive from the dissolution of added calcite dunite (olivine) directly at the sediment-water interface in contact with undersaturated bottom waters.

The fact that excess TA fluxes were ~3 times higher under anoxic to hypoxic conditions compared to oxic bottom waters, allows narrowing down the ideal timing for a possible application of especially calcite on seasonally hypoxic sediments of the Baltic Sea. A highlight of this study is the congruence of observed and previously published dissolution rate constants which underpins the usability of these constants for modelling approaches towards large scale assessment of EBW as a climate change mitigation measure.

The results of this study suggest that benthic weathering of dunite and calcite can lead to significantly increased TA fluxes with higher efficiencies observed for calcite. The latter is therefore the candidate material for EBW on organic rich sediments in seasonally anoxic to hypoxic regions in the Baltic Sea. Despite the fact that biohazardous elements such as nickel were below detection limit in both bottom and pore waters in this study, more applied research using larger benthocosms or in situ field experiments will be needed to exclude negative side effects of dunite addition on the fragile ecosystem in the Baltic Sea. Such studies would also augment the understanding of natural and enhanced weathering in a close-to-natural system compared to the laboratory conditions under which these processes were investigated in this study.

Data availability statement (IV)

The original contributions presented in the study are included in the article and supplementary files Further inquiries can be directed to the corresponding author.

Author Contributions (IV)

SG designed the study, MF conducted the experiment and wrote the manuscript, HK helped with pH measurements, SS supervised micro profiling and data logging, AD advised and supported lab procedures, KW helped discussions, MS helped with the experimental set-up and sensor measurements, CD helped with technical details for the experimental set-up, TS supported discussions, JK provided grain size distributions. All authors contributed to the article and approved the submitted version.

Funding (IV)

This study was funded by the Bundesministerium für Bildung und Forschung (BMBF) (Project RETAKE, granted to SG) in the framework of the Deutsche Allianz für Meeresforschung (DAM) mission "CDRmare".

Acknowledgements (IV)

We would like to thank Anke Bleyer, Bettina Domeyer and Regina Surberg for their help with technical and analytical procedures in the GEOMAR laboratory. Additionally, we thank the crew of FK Littorina for their support during recovery of sediment cores.

References (IV)

Béarat, H., J. McKelvy, M., V. G. Chizmeshya, A., Gormley, D., Nunez, R., W. Carpenter, R., Squires, K., H. Wolf, G., 2006. Carbon Sequestration via Aqueous Olivine Mineral Carbonation: Role of Passivating Layer Formation. Environ. Sci. & Technol. 40, 4802–4808. https://doi.org/10.1021/es0523340

Beuttler, C., Charles, L., Wurzbacher, J., 2019. The Role of Direct Air Capture in Mitigation of Anthropogenic Greenhouse Gas Emissions. Front. Clim. https://doi.org/10.3389/fclim.2019.00010

Borawska, Z., Szymczycha, B., Silberberger, M.J., Koziorowska-Makuch, K., Szczepanek, M., Kędra, M., 2022. Benthic fluxes of dissolved silica are an important component of the marine Si cycle in the coastal zone. Estuar. Coast. Shelf Sci. 273, 107880. https://doi.org/https://doi.org/10.1016/j.ecss.2022.107880

Boudreau, B.P., 1997. Diagenetic models and their implementation.Springer, Berlin, Germany.

Brunauer, S., Emmett, P.H., Teller, E., 1938. Adsorption of Gases in Multimolecular Layers. J. Am. Chem. Soc. 60, 309–319. https://doi.org/10.1021/ja01269a023

Burton, E.A., Walter, L.M., 1987. Relative precipitation rates of aragonite and Mg calcite from seawater: Temperature or carbonate ion control? Geology 15, 111–114. https://doi.org/10.1130/0091-7613(1987)15<111:RPROAA>2.0.CO;2

Campbell, J.S., Foteinis, S., Furey, V., Hawrot, O., Pike, D., Aeschlimann, S., Maesano, C.N., Reginato, P.L., Goodwin, D.R., Looger, L.L., Boyden, E.S., Renforth, P., 2022. Geochemical Negative Emissions Technologies: Part I. Review. Front. Clim. 4:879133. https://doi.org/10.3389/fclim.2022.879133

Carman, R., Cederwall, H., 2001. Sediments and Macrofauna in the Baltic Sea — Characteristics, Nutrient Contents and Distribution BT - A Systems Analysis of the Baltic Sea, in: Wulff, F. V, Rahm, L.A., Larsson, P. (Eds.), . Springer Berlin Heidelberg, Berlin, Heidelberg, pp. 289–327. https://doi.org/10.1007/978-3-662-04453-7_11

Caserini, S., Cappello, G., Righi, D., Raos, G., Campo, F., De Marco, S., Renforth, P., Varliero, S., Grosso, M., 2021. Buffered accelerated weathering of limestone for storing CO2: Chemical background. Int. J. Greenh. Gas Control 112, 103517. https://doi.org/10.1016/j.ijggc.2021.103517

Dale, A.W., Paul, K.M., Clemens, D., Scholz, F., Schroller-Lomnitz, U., Wallmann, K., Geilert, S., Hensen, C., Plass, A., Liebetrau, V., Grasse, P., Sommer, S., 2021. Recycling and Burial of Biogenic Silica in an Open Margin Oxygen Minimum Zone. Global Biogeochem. Cycles 35, e2020GB006583. https://doi.org/10.1029/2020GB006583

Dale, A.W., Sommer, S., Bohlen, L., Treude, T., Bertics, V.J., Bange, H.W., Pfannkuche, O., Schorp, T., Mattsdotter, M., Wallmann, K., 2011. Rates and regulation of nitrogen cycling in seasonally hypoxic sediments during winter (Boknis Eck, SW Baltic Sea): Sensitivity to environmental variables. Estuar. Coast. Shelf Sci. 95, 14–28. https://doi.org/https://doi.org/10.1016/j.ecss.2011.05.016

Dale, A.W., Sommer, S., Ryabenko, E., Noffke, A., Bohlen, L., Wallmann, K., Stolpovsky, K., Greinert, J., Pfannkuche, O., 2014. Benthic nitrogen fluxes and fractionation of nitrate in the Mauritanian oxygen minimum zone (Eastern Tropical North Atlantic). Geochim. Cosmochim. Acta 134, 234–256. https://doi.org/10.1016/j.gca.2014.02.026

Dickson, A.G., 1993. The measurement of sea water pH. Mar. Chem. 44, 131–142. https://doi.org/10.1016/0304-4203(93)90198-W

E. King, H., Plümper, O., Putnis, A., 2010. Effect of Secondary Phase Formation on the Carbonation of Olivine. Environ. Sci. & Technol. 44, 6503–6509. https://doi.org/10.1021/es9038193

Fakhraee, M., Li, Z., Planavsky, N.J., Reinhard, C.T., 2023. A biogeochemical model of mineral-based ocean alkalinity enhancement: impacts on the biological pump and ocean carbon uptake. Environ. Res. Lett. 18, 44047. https://doi.org/10.1088/1748-9326/acc9d4

Feng, E.Y., Koeve, W., Keller, D.P., Oschlies, A., 2017. Model-Based Assessment of the CO2 Sequestration Potential of Coastal Ocean Alkalinization. Earth's Futur. 5, 1252–1266. https://doi.org/10.1002/2017EF000659

Flipkens, G., Blust, R., Town, R.M., 2021. Deriving Nickel (Ni(II)) and Chromium (Cr(III)) Based Environmentally Safe Olivine Guidelines for Coastal Enhanced Silicate Weathering. Environ. Sci. Technol. 55, 12362–12371. https://doi.org/10.1021/ACS.EST.1C02974/SUPPL_FILE/ES1C02974_SI_001.PDF

Flipkens, G., Fuhr, M., Fiers, G., Meysman, F.J.R., Town, R.M., Blust, R., 2023. Enhanced olivine dissolution in seawater through continuous grain collisions. Geochim. Cosmochim. Acta 359, 84–99. https://doi.org/https://doi.org/10.1016/j.gca.2023.09.002

Foteinis, S., Campbell, J.S., Renforth, P., 2023. Life Cycle Assessment of Coastal Enhanced Weathering for Carbon Dioxide Removal from Air. Environ. Sci. Technol. 57, 6169–6178. https://doi.org/10.1021/acs.est.2c08633

Fuhr, M., Geilert, S., Schmidt, M., Liebetrau, V., Vogt, C., Ledwig, B., Wallmann, K., 2022. Kinetics of Olivine Weathering in Seawater: An Experimental Study. Front. Clim. 4:831587. https://doi.org/10.3389/fclim.2022.831587

Fuhr, M., Wallmann, K., Dale, A.W., Diercks, I., Kalapurakkal, H.T., Schmidt, M., Sommer, S., Böhnke, S., Perner, M., Geilert, S., 2023. Disentangling artificial and natural benthic weathering in organic rich Baltic Sea sediments. Front. Clim. https://doi.org/10.3389/fclim.2023.1245580

Fuss, S., Lamb, W.F., Callaghan, M.W., Hilaire, J., Creutzig, F., Amann, T., Beringer, T., De Oliveira Garcia, W., Hartmann, J., Khanna, T., Luderer, G., Nemet, G.F., Rogelj, J., Smith, P., Vicente, J.V., Wilcox, J., Del Mar Zamora Dominguez, M., Minx, J.C., 2018. Negative emissions - Part 2: Costs, potentials and side effects. Environ. Res. Lett. 13. https://doi.org/10.1088/1748-9326/aabf9f

Gasiūnaitė, Z.R., Cardoso, A.C., Heiskanen, A.-S., Henriksen, P., Kauppila, P., Olenina, I., Pilkaitytė, R., Purina, I., Razinkovas, A., Sagert, S., Schubert, H., Wasmund, N., 2005. Seasonality of coastal phytoplankton in the Baltic Sea: Influence of salinity and eutrophication. Estuar. Coast. Shelf Sci. 65, 239–252. https://doi.org/https://doi.org/10.1016/j.ecss.2005.05.018

Griffioen, J., 2017. Enhanced weathering of olivine in seawater: The efficiency as revealed by thermodynamic scenario analysis. Sci. Total Environ. 575, 536–544. https://doi.org/10.1016/j.scitotenv.2016.09.008

Hartmann, J., Kempe, S., 2008. What is the maximum potential for CO 2 sequestration by "stimulated" weathering on the global scale? Naturwissenschaften 95, 1159–1164. https://doi.org/10.1007/s00114-008-0434-4

Hartmann, J., Suitner, N., Lim, C., Schneider, J., Marín-Samper, L., Arístegui, J., Renforth, P., Taucher, J., Riebesell, U., 2023. Stability of alkalinity in ocean alkalinity enhancement (OAE) approaches – consequences for durability of CO2 storage. Biogeosciences 20, 781–802. https://doi.org/10.5194/bg-20-781-2023

Hiscock, W.T., Millero, F.J., 2006. Alkalinity of the anoxic waters in the Western Black Sea. Deep Sea Res. Part II Top. Stud. Oceanogr. 53, 1787–1801. https://doi.org/https://doi.org/10.1016/j.dsr2.2006.05.020

Hochstetter, F. von, 1859. Lecture on the Geology of the Province of Nelson. New Zeal. Governemt Gaz. (Province Nelson) 7, 90–102.

Iizuka, A., Fujii, M., Yamasaki, A., Yanagisawa, Y., 2004. Development of a new CO2 sequestration process utilizing the carbonation of waste cement. Ind. Eng. Chem. Res. 43, 7880–7887. https://doi.org/10.1021/ie0496176

IPCC, 2021. Climate Change 2021: The Physical Science Basis. Contribution of Working Group I to the Sixth Assessment Report of the Intergovernmental Panel on Climate Change [Masson-Delmotte, V., P. Zhai, A. Pirani, S.L. Connors, C. Péan, S. Berger, N. Caud, Y. Chen, Cambridge University Press.

Ivanenkov, V.N., Lyakhin, Y.I., 1978. Determination of the alkalinity of seawater. Methods Hydrochem. Stud. Ocean 110–115.

Jeroschewski, P., Steuckart, C., Kühl, M., 1996. An Amperometric Microsensor for the Determination of H2S in Aquatic Environments. Anal. Chem. 68, 4351–4357. https://doi.org/10.1021/ac960091b

Kremer, D., Etzold, S., Boldt, J., Blaum, P., Hahn, K.M., Wotruba, H., Telle, R., 2019. Geological mapping and characterization of possible primary input materials for the mineral sequestration of carbon dioxide in Europe. Minerals 9. https://doi.org/10.3390/min9080485

Lackner, K.S., 2003. A guide to CO2 sequestration. Science (80-.). 300, 1677–1678. https://doi.org/10.1126/science.1079033

Lal, R., 2004. Soil carbon sequestration to mitigate climate change. Geoderma. https://doi.org/10.1016/j.geoderma.2004.01.032

Lass, H.U., Matthäus, W., 2008. General Oceanography of the Baltic Sea. State Evol. Balt. Sea, 1952-2005 A Detail. 50-Year Surv. Meteorol. Clim. Physics, Chem. Biol. Mar. Environ. 5–43. https://doi.org/10.1002/9780470283134.ch2

Lein, A.Y., 2004. Authigenic Carbonate Formation in the Ocean. Lithol. Miner. Resour. 39, 1–30. https://doi.org/10.1023/B:LIMI.0000010767.52720.8f

Meier, H.E.M., Eilola, K., Almroth-Rosell, E., Schimanke, S., Kniebusch, M., Höglund, A., Pemberton, P., Liu, Y., Väli, G., Saraiva, S., 2019. Disentangling the impact of nutrient load and climate changes on

Baltic Sea hypoxia and eutrophication since 1850. Clim. Dyn. 53, 1145–1166. https://doi.org/10.1007/s00382-018-4296-y

Melzner, F., Thomsen, J., Koeve, W., Oschlies, A., Gutowska, M.A., Bange, H.W., Hansen, H.P., Körtzinger, A., 2013. Future ocean acidification will be amplified by hypoxia in coastal habitats. Mar. Biol. 160, 1875–1888. https://doi.org/10.1007/s00227-012-1954-1

Meysman, F.J.R., Montserrat, F., 2017. Negative CO2 emissions via enhanced silicate weathering in coastal environments. Biol. Lett. 13, 20160905. https://doi.org/10.1098/rsbl.2016.0905

Millero, F.J., Plese, T., Fernandez, M., 1988. The dissociation of hydrogen sulfide in seawater. Limnol. Oceanogr. 33, 269–274. https://doi.org/10.4319/lo.1988.33.2.0269

Montserrat, F., Renforth, P., Hartmann, J., Leermakers, M., Knops, P., Meysman, F.J.R., 2017. Olivine Dissolution in Seawater: Implications for CO2 Sequestration through Enhanced Weathering in Coastal Environments. Environ. Sci. Technol. 51, 3960–3972. https://doi.org/10.1021/acs.est.6b05942

Moras, C.A., Bach, L.T., Cyronak, T., Joannes-Boyau, R., Schulz, K.G., 2022. Ocean alkalinity enhancement – avoiding runaway CaCO3 precipitation during quick and hydrated lime dissolution. Biogeosciences 19, 3537–3557. https://doi.org/10.5194/bg-19-3537-2022

Müller, J.D., Bastkowski, F., Sander, B., Seitz, S., Turner, D.R., Dickson, A.G., Rehder, G., 2018. Metrology for pH measurements in brackish waters-part 1: Extending electrochemical pHT measurements of TRIS buffers to salinities 5-20. Front. Mar. Sci. 5, 1–12. https://doi.org/10.3389/fmars.2018.00176

Naviaux, J.D., Subhas, A. V, Dong, S., Rollins, N.E., Liu, X., Byrne, R.H., Berelson, W.M., Adkins, J.F., 2019. Calcite dissolution rates in seawater: Lab vs. in-situ measurements and inhibition by organic matter. Mar. Chem. 215, 103684. https://doi.org/https://doi.org/10.1016/j.marchem.2019.103684

Nilsson, M.M., Kononets, M., Ekeroth, N., Viktorsson, L., Hylén, A., Sommer, S., Pfannkuche, O., Almroth-Rosell, E., Atamanchuk, D., Andersson, J.H., Roos, P., Tengberg, A., Hall, P.O.J., 2019. Organic carbon recycling in Baltic Sea sediments – An integrated estimate on the system scale based on in situ measurements. Mar. Chem. 209, 81–93. https://doi.org/10.1016/j.marchem.2018.11.004

Oelkers, E.H., 2001. An experimental study of forsterite dissolution rates as a function of temperature and aqueous Mg and Si concentrations. Chem. Geol. 175, 485–494. https://doi.org/10.1016/S0009-2541(00)00352-1

Palandri, J.L., Kharaka, Y.K., 2004. A compilation of rate parameters of water-mineral interaction kinetics for application to geochemical modeling, USGS Open File Report. https://doi.org/10.3133/ofr20041068

Pratt, K.W., 2014. Measurement of pHT values of Tris buffers in artificial seawater at varying mole ratios of Tris: Tris·HCl. Mar. Chem. 162, 89–95. https://doi.org/10.1016/j.marchem.2014.03.003

Renforth, P., Henderson, G., 2017. Assessing ocean alkalinity for carbon sequestration. Rev. Geophys. 55, 636–674. https://doi.org/10.1002/2016RG000533

Rickert, D., 2000. Dissolution kinetics of biogenic silica in marine environments= Lösungskinetik von biogenem Opal in marinen Systemen. Berichte zur Polarforsch. (Reports Polar Res. 351.

Rigopoulos, I., Harrison, A.L., Delimitis, A., Ioannou, I., Efstathiou, A.M., Kyratsi, T., Oelkers, E.H., 2018. Carbon sequestration via enhanced weathering of peridotites and basalts in seawater. Appl. Geochemistry 91, 197–207. https://doi.org/10.1016/j.apgeochem.2017.11.001

Rimstidt, J.D., Brantley, S.L., Olsen, A.A., 2012. Systematic review of forsterite dissolution rate data. Geochim. Cosmochim. Acta 99, 159–178. https://doi.org/10.1016/j.gca.2012.09.019

Sternbeck, J., Sohlenius, G., 1997. Authigenic sulfide and carbonate mineral formation in holocene sediments of the baltic sea. Chem. Geol. 135, 55–73. https://doi.org/10.1016/S0009-2541(96)00104-0

Subhas, A. V, Rollins, N.E., Berelson, W.M., Dong, S., Erez, J., Adkins, J.F., 2015. A novel determination of calcite dissolution kinetics in seawater. Geochim. Cosmochim. Acta 170, 51–68. https://doi.org/https://doi.org/10.1016/j.gca.2015.08.011

Wallmann, K., Diesing, M., Scholz, F., Rehder, G., Dale, A.W., Fuhr, M., Suess, E., 2022. Erosion of carbonate-bearing sedimentary rocks may close the alkalinity budget of the Baltic Sea and support atmospheric CO2 uptake in coastal seas. Front. Mar. Sci. 9:968069. https://doi.org/10.3389/fmars.2022.968069

Walter, L.M., Morse, J.W., 1985. The dissolution kinetics of shallow marine carbonates in seawater: A laboratory study. Geochim. Cosmochim. Acta 49, 1503–1513. https://doi.org/https://doi.org/10.1016/0016-7037(85)90255-8

Zeebe, R.E., Wolf-Gladrow, D. (Eds.), 2001. Chapter 1 Equilibrium, in: CO2 in Seawater: Equilibrium, Kinetics, Isotopes, Elsevier Oceanography Series. Elsevier, pp. 1–84. https://doi.org/https://doi.org/10.1016/S0422-9894(01)80002-7

V. Calcite takes it all: Benthic weathering potential and costs of alkaline mineral addition to muddy shelf sediments

Michael Fuhr [a*], Andrew W. Dale [a], Klaus Wallmann [a], Rebecca Bährle [a], Habeeb Thanveer Kalapurakkal [a], Stefan Sommer [a], Timo Spiegel [a], Ryo Dobashi [c], Frank Melzner [a], Mark Schmidt [a], Sonja Geilert [b]

[a] GEOMAR Helmholtz Centre for Ocean Research Kiel, Wischhofstr. 1-3, 24148 Kiel, Germany
[b] Department of Earth Sciences, Utrecht University, Utrecht, The Netherlands
[c] Department of Oceanography, University of Hawai'i at Manoa, Honolulu, USA

* Corresponding author at: GEOMAR Helmholtz Centre for Ocean Research Kiel, Wischhofstr. 1-3, 24148 Kiel, Germany. Tel.: ++49 431 600 2888

Abstract

Recent studies have proposed calcite and dunite as possible alkaline materials for enhanced benthic weathering (EBW) in shallow depocenters of the Baltic Sea as a marine carbon dioxide removal (mCDR) strategy to limit global warming. In this study, new insights on calcite and dunite weathering from laboratory incubations and long-term benthocosm experiments are combined with a numerical box-model to assess the CO_2 uptake potential of mineral addition to organic rich sediments in the SW Baltic Sea. The results reveal that calcite has an up to 10-fold higher CO_2 uptake efficiency and is therefore the preferable material for EBW as a mCDR method, with costs per ton of sequestered CO_2 ranging between 82 € - 462€ for calcite and 558€ - 1920€ for dunite. These findings could be applicable to other areas in the Baltic Sea and also globally to sediments in the wider coastal shelf with similar geochemical properties.

V.1. Main text

Against the backdrop of increasing atmospheric carbon dioxide (CO_2) concentrations, a fast development towards net-zero emissions is urgently needed[1–4]. For achieving this goal, it is necessary to develop negative emissions technologies to account for residual emissions that cannot be avoided[5,6]. Aside from established methods, such as carbon capture and storage, the enhanced weathering of rocks in the ocean is gaining increasingly more attention, as the process consumes CO_2 via ocean alkalinity enhancement (OAE)[7–9].

Apart from highly reactive hydroxides, calcite (a calcium carbonate) and dunite (a mafic silicate rock that majorly consists of olivine[10]), have been invoked as possible materials for OAE[8,11–16]. Both materials consume protons upon dissolution, increasing total alkalinity (TA) and subsequently leading to an uptake of CO_2 in the water column and storage in the form of dissolved bicarbonate[17]. However, the dissolution of these materials in the water column is either chemically hindered due to oversaturation in the case of calcium carbonates or, in the case of olivine and dunite, not feasible due the slow dissolution kinetics[18,19].

A more promising method to achieve OAE, based on calcite or dunite, is enhanced benthic weathering (EBW). In this approach, the minerals are distributed directly on marine sediments, whereupon they are exposed to the 'benthic weathering engine'[12,20]. This describes a combination of benthic processes whereby particulate organic carbon (POC) is essentially degraded to CO2 thereby lowering the pH of the sedimentary porewaters. Bioturbation and bioirrigation enable oxygen to penetrate deeper into sediments,

stimulating POC degradation and thus CO2 production and acidification further. Besides microbes catalyzing these chemical reactions, invertebrates in- and digest sediment particles, where abrasion additionally contributes to mineral dissolution[12,20]. In the following, the combination of these processes will be referred to here as bioactivity.

The growing number of publications on marine carbon dioxide removal (mCDR) over the last years clearly indicates that science is rapidly advancing in this field[4]. Still, the majority of these studies are based on models, which use mineral dissolution rates derived from laboratory experiments that do not reflect natural conditions, which can alter the kinetics of mineral dissolution tremendously[21–24]. This study is the first to combine data from recent laboratory studies on EBW, where calcite and dunite were added to organic-rich sediments of the Baltic Sea[22,24] with results from long-term experiments (September 2022 – September 2023) in benthocosms – large plastic containers (~0.8 m^2) that are partly filled with sediments, with constant through-flow of Baltic Sea bottom water (Fig.1). The sediments were amended with calcite and dunite in triplicate. Three additional benthocosms were left unamended to serve as controls. These experiments elucidate the actual weathering behavior of calcite and dunite under conditions as close to the natural system as possible. These results are subsequently implemented in a 4-box numerical model to simulate the addition of calcite and dunite to a 25 km^2 application area in Eckernförde Bay (25 m water depth), a seasonally stratified and seasonally (~ late July – ~ early October) hypoxic to anoxic inlet in the southwestern Baltic Sea (Fig. 1). The model simulates the hydrological properties of this study area and calculates the additional CO_2 uptake from the atmosphere by EBW as well as the amount of calcite and dunite that needs to be added to achieve this uptake. Additionally, for both materials, efficiency and cost calculations were carried out to understand the overall efficiency and costing per ton of sequestered CO_2 for each source material. These results reveal that calcite is the more efficient candidate material for EBW as a mCDR method not only in the German part of the Baltic Sea, but also in any other marine system with similar geochemical properties.

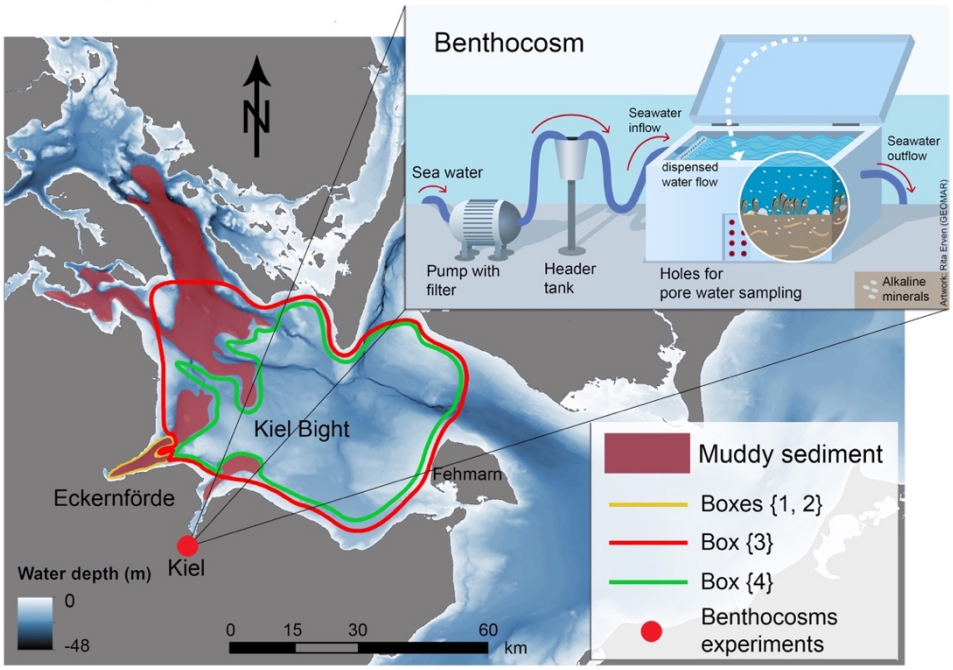

Figure V3: Map of the south western Baltic Sea. Blue shading indicates the bathymetry. Red areas denote the distribution of muddy sediments[42]. The adjacent sediment consists of gravel and sand with low organic carbon content. Yellow, red and green lines describe the approximate spatial extent of the boxes considered for the box-model (Additional data figure 1), where the yellow area is the area of application. The insert (upper right) shows a schematic sketch of the benthocosms used for the long-term experiment. Modified after Eisaman et al. (2023)[36].

V.1.1. Observed dissolution of calcite and dunite

The TA fluxes measured in mini-benthic chambers that were placed inside the benthocosms (see methods) follow a clear pattern for the different treatments (Fig. V2a). Within two weeks after the addition of alkaline minerals (0.36 g cm^{-2} with a mean grain radius of 5.58 µm for dunite and 0.22 g cm^{-2} with a mean grain radius of 19.39 µm for calcite), the TA fluxes increased in both treatment experiments from a background of 0.62±0.00 µmol cm^{-2} d^{-1} to 2.90±0.72 µmol cm^{-2} d^{-1} (calcite) and 1.66±0.36 µmol cm^{-2} d^{-1} (dunite). In contrast to dunite, the dissolution of calcite is strongly dependent on the saturation state of the aqueous phase[25,26]. The fact that calcite dissolved despite oversaturated bottom waters after two weeks (Fig. 2b), therefore, indicates that the material must have been worked into the sediment, where undersaturated pore waters or the benthic weathering engine might have fostered the dissolution[12,22]. Over the first 224 days of the experiment (until May 2023) the fluxes closely followed the change in temperature under well-oxygenated conditions (Figs. 2a,c). When oxygen concentrations in bottom waters declined (Fig. 2c), the TA fluxes in calcite treatments also decreased. This is likely a result of reduced bioactivity and a less oxidation in upper sediments, both of which would lead to lower dissolution rates. The undersaturation in porewaters in the upper 6 cm of sediment, expressed as a term ($Diss_{pot}$) that indicates the extent to which calcite can dissolve in porewaters[22] (see Methods), appears to be less critical over the same period (Fig. 2d). This is emphasized by the fact that in both other experiments (dunite treated and control), high $Diss_{Pot}$ values did not apparently induced measurable natural calcite dissolution. Furthermore, the dissolution rates calculated based on the TA fluxes are more temperature sensitive compared to previously published values for both materials[26,27](see supplementary Table S1). This suggests that the intra-sedimentary calcite dissolution is driven by a variety of oxygen- and temperature-dependent processes. Most likely, bioactivity, which depends on both factors, exacerbates abiotic mineral dissolution above that which is driven by the ambient pore water saturation state. This clearly substantiates the principle of the "benthic weathering engine"[12].

Since the material had already been worked into the sediment when the hypoxic phase in the benthocosms began, the fluxes were not as high as observed in previous studies under these conditions[24], where the material remained on top of the sediment. The TA fluxes induced by calcite addition during the oxic period were ~2 fold higher compared to dunite treated experiments (Fig. 2a). Overall, the TA fluxes induced by the addition of calcite and dunite are in good agreement with findings of prior studies on weathering on sediments from the same study area [22,24], given the difference in reactive surfaces of the added material. This, and the fact that the treatment with calcite and dunite was the only difference with respect to the controls, allows for the assumption that the increased TA flux compared to the control experiment resulted from the dissolution of the added alkaline minerals – despite the fact that corresponding cation fluxes (e.g. Ca^{2+}, Si) could not be resolved against the high background concentrations.

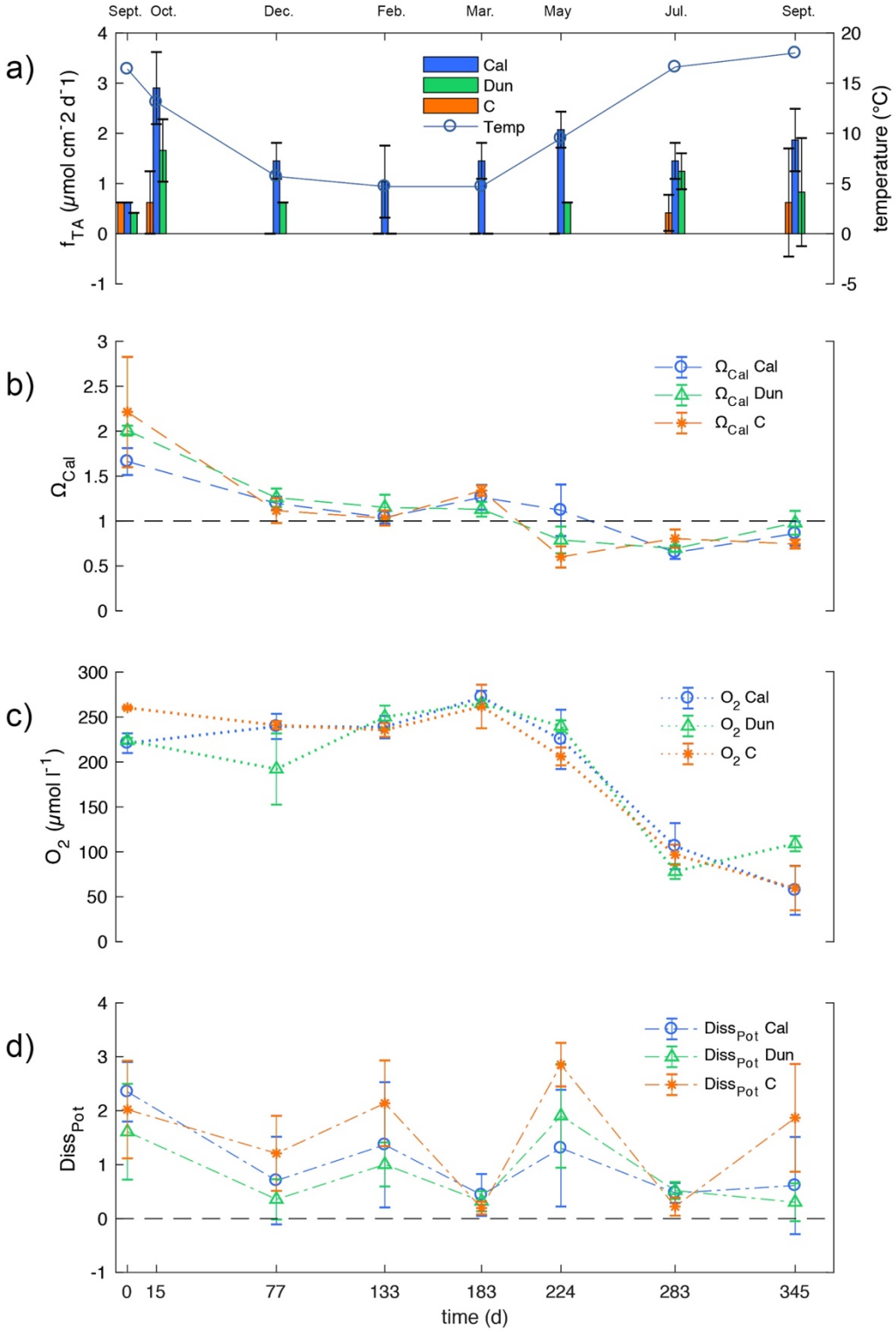

Figure V4: TA fluxes (bars, a) in comparison to temperature (curve, a), Ω_{Cal} (b), oxygen (c) $Diss_{pot}$ values (d) of bottom waters measured during the benthocosm experiment. Values at t=0 denote data obtained directly before the addition of alkaline materials. Cal denotes the calcite treatment, dun the dunite treatment and C the untreated control experiments. Ω_{Cal} is the saturation state of bottom waters with respect to calcite whereas $Diss_{pot}$ indicates the extent of calcite undersaturation in porewaters[19]. Error bars are reported as SD of the three replicas for each treatment. Several TA fluxes in the control and dunite-treated experiments were below detection limit (0.62 µmol cm^{-2} d^{-1}) and are therefore not shown in Fig. a. Sampling months are given at the top of the figure.

V.1.2. Modelled impact of the reactive surface area on the CO_2 uptake efficiency

For the assessment of additional CO_2 uptake induced by calcite and dunite addition to a 25 km^2 application site in Eckernförde Bay, the dissolution rates based on the benthocosm experiments and previous incubation experiments were used as inputs to a box model[22,24]. The model was run for 35 years with an annual mineral addition in autumn. The model considers two layers in the water column for Eckernförde Bay and the adjacent Kiel Bight (Fig. 1, Additional data figure 1) as well as dissolution of added alkaline materials on and within the sediment.

After 35 years, for both dunite and calcite, higher average annual uptake can be achieved via either increased addition of material or a higher reactive surface, implying a smaller grain size (Figs. 3 a,b). Note that for dunite the geometrical surface (A_{GEO}) was used, which is the theoretical surface if all grains were perfectly spherical, while for calcite the Brunauer-Emmett-Teller (BET)[28] surface is reported, which is the

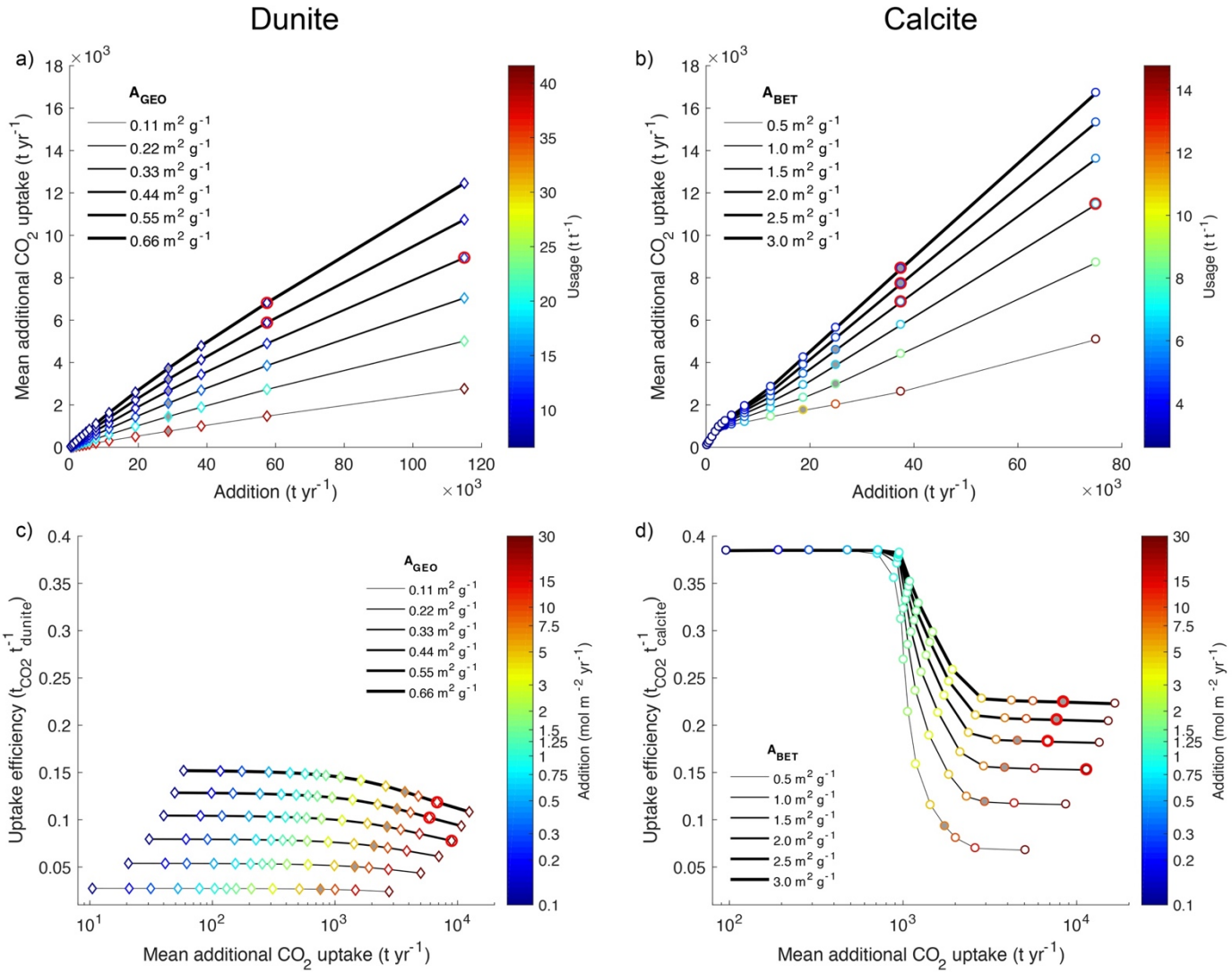

Figure V5: Mean additional CO_2 uptake per year (a,b) and uptake efficiency (c,d) for 30 years of dunite addition (a,c) and calcite addition (b,d) over an application area of 25 km^2. The width of the lines indicates the geometrical (dunite) and BET (calcite) surface area, respectively. Color codes of the symbols represent usage of material per ton of sequestered CO_2 (a,b) and the amount of material added in each model run (c,d). Grey filled symbols indicate the amount of added material, up to which experimentally derived dissolution kinetics are valid. Red circles indicate the maximum addition that can be applied before reprecipitation of calcite might compromise CO_2 uptake (see text).

actual surface of non-spherical grains (A_{BET}). The latter was ~4.55 times larger than the A_{GEO} for calcite grains. The ratio of uptake to addition is non-linear. For dunite, the additional uptake induced by higher additions decreases continuously for all grain sizes (Fig. 3a). For calcite, very low additions (up to ~2500 t yr^{-1}) lead to a fast-increasing uptake, regardless of the grain size. Afterwards, the additional uptake per ton of added material is smaller, linear and more dependent on the reactive surface area (Fig. 3b). The uptake efficiency, calculated as the total uptake in tons of CO_2 per ton of added material indicates that for both materials a higher mean annual uptake is achieved at the expense of lower uptake efficiency (Fig. 3c,d). This further requires a higher usage of material, that is, the amount of material needed to sequester 1 t of CO_2 (Fig. 3a,b).

Whilst the dependence of the efficiency of dunite weathering on the reactive surface and the amount of added material follows the expected trends, calcite dissolution shows a surprising behavior. The efficiency does not change significantly for low additions, and is also not affected by the BET surface of the added material up to a certain threshold. This pattern can be explained by the fact that in the model, calcite is added at the beginning of the anoxic phase, which occurs regularly in study area due to seasonal stratification of the water body[29–32]. Thus, in situ, the added substrate is unlikely to be directly worked into the sediment, as observed in the benthocosm experiment, but lies on the surface and dissolves at a rate depending on the bottom water saturation state[24] (Equation 3, methods). If the reactive surface is large, calcite dissolves quickly, and bottom waters in the model become oversaturated after a short time, which inhibits further dissolution. For smaller BET surface areas, the bottom waters remain undersaturated for a longer period of time, which leads to a longer phase of dissolution. Hence, the amount of calcite that dissolves before it is worked into the sediment depends solely on the time before oversaturation due to calcite dissolution is attained, rather than the physical properties of the added material.

These findings imply that the grain size range of added calcite material can be rather large in practice, which facilitates easier production and lowers costs. The precise amount of calcite that can dissolve in bottom waters before they reach supersaturation is dependent on the remineralization rate of particulate organic matter (POC) in bottom waters and surface sediments, which is the major source for CO_2 in bottom waters, and thus on the rate of primary production. Moreover, the water exchange rate with the adjacent sea and the upwelling rate determine the dilution of weathering products in bottom waters, and consequently the saturation state and the amount of calcite that can dissolve. In the model, mixing in the two larger Kiel Bight boxes reintroduces alkaline water into the smaller bottom water box (Additional data figure 1). This can lead to an overestimation of Ω_{Cal} values and thus diminish calcite dissolution. For this reason, a hydrologically more accurate model will be needed to assess the precise uptake threshold up to which EBW in the study area is highly efficient.

After the uptake threshold of ~1000 t yr^{-1}, dissolution takes place mainly within the sediment, as the majority of added calcite is worked into the sediment before it can fully dissolve in undersaturated bottom waters. Since the model does not consider changes in the saturation of pore waters induced by mineral dissolution, the rate does not change with larger calcite content in the sediment and thus the efficiency remains almost constant. The dissolution rates in sediments, however, may be higher if microbial activity leads to higher $Diss_{pot}$ values induced by extremely low pH values as observed in previous studies[22,33,34].

The initial addition of calcite and dunite in the benthocosm experiment was 22 mol m^{-2}. After 1 year, the material was mixed into the upper ~3.3 cm of sediment (Additional data figure 2). Hence, the dissolution rates calculated from the benthocosm experiments are valid for an amount of ~22 mol of calcite in the upper 3.3 cm of sediment, which subsequently constitutes a threshold up to which calculations by the

model can be assumed as reliable (grey symbols, Fig. 3). A second threshold is the maximum saturation state with respect to calcite, above which the spontaneous precipitation of $CaCO_3$ can occur diminishing the uptake efficiency due to the release of CO_2 (red circles, Fig. 3). This threshold depends on saturation state, as well as on equilibration with CO_2 and the used material[15,21,35]. Since carbonate precipitation was observed at Ω_{Cal} = ~6.1 in previous studies[21] in the presence of olivine, this value was defined as a threshold for both material additions, despite the fact that recent studies about the stability of alkalinity observed precipitation of $CaCO_3$ only at values of $\Omega_{Cal} > 12$ [35,36].

V.1.3. Identification of a candidate material for EBW based on cost estimates

For the estimation of overall efficiency and costs for the modelled application scenario, the single steps from the production of a respective calcite and dunite material to the actual spreading process in the application area were analyzed for their expenditure and their respective CO_2-footprint (Tables S8 – S10, Supplement). As to be expected, the costs per ton of sequestered CO_2 via addition of calcite and dunite (Fig. 4) follow the inverted uptake efficiency (Figs V3c,d), which explains the constant costs for calcite application up to ~1000 t annual uptake. For dunite, the lower energy demand for the production of coarser grains did not compensate for the lower uptake efficiency, which is why the total costs per ton of CO_2 decrease with smaller grain size over the grain size range assumed for the model (~5µm – ~30µm). Smaller grain sizes were not considered as these might remain in suspension and would thus not be suitable for EBW[19]. In sum, the low uptake efficiency, combined with the high energy demand for grinding exclude dunite as a potential material for efficient EBW in the investigated study area.

For calcite, these constraints do not apply. The softer material requires less energy for comminution, which lowers the costs and CO_2 footprint compared to dunite. Combined with the higher uptake efficiency (Fig. V3c) this leads to prices between 81.6 – 99.5 € t_{CO2}^{-1} for a total CO_2 uptake of up to ~1000 t over the entire application area (Fig. V4b). For higher, but less efficient total uptake, the costs vary between 172€ t_{CO2}^{-1} (A_{BET} = 3.0 m^2 g^{-1}) and 462€ t_{CO2}^{-1} (A_{BET} = 0.5 m^2 g^{-1}). For this uptake range, the lower uptake efficiency of the coarser material is – as for dunite – not outbalanced by the lower production costs and

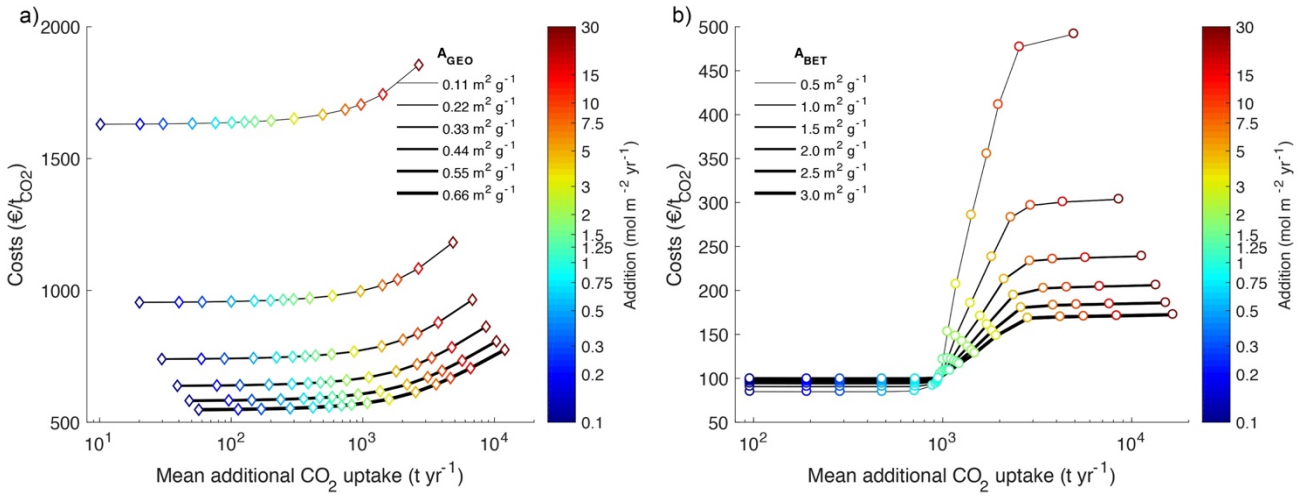

Figure V6: Mean costs including production, comminution, transport and spreading per ton of sequestered CO_2 for dunite (a) and calcite (b) for a 30-year application period. Color codes indicate the annual addition of material. Line width indicates the geometrical surface (olivine) and the corresponding BET surface (calcite), respectively. Note different range of x-axis in panels a and b.

CO_2 footprint. Furthermore, the additional uptake for all treatments increased over time for all treatments (Figs S1, S2; Supplement). Hence, an application over a longer time period would increase the overall uptake efficiency and lower the costs per ton of sequestered CO_2., Especially below the uptake of 1000 t, the prices for calcite based EBW would be highly competitive, when compared to other technical CDR methods such as direct air capture (DACCS) and bioenergy with carbon capture and storage (BECCS)[2,37]. Still, the exact potential for EBW and the precise threshold for high uptake efficiencies need further research before a final comparison can be made.

V.1.4. Enhanced benthic weathering in a global context

These new findings have implications for the perception of EBW as a climate change mitigation measure. The Baltic Sea alone comprise 133000 km^2 of muddy sediments[38]. Assuming a similar weathering behavior for calcite as in Eckernförde Bay, this would imply an uptake between ~4.5 and 30 Mt yr^{-1}. The latter, though, with lower efficiency.

Despite the fact that the study area is a rather small inlet, the chemical features bear some similarities to large-scale upwelling systems where nutrient rich waters transported to the sea surface foster high rates of primary production and organic carbon rain rates. The export of organic matter leads to high organic carbon contents in sediments that are similar to those in the study area Eckernförde Bay[20,22,39,40]. The degradation of this organic carbon combined with the upwelling of DIC rich waters alters the bottom water chemistry in a way that makes these large systems comparable to the inlet investigated in this study. Thus, the presented results may well be extrapolated to a globally relevant scale as the total area of eastern boundary upwelling systems alone accounts for ~$1.04 \cdot 10^6$ km^2 [41]. When including the highly productive East China Sea continental margin, the potential application area could be up to ~$2.0 \cdot 10^6$ km^2 plus several smaller upwelling regions[41]. Considering a higher, but less efficient uptake of 320 t km^{-2} yr^{-1} and also including smaller potential application sites, annual global potential CO_2 uptake might reach several gigatonnes. Although it is unlikely that EBW will reach a potential to serve as a sole sink for global non-abatable CO_2 emissions, it may well be an efficient way to off-set non-point-sourced residual emissions for countries with upwelling systems or organic rich sediments in their exclusive economic zones.

References (V.1)

1. IPCC. Summary for Policymakers. In: Global Warming of 1.5°C. An IPCC Special Report on the impacts of global warming of 1.5°C above pre-industrial levels and related global greenhouse gas emission pathways, in the context of strengthening the global response to. *Cambridge Univ. Press* 3–24 (2018) doi:10.1017/9781009157940.001.
2. Fuss, S. *et al.* Negative emissions - Part 2: Costs, potentials and side effects. *Environ. Res. Lett.* **13**, (2018).
3. Minx, J. C. *et al.* Negative emissions - Part 1: Research landscape and synthesis. *Environ. Res. Lett.* **13**, (2018).
4. Smith, S. M. *et al. The state of Carbon Dioxide Removal.* https://www.stateofcdr.org/ (2023).
5. Buck, H. J., Carton, W., Lund, J. F. & Markusson, N. Why residual emissions matter right now. *Nat. Clim. Chang.* **13**, 351–358 (2023).
6. Luderer, G. *et al.* Residual fossil CO2 emissions in 1.5–2 °C pathways. *Nat. Clim. Chang.* **8**, 626–633 (2018).
7. Kheshgi, H. S. Sequestering atmospheric carbon dioxide by increasing ocean alkalinity. *Energy* **20**, 915–922 (1995).
8. Bach, L. T., Gill, S. J., Rickaby, R. E. M., Gore, S. & Renforth, P. CO2 Removal With Enhanced Weathering and Ocean Alkalinity Enhancement: Potential Risks and Co-benefits for Marine Pelagic Ecosystems . *Frontiers in Climate* vol. 1 (2019).
9. Lamb, W. F. *et al.* The carbon dioxide removal gap. *Nat. Clim. Chang.* (2024) doi:10.1038/s41558-024-01984-6.
10. Hochstetter, F. von. Lecture on the Geology of the Province of Nelson. *New Zeal. Governemt Gaz. (Province Nelson)* **7**, 90–102 (1859).
11. Rigopoulos, I. *et al.* Carbon sequestration via enhanced weathering of peridotites and basalts in seawater. *Appl. Geochemistry* **91**, 197–207 (2018).
12. Meysman, F. J. R. & Montserrat, F. Negative CO2 emissions via enhanced silicate weathering in coastal environments. *Biology Letters* (2017) doi:10.1098/rsbl.2016.0905.
13. Schuiling, R. D. & Krijgsman, P. Enhanced Weathering: An Effective and Cheap Tool to Sequester Co2. *Clim. Change* **74**, 349–354 (2006).
14. Griffioen, J. Enhanced weathering of olivine in seawater: The efficiency as revealed by thermodynamic scenario analysis. *Sci. Total Environ.* **575**, 536–544 (2017).
15. Moras, C. A., Bach, L. T., Cyronak, T., Joannes-Boyau, R. & Schulz, K. G. Ocean alkalinity enhancement – avoiding runaway CaCO3 precipitation during quick and hydrated lime dissolution. *Biogeosciences* **19**, 3537–3557 (2022).
16. Rau, G. H. & Caldeira, K. Enhanced carbonate dissolution:: a means of sequestering waste CO2 as ocean bicarbonate. *Energy Convers. Manag.* **40**, 1803–1813 (1999).

17. Revelle, R. & Suess, H. E. Carbon Dioxide Exchange Between Atmosphere and Ocean and the Question of an Increase of Atmospheric CO2 during the Past Decades. *Tellus* **9**, 18–27 (1957).

18. Hangx, S. J. T. & Spiers, C. J. Coastal spreading of olivine to control atmospheric CO2 concentrations: A critical analysis of viability. *Int. J. Greenh. Gas Control* **3**, 757–767 (2009).

19. Köhler, P., Abrams, J. F., Völker, C., Hauck, J. & Wolf-Gladrow, D. A. Geoengineering impact of open ocean dissolution of olivine on atmospheric CO2, surface ocean pH and marine biology. *Environ. Res. Lett.* **8**, (2013).

20. Bice, K., Myers, T., Waldbusser, G. & Meile, C. Countering the effect of ocean acidification in coastal sediments through carbonate mineral additions. *EGUsphere* **2024**, 1–28 (2024).

21. Fuhr, M. *et al.* Kinetics of Olivine Weathering in Seawater: An Experimental Study. *Front. Clim.* **4:831587**, (2022).

22. Fuhr, M. *et al.* Disentangling artificial and natural benthic weathering in organic rich Baltic Sea sediments. *Frontiers in Climate* vol. 5:1245580 (2023).

23. Flipkens, G. *et al.* Enhanced olivine dissolution in seawater through continuous grain collisions. *Geochim. Cosmochim. Acta* **359**, 84–99 (2023).

24. Fuhr, M. *et al.* Alkaline mineral addition to anoxic to hypoxic Baltic Sea sediments as a potentially efficient CO2-removal technique. *Frontiers in Climate* vol. 6 (2024).

25. Walter, L. M. & Morse, J. W. The dissolution kinetics of shallow marine carbonates in seawater: A laboratory study. *Geochim. Cosmochim. Acta* **49**, 1503–1513 (1985).

26. Rimstidt, J. D., Brantley, S. L. & Olsen, A. A. Systematic review of forsterite dissolution rate data. *Geochim. Cosmochim. Acta* **99**, 159–178 (2012).

27. Naviaux, J. D. *et al.* Temperature dependence of calcite dissolution kinetics in seawater. *Geochim. Cosmochim. Acta* **246**, 363–384 (2019).

28. Brunauer, S., Emmett, P. H. & Teller, E. Adsorption of Gases in Multimolecular Layers. *J. Am. Chem. Soc.* **60**, 309–319 (1938).

29. Melzner, F. *et al.* Future ocean acidification will be amplified by hypoxia in coastal habitats. *Mar. Biol.* **160**, 1875–1888 (2013).

30. Balzer, W. Organic matter degradation and biogenic element cycling in a nearshore sediment (Kiel Bight)1. *Limnol. Oceanogr.* **29**, 1231–1246 (1984).

31. Lennartz, S. T. *et al.* Long-term trends at the Boknis Eck time series station (Baltic Sea), 1957–2013: does climate change counteract the decline in eutrophication? *Biogeosciences* **11**, 6323–6339 (2014).

32. Dietze, H. & Löptien, U. Retracing Hypoxia in Eckernförde Bight (Baltic Sea). *Biogeosciences Discuss.* **2021**, 1–42 (2021).

33. Seitaj, D. *et al.* Cable bacteria generate a firewall against euxinia in seasonally hypoxic basins. *Proc. Natl. Acad. Sci.* **112**, 13278–13283 (2015).

34. Meysman, F. J. R., Risgaard-Petersen, N., Malkin, S. Y. & Nielsen, L. P. The geochemical fingerprint of microbial long-distance electron transport in the seafloor. *Geochim. Cosmochim. Acta* **152**, 122–142 (2015).

35. Hartmann, J. *et al.* Stability of alkalinity in ocean alkalinity enhancement (OAE) approaches – consequences for durability of CO2 storage. *Biogeosciences* **20**, 781–802 (2023).

36. Suitner, N. *et al.* Ocean alkalinity enhancement approaches and the predictability of runaway precipitation processes - Results of an experimental study to determine critical alkalinity ranges for safe and sustainable application scenarios. *EGUsphere* **2023**, 1–35 (2023).

37. Eisaman, M. D. *et al.* Assessing the technical aspects of ocean-alkalinity-enhancement approaches. *Guid. to Best Pract. Ocean Alkalinity Enhanc. Res.* **2-oae2023**, 3 (2023).

38. Wallmann, K. *et al.* Erosion of carbonate-bearing sedimentary rocks may close the alkalinity budget of the Baltic Sea and support atmospheric CO2 uptake in coastal seas. *Front. Mar. Sci.* **9:968069**, (2022).

39. Dale, A. W. *et al.* Rates and regulation of nitrogen cycling in seasonally hypoxic sediments during winter (Boknis Eck, SW Baltic Sea): Sensitivity to environmental variables. *Estuar. Coast. Shelf Sci.* **95**, 14–28 (2011).

40. Dale, A. W. *et al.* Recycling and Burial of Biogenic Silica in an Open Margin Oxygen Minimum Zone. *Global Biogeochem. Cycles* **35**, e2020GB006583 (2021).

41. Kämpf, J. & Chapman, P. *Upwelling Systems of the World. Upwelling Systems of the World* (Springer Nature, 2016). doi:10.1007/978-3-319-42524-5.

42. Zeiler, M., Schwarzer, K., Ricklefs, K., 2008. Seabed morphology and sediment dynamics. Die Küste 74, 31–44.

V.2. Materials and Methods

V.2.1. Experimental set-up

Between 22 and 24 February 2022, a total of nine polyethylene boxes with a base area of 111cm × 71 cm were filled with ~20 cm of organic rich sediment from Boknis Eck (Eckernförde Bay, south-western Baltic Sea) using a sediment grab. Beforehand, a side wall of each benthocosms was drilled with sealable holes to insert rhizons for porewater extraction and subsequent porewater analysis. The depth of the supernatant bottom water in each box was ~30 cm. Subsequent to recovering the sediment, the boxes were placed on a quay in Kiel Fjord adjacent to GEOMAR. In groups of three, the boxes were connected to a header tank that ensured constant flow rates. From these header tanks, ~10 m^3 d^{-1} of bottom water (~15 m depth) was pumped into the 9 benthocosms via a dispenser to avoid resuspension of the fine-grained sediment (Fig.1). The benthocosms were then left for 6 months to equilibrate and to allow for natural chemical pore water gradients to develop.

On 27 September 2022, 22 mol m^{-2} of limestone (99.8 % calcite, German Limestone Association) and dunite (90% olivine, Sibelco^{TM}) powder was distributed evenly on the sediment surface of six benthocosms with three replicates for each treatment. The other three benthocosms were left unamended to serve as controls. An overview of the precise treatments is given in the supplementary Table S11.

V.2.2. Sampling and measurements

Benthic fluxes in each benthocosm were measured with sealed polycarbonate mini-benthic chambers with a base area of 100 cm^2 and a total volume of 400 cm^3. The chambers were placed carefully on the sediment. A ~0.5 cm rim around the chamber penetrated into the sediment to assure that the chamber water was isolated from the surrounding water. Directly before deployment, a bottom water sample was taken to determine initial conditions. After 3 h, a sample from inside the chamber was taken via a PVC tube that was attached to the chamber in the middle of the side wall. The first 15 ml of water were discarded. Afterwards, a 20 ml sample was filtered using 0.2 µm regenerated cellulose syringe filters and refrigerated in polyethylene (PE) vials without headspace for further measurements. Total alkalinity (TA) was determined via titration using 0.02N HCl[1] as described in previous studies[2–5]. 1 ml of aliquot was acidified with 10 µl suprapure HNO_3 for cation analysis via inductively coupled plasma optical emission spectrometry (ICP-OES, Varian 720-ES).

Before the addition of substrates, pore water samples were taken using 10 cm long 0.15 µm standard rhizon samplers attached to 20 ml PE syringes. After recovery of the pore waters, the syringes were sealed, refrigerated and transported to the laboratory for further processing. In a N_2 filled glove bag, the samples were transferred to 20 ml PE vials. TA and cations were determined the same way as for the benthic chamber samples.

Micro-profiling of oxygen and pH in each benthocosm was conducted with Unisense^{TM} micro-sensors Ox-100 and pH-100, mounted on a motorized Unisense^{TM} micromanipulator. To maximize measuring resolution for oxygen profiles the step size was adjusted to 100 µm. Oxygen sensors were calibrated according to Unisense^{TM} guidelines. For pH profiles the resolution was lowered to 300 µm to minimize

profiling time. In addition to technical buffers (pH 4 and 7), the pH sensors were calibrated with TRIS-buffers [6,7]. pH values in this study are reported on the total scale.

Samples for analysis of solid components over the upper 6 cm were taken using cut-off syringes (2.5 cm diameter). The samples were obtained directly after addition of the alkaline substrates to determine conditions at the starting point of the experiment as well as the end of the experiment. Sediment samples were freeze-dried, ground, and analyzed via flash combustion using the EuroEA 3000 element analyzer (EuroVector, Pavia, Italy) to determine total carbon (TC), total organic carbon (TOC), total nitrogen (TN), and total sulfur (TS). The total inorganic carbon (TIC) content was calculated by subtracting the TOC value from the TC measurement. To assess the accuracy of the analytical method, method blanks and two reference standards were employed: 2.5-Bis(5-tert-butyl-2-benzo-oxazol-2-yl)thiophene (BBOT, HEKAteckTM), and an internal sediment standard.

V.2.3. Flux calculations from the mini-benthic chambers

Fluxes of solutes, F_{sol}, were determined from the initial and final concentrations with the following equation:

$$F_{sol} = \frac{dC_{sol}}{dt} \times H_{Chamber} \quad \text{(V1)}$$

where dC_{sol} / dt is concentration change and $H_{Chamber}$ is the height of the overlying water.

V.2.4. Calculation of $Diss_{pot}$ values

To assess the impact on porewater saturation state on calcite dissolution, the $Diss_{pot}$ values were calculated following Fuhr et al. (2023) by integrating Ω_{Cal} values over the region where pore waters were undersaturated as

$$Diss_{pot} = \int_{z(\Omega<1)}^{z(\Omega>1)} (1 - \Omega_{cal}(z))\, dz \quad \text{(V2)}$$

where $\Omega_{cal}(z)$ is the saturation state at a certain depth and z is the depth in the sediment given in cm. $z(\Omega<1)$ and $z(\Omega>1)$ denote depths where Ω_{cal} values fall below 1 and above 1, respectively.

Ω_{Cal} values were calculated based on the pH profiles at the respective time step and the porewater TA as well as pore water Ca concentrations sampled at the beginning of the experiment. To reach the resolution of the pH profile (300µm), TA and Ca concentrations were interpolated linearly. These data are available online (see data availability statement) and in the supplementary tables S12 and S13.

V.2.5. Box model set-up

To assess the impact of calcite and dunite addition to an application area of 25 km^2 a numerical box model was set up using Wolfram™ Mathematica™ v12. The model considers four boxes, which represent a two-layered water body including the mineral application area in Eckernförde Bay and the adjacent Kiel Bight (Fig. 1, Additional data Fig. 1). Box sizes were chosen accordingly. The water depth was defined as 25 m. A boundary between the upper and lower boxes was defined at 15 m depth as this is the depth where

the halocline usually occurs during summer[8]. The Kiel Bight box was considered to be 100 times larger than the Eckernförde Bay box. The area of the bottom box of Kiel Bight was 34 % smaller than the surface box in order to represent the area of Kiel Bight that is covered with sandy sediments [9–11]. Thus, the benthic fluxes contributing from sandy sediments [12] were not considered for the model. The model considers primary production (PP) that transports reduced dissolved inorganic carbon (DIC) in the surface layer and exports it to the lower box as particulate organic carbon (POC), where POC is then remineralized to DIC. Furthermore, the model accounts for water mass mixing between the upper and lower boxes, as well as water mass exchange between the two surface boxes. To account for a quasi-upwelling, that is induced by a saltwater wedge that invades and replaces bottom water in spring[13], the model is equipped with an overall upwelling term (Additional data Fig. 1). The upwelling flux enters the Kiel Bight bottom box and flushes the entire system before it exits via the Kiel Bight surface box. Hence, the Kiel Bight bottom box serves to pre-form the water that circulates through Eckernförde Bay. Accordingly, the model was tuned to produce naturally prevailing conditions in both bottom boxes [8,14]. Hydrological parameters were estimated based on a 3-D numerical model [13]. Primary production was qualitatively assessed based on chlorophyll measurements [8,15], normalized and then tuned in such a way that the bottom water properties matched observed values [14].

The upper two boxes can exchange CO_2 with the atmosphere, which allows quantifying the natural (without addition of alkaline materials) as well as the enhanced (induced by addition of alkaline materials) CO_2 flux across the sea-atmosphere interface. The lower Eckernförde Bay box includes DIC and TA fluxes from the sediment that derive from natural $CaCO_3$ dissolution and degradation of sedimentary POC. Natural background fluxes were determined via the unamended benthocosm experiment. The sediment model consists of three equally sized layers that describe dissolution of added minerals within the upper 10 cm of the sediment (not shown in the schematic Additional data Fig. 1). Due to the long simulation period of 35 years, the TA and DIC fluxes from the sediment were assumed to directly enter the bottom water without delay via molecular diffusion.

The model solves the carbonate system in each of the boxes based on DIC and TA via a set of coupled mass balance equations (ordinary differential equations) using finite differences and the method-of-lines approach as implemented in the partial differential equation solver. For simplicity, other chemical processes such as oxidation and higher-level food chains are not considered in the model. Initial conditions for carbonate system properties were inferred from long-term observations at Boknis Eck [8,14]. Salinity, temperature and oxygen concentrations were implemented as time dependent parameters for upper and lower boxes. Salinity and temperature were used to calculate the solubility and dissociation constants for the different carbonate species [16]. For bottom water oxygen concentrations, the observed long-term decreasing trend of -1.4 $\mu mol\ l^{-1}$ was considered [8].

To ensure full equilibration, the model was spun-up for five years before calcite or dunite were added in July, at the beginning of the anoxic phase, and then every July for another 30 years (Table S2, supplement). The added materials were assumed to stay on top of the sediment until bottom water oxygen concentrations reached 100 $\mu mol\ l^{-1}$, which is in line with observations from the benthocosm experiment and previous studies [3,4]. Above this threshold, the material is allowed to be transported into the upper 3.3 cm of sediment by bioturbation. This depth stems from previous reports [17] including our own observations [3]. The transport was parameterized using a first-order rate constant that was chosen such that 80% of the material was worked into the sediment after ~ 3 weeks and 99% after 7 weeks. This is based on observations from the benthocosm experiment and previous studies [3,4]. For the transport into the deeper sediment (i.e., the third

layer) the model assumed burial using a sedimentation rate of ~3.3 mm yr^{-1} [18,19]. Below 10 cm, no further dissolution was assumed as porewaters below this depth are oversaturated with respect to calcite [3,4] and bioturbation does usually not reach deeper than 10 cm [20]. The combination of sedimentation rate and depth of bioturbation implies that the residence time of added material in the top 10 cm is ~30 years, which defines the chosen model simulation period.

For each box, an ordinary differential equation was formulated as

$$\frac{dC_i}{dt} = T_{upw,i} + T_{mix,i} + T_{ex,i} + F_{CO2} + \sum_i R_i \quad \text{(V3)}$$

where *i* is DIC and TA and T_{upw} T_{mix} and T_{ex} describe the water transport between adjacent boxes due to upwelling, mixing and lateral exchange, respectively (additional Data Fig. 1) and *R* defines changes due to formation/remineralization of POC and dissolution of minerals. F_{CO_2} describes the CO_2 exchange with the atmosphere for DIC only.

V.2.6. Dissolution of calcite

in undersaturated bottom waters (Ω_{Cal}<1) was simulated as follows:

$$CaCO_3 + H_2O + CO_2 \rightarrow Ca^{2+} + 2HCO_3^- \quad \text{(V4)}$$

The rate for this dissolution process, $r_{CalDiss}$, was defined as:

$$r_{CalDiss}(t) = Cal_{top}(t) \times A_{BET} \times k_{CalDiss} \times (1 - \Omega_{cal})^{n_{CalDiss}} \quad \text{(V5)}$$

where Cal_{top} is the amount of calcite on the sediment in mol, A_{BET} is the reactive surface of the calcite grains in cm mol^{-1}, $k_{CalDiss}$ is a first order reaction constant in mol cm^{-1} d^{-1}, Ω_{Cal} is the saturation state with respect to calcite and $n_{CalDiss}$ is the reaction order. $k_{CalDiss}$ and $n_{CalDiss}$ were dependent on Ω_{Cal} following previous studies [21]. Ω_{Cal} was defined as

$$\Omega_{Cal} = \frac{[Ca^{2+}] \times [CO_3^{2-}]}{K_{sp}} \quad \text{(V6)}$$

$[Ca^{2+}]$, $[CO_3^{2-}]$ and K_{sp} are the porewater concentrations of calcium and carbonate ions, and the solubility product of calcite, respectively [16].

Calcite dissolution in the upper 3.3 cm of sediment ($r_{CallDissSed}$) was estimated based on the enhanced TA fluxes measured during the benthocosm experiments (Table S4, supplement) following:

$$r_{CallDissSed}(t, z) = k_{depth}(z) \times Cal_{Sed\,i}(t) \times A_{BET} \times rT_{Cal}(t) \times r_{mean} \quad \text{(V7)}$$

where z denotes the average depth of each of the three sediment boxes, $Cal_{Sed\,i}(t)$ is the amount of calcite in the respective sediment box in mol, A_{BET} is the reactive surface, rT (t) is the temperature sensitivity (Supplement) and r_{mean} is the mean calculated dissolution rate (Supplement). Since the added material only mixes into the upper three centimeters of sediment after one year in the benthocosms, the bulk dissolution kinetics for sedimentary dissolution of calcite is only valid for the upper sediment box. For deeper sediment layers, an exponential decrease of dissolution was assumed and dissolution was calculated by multiplying Eq. V5 with a pre-factor $k_{depth}(z)$:

$$k_{depth}(z) = 10^{(-0.538z + 0.778)} \quad \text{(V8)}$$

where z is the depth in the sediment. k_{depth} was chosen in a way that it is equal to 1 when averaged over the upper 3.3 cm and 0.01 at 10 cm depth, which constitutes the depth at which no further bioturbation and thus dissolution is assumed.

V.2.7. Olivine dissolution

was defined as:

$$(Mg_{0.93}, Fe_{0.07})_2SiO_4 + 4.07H_2O + 0.035O_2 + 3.72CO_2 \rightarrow$$
$$1.86Mg^{2+} + H_4SIO_4 + 0.14Fe(OH)_3 + 3.72HCO_3^- \quad (V9)$$

Assuming that olivine consists of 93% forsterite and 7% fayalite, the dissolution rate can be parameterized following literature values[22] and adjusted based on sediment incubation experiments for anoxic to hypoxic conditions [4] as:

$$\log(r_{ol}(t)) = 4.07 - 0.256 \times pH - \frac{3465}{T} \quad (V10)$$

where r_{ol} is the dissolution rate given in mol m^{-2} s^{-1}, T is temperature in K and pH is the pH in bottom waters. Dissolution in the sediment was assumed following the same approach as for calcite, with mean dissolution rates calculated from benthocosm experiments with dunite addition (Supplement).

V.2.8. pH simulation

TA and DIC were defined as follows:

$$TA = [HCO_3^-] + [2CO_3^{2-}] + [B(OH)_4^-] + [OH^-] - [H^+] \quad (V11)$$

$$DIC = [CO_2] + [HCO_3^-] + [CO_3^{2-}] \quad (V12)$$

Each term on the right-hand side of Eq. V11 was replaced for an expression based on the total concentration of each weak acid, leading to:

$$TA = \frac{K_1 \cdot [H^+] \cdot [DIC]}{[H^+]^2 + [H^+] \cdot K_1 + K_1 \cdot K_2} + \frac{2 \cdot K_1 \cdot K_2 \cdot [DIC]}{[H^+]^2 + [H^+] \cdot K_1 + K_1 \cdot K_2} + \frac{K_B \cdot [TB]}{K_B + [H^+]} + \frac{K_W}{[H^+]} - [H^+] \quad (V13)$$

The calculation of protons was calculated at each time step by solving Eq. V13 as described by Zeebe and Wolf-Gladrow[16]. Stoichiometric equilibrium coefficients were calculated based on temperature and salinity following Zeebe and Wolf-Gladrow[16].

The carbonate ion concentration in each box (Eq. V6) was then calculated as:

$$CO_3^{2-} = \frac{K_1 \cdot K_2}{[H^+]^2 + [H^+] \cdot K_1 + K_1 \cdot K_2} \cdot DIC \quad (V14)$$

and the partial pressure of CO2 we calculated as:

$$pCO_2 = \frac{[CO_2]}{K_0} \quad (V15)$$

where K0 is the Solubility constant for CO2, and where

$$[CO_2] = \frac{[HCO_3^-] \cdot [H^+]}{K_1} \quad (V16)$$

Initial conditions for TA and DIC were chosen based on values reported by Melzner et al14 and reported in the supplementary table 3.

V.2.9. Additional CO_2 uptake induced by addition of alkaline substrates

The model considers equilibration of CO_2 with the atmosphere to estimate the additional uptake after addition of alkaline substrates. For this purpose, the model was run for 35 years without addition of alkaline materials to obtain the natural baseline. Subsequently the natural CO_2 uptake was subtracted from the uptake with addition of calcite and dunite, respectively.

The air-sea gas flux (Eq. V3) from surface box *i*, $F_{CO2,i}$, was defined as

$$F_{CO2,i} = k_{CO2} \times K_0 \times (pCO_{2atm} - pCO_{2,i}) \quad \text{(V17)}$$

where k_{CO2} is the gas transfer velocity for CO_2, and $pCO_{2,atm}$ and $pCO_{2,i}$ are the partial pressures of CO_2 in the atmosphere and the surface water of box *i*, respectively. A value of 419 µatm was used as the initial condition for $pCO_{2,atm}$. An annual increase of 2.4 µatm was assumed [23].

The gas transfer velocity normalized for CO_2 at 20 °C and zero salinity (k(600), cm h^{-1}) was determined via in-situ measurements in coastal Baltic Sea in June and September 2018 (Dobashi and Ho, in preparation) and simply parameterized as:

$$k(600) = 1.26 \times u_{10m} \text{ (for } u_{10m} < 7 \text{ ms}^{-1}\text{)} \quad \text{(V18)}$$

and

$$k(600) = 8.83 \text{ (for } u_{10m} \geq 7 \text{ ms}^{-1}\text{)} \quad \text{(V19)}$$

where u_{10m} is the wind speed at 10 m height. Subsequently, the k(600) values were corrected for in-situ salinity and temperature as

$$k_{CO2} = k(600) \times \left(\frac{Sc_{CO2}}{600}\right)^{-\frac{1}{2}} \quad \text{(V20)}$$

where Sc_{CO2} is the Schmidt number (i.e., kinematic viscosity of water divided by diffusion coefficient of gas in water) for CO_2, which was calculated following Dobiashi & Ho [24]

$$Sc_{CO2} = 1914.2 + 5.6330 \times Sal_{up} - (123.18 + 0.32481 \times Sal_{up}) \times T_{up} + (4.2040 + 0.010208 \times Sal_{up}) \times {T_{up}}^2 - (0.079322 + 0.00018296 \times Sal_{up}) \times {T_{up}}^3 + (0.00062463 + 1.3992 \times 10^{-6} * Sal_{up}) \times {T_{up}}^4 \quad \text{(V21)}$$

where Sal_{up} is salinity in surface waters in PSU and T_{up} is temperature in °C.

A detailed description of the model, including all model parameters and boundary conditions is provided in the supplement.

V.2.10. Efficiency and cost assessment

CO_2 emissions from production, transport and spreading of calcite and dunite were calculated. For dunite, this assumes production in Åarheim, Norway, a 1400 km transport by ship to Kiel harbor, milling (at a theoretical facility in Kiel harbour), and spreading by ship in Eckernförde Bay (~150 km in a small vessel). For calcite, we considered production and milling in a quarry 300 km south of Kiel, transport to Kiel by train, and subsequent spreading in the application area. Further impacts from mining, such as altered land use were not considered.

Based on Strefler et al.[25] the production costs per ton of dunite were calculated excluding grinding and transport. Additionally, energy demand (E_{gr}) in kWh for grinding based on the grainsize (gr) in µm was calculated following[25]:

$$E_{gr} = 6.62 \times gr^{-1.162} \quad (V22)$$

Costs for grinding were then estimated on the current industry electricity price. For these calculations, we assumed a near-shore grinding facility, negating the need for further transport from the harbor to the mill and back.

The CO_2 emissions for the production of raw dunite were added to emissions for grinding estimated based on the energy demand (Eq. V22) and calculated for the energy mix in Germany in 2020[26].

For calcite, the production costs and CO_2 emissions for the different grain sizes were provided by the German Limestone Association. To these, the costs and emissions for transport and spreading were added. A precise description of the assumptions made for cost and emission calculations can be found in the supplement. Finally, the combined emissions for each material were subtracted from the uptake and the final usage of material multiplied with the total costs per ton of material.

In order to derive comparable efficiency and cost estimates, the geometrical surfaces of dunite grains were calculated for grain sizes that correspond to the BET surfaces assumed for calcite addition. For this purpose, we calculated the ratio of A_{BET} to A_{GEO} for calcite and assumed the same ratio for all BET surfaces. The uncertainty inherent with this assumption needs to be accepted. The A_{Geo} was then calculated accordingly.

Data availability statement(V)

The original contributions presented in the study are included in the article and supplementary files. pH profiles are publicly available under https://github.com/MichaelFuhrGEO/Fuhr_et_al_2024. Further inquiries can be directed to the corresponding author.

Author Contributions(V)

SG designed the study, MF conducted the experiment and wrote the manuscript, HK helped with pH measurements, SS supervised micro profiling. AD advised and supported lab procedures, KW helped with discussions, MS helped with the experimental set-up and sensor measurements, RD conducted gas transfer velocity measurements, TS supported discussions. FM supported the benthocosm experiment. All authors contributed to the article and approved the submitted version.

Funding(V)

This study was funded by the Bundesministerium für Bildung und Forschung (BMBF) **(Project** RETAKE**, granted to SG) in the framework of the Deutsche Allianz für Meeresforschung (DAM) mission "CDRmare".**

Acknowledgements(V)

We would like to thank Anke Bleyer, Bettina Domeyer and Regina Surberg for their help with technical and analytical procedures in the GEOMAR laboratory and Björn Bucholz for his help with the benthocosm experiment. We are also grateful to David T. Ho for valuable advice on the air-sea gas exchange of the study area. RD appreciates financial support from the Uehiro

Foundation. **Additionally, we thank the crew of FK Littorina for their support during recovery of sediments.**

References (V.2)

1. Ivanenkov, V. N. & Lyakhin, Y. I. Determination of the alkalinity of seawater. *Methods Hydrochem. Stud. Ocean* 110–115 (1978).
2. Fuhr, M. *et al.* Kinetics of Olivine Weathering in Seawater: An Experimental Study. *Front. Clim.* **4:831587**, (2022).
3. Fuhr, M. *et al.* Disentangling artificial and natural benthic weathering in organic rich Baltic Sea sediments. *Frontiers in Climate* vol. 5:1245580 (2023).
4. Fuhr, M. *et al.* Alkaline mineral addition to anoxic to hypoxic Baltic Sea sediments as a potentially efficient CO2-removal technique. *Frontiers in Climate* vol. 6 (2024).
5. Dale, A. W., Regnier, P., Knab, N. J., Jørgensen, B. B. & Van Cappellen, P. Anaerobic oxidation of methane (AOM) in marine sediments from the Skagerrak (Denmark): II. Reaction-transport modeling. *Geochim. Cosmochim. Acta* **72**, 2880–2894 (2008).
6. Müller, J. D. *et al.* Metrology for pH measurements in brackish waters-part 1: Extending electrochemical pHT measurements of TRIS buffers to salinities 5-20. *Front. Mar. Sci.* **5**, 1–12 (2018).
7. Pratt, K. W. Measurement of pHT values of Tris buffers in artificial seawater at varying mole ratios of Tris: Tris·HCl. *Mar. Chem.* **162**, 89–95 (2014).
8. Lennartz, S. T. *et al.* Long-term trends at the Boknis Eck time series station (Baltic Sea), 1957–2013: does climate change counteract the decline in eutrophication? *Biogeosciences* **11**, 6323–6339 (2014).
9. Gingele, F. X. & Leipe, T. Southwestern Baltic Sea—A sink for suspended matter from the North Sea? *Geology* **29**, 215–218 (2001).
10. Leipe, T. *et al.* Regional distribution patterns of chemical parameters in surface sediments of the south-western Baltic Sea and their possible causes. *Geo-Marine Lett.* **37**, 593–606 (2017).
11. Zeiler, M., Schwarzer, K. & Ricklefs, K. Seabed morphology and sediment dynamics. *Die Küste* **74**, 31–44 (2008).
12. Van Dam, B. *et al.* Benthic alkalinity fluxes from coastal sediments of the Baltic and North seas: comparing approaches and identifying knowledge gaps. *Biogeosciences* **19**, 3775–3789 (2022).
13. Dietze, H. & Löptien, U. Retracing Hypoxia in Eckernförde Bight (Baltic Sea). *Biogeosciences Discuss.* **2021**, 1–42 (2021).
14. Melzner, F. *et al.* Future ocean acidification will be amplified by hypoxia in coastal habitats. *Mar. Biol.* **160**, 1875–1888 (2013).
15. Ma, X., Sun, M., Lennartz, S. T. & Bange, H. W. A decade of methane measurements at the Boknis Eck Time Series Station in Eckernförde Bay (southwestern Baltic Sea). *Biogeosciences* **17**, 3427–3438 (2020).
16. Chapter 1 Equilibrium. in *CO2 in seawater: Equilibrium, kinetics, isotopes* (eds. Zeebe, R. E. & Wolf-Gladrow, D.) vol. 65 1–84 (Elsevier, 2001).
17. Balzer, W. Organic matter degradation and biogenic element cycling in a nearshore sediment (Kiel Bight)1. *Limnol. Oceanogr.* **29**, 1231–1246 (1984).
18. Whiticar, M. J. Diagenetic relationships of methanogenesis, nutrients, acoustic turbidity, pockmarks and freshwater seepages in Eckernförde Bay. *Mar. Geol.* **182**, 29–53 (2002).
19. Nittrouer, C. A. *et al.* Oceanographic processes and the preservation of sedimentary structure in Eckernförde Bay, Baltic Sea. *Cont. Shelf Res.* **18**, 1689–1714 (1998).
20. Morys, C., Forster, S. & Graf, G. Variability of bioturbation in various sediment types and on different spatial scales in the southwestern Baltic Sea . *Mar. Ecol. Prog. Ser.* **557**, 31–49 (2016).
21. Naviaux, J. D. *et al.* Calcite dissolution rates in seawater: Lab vs. in-situ measurements and

inhibition by organic matter. *Mar. Chem.* **215**, 103684 (2019).
22. Rimstidt, J. D., Brantley, S. L. & Olsen, A. A. Systematic review of forsterite dissolution rate data. *Geochim. Cosmochim. Acta* **99**, 159–178 (2012).
23. Lan, X., Tans, P. & Thoning, K. W. Trends in globally-averaged CO2 determined from NOAA Global Monitoring Laboratory measurements. Version 2024-03. (2024) doi:10.15138/9N0H-ZH07.
24. Dobashi, R. & Ho, D. T. Air–sea gas exchange in a seagrass ecosystem – results from a 3He / SF6 tracer release experiment. *Biogeosciences* **20**, 1075–1087 (2023).
25. Strefler, J., Amann, T., Bauer, N., Kriegler, E. & Hartmann, J. Potential and costs of carbon dioxide removal by enhanced weathering of rocks. *Environ. Res. Lett.* **13**, (2018).
26. Blizniukova, D., Holzapfel, P., Unnewehr, J. F., Bach, V. & Finkbeiner, M. Increasing temporal resolution in greenhouse gas accounting of electricity consumption divided into Scopes 2 and 3: case study of Germany. *Int. J. Life Cycle Assess.* **28**, 1622–1639 (2023).

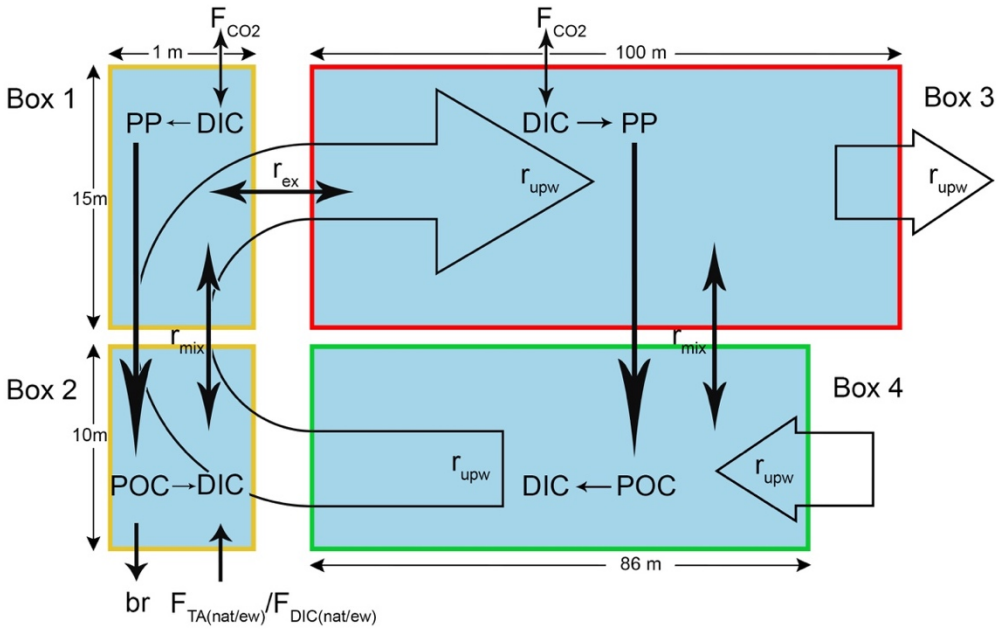

Additional data Fig. 1: Schematic sketch of the numerical box-model used to estimate additional uptake from EBW. The two yellow boxes represent the application area, the red and green box represent the adjacent sea (Fig.1). Arrows describe mass transport between the different boxes. r_i values next to arrows show the rates steering the respective process. Large non-filled arrows describe the overall upwelling.

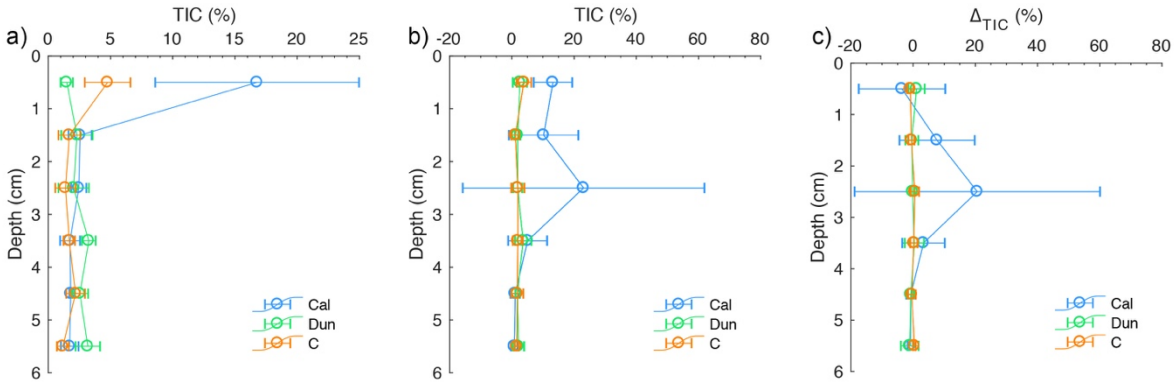

Figure 7: Additional data Fig. 2: TIC content in the sediment measured directly, after addition (a), at the end of the benthocosm experiment (b) and difference in DIC content between beginning and end (c). Error bars report the SD of the three replicas for each treatment.

VI. Summary, conclusion and broader implications

VI.1. Summary and conclusion

The aim in this thesis was to assess the potential, the efficiency and thus the techno-economic feasibility of EBW, based on calcite and dunite addition to organic rich sediments of the Baltic Sea. The key findings in Chapter two made clear that secondary mineral precipitation can diminish the CO_2 sequestration efficiency of dunite weathering. This precipitation was likely fostered by the fact that the experiments were conducted in a closed system with very limited exchange with the atmosphere and thus low availability of CO_2 for equilibration. In equilibration with the atmosphere, this side effect might be negligible. Nevertheless, during the application in the frame of EBW, the dissolution would likely take place in the pore space between the grains, where the exchange of water is restricted to diffusion. Hence, the conditions might be similar to a closed system, which implies that dunite based EBW requires sediments in which CO_2 is formed metabolically, or where bottom waters feature high pCO_2. Thus, a shallow depocenter, such as Boknis Eck, would be a suitable possible application site. The fact that bottom and pore waters in the area are often undersaturated with respect to calcite, suggest additional investigation on calcite as a potential source material for EBW and comparing its overall CO_2 uptake efficiency to that of dunite.

The experiments carried out on sediments from Boknis Eck thereupon, revealed that the weathering regime – namely, whether added materials dissolve on or inside the sediment – plays a key role for the dissolution kinetics of both materials. Under anoxic to hypoxic conditions, where they remain on the sediment, bottom water chemistry is majorly responsible for the dissolution. During this time, dissolution follows closely the kinetics that can be expected from previous studies under the same temperatures and saturation sates. Under oxic conditions they are soon worked into the upper layer of the sediment. Here, the dissolution is slower, as the major mechanism responsible for transporting weathering products away from the weathering site is diffusion. This leads to the formation of diffusive boundary layers around the grains, which slows down dissolution. During the incubation experiments under oxygenated conditions, microbial activity lead to extremely low pore water pH values which altered the saturation state with respect to calcite and governed natural and enhanced calcite dissolution. This leads to the conclusion that the precise understanding of the microbial community is crucial for evaluating the possible efficiency of EBW on this sort of sediment. Interestingly, during the long-term benthocosm experiment – under oxygenated conditions – the best correlation was found between calculated dissolution kinetics and temperature, rather than pore water saturation state, expressed by $Diss_{Pot}$ values. This implies that either the sampling resolution was too coarse to capture periods when high $Diss_{Pot}$ values governed dissolution, or that due to the different experimental setups the microbial community during incubation and benthocosm experiments developed differently. However, the fact that the temperature sensitivity in the benthocosm experiment was stronger than found by previous studies for dissolution in corrosive water only, suggests that a second mechanism is operating that is dependent on temperature and oxygen. This clearly indicates that the macrofaunal activity plays a key role for EBW and does not only substantiate that the benthic weathering works but that it is also important to consider all aspects of it when evaluating possible application sites for EBW.

The overall cost and efficiency calculations via a numerical box-model that was based on the combined findings of all experiments underpinned that calcite based EBW is not only more efficient in terms of the amount of CO_2 that can be sequestered, but that it is also more cost-effective compared to EBW of dunite. This is mainly due to the faster dissolution kinetics and the lower emissions during the production of the

softer material, which cannot be outcompeted by the theoretically higher uptake efficiency of dunite weathering.

With regards to the aim of this thesis it can thus not only be stated that calcite is the more suitable material for EBW, but it has also become clear that calcite based EBW is techno-economically competitive in comparison to other CDR methods.

VI.1. Broader implications and outlook

The new insights revealed in this thesis change the broader meaning of EBW in the context of CDR. Considering a potential uptake of ~4.5 and 30 Mt yr^{-1} Baltic Sea alone, it becomes clear that via this strategy a substantial portion of hard-to-abate emissions in Germany could be outbalanced. However, EBW will not have the potential to serve as a sole NET to achieve net zero emissions on a global scale, mainly because the areas with suitable sediments are limited. Even when larger productive shelf areas and eastern boundary upwelling systems should prove usable as an application site, the total amount of sequestered CO_2 would most likely not overweigh global residual emissions. Still, since it may be an efficient way to off-set non-point-sourced residual emissions in regions with suitable application sites, these should be identified and dedicated research needs to foster the precise understanding of these regions in order to scoop the full potential of EBW as a climate change mitigation method.

Supplement

Supplementary Material to "Kinetics of olivine weathering in seawater: an experimental study"

S1 Supplementary model information

The dissolution of olivine and precipitation of serpentine (chrysotile), sepiolite, talc, $Fe(OH)_3$ and aragonite/calcite were applied as followed:

Olivine:

$$(Mg_{0.89}Fe_{0.11})_2SiO_4 + 4H^+ \rightarrow 1.78Mg^{2+} + 0.22Fe^{2+} + H_4SiO_4 \quad (1S)$$

Serpentinite:

$$3Mg^{2+} + 2H_4SiO_4 + H_2O \rightarrow Mg_3Si_2O_5(OH)_4 + 6H^+ \quad (2S)$$

Sepiolite:

$$2Mg^{2+} + 3H_4SiO_4 \rightarrow Mg_2Si_3O_{7.5}(OH)(H_2O)_3 + 4H^+ + 0.5H_2O \quad (3S)$$

Talc:

$$3Mg^{2+} + 4H_4SiO_4 + 4H_2O \rightarrow Mg_3Si_4O_{10}(OH)_2 + 6H^+ \quad (4S)$$

$Fe(OH)_3$:

$$Fe^{3+} + 3H_2O \rightarrow Fe(OH)_3 + 3H^+ \quad (5S)$$

Aragonite/Calcite:

$$Ca^{2+} + 2HCO_3^- \rightarrow CaCO_3 + CO_2 + H_2O \quad (6S)$$

The oxidation of Fe^{2+} to Fe^{3+} was accounted for with:

$$Fe^{2+} + 0.25O_2 + H^+ \rightarrow Fe^{3+} + 0.5H_2O \quad (7S)$$

Measured and subsequently interpolated temperature and pH values were applied in the modeling as time-dependent variables. The saturation indices for calcite and aragonite were calculated using conditional solubility products valid for seawater (Zeebe and Wolf-Gladrow, 2001b). Thermodynamic solubility products and activity coefficients for dissolved species were used to calculate saturation states with respect to silicate phases and amorphous $Fe(OH)_3$. They were taken from the PHREEQC software (Parkhurst and Appelo, 1999).

In order to account for the discontinuous sampling and the subsequent replacement of the sample volume by fresh ASW the sample rate r_s was defined following:

$$r_s = r_{sv} * \sum \left(\frac{1}{1+e^{\frac{t-i-t_s}{0.0001}}} - \frac{1}{1+e^{\frac{t-i}{0.0001}}} \right) \quad (8S)$$

Where r_{sv} is the theoretical flow rate during sampling defined as:

$$r_{sv} = \frac{v_s}{t_s} \quad (9S)$$

v_s is the sample volume (7 ml) and t_s is the theoretical duration of sampling, here defined as $\frac{1}{24*30}\ d$ equaling 2 minutes. *t* is the time during the experiment and *i* represents each time step at which samples were taken. Hence the function $r_s(t, i)$ expresses a flow rate that occurs at each time *i* when samples are taken, with the duration of t_s and the magnitude of r_{sv}.

For the dissolution of olivine, the kinetic rate law established by Rimstidt et al. (2012) was used, following

$$\log(r_{ol}) = 4.07 - 0.256 * pH(t) - \frac{3465}{T} \quad (10S)$$

where the dissolution rate (r_{ol}) is given in $\frac{mol}{m^2*s}$.

The UMS particles were assumed spherical with an average grain radius of 50 µm and a geometric surface area of 150.459 * 10^{-4} $\frac{m^2}{g\ (UMS)}$. With a density of 3.27 $\frac{g}{cm^3}$ and a molar mass of 143.2 $\frac{g}{mol}$ the dissolution rate was translated to $\frac{\mu mol}{l*d}$.

The enhanced reactive surface of olivine, which is a result of surface roughness and small olivine particles that had not been removed entirely during the cleaning procedure of the UMS, was accounted for with an exponential tuning parameter leading to the formulation:

$$surf_{ol\ tot}(t) = surf_{ol} * (1 + \varepsilon_{1surf}{}^{-\varepsilon_{2surf}*t}) \quad (11S)$$

where $surf_{ol\ tot}(t)$ is the total surface area that declines exponentially with time due to the dissolution of fine particles and surface roughness, $surf_{ol}$ is the geometric surface area, ε_{1surf} represents the factor by which the total surface is enhanced and ε_{2surf} indicates the speed with which $surf_{ol\ tot}$ and $surf_{ol}$ converge (~3 days).

For the carbonate equilibrium system, TA was assumed to result solely from carbonate and bicarbonate since the ASW used in the experiment contained no borate:

$$TA = 2 * [CO_3{}^{2-}] + [HCO_3{}^{-}] \quad (12S)$$

and the subsequent general formulations:

$$[CO_3{}^{2-}] = \frac{K_2*TA}{\{H^+\}+2*K_2} \quad (13S)$$

$$[HCO_3{}^{-}] = \frac{\{H^+\}*TA}{\{H^+\}+2*K_2} \quad (14S)$$

$$[CO_2] = \frac{\{H^+\}^2*TA}{\{H^+\}*K_1+2*K_1*K_2} \quad (15S)$$

and

$$[CO_3{}^{2-}] = \frac{K_2(t)*TA(t)}{\{H^+\}(t)+2*K_2(t)*\rho_{SW}} \quad (16S)$$

where K_1 and K_2 are the first and second dissociation constants of CO_2 in seawater taken from Zeebe and Wolf-Gladrow (2001).

The dissolved inorganic carbon (DIC) was subsequently calculated as

$$DIC = CO_3{}^{2-} + HCO_3{}^{-} + CO_2 \quad (17S)$$

Reaction rates were determined by tuning the unknown rate parameters until the misfit between the predicted and measured concentrations of Mg, Si, Ca an TA reached a minimum. The squared errors summed over time and all species was employed as merit function where the errors for each species were normalized over the mean concentration of the respective species (C_i(mean)):

$$ssr = \frac{(C_i(t)-C_i(t_m))^2}{C_i(mean)^2} \quad (19S)$$

where $C_i(t)$ is the modelled concentration of a species (i) and $C_i(t_m)$ stands for the measured concentration at a respective time.

The tuning parameters and the values apply in the modeling are listed in Tab. S1. They include the kinetic constants (k_{pre_i}), the rate order (ε_{pre2_i}), and the parameters defining the initial delay before the onset of precipitation (α_i, β_i). First, the model was tuned for one batch starting with fitting [Ca] values via aragonite precipitation (as this process is the only one affecting Ca concentrations). Afterwards, secondary phyllosilicate precipitation was fitted via TA, [Si] and [Mg] values. During the tuning, we aimed to apply the same values for all three batches.

S2 Supplementary tables

Table 1S: Values for tuning parameters obtained for the best model fit.

Parameter	symbol	Batch20	Batch10	Batch5	unit
first tuning parameter for olivine surface	ε_{1surf}	10	8	9	-
second tuning parameter for olivine surface	ε_{2surf}	2.95	2.95	2.95	d^{-1}
first tuning parameter for sepiolite precipitation	$k_{pre_{sep}}$	1.3	0.7	0.42	$\frac{\mu mol}{l*d}$
second tuning parameter for sep. precipitation	$\varepsilon_{pre2_{sep}}$	0.04	0.04	0.04	-
first tuning parameter for serpentine precipitation	$k_{pre_{serp}}$	10.8	6.96	4.05	$\frac{\mu mol}{l*d}$
second tuning parameter for serp. precipitation	$\varepsilon_{pre2_{serp}}$	0.04	0.04	0.04	-
first tuning parameter for talc precipitation	$k_{pre_{talc}}$	0.3	0.18	0.09	$\frac{\mu mol}{l*d}$
second tuning parameter for talc precipitation	$\varepsilon_{pre2_{talc}}$	0.04	0.04	0.04	-
first tuning parameter for aragonite precipitation	$k_{pre_{ara}}$	-1.27	-1.55	-1.85	$\frac{\mu mol}{l*d}$
second tuning parameter for arag. precipitation	$\varepsilon_{pre2_{ara}}$	2.4	2.4	1.7	-
delay of sepiolite precipitation	α_{sep}	4.4	4.4	4.4	d
delay of serpentine precipitation	α_{serp}	4.4	4.4	4.4	d
delay of talc precipitation	α_{talc}	4.4	4.4	4.4	d
delay for sepiolite precipitation	β_{sep}	0.2	0.2	0.2	d
delay for serpentine precipitation	β_{serp}	0.2	0.2	0.2	d
delay for talc precipitation	β_{talc}	0.2	0.2	0.2	d
delay of aragonite precipitation	α_{ara}	1.1	1.4	3.9	d
delay for aragonite precipitation	β_{ara}	0.1	0.1	0.3	d

Table 2S: Initial conditions and time-dependent input parameters for models of all batches.

Species	Value	Unit
$C_{Si}(0)$	0	µmol/l
TA (0)	2.4	meq/l
$C_{Mg}(0)$	53.4	mmol/l
$C_{Ca}(0)$	7.98	mmol/l
$C_{Cai}(t)$	$C_{Cai} + 2.4 * (1 - \frac{1}{1+e^{\frac{t-50}{0.1}}})$	mmol/l
$C_{Fe3}(0)$	0	nmol/l
$C_{Fe2(0)}$	0	nmol/l

Table 3S: List of chemical components contained in artificial seawater.

Component	g/l
NaCl	22.94
KCl	0.7815
$MgCl_2$	5.1797
$CaCl_2$	1.1694
Na_2SO_4	4.1076
$NaHCO_3$	0.1933

S 2.1 Supplementary results from solid phase analysis

Table 4S: ICP-OES and XRF measured composition of UMS and calculated composition normalized to 100% along with chemical composition of olivine as provided by manufacturer in mass %.

Oxide	Cont. (mg/g) ICP-OES	Cont. (wt. %) ICP-OES	Cont. (wt. %) XRF	manufacturer
MgO	292.74	44.61	40.25	49.6
SiO_2	282.80	43.1	44.14	41.7
Fe_2O_3	58.69	8.95	8.93	7.4
Cr_2O_3	0.83	0.13	0.39	0.31
NiO	2.17	0.33	0.28	0.32
Al_2O_3	8.31	1.27	2.89	-
CaO	8.90	1.35	2.67	-
K_2O	0.00	0.00	2.67	-
Mn_2O_3	0.96	0.15	0.13	-
UMS	656.09	100	100	100

Table 5S: Major phases of UMS as measured vie WDX. Atomic proportions are normalized to 24 oxygen.

Forsterite

Element	El. mass %	Ox %	Norm El%	Norm %	At prop	c/k-ratio	k-ratio	k-(calc)
Na	0.0083	0.0112	0.0082	0.0110	0.0031	0.8776	0.0001	0.0093
Ni	0.2399	0.3053	0.2364	0.3008	0.0357	1.1312	0.0021	0.0027
Fe	7.5613	9.7292	7.4495	9.5837	1.1820	0.9975	0.0758	1.5465
Si	18.8806	40.3900	18.6008	39.7905	5.8677	1.0851	0.1742	0.7384
K	0.0015	0.0018	0.0015	0.0018	0.0003	0.9742	0.0000	0.0000
Mg	30.6773	50.8678	30.2225	50.1151	11.0167	0.9648	0.3186	3.1912
Cr	0.0099	0.0145	0.0098	0.0143	0.0017	0.9437	0.0001	0.0182
Mn	0.1117	0.1442	0.1100	0.1421	0.0178	1.0486	0.0011	0.0032
Al	0.0065	0.0123	0.0065	0.0122	0.0021	0.9471	0.0001	0.0012
Ca	0.0159	0.0222	0.0156	0.0219	0.0035	1.0040	0.0002	0.0014
Ti	0.0044	0.0074	0.0044	0.0073	0.0008	0.9656	0.0000	0.0097
O	43.9863	-	43.3338	-	24	-	-	-

Opx

Element	El. mass %	Ox %	Norm El%	Norm %	At prop	c/k-ratio	k-ratio	k-(calc)
Na	0.0411	0.0554	0.0411	0.0554	0.0149	0.9320	0.0004	0.0465
Ni	0.0542	0.0690	0.0540	0.0687	0.0077	1.1340	0.0005	0.0006
Fe	5.1560	6.6326	5.1331	6.6037	0.7669	1.0024	0.0514	1.0491
Si	25.3763	54.2843	25.2663	54.0491	7.5040	1.0342	0.2454	1.0405
K	0.0024	0.0028	0.0024	0.0028	0.0005	0.9924	0.0000	0.0012
Mg	20.5771	34.1203	20.4891	33.9746	7.0322	0.9540	0.2156	2.1592
Cr	0.2122	0.3102	0.2113	0.3088	0.0339	0.9871	0.0021	0.3858
Mn	0.1270	0.1641	0.1265	0.1634	0.0192	1.0534	0.0012	0.0036
Al	2.1559	4.0735	2.1466	4.0564	0.6635	1.0785	0.0200	0.4355
Ca	0.4488	0.6281	0.4481	0.6266	0.0934	1.0120	0.0044	0.0394
Ti	0.0551	0.0919	0.0549	0.0915	0.0096	0.9890	0.0006	0.1271
O	46.2269	-	46.0271	-	24	-	-	-

Cpx1

Element	El. mass %	Ox %	Norm El%	Norm %	At prop	c/k-ratio	k-ratio	k-(calc)
Na	0.9431	1.2708	0.9497	1.2798	0.3598	0.9778	0.0096	1.0310
Ni	0.0228	0.0290	0.0229	0.0291	0.0034	1.1225	0.0002	0.0002
Fe	1.8368	2.3600	1.8464	2.3760	0.2882	1.0043	0.0183	0.3726

Si	23.9268	51.1860	24.0856	51.5224	7.4706	0.9802	0.2440	1.0344
K	0.0014	0.0016	0.0014	0.0017	0.0003	0.9454	0.0000	0.0008
Mg	9.2844	15.3936	9.3472	15.5008	3.3503	0.9850	0.0942	0.9430
Cr	0.5411	0.7908	0.5446	0.7959	0.0912	1.0082	0.0054	0.9634
Mn	0.0622	0.0803	0.0625	0.0807	0.0099	1.0576	0.0006	0.0017
Al	3.3956	6.4160	3.4184	6.4568	1.1036	0.9830	0.0345	0.7505
Ca	15.3172	21.4324	15.4164	21.5708	3.3513	1.0010	0.1530	1.3598
Ti	0.2281	0.3804	0.2296	0.3830	0.0418	1.0102	0.0023	0.5154
O	43.7844	-	44.0736	-	24	-	-	-

Cpx2

Elemen	El. mass	Ox	Norm	Norm	At prop	c/k-	k-	k-
Na	0.9558	1.2881	0.9879	1.3329	0.3689	0.9562	0.0100	1.0640
Ni	0.0553	0.0704	0.0572	0.0728	0.0083	1.1300	0.0005	0.0006
Fe	2.4833	3.1933	2.5717	3.3050	0.3933	1.0036	0.0247	0.5047
Si	23.0300	49.2683	23.8417	51.0000	7.2420	1.0086	0.2279	0.9662
K	0.1383	0.1665	0.1426	0.1718	0.0318	1.0134	0.0014	0.0800
Mg	12.4333	20.6200	12.8717	21.3467	4.5180	0.9715	0.1279	1.2814
Cr	0.4203	0.6143	0.4348	0.6354	0.0714	1.0020	0.0042	0.7522
Mn	0.0569	0.0734	0.0589	0.0761	0.0092	1.0560	0.0005	0.0016
Al	4.4283	8.3700	4.5800	8.6567	1.4543	1.0112	0.0438	0.9527
Ca	8.6417	12.0900	8.9400	12.5117	1.9050	1.0055	0.0859	0.7634
Ti	0.5170	0.8618	0.5333	0.8896	0.0964	1.0021	0.0052	1.1805
O	43.4550	-	44.9767	-	24	-	-	-

Spinel

Element	El. mass %	Ox mass%	Norm El%	Norm ox%	At prop	c/k-std	k-value	k-(std)
Na	0.0115	0.0154	0.0112	0.0151	0.0046	1.0857	0.0001	0.0115
Ni	0.1860	0.2367	0.1829	0.2328	0.0295	1.1083	0.0017	0.0021
Fe	9.6950	12.4800	9.5400	12.2750	1.6195	0.9799	0.0990	2.0190
Si	0.0000	0.0000	0.0000	0.0000	0.0000	0.7777	0.0000	0.0000
K	0.0037	0.0045	0.0036	0.0044	0.0009	1.0003	0.0000	0.0022
Mg	11.8900	19.7150	11.7000	19.4000	4.5600	1.0415	0.1143	1.1450
Cr	8.9200	13.0350	8.7800	12.8300	1.6030	0.9485	0.0941	16.8899
Mn	0.0865	0.1117	0.0852	0.1100	0.0148	1.0218	0.0008	0.0025
Al	29.6400	56.0000	29.1550	55.0950	10.2395	1.0508	0.2828	6.1474
Ca	0.0075	0.0105	0.0074	0.0104	0.0017	0.9727	0.0001	0.0007
Ti	0.0187	0.0312	0.0184	0.0307	0.0037	0.9340	0.0002	0.0458
O	41.1800	-	40.5200	-	24.0000	-	-	-

S3 Supplementary figures

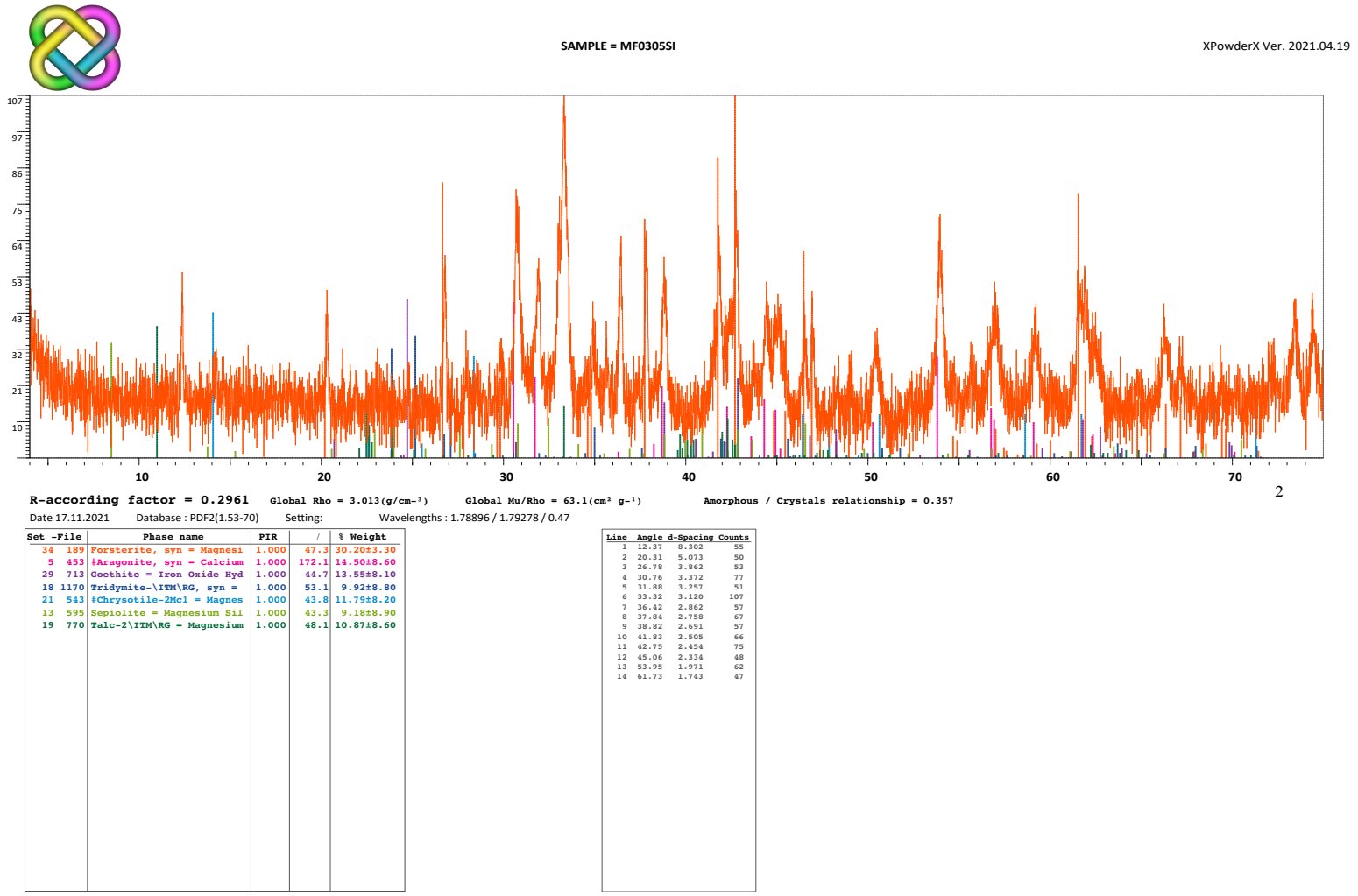

Set -File	Phase name	PIR	/	% Weight
34 189	Forsterite, syn = Magnesi	1.000	47.3	30.20±3.30
5 453	#Aragonite, syn = Calcium	1.000	172.1	14.50±8.60
29 713	Goethite = Iron Oxide Hyd	1.000	44.7	13.55±8.10
18 1170	Tridymite-\ITM\RG, syn =	1.000	53.1	9.92±8.80
21 543	#Chrysotile-2Mc1 = Magnes	1.000	43.8	11.79±8.20
13 595	Sepiolite = Magnesium Sil	1.000	43.3	9.18±8.90
19 770	Talc-2\ITM\RG = Magnesium	1.000	48.1	10.87±8.60

Line	Angle	d-Spacing	Counts
1	12.37	8.302	55
2	20.31	5.073	50
3	26.78	3.862	53
4	30.76	3.372	77
5	31.88	3.257	51
6	33.32	3.120	107
7	36.42	2.862	57
8	37.84	2.758	67
9	38.82	2.691	57
10	41.83	2.505	66
11	42.75	2.454	75
12	45.06	2.334	48
13	53.95	1.971	62
14	61.73	1.743	47

Figure 2S: XRD measurement of Bottle 2_2 (Batch10) with possible mineralogical composition.

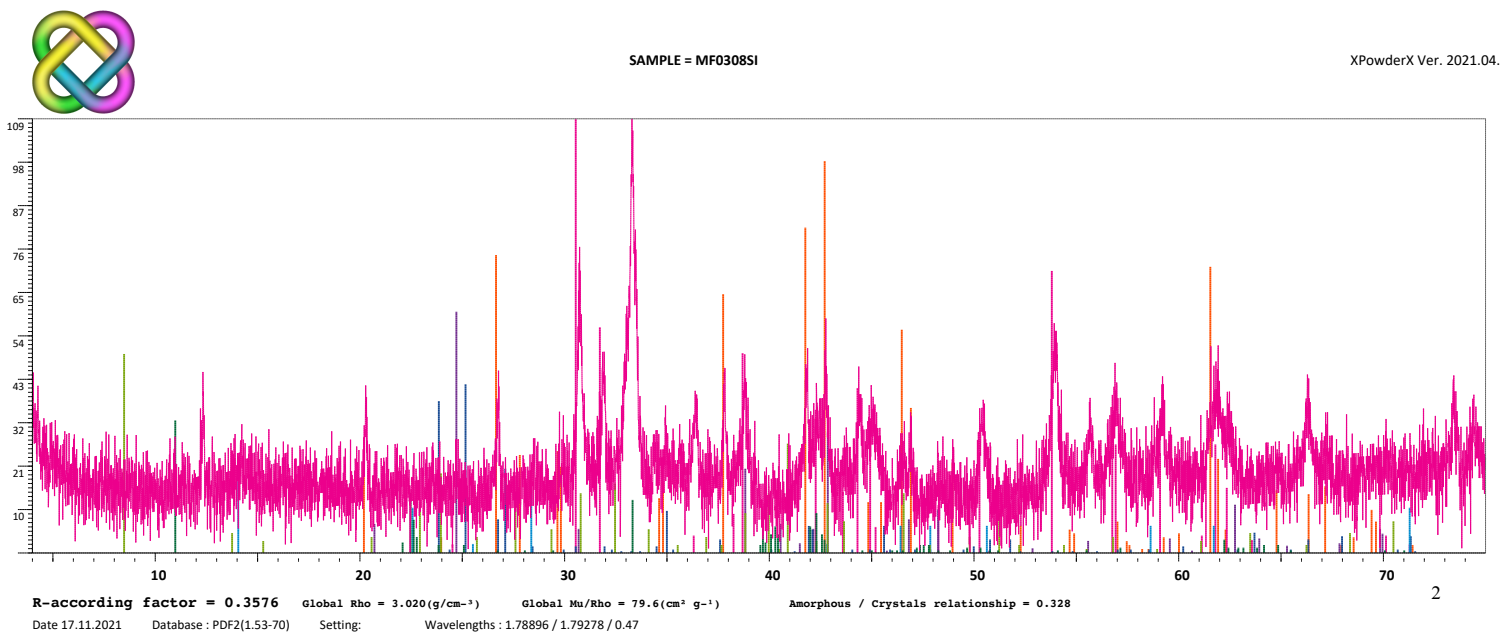

Set	-File	Phase name	PIR	/	% Weight
34	189	Forsterite, syn = Magnesi	1.000	47.3	23.11±3.90
5	453	#Aragonite, syn = Calcium	1.000	172.1	28.51±3.10
29	713	Goethite = Iron Oxide Hyd	1.000	44.7	14.52±6.60
18	1170	Tridymite-\ITM\RG, syn =	1.000	53.1	9.72±7.80
21	543	#Chrysotile-2Mc1 = Magnes	1.000	43.8	5.18±5.20
13	595	Sepiolite = Magnesium Sil	1.000	43.3	11.23±7.10
19	770	Talc-2\ITM\RG = Magnesium	1.000	48.1	7.72±7.70

Line	Angle	d-Spacing	Counts	Line	Angle	d-Spacing	Counts	Line	Angle	d-Spacing	Counts	Line	Angle	d-Spacing	Counts	Line	Angle	d-Spacing	Counts
1	4.30	23.842	31	36	17.04	6.037	20	71	31.42	3.303	29	106	52.71	2.014	21	141	70.18	1.555	28
2	5.02	20.424	28	37	17.07	6.026	26	72	31.88	3.257	44	107	52.82	2.011	20	142	71.21	1.536	22
3	5.79	17.710	30	38	17.09	6.019	20	73	33.31	3.120	97	108	53.95	1.971	47	143	71.26	1.535	22
4	6.56	15.633	25	39	17.11	6.012	26	74	34.47	3.018	30	109	55.67	1.915	39	144	71.28	1.535	21
5	6.71	15.284	21	40	17.29	5.950	22	75	34.93	2.980	37	110	56.92	1.877	40	145	72.36	1.515	21
6	6.78	15.126	27	41	17.69	5.817	18	76	35.62	2.924	32	111	58.18	1.839	19	146	72.68	1.509	29
7	7.42	13.823	24	42	17.71	5.810	22	77	36.37	2.866	38	112	58.23	1.838	23	147	73.43	1.496	44
8	7.95	12.903	21	43	18.37	5.603	26	78	37.16	2.807	25	113	58.26	1.837	25	148	74.43	1.478	32
9	8.08	12.696	18	44	19.04	5.408	21	79	37.33	2.794	25	114	59.18	1.811	42				
10	8.15	12.587	22	45	19.78	5.207	22	80	37.82	2.760	46	115	60.13	1.785	29				
11	8.17	12.556	20	46	20.28	5.080	42	81	38.80	2.692	50	116	60.20	1.783	25				
12	8.83	11.619	22	47	20.75	4.966	25	82	41.83	2.505	44	117	60.33	1.780	28				
13	9.34	10.974	21	48	20.77	4.962	19	83	42.39	2.474	27	118	60.37	1.779	22				
14	9.61	10.678	22	49	20.79	4.957	22	84	42.73	2.455	41	119	60.45	1.776	28				
15	9.69	10.590	22	50	21.17	4.869	22	85	43.76	2.400	31	120	60.54	1.774	29				
16	9.78	10.493	19	51	21.19	4.864	22	86	43.98	2.388	23	121	60.95	1.763	22				
17	9.97	10.293	21	52	21.29	4.842	24	87	44.42	2.366	34	122	61.03	1.761	19				
18	10.29	9.974	19	53	21.83	4.723	27	88	45.07	2.333	39	123	61.84	1.740	41				
19	10.34	9.926	23	54	21.87	4.715	20	89	46.54	2.264	28	124	62.37	1.727	38				
20	10.72	9.575	28	55	22.11	4.664	23	90	46.59	2.261	25	125	63.36	1.703	27				
21	10.81	9.496	21	56	22.27	4.631	26	91	46.85	2.249	26	126	63.41	1.702	21				
22	10.87	9.443	20	57	23.06	4.475	21	92	48.30	2.186	22	127	64.15	1.684	22				
23	11.47	8.951	24	58	23.56	4.381	27	93	49.04	2.155	22	128	64.29	1.681	27				
24	12.34	8.322	39	59	24.71	4.180	20	94	49.55	2.134	22	129	64.36	1.679	27				
25	13.16	7.805	23	60	25.14	4.110	22	95	50.41	2.100	32	130	64.53	1.675	26				
26	13.31	7.718	22	61	26.06	3.967	26	96	51.10	2.073	22	131	64.85	1.668	22				
27	14.23	7.221	32	62	26.74	3.868	37	97	51.16	2.071	24	132	66.32	1.635	28				
28	15.02	6.843	25	63	27.54	3.757	23	98	51.19	2.070	19	133	67.23	1.615	24				
29	15.23	6.750	27	64	27.66	3.741	20	99	51.22	2.069	19	134	67.74	1.604	24				
30	15.55	6.611	31	65	27.93	3.706	20	100	51.56	2.056	18	135	67.89	1.601	25				
31	16.26	6.325	28	66	28.53	3.630	22	101	51.63	2.054	19	136	68.05	1.598	24				
32	16.63	6.185	19	67	28.64	3.616	26	102	51.68	2.052	21	137	68.54	1.588	20				
33	16.70	6.159	19	68	29.94	3.462	34	103	51.77	2.048	21	138	68.97	1.579	27				
34	16.72	6.152	18	69	30.18	3.435	21	104	52.38	2.026	29	139	69.01	1.579	23				
35	16.97	6.062	21	70	30.74	3.374	63	105	52.51	2.022	18	140	69.53	1.568	21				

Figure 3S: XRD measurement of Bottle 2_3 (Batch5) with possible mineralogical composition.

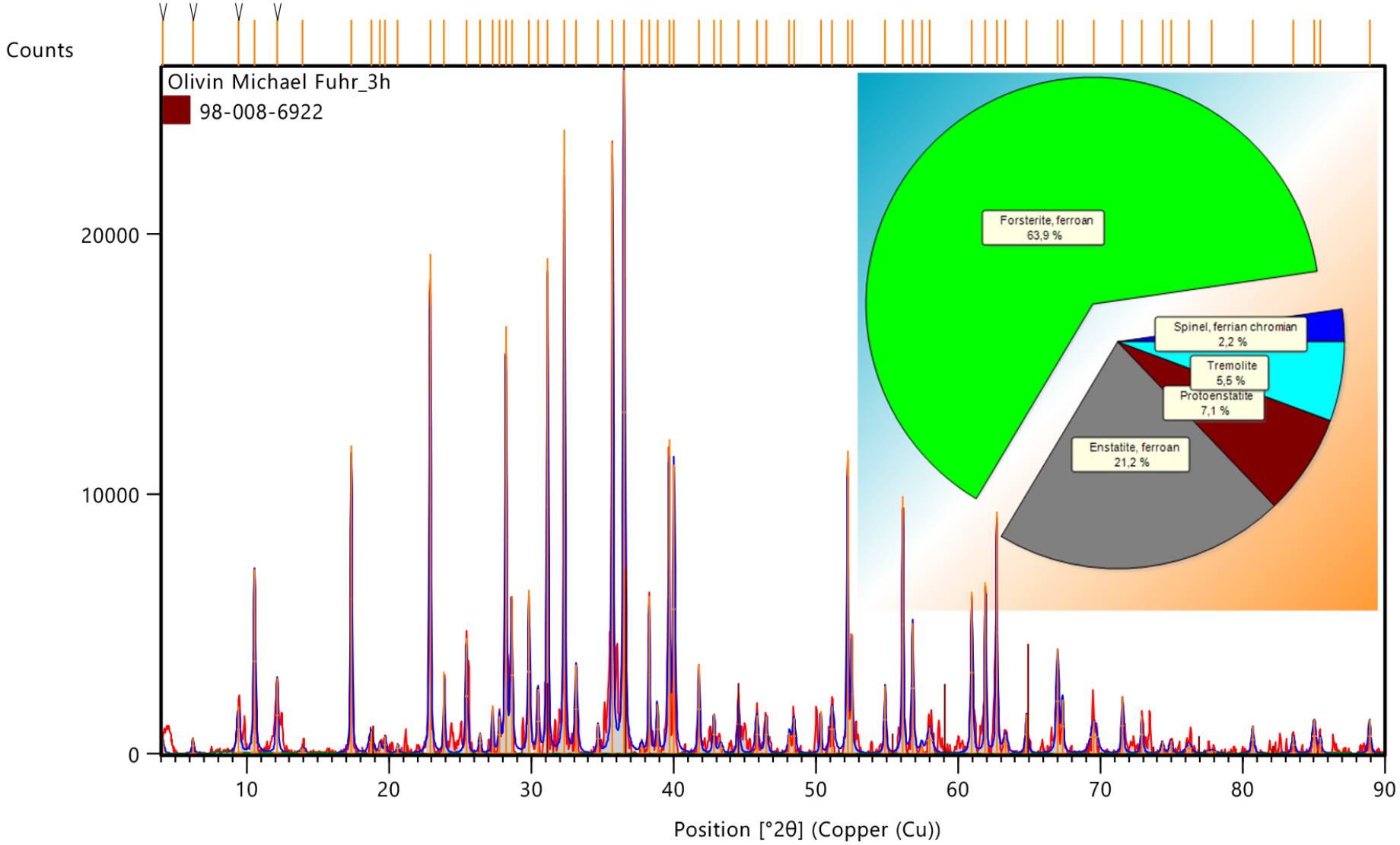

Figure 4S: XRD measurement of UMS with possible mineralogical composition after Rietveld quantification.

Table 6S: Chemical composition of precipitates (1_1 – 3_3) and UMS (ol1 – ol3) measured with ICP-OES after full digestion. Si1 – Si3 are internal Si-standards, St.4 is IAPSO.

	weighe	olum	Al	RSD	Ba_PW	RSD	Ca	RSD	Cr	RSD	Fe	RSD	K	RSD	Li	RSD	Mg	RSD	Mn	RSD	Na_PW		Ni	RSD	Sr	RSD	Ti	RSD	Si	RSD
	g	ml	ppm	%	ppb	%	ppm	%	ppb	%	ppm	%	ppm	%	ppm	%	ppm	%	ppb	%	ppm		ppb	%	ppb	%	ppm	%	ppm	%
St.4			100.47	0.15	84.89	0.12	25.2	0.13	302	1.30	75.1	0.19	37.52	0.23	0.05	0.37	24.99	0.11	986.86	0.33	11024.38	0.18	151.39	4.54	301.44	0.32	7.52	0.1		
1_1	0.001	4.40	1.30	0.66	19.2	1.11	31.2	0.31	166	1.65	6.00	0.70	2.13	0.89	0.01	7.95	21.34	0.28	90.31	0.79	6372.82	0.16	230.72	3.16	36.26	0.80	0.09	4.0	19.16	1.11
2_1	0.001	4.40	1.15	1.13	21.0	0.24	34.6	0.08	166	0.18	7.01	0.72	2.10	1.44	0.01	4.49	24.69	0.12	105.36	1.03	6218.27	0.14	294.23	3.97	35.94	1.49	0.09	2.6	21.02	0.24
3_1	0.001	4.40	1.54	0.73	21.8	0.13	46.7	0.11	212	0.86	6.99	0.10	3.22	0.37	0.01	5.60	24.30	0.17	109.99	0.36	6698.79	0.18	274.75	6.08	42.07	1.24	0.10	4.4	21.78	0.13
1_2	8E-04	4.40	1.20	1.64	20.0	1.82	19.7	0.17	182	1.11	6.90	0.21	1.85	1.72	0.01	5.28	23.11	0.04	95.67	1.29	6130.14	0.11	283.45	3.84	29.26	0.74	0.09	5.6	20.00	1.82
2_2	0.001	4.40	1.93	0.42	38.9	0.63	38.4	0.07	274	1.29	7.90	0.36	2.22	0.87	0.01	8.61	26.71	0.08	115.98	0.50	6513.37	0.10	323.24	10.57	37.28	1.91	0.12	2.4	38.04	0.21
3_2	0.001	4.40	2.04	0.34	15.1	0.32	31.5	0.07	285	0.57	9.57	0.48	4.12	0.40	0.01	3.96	32.00	0.07	137.76	0.72	7266.14	0.07	405.26	4.24	39.13	0.43	0.13	2.5	15.08	0.32
1_3	9E-04	4.40	1.48	0.86	20.3	0.29	34.1	0.15	212	0.38	6.67	0.21	2.55	0.32	0.01	5.80	22.41	0.15	90.95	0.65	6794.26	0.05	270.95	7.09	36.97	1.09	0.10	3.1	20.28	0.29
2_3	1E-03	4.40	1.47	0.64	19.3	0.31	36.5	0.04	208	1.62	6.34	0.08	3.77	0.46	0.01	3.46	20.62	0.08	89.87	1.11	6287.14	0.16	258.50	1.68	37.68	0.60	0.10	2.6	19.27	0.31
3_3	0.001	4.40	1.70	0.37	21.5	0.31	50.0	0.26	244	1.76	7.01	0.40	2.32	0.64	0.01	9.24	22.78	0.23	95.50	0.47	6312.26	0.11	257.31	5.91	41.63	0.75	0.11	3.9	21.49	0.31
St.4			101.01	0.19	84.5	0.77	25.4	0.21	298	2.39	75.2	0.81	37.59	0.07	0.05	1.10	25.05	0.20	988.80	0.36	11031.81	0.18	159.71	6.26	301.12	0.63	7.52	0.1		
Si1	1E-03	4.40	13.61	1.46	44.2	0.25	14.4	0.04	54	10.68	17.2	0.35	3.89	0.70	0.01	2.76	8.11	0.08	245.44	0.30	5933.38	0.10	19.97	47.83	93.38	0.28	3.34	0.0	43.09	0.21
Si2	1E-03	4.40	13.99	0.88	45.4	0.61	14.4	0.08	51	4.18	16.9	0.55	4.16	0.50	0.01	4.01	7.84	0.10	239.81	0.56	7436.80	0.14	13.56	31.50	98.76	0.26	3.49	0.0	43.88	0.45
Si3	0.001	4.40	18.26	0.26	58.4	0.07	19.1	0.09	62	4.81	22.4	0.66	5.07	0.41	0.01	7.73	10.48	0.09	318.73	0.38	5900.44	0.02	28.55	11.97	118.50	0.36	3.52	0.1	57.15	0.09
Ol1	0.001	4.40	1.36	0.13	38.5	0.49	1.9	0.10	189	9.38	12.6	0.40	3.67	0.55	0.01	2.87	48.84	0.19	187.71	0.24	6865.51	0.05	473.65	1.26	25.14	1.13	0.09	2.6	37.84	0.99
Ol2	0.001	4.40	1.08	1.56	35.4	0.96	1.7	0.29	133	0.85	13.0	0.74	3.25	1.22	0.01	8.15	48.35	0.12	185.87	0.57	6297.60	0.10	470.37	1.02	24.08	1.89	0.07	2.5	34.79	0.51
Ol3	9E-04	4.40	0.92	0.45	28.9	0.26	1.3	0.19	115	2.30	9.32	0.14	3.26	1.18	0.01	10.76	37.43	0.11	138.14	0.21	7009.01	0.20	354.80	2.42	24.78	1.06	0.07	3.5	28.17	1.14
B1		4.40	-0.02	-28.67	0.03	281.87	0.12	1.59	11.1	43.66	0.16	4.01	5.39	0.41	0.01	5.47	0.00	####	1.72	82.47	14456.36	0.17	14.05	125.83	48.81	0.70	0.02	8.8	0.03	281.87
B2		4.40	-0.03	-8.39	-0.12	-55.15	0.08	3.21	8.0	76.22	0.15	4.23	4.62	0.37	0.01	2.77	-0.01	-1.03	-0.70	-82.28	12540.00	0.13	21.47	30.14	42.57	0.35	0.02	15.9	-0.12	-55.15
B3		4.40	-0.03	-32.44	-0.11	-23.91	0.12	1.13	9.8	9.61	0.16	3.17	5.71	0.50	0.01	5.81	0.03	1.59	2.85	40.64	14585.79	0.12	22.06	41.45	50.51	0.69	0.02	6.6	-0.11	-23.91
St.4			100.98	0.10	84.66	0.44	25.4	0.17	299	1.27	75.1	0.17	37.62	0.09	0.05	0.38	25.02	0.04	988.73	0.10	11033.86	0.16	152.21	13.52	301.03	0.15	7.50	0.1		

St.4 taget value	100.3		25.01	300	74.9	37.5	0.05	25	999	11035	150.5	300.6	7.493
mean value	100.82	84.68	25.36	299.70	75.14	37.58	0.05	25.02	988.13	11030.01	154.44	301.20	7.51
SD	0.305	0.2	0.106	1.796	0.01	0.05	0	0.029	1.1002	4.98712	4.583	0.218	0.009
RSD	0.302	0.24	0.419	0.599	0.02	0.14	1.41	0.116	0.1113	0.04521	2.967	0.072	0.123
dev. of target value	0.5		1.404	-0.099	0.27	0.2	-1.74	0.081	-1.088	-0.04517	2.649	0.199	0.27

Table 7S: Idealized composition of the precipitates as recovered from the bottles, according to the calculation explained in the methods part.

	Al	Ba	Ca	Cr	Fe	K	Li	Mg	Mn	Na	Ni	Sr	Ti	Si	C	O	H	mol-%	wt-%
Batch5																			
UMS	0.035	0	0.034	0.002	0.174	0	0.001	1.543	0.003		0.006	0	0.001	1	0	4.028		25	31.919
Sepiolit								0.667						1		3.833	2.333	12.35	12.193
Chrysotile								1.5						1		4.5	2	2.6	3.158
Talc								0.75						1		3	0.5	1.1	0.914
Aragonite			1									0		0	1	3		55.4	48.604
$Fe(OH)_3$					1											3	3	2.35	2.139
Al_2O_3	2															3		1.2	1.073
$C_{i,blk}$	0.080	0	1.370	0.001	0.163	0	0.001	1.256	0.002	0	0.004	0	0.001	1	1.350	8.154	0.922	100	100
$C_{i,prec}$	0.079	0	1.370	0.006	0.165	0	0.001	1.247	0.002	0	0.006	0	0.003	1	1.350	4.524	0		
Batch10																			
UMS	0.035	0	0.034	0.002	0.174	0	0.001	1.543	0.003	0	0.006	0	0.001	1	0	4.02		37.05	45.965
Sepiolite								0.667						1		3.833	2.333	14.4	13.254
Chrysotile								1.5						1		4.5	2	1.1	1.299
Talc								0.75						1		3	0.5	0.4	0.323
Aragonite			1									0		0	1	3		43.4	37.033
$Fe(OH)_3$					1											3	3	2.4	2.125
Al_2O_3	2															3		1.25	1.087
$C_{i,blk}$	0.072	0	0.844	0.005	0.168	0	0.001	1.298	0.002	0	0.004	0	0.001	1	0.820	6.498	0.816	100	100
$C_{i,prec}$	0.072	0	0.844	0.005	0.168	0	0.001	1.296	0.002	0	0.007	0	0.003	1	0.827	4.196	0		

	Al	Ba	Ca	Cr	Fe	K	Li	Mg	Mn	Na	Ni	Sr	Ti	Si	C	O	H	mol-%	wt-%
Batch20																			
UMS	0.035	0	0.034	0.002	0.174	0	0.001	1.543	0.003	0	0.006	0	0.001	1	0	4.02		29.9	38.012
Sepiolite								0.667						1		3.833	2.333	11.1	10.469
Chrysotile								1.5						1		4.5	2	2	2.421
Talc								0.75						1		3	0.5	0.4	0.331
Aragonite			1									0		0	1	3		53.8	47.042
$Fe(OH)_3$					1											3	3	1.9	1.724
Al_2O_3	2															3		0.9	0.802
$C_{i,blk}$	0.065	0	1.262	0.002	0.163	0	0.001	1.310	0.001	0	0.004	0	0.001	1	1.24	7.761	0.825	100	100
$C_{i,prec}$	0.067	0	1.260	0.005	0.162	0	0.001	1.312	0.003	0	0.006	0	0.003	1	1.24	4.490	0		

Table 8S: Measured mean temperature (T), pH, TA, major and trace element (ICP-OES) for water samples of Batch20. Other values are calculated according to the methods section.

Sample	temp. (°C)	time (d)	[Si] (µmol/l)	SD [Si]	TA (mmol/l)	SD TA	[Ni] (µmol/l)	SD [Ni]	[Mn] (µmol/l)	SD Mn	[Ca]	SD [Ca]	[Mg]	SD [Mg]	pH	SD pH	pCO2 (µatm)	SD pCO2 (µatm)
Blank	21.50	0.00	-0.74	0.55	2.36	0.01	0.01	0.15	-0.07	0.01	7.92	0.02	53.34	0.13	7.94		542.63	
1	21.47	0.02	11.38	0.33	2.46	0.01	0.02	0.20	0.05	0.01	8.05	0.01	53.77	0.48	8.02	0.01	455.43	10.59
2	22.03	0.08	22.27	0.44	2.47	0.01	0.17	0.23	0.13	0.01	8.26	0.01	55.16	1.31	8.04	0.01	427.55	15.17
3	22.73	0.16	32.78	0.83	2.54	0.02	0.22	0.34	0.18	0.01	8.00	0.01	53.50	0.44	8.07	0.01	411.01	7.82
4	23.10	0.34	48.25	0.74	2.62	0.01	0.49	0.18	0.27	0.01	8.01	0.01	53.63	0.30	8.10	0.00	384.66	10.53
5	22.90	0.95	75.82	1.17	2.65	0.01	0.59	0.21	0.39	0.01	8.10	0.01	54.25	0.82	8.15	0.01	337.47	6.42
6	23.20	1.26	83.91	0.83	2.59	0.01	0.66	0.16	0.39	0.02	7.94	0.01	53.60	0.44	8.12	0.00	364.55	2.62
7	23.17	2.07	108.02	1.33	2.29	0.02	0.88	0.18	0.53	0.01	7.77	0.01	53.76	0.45	7.99	0.01	462.70	7.86
8	23.13	3.05	130.52	4.15	2.24	0.01	0.96	0.32	0.61	0.01	7.72	0.02	54.19	0.17	7.98	0.00	461.06	5.09
9	23.13	4.06	146.04	2.12	2.15	0.01	1.05	0.29	0.53	0.01	7.57	0.02	54.18	0.44	7.99	0.00	432.83	5.24
10	22.87	7.05	181.37	1.25	1.97	0.01	1.21	0.17	0.59	0.02	7.39	0.01	53.91	0.47	8.01	0.01	377.92	7.69
11	23.30	10.09	205.92	0.50	1.90	0.01	1.27	0.18	0.59	0.02	7.28	0.01	54.03	0.19	8.01	0.01	362.41	4.95
12	22.40	15.11	244.88	2.20	1.78	0.01	1.35	0.20	0.58	0.01	7.16	0.02	54.24	0.19	8.02	0.03	326.52	24.95
13	22.30	22.13	285.83	2.43	1.65	0.01	1.23	0.31	0.53	0.02	6.95	0.01	54.08	0.56	8.10	0.00	246.84	1.69
14	22.90	29.26	316.21	2.02	1.59	0.01	1.29	0.22	0.49	0.01	6.84	0.02	54.17	0.30	8.11	0.01	226.04	7.73
15	22.73	36.24	337.45	2.38	1.50	0.02	1.33	0.17	0.45	0.02	6.81	0.01	54.78	0.52	8.15	0.00	190.79	1.13
16	22.53	43.29	355.45	0.86	1.42	0.00	1.47	0.31	0.44	0.01	6.67	0.01	54.17	0.20	8.18	0.02	165.42	7.75
17	22.53	50.18	361.88	2.62	1.39	0.01	1.45	0.21	0.41	0.02	6.67	0.01	54.36	0.41	8.19	0.01	158.09	6.34
18	22.27	64.19	375.92	0.76	1.36	0.02	1.31	0.22	0.34	0.01	6.61	0.01	54.49	0.46	8.22	0.00	140.90	2.77
19	21.97	78.25	384.01	1.25	1.41	0.03	1.37	0.13	0.34	0.02	6.58	0.01	54.06	0.54	8.24	0.01	138.21	6.21
20	21.90	92.33	399.69	8.53	1.36	0.02	1.29	0.29	0.30	0.02	6.66	0.01	54.58	0.16	8.23	0.01	140.44	3.28
21	21.93	106.33	401.01	5.22	1.29	0.01	1.12	0.22	0.28	0.01	6.73	0.01	54.82	0.22	8.21	0.00	138.07	2.55
22	21.93	120.31	414.22	1.88	1.29	0.00	1.33	0.15	0.29	0.01	6.77	0.01	54.72	0.18	8.21	0.02	137.88	7.91
23	22.80	134.16	421.82	1.31	1.27	0.02	1.23	0.26	0.31	0.02	6.83	0.01	55.14	0.39	8.21	0.01	138.83	9.52

Table 9S: Measured mean temperature (T), pH, TA, major and trace element (ICP-OES) for water samples of Batch10. Other values are calculated according to the methods section.

Sample	temp. (°C)	time (d)	[Si] (µmol/l)	SD [Si]	TA (mmol/l)	SD TA	[Ni] (µmol/l)	SD [Ni]	[Mn] (µmol/l)	SD Mn	[Ca]	SD [Ca]	[Mg]	SD [Mg]	pH	SD pH	pCO2 (µatm)	SD pCO2 (µatm)
Blank	21.50	0.00	-0.74		2.36	0.01	0.01	0.15	-0.07	0.01	7.92	0.02	53.34	0.13	7.94		542.63	
1	21.50	0.03	6.20	0.42	2.46	0.01	-0.17	0.11	0.00	0.00	8.04	0.02	53.83	0.73	8.03	0.00	443.07	2.09
2	22.23	0.08	10.61	0.50	2.46	0.01	0.14	0.28	0.03	0.02	8.02	0.02	53.64	0.44	8.03	0.00	444.34	3.44
3	23.20	0.17	15.45	0.38	2.50	0.01	0.07	-0.01	0.06	0.01	8.12	0.02	54.43	1.33	8.04	0.00	436.50	1.95
4	23.50	0.35	22.99	0.63	2.50	0.01	0.23	0.24	0.12	0.01	7.98	0.02	53.49	0.28	8.05	0.01	420.28	9.47
5	23.33	0.96	37.02	0.67	2.56	0.02	0.27	0.17	0.21	0.01	7.95	0.02	53.33	0.44	8.06	0.02	425.28	25.80
6	23.53	1.27	41.32	0.34	2.55	0.02	0.34	0.18	0.25	0.02	7.97	0.01	53.58	0.22	8.06	0.03	418.80	35.22
7	23.47	2.07	52.82	1.31	2.39	0.03	0.61	0.33	0.29	0.02	7.98	0.01	53.67	0.29	8.04	0.06	420.86	63.98
8	23.33	3.06	63.00	1.16	2.32	0.02	0.77	0.31	0.35	0.01	7.86	0.02	53.59	0.02	7.99	0.02	462.81	21.45
9	23.43	4.07	70.65	1.98	2.23	0.01	0.80	0.17	0.26	0.02	7.85	0.01	54.43	0.31	7.96	0.01	487.34	9.01
10	23.03	7.06	89.91	2.02	2.19	0.03	1.00	0.21	0.37	0.01	7.61	0.01	53.41	0.21	7.95	0.01	491.54	15.46
11	23.37	10.09	102.95	1.75	2.12	0.01	1.14	0.12	0.42	0.02	7.64	0.01	53.93	0.19	7.91	0.01	519.99	10.93
12	22.37	15.12	121.83	1.57	2.06	0.01	1.17	0.24	0.41	0.02	7.52	0.01	53.56	0.12	7.93	0.00	487.08	4.70
13	22.17	22.14	142.96	3.25	1.95	0.02	1.04	0.25	0.44	0.01	7.44	0.01	53.57	0.27	7.95	0.01	438.31	4.88
14	22.90	29.26	160.79	1.72	1.97	0.02	1.29	0.19	0.46	0.02	7.41	0.02	53.85	0.12	7.95	0.00	436.43	5.87
15	22.70	36.25	176.42	2.81	1.91	0.02	1.24	0.18	0.48	0.01	7.33	0.01	53.77	0.29	7.97	0.00	402.82	4.01
16	22.70	43.30	188.86	2.73	1.84	0.01	1.08	0.17	0.46	0.02	7.26	0.01	53.57	0.26	7.97	0.01	375.56	24.18
17	22.63	50.19	198.55	2.20	1.84	0.01	1.10	0.25	0.46	0.01	7.28	0.01	53.97	0.17	7.96	0.01	401.30	11.47
18	22.53	64.20	223.04	3.65	1.81	0.03	1.10	0.25	0.48	0.01	7.28	0.02	54.57	0.68	8.00	0.00	351.26	5.04
19	21.87	78.25	236.41	6.74	1.81	0.05	1.15	0.10	0.48	0.01	7.19	0.01	53.82	0.38	8.01	0.01	343.41	15.62
20	22.00	92.33	256.55	5.74	1.74	0.02	1.28	0.21	0.48	0.02	7.20	0.01	53.77	0.12	8.00	0.01	339.26	2.36
21	22.27	106.33	266.13	1.51	1.66	0.02	1.15	0.18	0.49	0.01	7.26	0.01	54.08	0.30	8.01	0.00	314.77	4.29
22	22.27	120.31	279.00	6.19	1.62	0.03	1.39	0.22	0.50	0.01	7.28	0.02	54.04	0.14	7.99	0.01	324.64	12.45
23	22.90	134.16	286.60	6.44	1.62	0.02	1.31	0.23	0.49	0.02	7.32	0.02	54.04	0.16	7.99	0.01	330.85	17.11

Table 10S: Measured mean temperature (T), pH, TA, major and trace element (ICP-OES) for water samples of Batch5. Other values are calculated according to the methods section.

Sample	temp. (°C)	time (d)	[Si] (µmol/l)	SD [Si]	TA (mmol/l)	SD TA	[Ni] (µmol/l)	SD [Ni]	[Mn] (µmol/l)	SD Mn	[Ca]	SD [Ca]	[Mg]	SD [Mg]	pH	SD pH	pCO2 (µatm)	SD pCO2 (µatm)
Blank	21.50	0.00	-0.74		2.36	0.01	0.01	0.15	-0.07	0.01	7.92	0.02	53.34	0.13	7.94		542.63	
1	21.63	0.03	2.90	0.25	2.44	0.01	-0.12	-0.23	-0.03	0.02	7.97	0.01	53.37	0.37	8.00	0.02	474.31	29.76
2	22.57	0.09	5.10	0.29	2.47	0.00	-0.09	0.15	-0.02	-0.01	8.07	0.01	54.08	0.46	8.00	0.03	481.98	39.24
3	23.40	0.17	7.47	0.34	2.48	0.01	-0.05	-0.20	0.02	0.02	8.04	0.01	53.82	0.19	8.00	0.02	478.29	27.62
4	23.80	0.35	10.88	0.44	2.44	0.01	0.08	0.00	0.03	0.00	8.02	0.01	53.73	0.56	8.01	0.02	462.68	25.61
5	23.53	0.96	18.64	0.60	2.45	0.01	0.25	0.17	0.10	0.02	8.08	0.01	54.20	0.08	8.01	0.02	463.25	24.20
6	23.23	1.28	21.06	0.53	2.49	0.02	0.14	0.22	0.10	0.02	7.98	0.01	53.53	0.28	8.03	0.02	446.89	25.31
7	23.67	2.08	26.35	0.53	2.51	0.02	0.33	0.15	0.15	0.01	8.10	0.01	54.29	0.37	8.03	0.01	444.62	13.62
8	23.67	3.06	31.08	0.76	2.52	0.01	0.53	0.15	0.09	0.01	7.93	0.01	53.55	0.31	8.05	0.01	422.41	12.31
9	23.67	4.07	34.33	0.87	2.50	0.02	0.53	0.06	0.06	0.02	7.98	0.01	54.15	0.89	8.05	0.01	416.85	3.82
10	23.27	7.07	42.91	0.33	2.39	0.04	0.50	0.17	0.10	0.02	7.85	0.01	53.77	0.34	7.99	0.03	480.10	23.71
11	23.37	10.10	50.34	0.66	2.27	0.01	0.60	0.11	0.15	0.01	7.73	0.01	53.42	0.09	7.90	0.01	575.42	12.26
12	22.27	15.12	60.08	0.44	2.21	0.01	0.71	0.12	0.22	0.02	7.73	0.02	53.57	0.20	7.89	0.00	574.05	5.34
13	22.23	22.15	68.67	0.33	2.18	0.01	1.15	0.28	0.25	0.01	7.69	0.01	53.68	0.12	7.89	0.00	569.15	3.79
14	22.90	29.26	76.59	0.57	2.18	0.01	1.00	0.14	0.27	0.02	7.65	0.01	53.65	0.41	7.87	0.00	600.72	4.80
15	22.53	36.25	82.98	0.50	2.12	0.02	0.93	0.26	0.29	0.02	7.63	0.01	53.66	0.21	7.88	0.00	559.65	0.16
16	22.33	43.30	87.98	0.38	2.10	0.01	0.88	0.21	0.30	0.01	7.63	0.02	53.88	0.20	7.88	0.01	570.23	19.46
17	22.43	50.19	91.01	0.19	2.08	0.02	0.78	0.21	0.29	0.01	7.67	0.01	54.25	0.23	7.87	0.01	576.61	14.87
18	22.20	64.20	102.84	3.57	2.07	0.01	0.88	0.20	0.33	0.01	7.61	0.01	54.21	0.32	7.90	0.03	523.98	36.91
19	22.03	78.25	144.94	18.21	2.15	0.11	1.25	0.10	0.43	0.01	7.63	0.01	54.10	0.08	7.82	0.10	689.03	210.17
20	22.10	92.33	161.12	39.34	2.09	0.15	1.35	0.24	0.44	0.01	7.64	0.01	53.93	0.26	7.86	0.07	603.63	140.82
21	22.00	106.33	179.12	40.35	2.04	0.17	1.40	0.20	0.47	0.02	7.64	0.01	53.78	0.36	7.86	0.05	575.40	62.38
22	22.00	120.31	186.22	41.60	2.01	0.20	1.36	0.18	0.46	0.01	7.73	0.01	54.21	0.18	7.86	0.04	577.52	110.60
23	22.57	134.16	190.35	42.10	1.97	0.20	1.42	0.26	0.47	0.01	7.78	0.01	54.24	0.40	7.84	0.04	609.50	108.63

Table 11S: Total amounts of secondary phases precipitated over model period for Batch20.

Total amount of olivine dissolved over model period in mmol olivine	0.59202
Total amount of serpentinite precipitated over model period in mmol chrysotile	0.193342
Total amount of sepiolite precipitated over model period in mmol sepiolite	0.014031
Total amount of talc precipitated over model period in mmol talc	0.002778
Total amount of aragonite precipitated over model period in mmol aragonite	0.525497
Total amount of calcite precipitated over model period in mmol calcite	0
Total amount of carbonate precipitated over model period in mmol carbonate	0.525497
Total amount of am. $Fe(OH)_3$ precipitated over model period in mmol $Fe(OH)_3$	0.119815
DIC loss in mol DIC/(mol olivine dissolved)	0.887633
TA loss in mol TA/(mol olivine dissolved)	0.297715

Table 12S: Total amounts of secondary phases precipitated over model period for Batch10.

Total amount of olivine dissolved over model period in mmol olivine	0.327079
Total amount of serpentinite precipitated over model period in mmol chrysotile	0.10667
Total amount of sepiolite precipitated over model period in mmol sepiolite	0.005981
Total amount of talc precipitated over model period in mmol talc	0.001335
Total amount of aragonite precipitated over model period in mmol aragonite	0.316731
Total amount of calcite precipitated over model period in mmol calcite	0
Total amount of carbonate precipitated over model period in mmol carbonate	0.316731
Total amount of am. $Fe(OH)_3$ precipitated over model period in mmol $Fe(OH)_3$	0.067675
DIC loss in mol DIC/(mol olivine dissolved)	0.968363
TA loss in mol TA/(mol olivine dissolved)	0.431309

Table 13S: Total amounts of secondary phases precipitated over model period for Batch5.

Total amount of olivine dissolved over model period in mmol olivine	0.172721
Total amount of serpentinite precipitated over model period in mmol chrysotile	0.055401
Total amount of sepiolite precipitated over model period in mmol sepiolite	0.001323
Total amount of talc precipitated over model period in mmol talc	0.000388
Total amount of aragonite precipitated over model period in mmol aragonite	0.173486
Total amount of calcite precipitated over model period in mmol calcite	0
Total amount of carbonate precipitated over model period in mmol carbonate	0.173486
Total amount of am. $Fe(OH)_3$ precipitated over model period in mmol $Fe(OH)_3$	0.035582
DIC loss in mol DIC/(mol olivine dissolved)	1.00443
TA loss in mol TA/(mol olivine dissolved)	0.416229

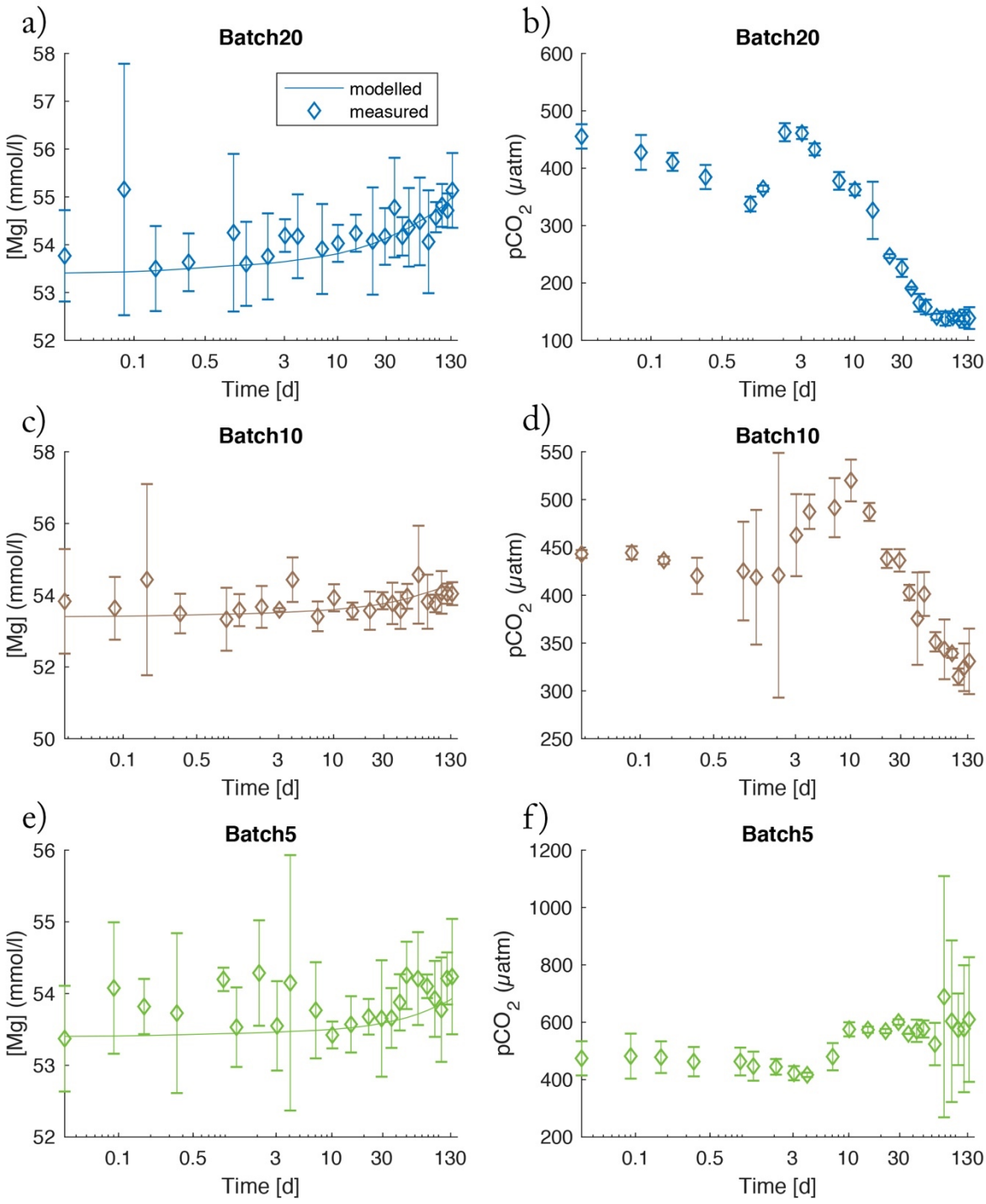

Figure5S: Left: Mg concentrations [Mg] for all batches. a) Batch20, c) Batch10, e) Beatch5. Right: pCO_2 for all batches. B) Batch20, d) Batch10, f) Batch5. Diamonds show measured values, solid lines (a,c,e), represent modelled values. Error bars are reported as ±2SD.

Supplementary references

Parkhurst, D.L., Appelo, C.A.J., 1999. User's Guide to PHREEQC (Version 2): A Computer Program for Speciation, Batch-Reaction, One-Dimensional Transport, and Inverse Geochemical Calculations, Water-Resources Investigations Report 99-4259. https://doi.org/10.3133/wri994259

Rimstidt, J.D., Brantley, S.L., Olsen, A.A., 2012. Systematic review of forsterite dissolution rate data. Geochim. Cosmochim. Acta 99, 159–178. https://doi.org/10.1016/j.gca.2012.09.019

Zeebe, R.E., Wolf-Gladrow, D., 2001. CO2 in seawater: equilibrium, kinetics, isotopes. Gulf Professional Publishing. https://doi.org/10.1016/s0422-9894(01)x8001-x

Supplementary Material to "Disentangling artificial and natural benthic weathering in organic rich Baltic Sea sediments"

S1 Supplementary Methods

S1.1 Visualization of flux data

In order to increase the readability of flux data they were smoothened via gaussian smoothening method applying a standard deviation of 6. Afterwards, the data was interpolated using the spline method following Schoenberg (1988). An exemplary impression of the original versus smoothened data is given in Figure 1S. Note that smoothened data is only used for visualization and not for any further calculations.

S2 Supplementary Tables

Table 1S: Mineralogical composition of dunite used in the experiment as provided by the producer (Sibelco^{TM}, Olivine AFS 80).

	Description (grading)		Olivine AFS 80 PR-017377-004
Mineralogical XRD	Mineral	Unit	Results
	Quartz	%	0.0
	Olivine	%	88.8
	Pyroxene (enstatite)	%	6.7
	Amphibole	%	0.3
	Serpentine	%	2.3
	Chlorite	%	1.4
	Talc	%	0.5
	Mica	%	0.0
	Amorphous	%	0.0
	Sum		100

Table 2S: Chemical composition of used lime stone as provided by producer (Sibelco™, Olivine AFS 80).

Sample name	Sample 05/21	Unit
CO_2	43.1	%
SO_3	0.02	%
CaO	54.8	%
MgO	0.24	%
SiO_2	1.16	%
Fe_2O_3	0.14	%
Al_2O_3	0.1	%
Sum	99.86	%
Minor elements		
Ba	1.96	mg/kg
Na	51.9	mg/kg
K	67.1	mg/kg
P	43.6	mg/kg
Sr	75.0	mg/kg
Trace elements		
As	1.46	mg/kg
Cd	0.61	mg/kg
Cr	1.54	mg/kg
Hg	<0.01	mg/kg
Ni	1.72	mg/kg
Pb	1.13	mg/kg
Sb	0.04	mg/kg
Se	<0.02	mg/kg

Table 3S: Accession and metadata for BioSamples processed in the present study.

Bio-Sample accession	Sample Name	Treatment	Sub-sample	Time [day]s	Date	Depth	Sample label	BioProject ID	Organism
SAMN36035013	B01-DS-L2	Blank	t7	91	2022-05-10/11	1-2cm	B1t7_2	PRJNA988924	marine sediment metagenome
SAMN36035014	C01-DS-L2	Blank	t7	91	2022-05-10/11	2-3cm	B1t7_3	PRJNA988924	marine sediment metagenome
SAMN36035015	D01-DS-L2	Blank	t7	91	2022-05-10/11	3-4cm	B1t7_4	PRJNA988924	marine sediment metagenome
SAMN36035016	E01-DS-L2	Blank	t7	91	2022-05-10/11	4-6cm	B1t7_5	PRJNA988924	marine sediment metagenome
SAMN36035017	F04-DS-L2	Core	t0	0	2022-01-13	1-2cm	BE1301_2	PRJNA988924	marine sediment metagenome
SAMN36035018	G04-DS-L2	Core	t0	0	2022-01-13	2-3cm	BE1301_3	PRJNA988924	marine sediment metagenome
SAMN36035019	H04-DS-L2	Core	t0	0	2022-01-13	3-4cm	BE1301_4	PRJNA988924	marine sediment metagenome
SAMN36035020	A05-DS-L2	Core	t0	0	2022-01-13	4-6cm	BE1301_5	PRJNA988924	marine sediment metagenome
SAMN37271069	230800000544-DS163_23Aug544-DL163_S163	Blank	t0	0	2022-02-08	0-2cm	B1t0	PRJNA988924	marine sediment metagenome
SAMN37271070	230800000544-DS164_23Aug544-DL164_S164	Blank	t0	0	2022-02-08	0-2cm	B2t0	PRJNA988924	marine sediment metagenome
SAMN37271071	230800000544-DS171_23Aug544-DL171_S171	Blank	t5	42	2022-03-22	0-2cm	B1t5	PRJNA988924	marine sediment metagenome
SAMN37271072	230800000544-DS173_23Aug544-DL173_S173	Olivine	t5	42	2022-03-22	0-2cm	M5t5	PRJNA988924	marine sediment metagenome
SAMN37271073	230800000544-DS172_23Aug544-DL172_S172	Carbonate	t5	42	2022-03-22	0-2cm	M2t5	PRJNA988924	marine sediment metagenome
SAMN37271074	230800000544-DS165_23Aug544-DL165_S165	Carbonate	t0	0	2022-02-08	0-2cm	M1t0	PRJNA988924	marine sediment metagenome
SAMN37271075	230800000544-DS166_23Aug544-DL166_S166	Carbonate	t0	0	2022-02-08	0-2cm	M2t0	PRJNA988924	marine sediment metagenome
SAMN37271076	230800000544-DS167_23Aug544-DL167_S167	Carbonate	t0	0	2022-02-08	0-2cm	M3t0	PRJNA988924	marine sediment metagenome
SAMN37271077	230800000544-DS176_23Aug544-DL176_S176	Carbonate	t6	72	2022-04-21	0-2cm	M1t6	PRJNA988924	marine sediment metagenome
SAMN37271078	230800000544-DS177_23Aug544-DL177_S177	Carbonate	t6	72	2022-04-21	0-2cm	M2t6	PRJNA988924	marine sediment metagenome
SAMN37271079	230800000544-DS178_23Aug544-DL178_S178	Carbonate	t6	72	2022-04-21	0-2cm	M3t6	PRJNA988924	marine sediment metagenome

SAMN37271080	230800000544-DS174_23Aug544-DL174_S174	Blank	t6	72	2022-04-21	0-2cm	B1t6	PRJNA988924	marine sediment metagenome
SAMN37271081	230800000544-DS175_23Aug544-DL175_S175	Blank	t6	72	2022-04-21	0-2cm	B2t6	PRJNA988924	marine sediment metagenome
SAMN37271082	230800000544-DS179_23Aug544-DL179_S179	Olivine	t6	72	2022-04-21	0-2cm	M4t6	PRJNA988924	marine sediment metagenome
SAMN37271083	230800000544-DS180_23Aug544-DL180_S180	Olivine	t6	72	2022-04-21	0-2cm	M5t6	PRJNA988924	marine sediment metagenome
SAMN37271084	230800000544-DS181_23Aug544-DL181_S181	Olivine	t6	72	2022-04-21	0-2cm	M6t6	PRJNA988924	marine sediment metagenome
SAMN37271085	230800000544-DS168_23Aug544-DL168_S168	Olivine	t0	0	2022-02-08	0-2cm	M4t0	PRJNA988924	marine sediment metagenome
SAMN37271086	230800000544-DS169_23Aug544-DL169_S169	Olivine	t0	0	2022-02-08	0-2cm	M5t0	PRJNA988924	marine sediment metagenome
SAMN37271087	230800000544-DS170_23Aug544-DL170_S170	Olivine	t0	0	2022-02-08	0-2cm	M6t0	PRJNA988924	marine sediment metagenome
SAMN37271088	B1t1_Bac_S66	Blank	t1	1	2022-02-09	0-2cm	B1t1	PRJNA988924	marine sediment metagenome
SAMN37271089	B1t2_Bac_S67	Blank	t2	3	2022-02-11	0-2cm	B1t2	PRJNA988924	marine sediment metagenome
SAMN37271090	B1t3_Bac_S68	Blank	t3	7	2022-02-15	0-2cm	B1t3	PRJNA988924	marine sediment metagenome
SAMN37271091	B1t4_Bac_S69	Blank	t4	22	2022-03-02	0-2cm	B1t4	PRJNA988924	marine sediment metagenome
SAMN37271092	M2t1_Bac_S73	Carbonate	t1	1	2022-02-09	0-2cm	M2t1	PRJNA988924	marine sediment metagenome
SAMN37271093	M2t2_Bac_S74	Carbonate	t2	3	2022-02-11	0-2cm	M2t2	PRJNA988924	marine sediment metagenome
SAMN37271094	M2t3_Bac_S75	Carbonate	t3	7	2022-02-15	0-2cm	M2t3	PRJNA988924	marine sediment metagenome
SAMN37271095	M2t4_Bac_S76	Carbonate	t4	22	2022-03-02	0-2cm	M2t4	PRJNA988924	marine sediment metagenome
SAMN37271096	M5t1_Bac_S12	Olivine	t1	1	2022-02-09	0-2cm	M5t1	PRJNA988924	marine sediment metagenome
SAMN37271097	M5t2_Bac_S81	Olivine	t2	3	2022-02-11	0-2cm	M5t2	PRJNA988924	marine sediment metagenome
SAMN37271098	M5t3_Bac_S82	Olivine	t3	7	2022-02-15	0-2cm	M5t3	PRJNA988924	marine sediment metagenome
SAMN37271099	M5t4_Bac_S83	Olivine	t4	22	2022-03-02	0-2cm	M5t4	PRJNA988924	marine sediment metagenome
SAMN37271100	A03-DS-L2_S3	Carbonate	t7	91	2022-05-10/11	0-1cm	M1t7_1	PRJNA988924	marine sediment metagenome
SAMN37271101	B03-DS-L2_S15	Carbonate	t7	91	2022-05-10/11	1-2cm	M1t7_2	PRJNA988924	marine sediment metagenome
SAMN37271102	C03-DS-L2_S27	Carbonate	t7	91	2022-05-10/11	0-1cm	M2t7_1	PRJNA988924	marine sediment metagenome
SAMN37271103	D03-DS-L2_S39	Carbonate	t7	91	2022-05-10/11	1-2cm	M2t7_2	PRJNA988924	marine sediment metagenome
SAMN37271104	E03-DS-L2_S51	Carbonate	t7	91	2022-05-10/11	0-1cm	M3t7_1	PRJNA988924	marine sediment metagenome
SAMN37271105	F03-DS-L2_S63	Carbonate	t7	91	2022-05-10/11	1-2cm	M3t7_2	PRJNA988924	marine sediment metagenome
SAMN37271106	G03-DS-L2_S75	Olivine	t7	91	2022-05-10/11	0-1cm	M4t7_1	PRJNA988924	marine sediment metagenome
SAMN37271107	H03-DS-L2_S87	Olivine	t7	91	2022-05-10/11	1-2cm	M4t7_2	PRJNA988924	marine sediment metagenome
SAMN37271108	A04-DS-L2_S4	Olivine	t7	91	2022-05-10/11	0-1cm	M5t7_1	PRJNA988924	marine sediment metagenome

SAMN37271109	B04-DS-L2_S16	Olivine	t7	91	2022-05-10/11	1-2cm	M5t7_2	PRJNA988924	marine sediment metagenome
SAMN37271110	C04-DS-L2_S28	Olivine	t7	91	2022-05-10/11	0-1cm	M6t7_1	PRJNA988924	marine sediment metagenome
SAMN37271111	D04-DS-L2_S40	Olivine	t7	91	2022-05-10/11	1-2cm	M6t7_2	PRJNA988924	marine sediment metagenome
SAMN37271112	G02-DS-L2_S74	Blank	t7	91	2022-05-10/11	0-1cm	B2t7_1	PRJNA988924	marine sediment metagenome
SAMN37271113	H02-DS-L2_S86	Blank	t7	91	2022-05-10/11	1-2cm	B2t7_2	PRJNA988924	marine sediment metagenome
SAMN37271114	B05-DS-L2_S17	Core	t0	0	2022-01-13	6-8cm	BE1301_6	PRJNA988924	marine sediment metagenome
SAMN37271115	C05-DS-L2_S29	Core	t0	0	2022-01-13	8-10cm	BE1301_7	PRJNA988924	marine sediment metagenome
SAMN37271116	D05-DS-L2_S41	Core	t0	0	2022-01-13	10-12cm	BE1301_8	PRJNA988924	marine sediment metagenome
SAMN37271117	E05-DS-L2_S53	Core	t0	0	2022-01-13	12-14cm	BE1301_9	PRJNA988924	marine sediment metagenome
SAMN37271118	F05-DS-L2_S65	Core	t0	0	2022-01-13	14-16cm	BE1301_10	PRJNA988924	marine sediment metagenome
SAMN37271119	G05-DS-L2_S77	Core	t0	0	2022-01-13	16-18cm	BE1301_11	PRJNA988924	marine sediment metagenome
SAMN37271120	H05-DS-L2_S89	Core	t0	0	2022-01-13	18-20cm	BE1301_12	PRJNA988924	marine sediment metagenome
SAMN37271121	A06-DS-L2_S6	Core	t0	0	2022-01-13	20-22cm	BE1301_13	PRJNA988924	marine sediment metagenome
SAMN37271122	B06-DS-L2_S18	Core	t0	0	2022-01-13	22-24cm	BE1301_14	PRJNA988924	marine sediment metagenome
SAMN37271123	A01-DS-L2_S1	Blank	t7	91	2022-05-10/11	0-1cm	B1t7_1	PRJNA988924	marine sediment metagenome
SAMN37271124	F01-DS-L2_S61	Blank	t7	91	2022-12-05	6-8cm	B1t7_6	PRJNA988924	marine sediment metagenome
SAMN37271125	G01-DS-L2_S73	Blank	t7	91	2022-05-10/11	8-10cm	B1t7_7	PRJNA988924	marine sediment metagenome
SAMN37271126	H01-DS-L2_S85	Blank	t7	91	2022-05-10/11	10-12cm	B1t7_8	PRJNA988924	marine sediment metagenome
SAMN37271127	A02-DS-L2_S2	Blank	t7	91	2022-05-10/11	12-14cm	B1t7_9	PRJNA988924	marine sediment metagenome
SAMN37271128	B02-DS-L2_S14	Blank	t7	91	2022-05-10/11	14-16cm	B1t7_10	PRJNA988924	marine sediment metagenome
SAMN37271129	C02-DS-L2_S26	Blank	t7	91	2022-05-10/11	16-18cm	B1t7_11	PRJNA988924	marine sediment metagenome
SAMN37271130	D02-DS-L2_S38	Blank	t7	91	2022-05-10/11	18-20cm	B1t7_12	PRJNA988924	marine sediment metagenome
SAMN37271131	E02-DS-L2_S50	Blank	t7	91	2022-05-10/11	22-24cm	B1t7_13	PRJNA988924	marine sediment metagenome
SAMN37271132	F02-DS-L2_S62	Blank	t7	91	2022-05-10/11	24-26cm	B1t7_14	PRJNA988924	marine sediment metagenome
SAMN37271133	E04-DS-L2_S52	Core	t0	0	2022-01-13	0-1cm	BE1301_1	PRJNA988924	marine sediment metagenome

S3 Supplementary Figures

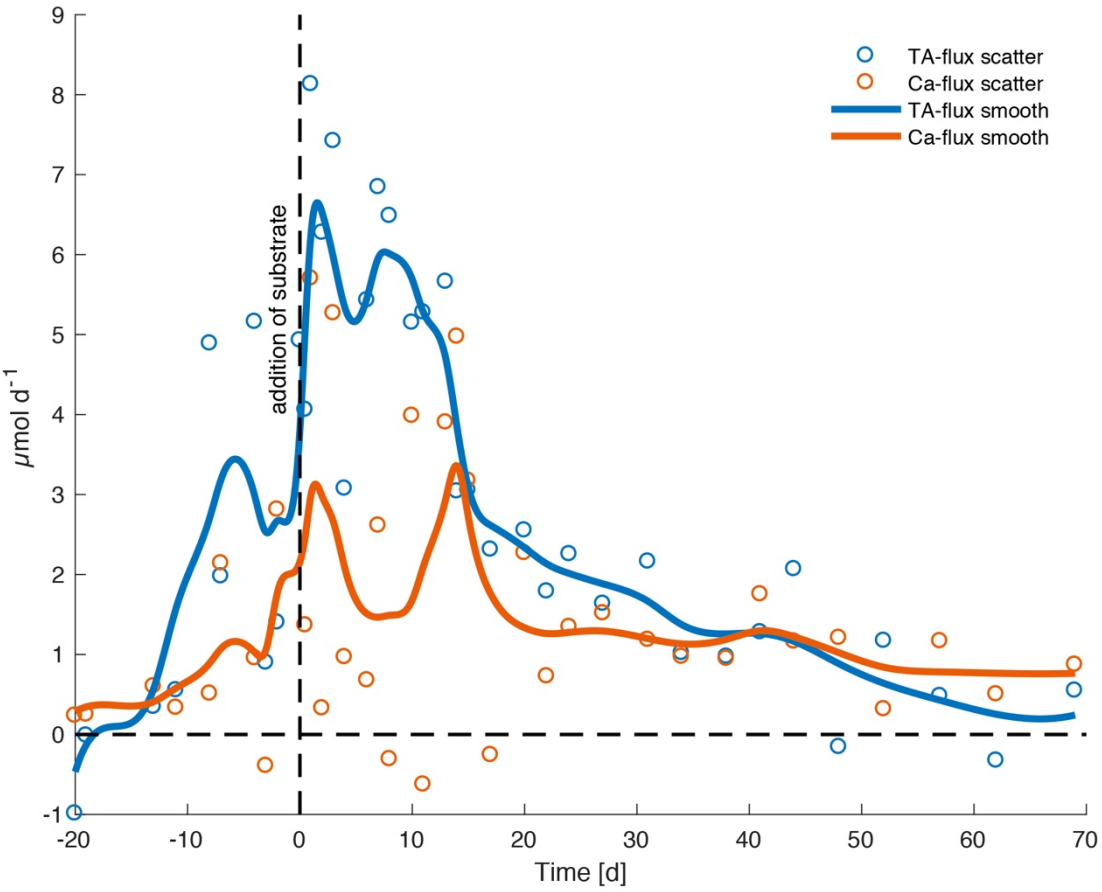

Figure 8S: Example of scattered (dots) versus smoothened (lines) flux data (Core C2). Blue dots and line show TA fluxes. Orange dots and line show Ca fluxes.

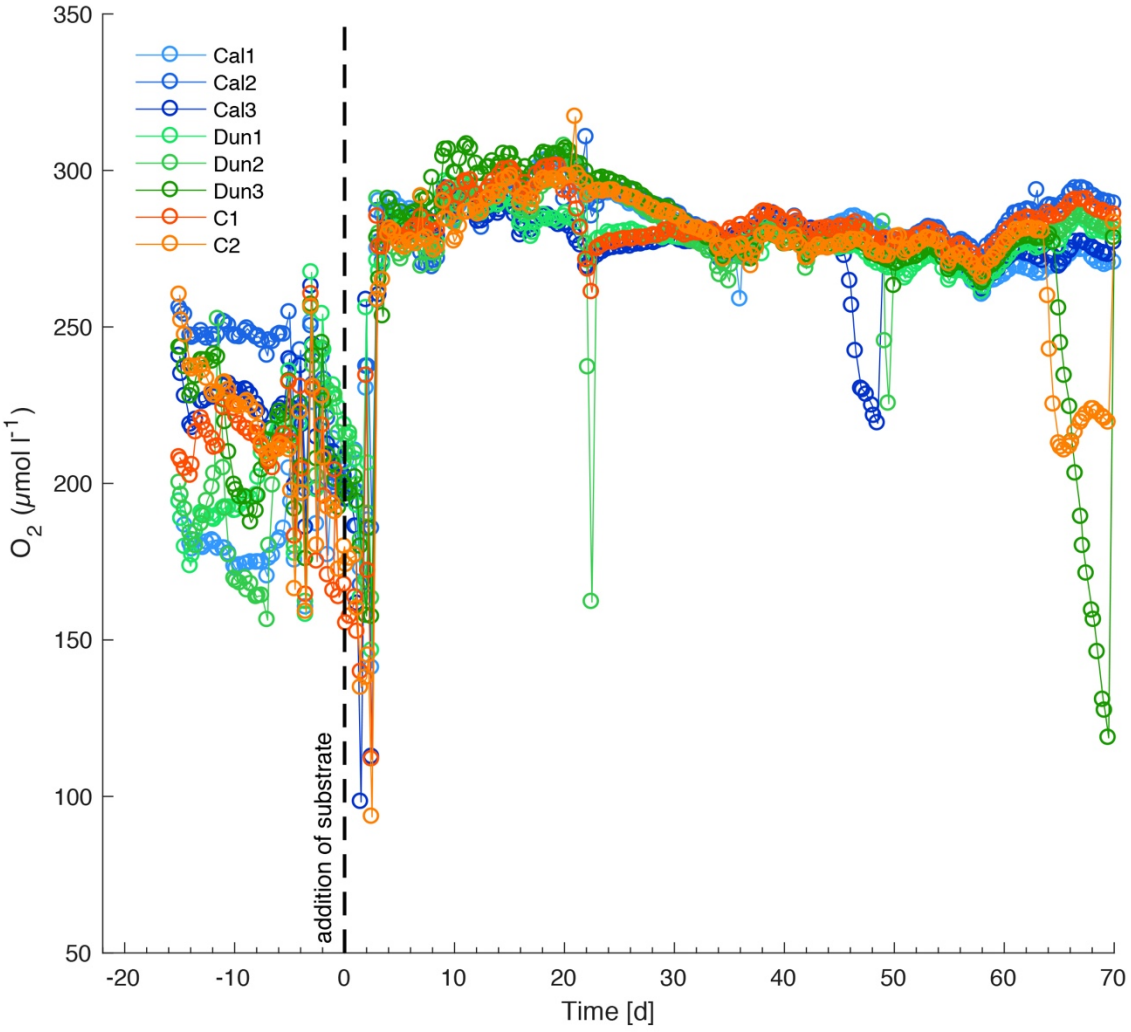

Figure 9S: Oxygen concentration in bottom waters over the course of the experiment in all cores. Dashed line indicates addition of substrates.

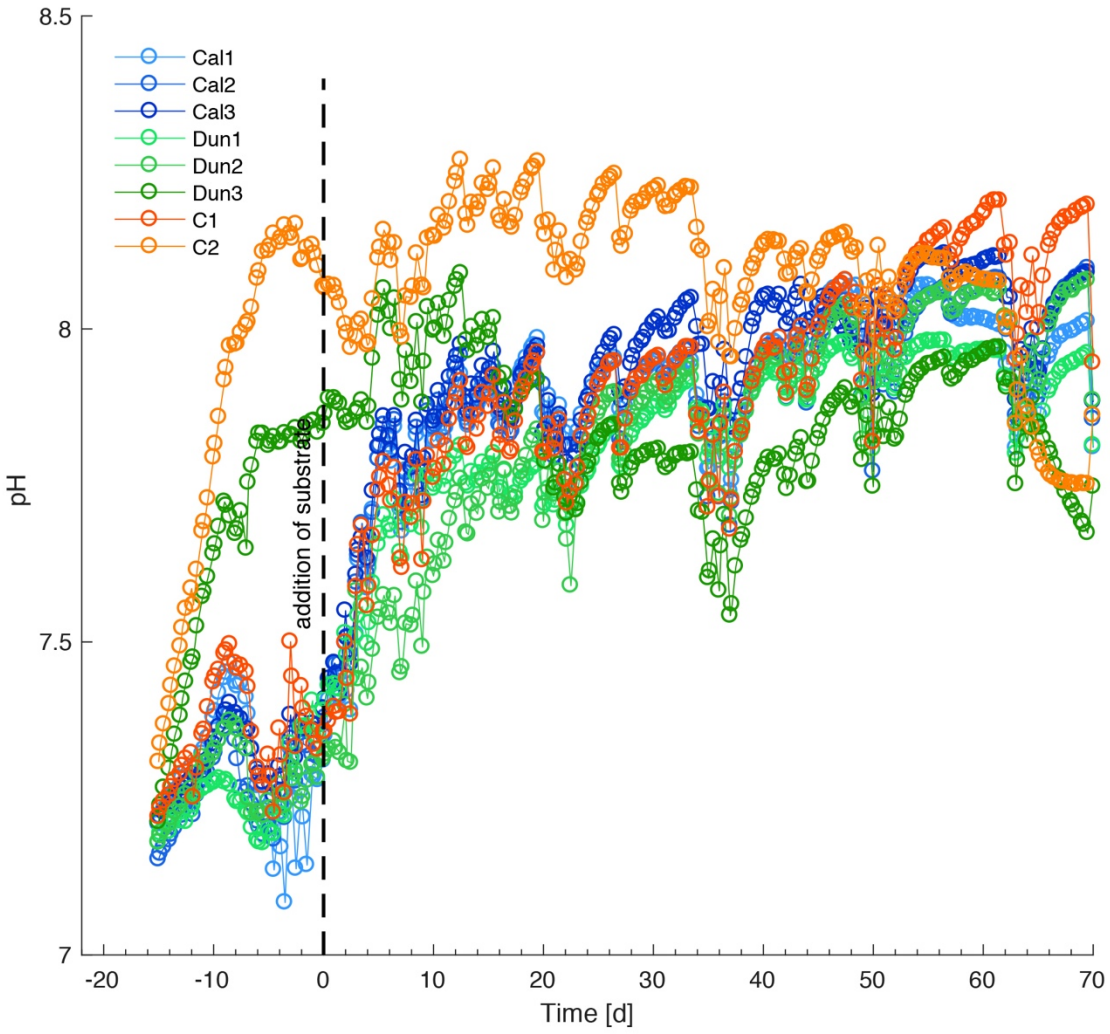

Figure 10S: pH values in bottom waters over the course of the experiment in all cores. Dashed line indicates addition of substrates.

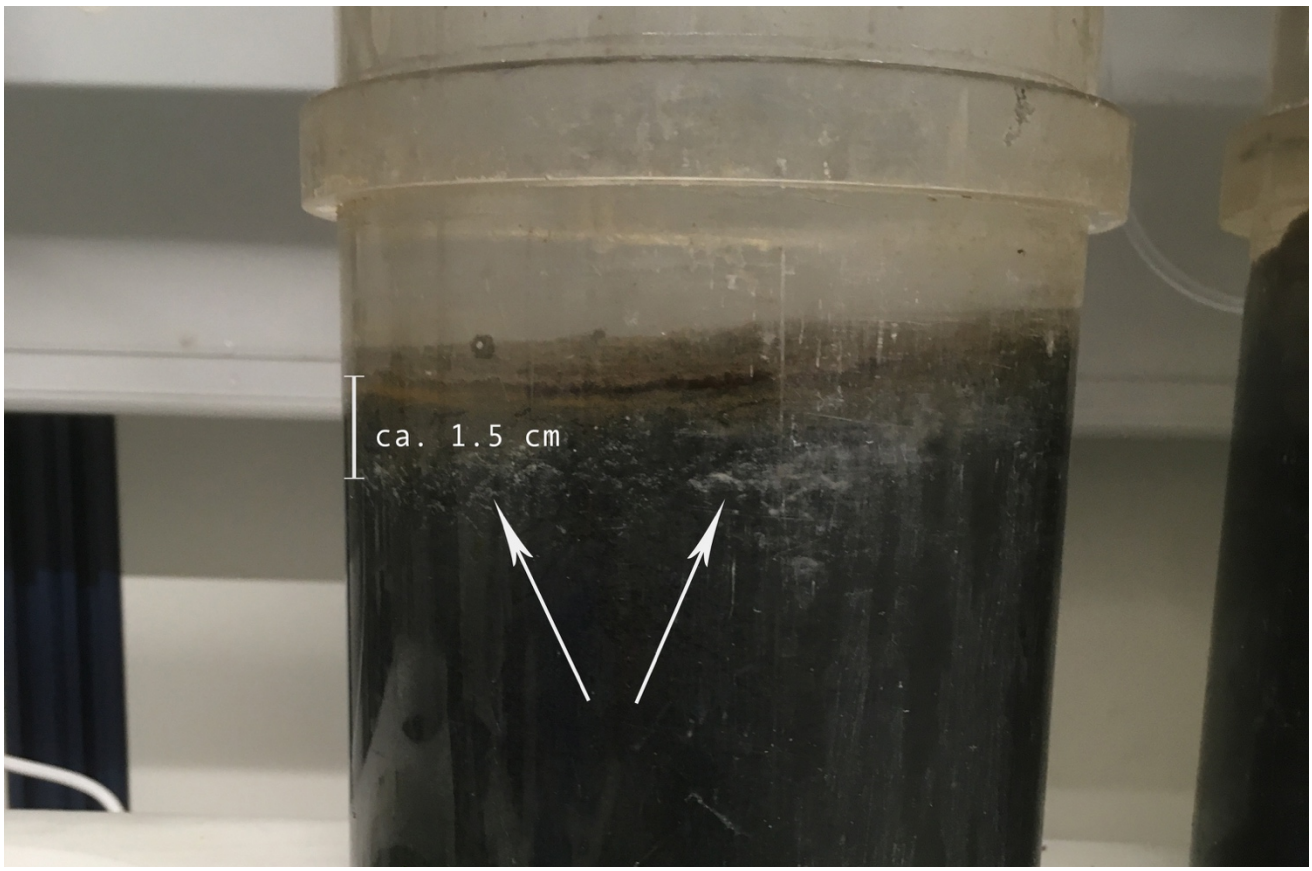

Figure 4S: Close up of Cal2 towards the end of the experiment illustrating the fate of the added calcite powder (white traces in dark brown sediment) indicated by white arrows.

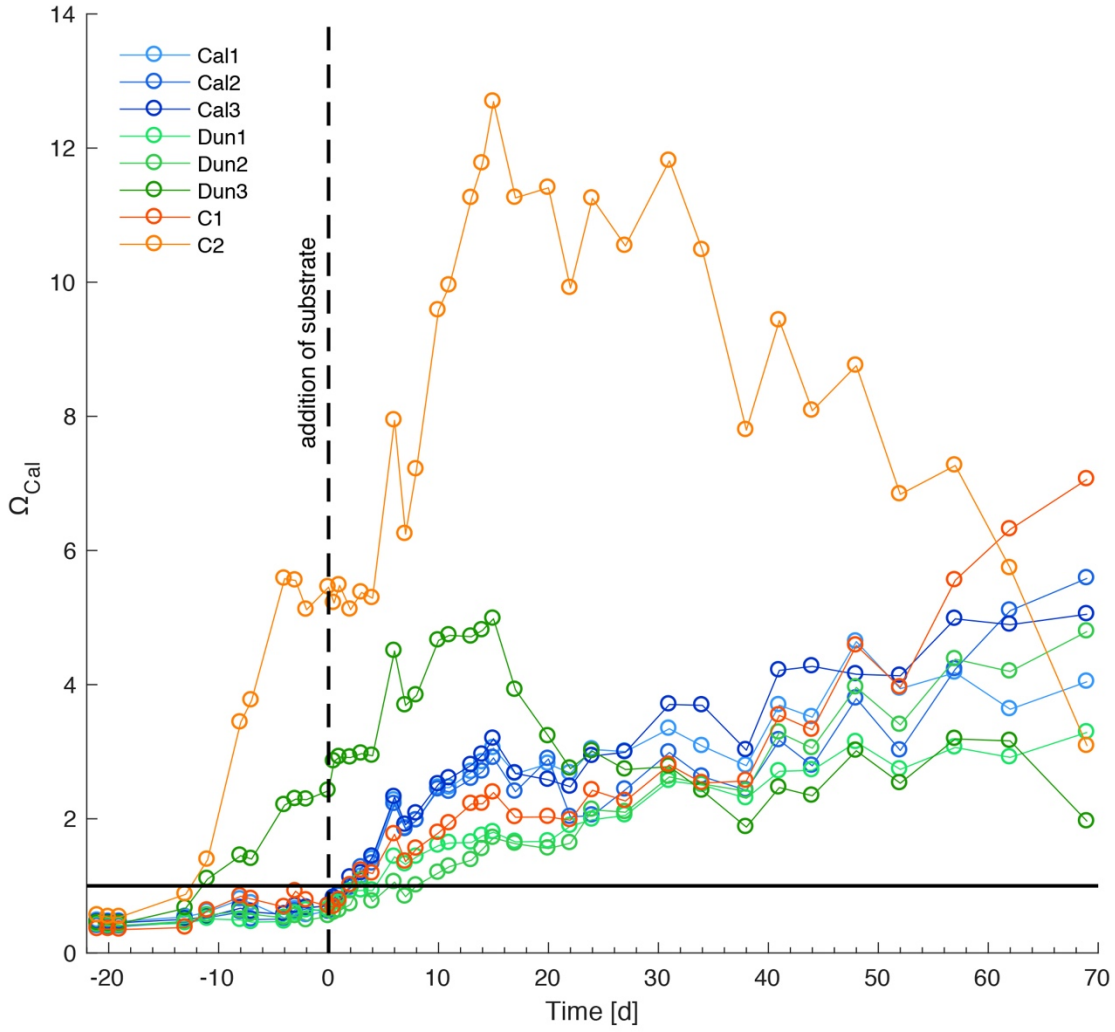

Figure 5S: Ω_{Cal} values in bottom waters over the course of the experiment in all cores. Dashed line indicates addition of substrates. Solid line shows calcite saturation (Ω_{Cal} = 1).

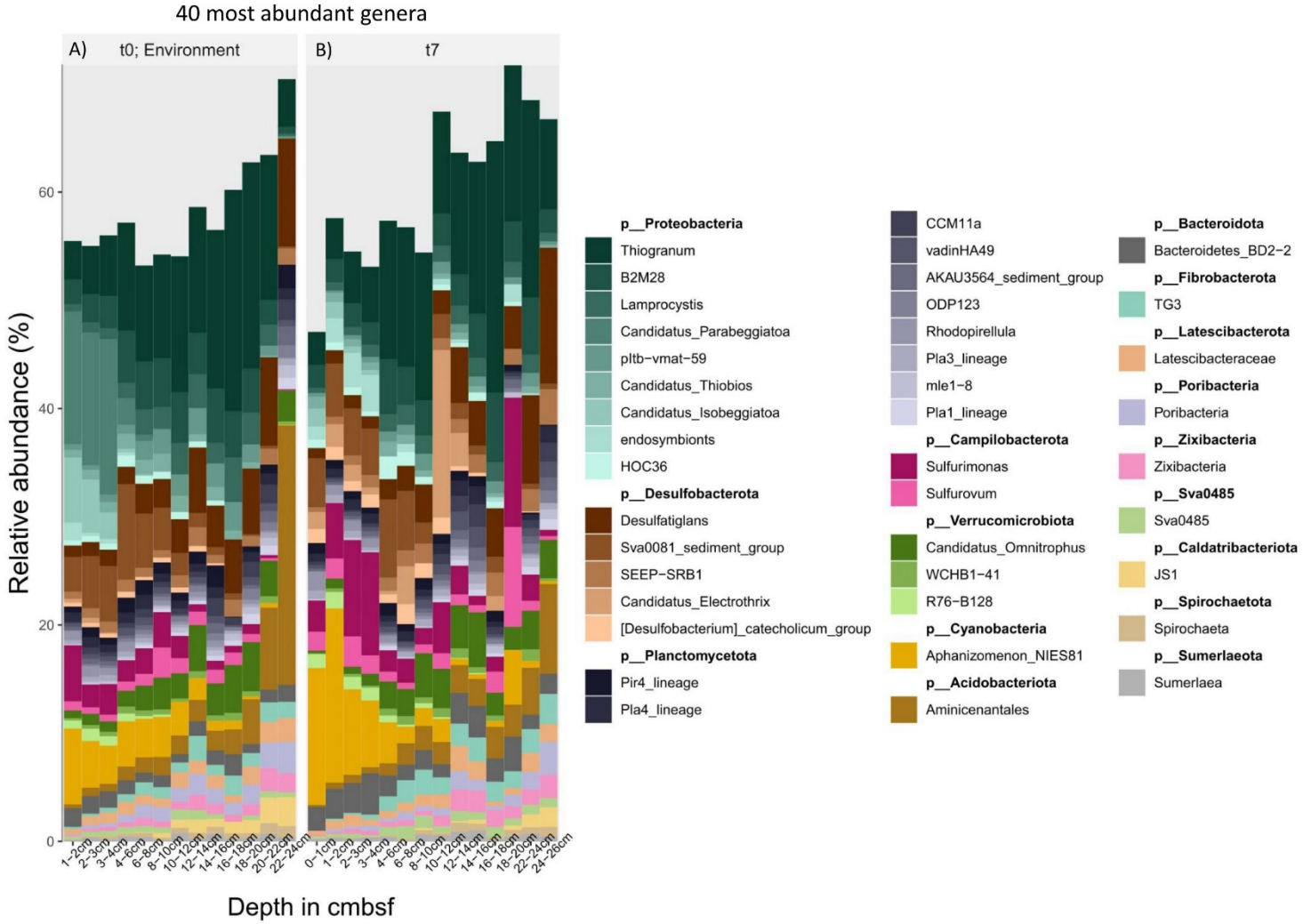

Figure 11S: Taxonomy plots of bacterial 16S tags for RNA isolated from the (A) environmental sediment start core and (B) the untreated control core C1 after 72 days of incubation. The 40 most abundant genera are shown.

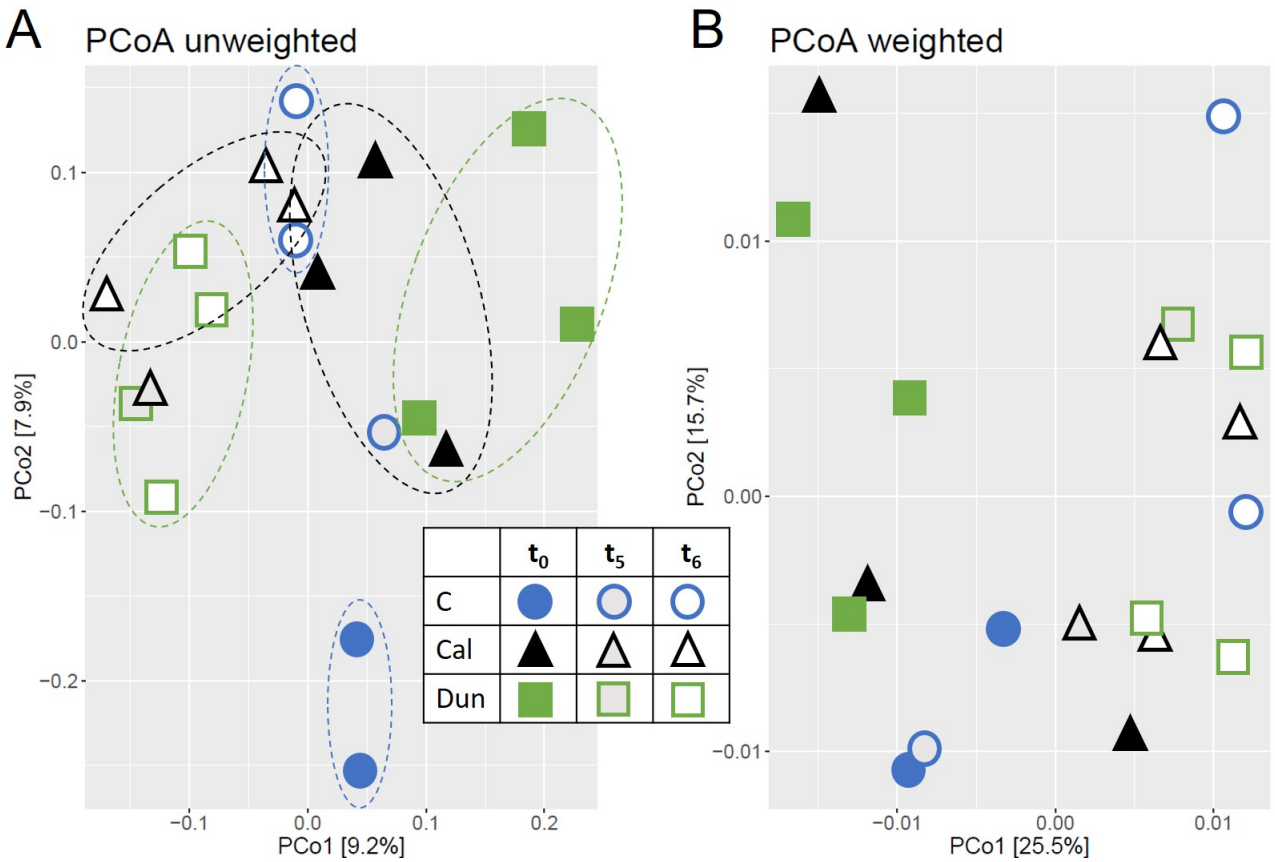

Figure 12S: Weighted (A) and Unweighted (B) Principal coordinate analyses (PCoA) for 16S rRNA gene analyses of Bacteria. Rarefaction for PCoA analyses was performed with a subsampling size of 56 333. The first two principal coordinates (PCo1 and PCo2) are plotted. Similarities and dissimilarities of the microbial communities are visualized for the untreated control cores (C, blue) and for the cores to which calcite (Cal, black) and dunite (Dun, green) were added. The different subsampling time points are color coded with symbols being outlined in the color associated with the treatment and filled in with the same color for t0 (0 days), gray for t5 (42 days) and white for t6 (72 days), respectively.

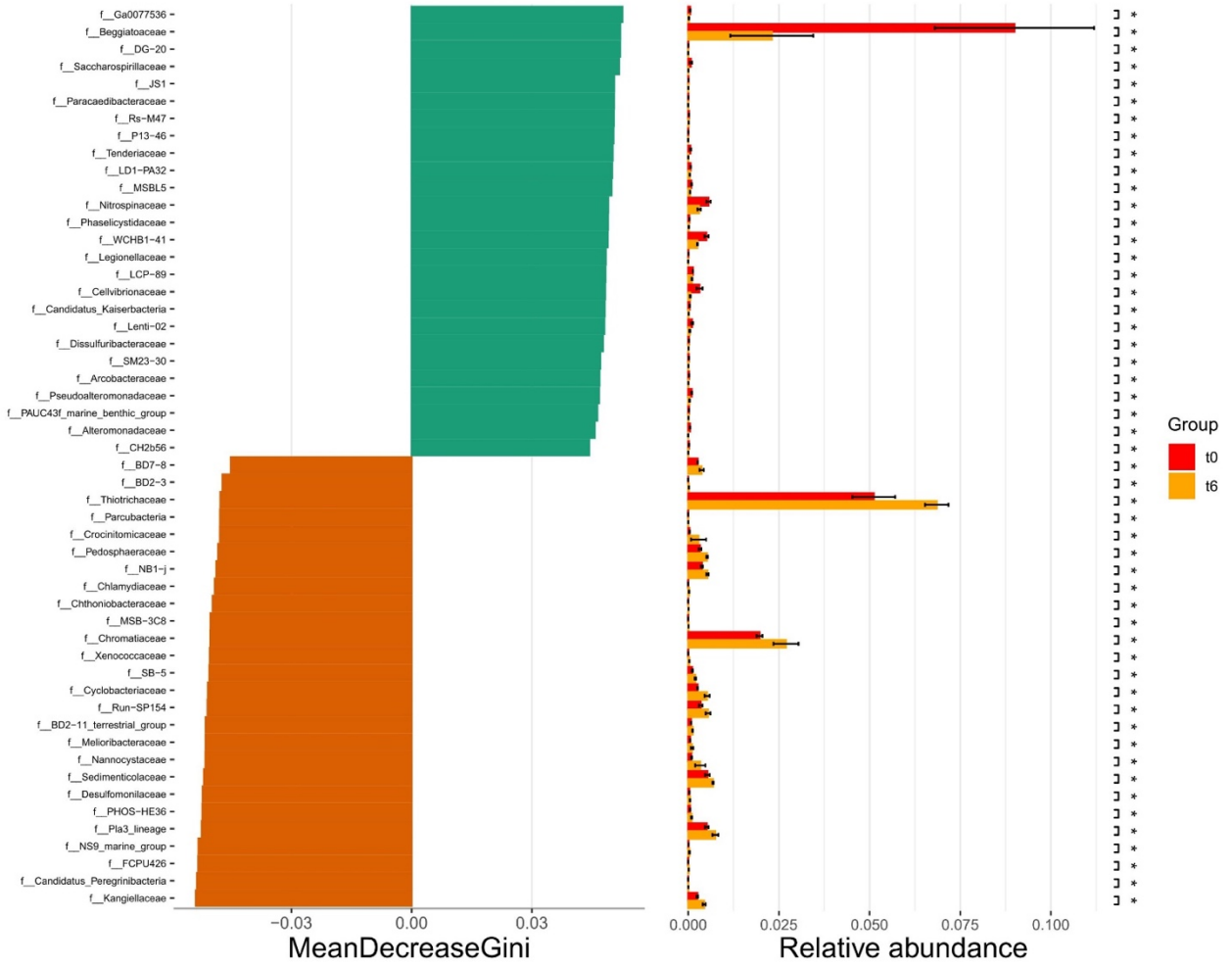

Figure 13S: Differential abundance analyses for Bacteria on the family level for treatments with calcite addition. The name of the family is shown on the left. Green and orange bars in the left panel show the value for "Mean decrease Gini," which is a measure for the importance of the taxon for the difference between the samples. Colored bars in the right panel show the relative abundance per subsample (averages and standard deviation) for the different taxonomic groups. Stars indicate the significance of the difference between sample time points, with one star corresponding to a p-value between 0.01-0.05.

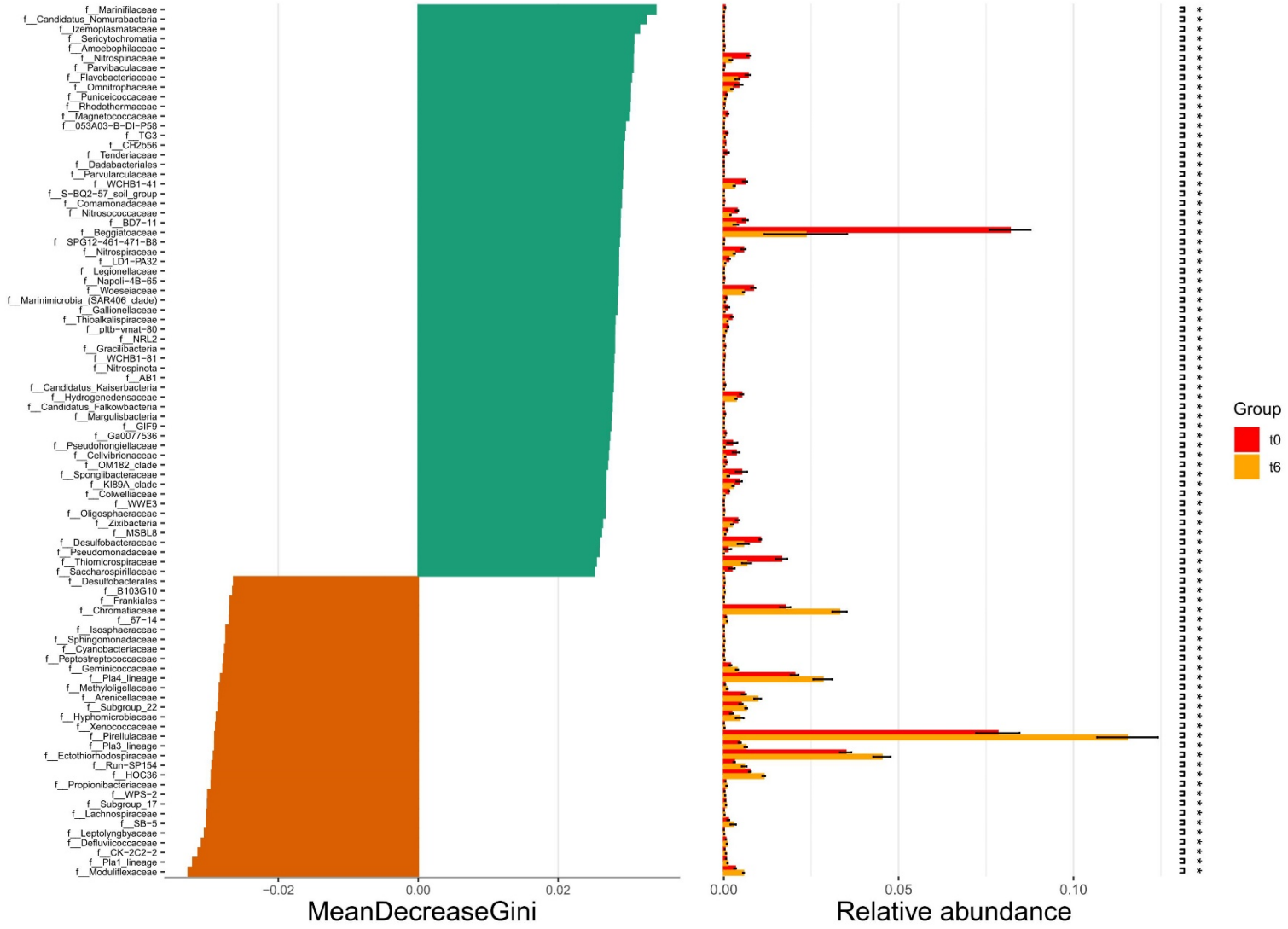

Figure 14S: Differential abundance analyses for Bacteria on the family level for treatments with dunite addition. The name of the family is shown on the left. Green and orange bars in the left panel show the value for "Mean decrease Gini," which is a measure for the importance of the taxon for the difference between the samples. Colored bars in the right panel show the relative abundance per subsample (averages and standard deviation) for the different taxonomic groups. Stars illustrate the significance of the difference between cores.

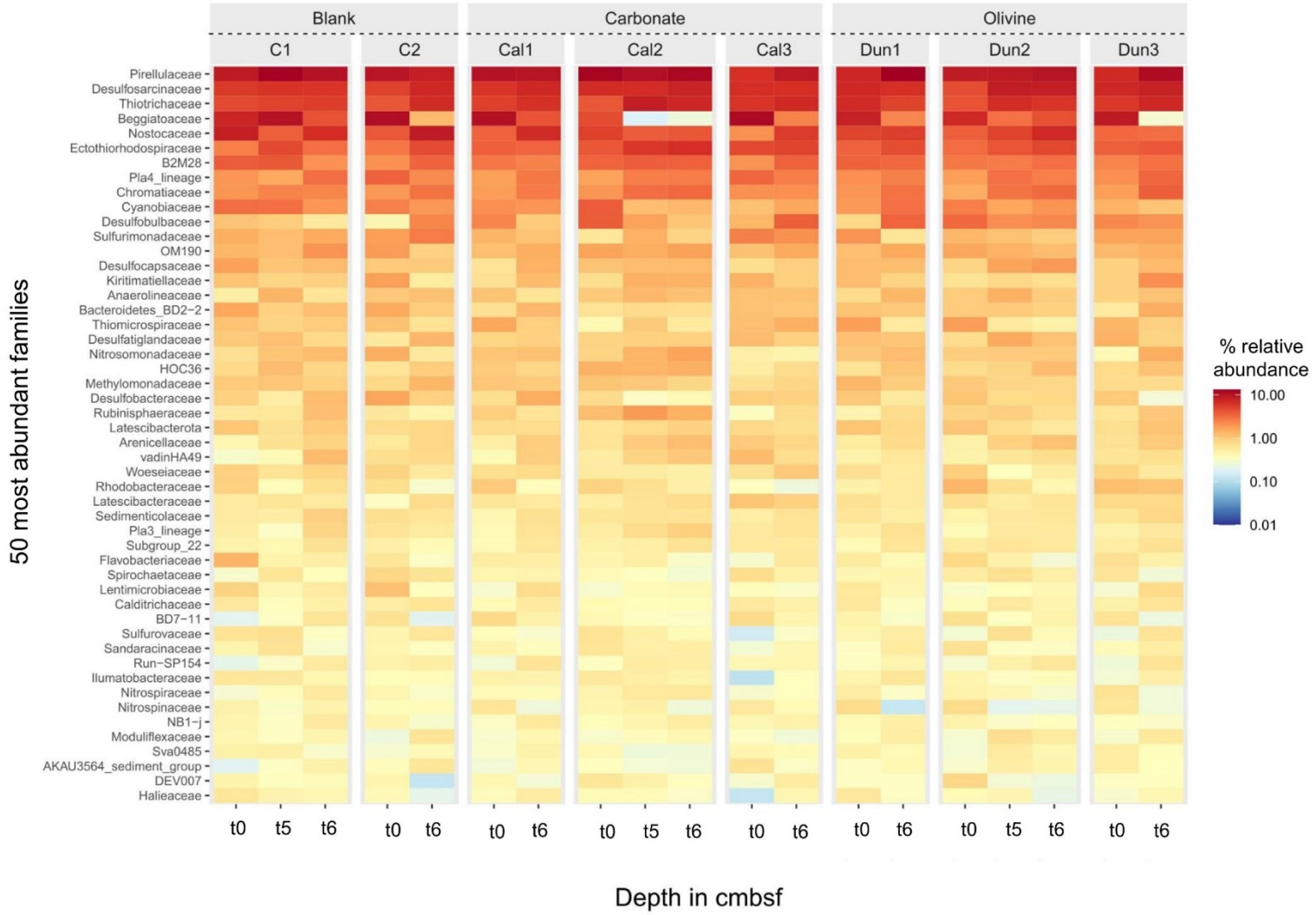

Figure 15S: Heatmap of species abundances for the 50 most abundant families. The name of the family is shown on the left, the subsample time-point is shown at the bottom and the facet above indicates the treatment including controls (C1 and C2), carbonate (Cal1, Cal2 and Cal3) and olivine addition (Dun1, Dun2 and Dun3). The intensity of the color in the heatmap represents the abundance of each family ranging from dark red to dark blue for high and low abundances, respectively.

S3 Supplementary Discussion

S3.1 Bacterial community shifts during incubation

As stated in the main script, a discrepancy between shifting pore water pH profiles, that point towards cable bacteria and 16S rRNA cannot be denied. Possible explanations could be that extraction methods and processing of the nucleic acids had a bias against cable bacteria or that this pH profile is generated by other (uncultured) bacteria. It should be stated though that after 91 days we did detect *Candidatus* Electrothrix in one control experiment with up to 16% indicating that our working procedure can detect known cable bacteria (Figure 6S). At the same time 16S rRNA data show no strong increase or clear dominance of any uncultured type of bacteria that could be responsible for the observed pH changes.

Only for the calcite amendments affiliates of *Thiotrichaceae,* not further classified, increased over time (72 days) (Figure 8S). This group includes sulfide oxidizing autotrophs, some of which are able to store nitrate under oxygen low conditions forming cm thick mats (Garrity et al., 2005). In the dunite treatments affiliates of the *Ectothiorhodospiraceae* (*Thiogranum*) and planctomycetes, namely *Pirellulaceae* and Pla4 lineage increased over time (Figure 9S). *Thiogranum* is an obligately chemolithoautotrophic sulfur oxidizing strain (Mori et al., 2015). Planctomycetes are expected to degrade organic compounds that are released by phototrophs. In case of *Pirellulaceae,* a large number of carbohydrate active enzymes support this idea (Gade et al., 2005; Wegner et al., 2013).

The PCoA clearly demonstrate that at the start of the experiments (t0) the bacterial communities already differed between the different cores (Figure 7S). Thus, starting conditions varied with respect to bacterial composition and metabolic activities. The initial heterogeneity between microbial communities of different sediment cores makes it difficult to draw conclusions about the relationship between mineral addition and community change. Without considering abundance of 16S rRNA genes in the bacterial communities the control, calcite and dunite treatments exhibit a clustering after 72 days (Figure 7Sa) suggesting that shifts occurred to a certain degree in relation to the exposed conditions. However, since starting communities differed it cannot be stated that these are explicitly linked to the addition of calcite or dunite (Figure 7Sa). In the abundance of 16S rRNA genes in the bacterial community compositions, no apparent clustering can be observed at all (Figure 7Sb) indicating that the addition of calcite or dunite did not influence the microbial development.
Some clear trends are visible though for all treatments. The decline of *Beggiatoacea* primarily consisting of the large *Candidatus* Parabeggiatoa and *Candidatus* Isobeggiatoa, and the rise of *Chromatiaceae* in all treatments, independent of mineral addition, is statistically verified (Figure 8S, 9S). *Chromatiaceae* are purple sulfur bacteria commonly known to perform anoxygenic photosynthesis, but several species are chemolithoautotrophs or chemoorganoheterotrophs capable of growing under dark and low oxygen conditions utilizing sulfide and storing elemental sulfur inside their cells (Dahl et al., 2008; Imhoff, 2014).
In most treatments (except for C1, Cal2 and Dun3), Cyanobacteria - mostly *Nostocaceae* of the genus *Aphanizomenon*) increase over time (Figures 10S, 7 (main script)). This is somewhat surprising since the treatments were kept in the dark and cyanobacteria are commonly associated with sunlight-driven energy generation via photosynthesis. It is well known though that under severely light-limiting conditions, *Aphanizomenon* show a broader absorption spectrum (De Nobel et al., 1998). More so, recent work has demonstrated how some cyanobacteria can switch to photosynthesis-alternative pathways in response to abrupt light-dark transitions (Lu et al., 2023). Recent metagenomic work with deep subsurface rock samples has shown the ability of some Cyanobacteria species to grow

independent of sunlight with the potential for hydrogen based lithoautotrophic growth (Puente-Sánchez et al., 2018). *Aphanizomenon* is a filamentous colony forming cyanobacterium which frequently forms blooms and can store inorganic phosphate (Walve and Larsson, 2007). Some species of this genus can produce toxins (Cirés and Ballot, 2016), which may affect growth in the treatments. Patterns of cyanobacterial blooms have been demonstrated to align with alkalinity changes and dissolved silicon in water (cf Zhang, 2023). Recent work has shown that the blooms draw down dissolved inorganic carbon and increased water pH resulting in calcium carbonate precipitation (Zhang, 2023).

Overall, all microcosms exhibited shifts in the bacterial community, primarily related to a diversification of sulfide oxidizing bacteria and of some organic degraders. The microbiology data demonstrate the heterogeneity and complexity of the system, making such experiments in a reproducible fashion extremely difficult.

Supplementary references

Cirés, S., Ballot, A., 2016. A review of the phylogeny, ecology and toxin production of bloom-forming Aphanizomenon spp. and related species within the Nostocales (cyanobacteria). Harmful Algae. https://doi.org/10.1016/j.hal.2015.09.007

Dahl, C., Hell, R., Leustek, T., Knaff, D., 2008. Introduction to Sulfur Metabolism in Phototrophic Organisms BT - Sulfur Metabolism in Phototrophic Organisms, in: Hell, R., Dahl, C., Knaff, D., Leustek, T. (Eds.), . Springer Netherlands, Dordrecht, pp. 1–14. https://doi.org/10.1007/978-1-4020-6863-8_1

De Nobel, W.T., Matthijs, H.C.P., Von Elert, E., Mur, L.R., 1998. Comparison of the light-limited growth of the nitrogen-fixing cyanobacteria Anabaena and Aphanizomenon. New Phytol. 138, 579–587. https://doi.org/10.1046/j.1469-8137.1998.00155.x

Gade, D., Gobom, J., Rabus, R., 2005. Proteomic analysis of carbohydrate catabolism and regulation in the marine bacterium Rhodopirellula baltica. Proteomics 5, 3672–3683. https://doi.org/https://doi.org/10.1002/pmic.200401200

Garrity, G.M., Bell, J.A., Lilburn, T., 2005. Family I. *Thiotrichaceae* fam. nov, in: *Bergey's Manual of Systematic Bacteriology Second Edition.* Brenner DJ, Krieg NR, Staley JT, Garrity G (eds.). New York: Springer, p. 131.

Imhoff, J.F., 2014. The Family Chromatiaceae BT - The Prokaryotes: Gammaproteobacteria, in: Rosenberg, E., DeLong, E.F., Lory, S., Stackebrandt, E., Thompson, F. (Eds.), . Springer Berlin Heidelberg, Berlin, Heidelberg, pp. 151–178. https://doi.org/10.1007/978-3-642-38922-1_295

Lu, K.-J., Chang, C.-W., Wang, C.-H., Chen, F.Y.-H., Huang, I.Y., Huang, P.-H., Yang, C.-H., Wu, H.-Y., Wu, W.-J., Hsu, K.-C., Ho, M.-C., Tsai, M.-D., Liao, J.C., 2023. An ATP-sensitive phosphoketolase regulates carbon fixation in cyanobacteria. Nat. Metab. 5, 1111–1126. https://doi.org/10.1038/s42255-023-00831-w

Mori, K., Suzuki, K.I., Yamaguchi, K., Urabe, T., Hanada, S., 2015. Thiogranum longum gen. nov., sp. nov., an obligately chemolithoautotrophic, sulfur-oxidizing bacterium of the family Ectothiorhodospiraceaeisolated from a deep-sea hydrothermal field, and an emended description of the genus Thiohalomonas. Int. J. Syst. Evol. Microbiol. 65, 235–241. https://doi.org/10.1099/ijs.0.070599-0

Puente-Sánchez, F., Arce-Rodríguez, A., Oggerin, M., García-Villadangos, M., Moreno-Paz, M., Blanco, Y., Rodríguez, N., Bird, L., Lincoln, S.A., Tornos, F., Prieto-Ballesteros, O., Freeman, K.H., Pieper, D.H., Timmis, K.N., Amils, R., Parro, V., 2018. Viable cyanobacteria in the deep continental subsurface. Proc. Natl. Acad. Sci. U. S. A. 115, 10702–10707. https://doi.org/10.1073/pnas.1808176115

Schoenberg, I.J., 1988. Contributions to the problem of approximation of equidistant data by analytic functions: Part A.—On the problem of smoothing or graduation. A first class of analytic approximation formulae. IJ Schoenb. Sel. Pap. 3–57. https://doi.org/10.1007/978-1-4899-0433-1_1

Walve, J., Larsson, U., 2007. Blooms of Baltic Sea Aphanizomenon sp. (Cyanobacteria) collapse after internal phosphorus depletion . Aquat. Microb. Ecol. 49, 57–69.

Wegner, C.E., Richter-Heitmann, T., Klindworth, A., Klockow, C., Richter, M., Achstetter, T., Glöckner, F.O., Harder, J., 2013. Expression of sulfatases in Rhodopirellula baltica and the diversity of sulfatases in the genus Rhodopirellula. Mar. Genomics 9, 51–61. https://doi.org/10.1016/j.margen.2012.12.001

Zhang, J.-Z., 2023. Cyanobacteria blooms induced precipitation of calcium carbonate and dissolution of silica in a subtropical lagoon, Florida Bay, USA. Sci. Rep. 13, 4071. https://doi.org/10.1038/s41598-023-30905-4

Supplementary material to "Alkaline mineral addition to anoxic to hypoxic Baltic Sea sediments as a potentially efficient CO_2-removal technique"

Table 1S: Mineralogical composition of dunite used in the experiment as provided by the producer (Sibelco™, Olivine AFS 80).

	Description (grading)		Olivine AFS 80
			PR-017377-004
Mineralogical XRD	Mineral	Unit	Results
	Quartz	%	0.0
	Olivine	%	88.8
	Pyroxene (enstatite)	%	6.7
	Amphibole	%	0.3
	Serpentine	%	2.3
	Chlorite	%	1.4
	Talc	%	0.5
	Mica	%	0.0
	Amorphous	%	0.0
	Sum		100

Table 2S: Chemical composition of used limestone as provided by the producer.

Sample name	Sample 05/21	Unit
CO_2	43.1	%
SO_3	0.02	%
CaO	54.8	%
MgO	0.24	%
SiO_2	1.16	%
Fe_2O_3	0.14	%
Al_2O_3	0.1	%
Sum	99.86	%
Minor elements		
Ba	1.96	mg/kg
Na	51.9	mg/kg
K	67.1	mg/kg
P	43.6	mg/kg
Sr	75.0	mg/kg
Trace elements		
As	1.46	mg/kg
Cd	0.61	mg/kg
Cr	1.54	mg/kg
Hg	<0.01	mg/kg
Ni	1.72	mg/kg
Pb	1.13	mg/kg
Sb	0.04	mg/kg
Se	<0.02	mg/kg

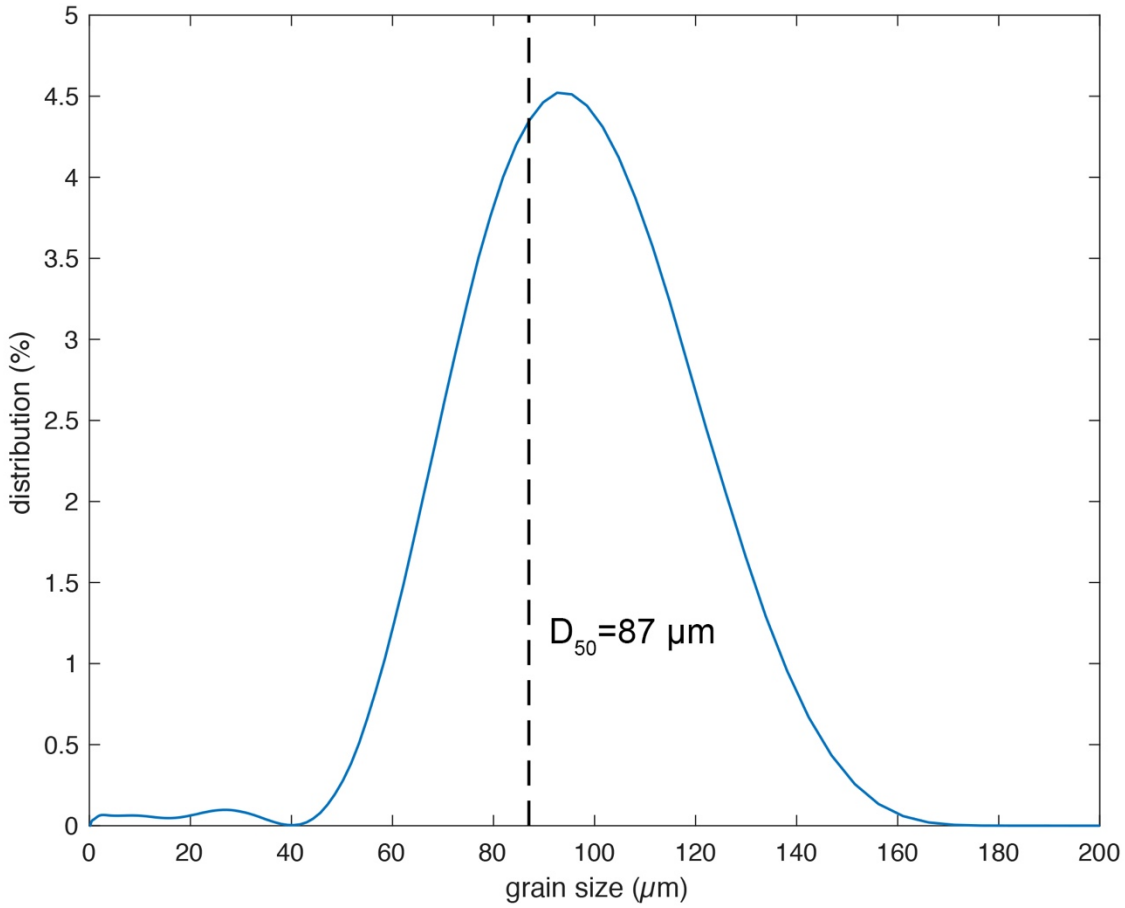

Figure S16: Grain size distribution of the washed calcite material. Vertical dashed line denotes median grainsize (D_{50}).

Figure S17: Exemplary photos of the surfaces of a dunite treated core (left) and a calcite treated core (right) at the end of the experiment. Darker patches are disturbances caused by removing the bottom water and pushing the sediment upwards in the cores.

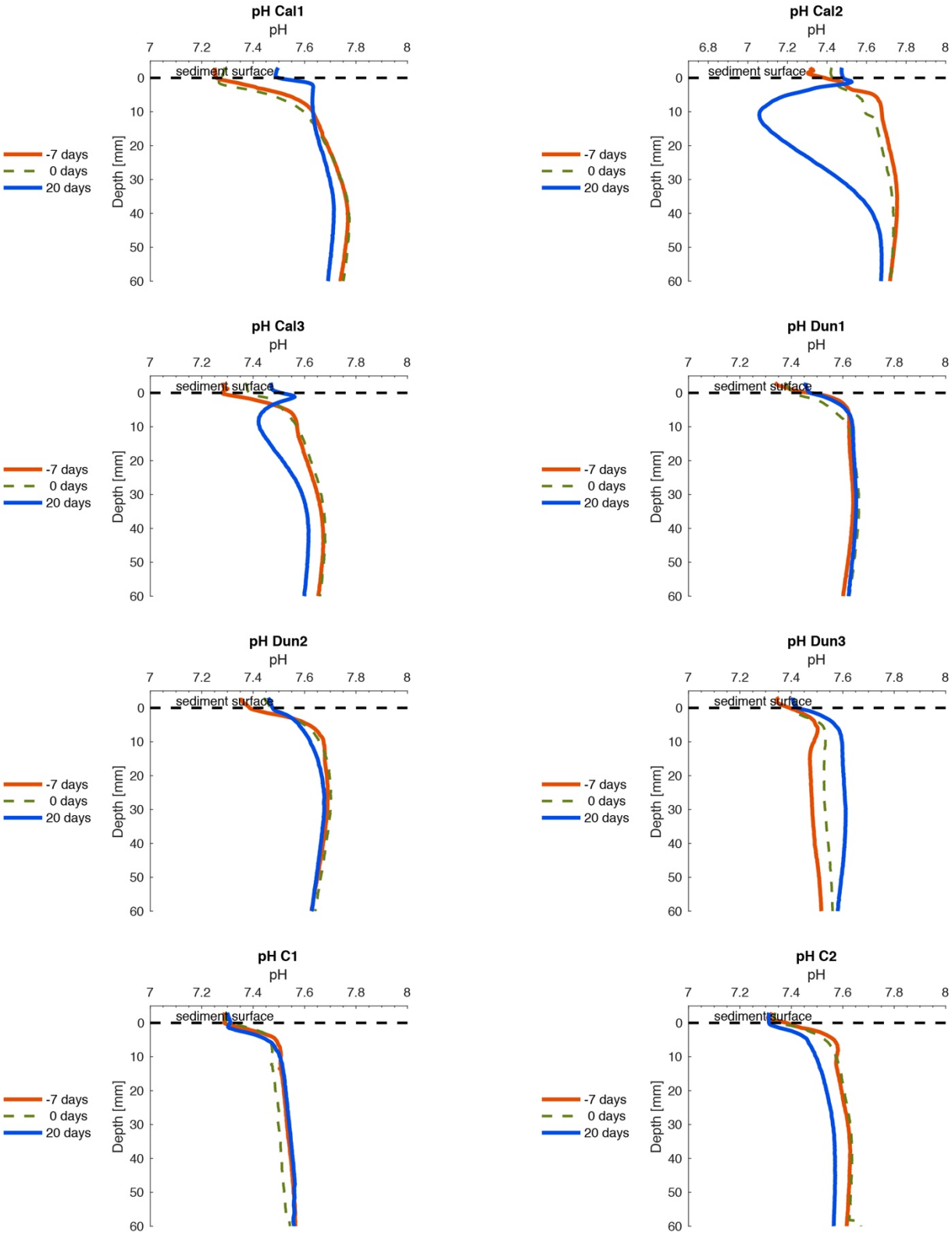

Figure S18: pH-profiles over the course of the experiment. Solid red and blue lines indicate the initial (seven days before addition of substrates) and final profiles, respectively. Dashed lines represent the profiles measured directly before addition of alkaline minerals.

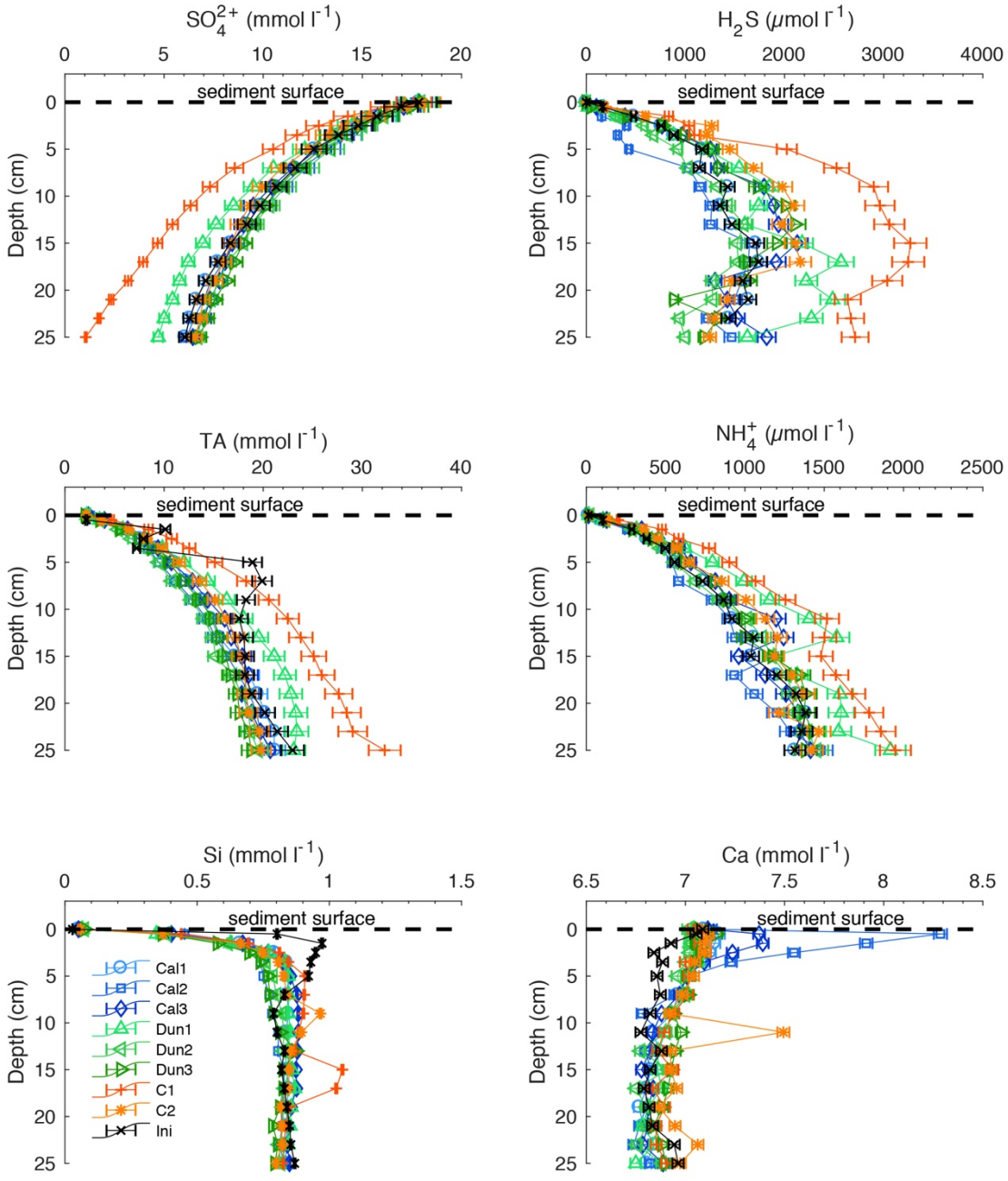

Figure S19: SO_4^{2-}, H_2S, TA NH_4^+ Si and Ca concentrations in all sediment cores. Colored markers indicate concentrations in each core at the end of the experiment. Black crosses indicate the concentrations in the initial core. Horizontal dashed line represents the sediment surface. Data above the sediment surface are bottom waters. Error bars report analytical precision.

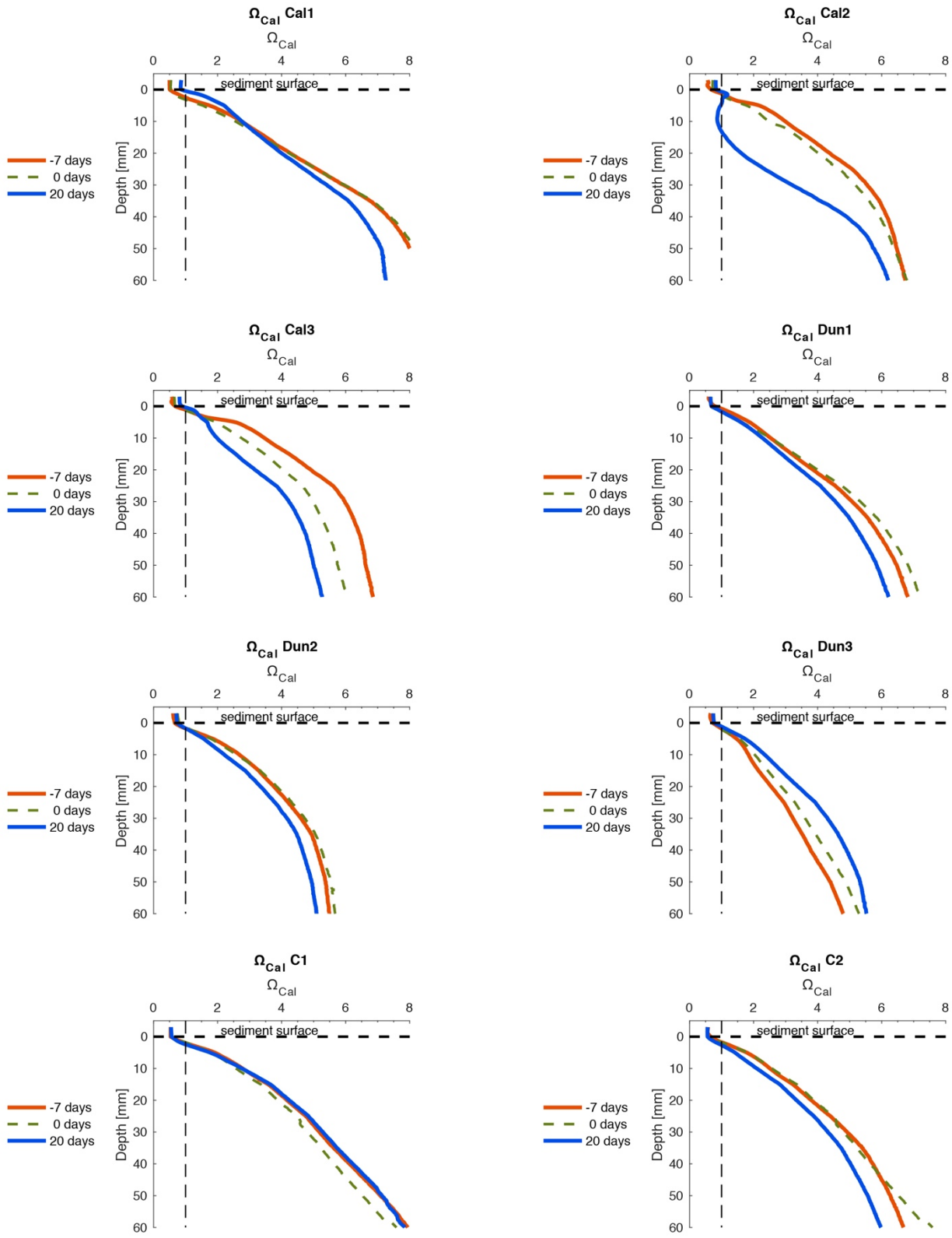

Figure S20: Ω_{Cal}-profiles over the course of the experiment. Solid red and blue lines indicate the initial (seven days before addition of substrates) and final profiles, respectively. Dashed lines represent the profiles measured directly before addition of alkaline minerals.

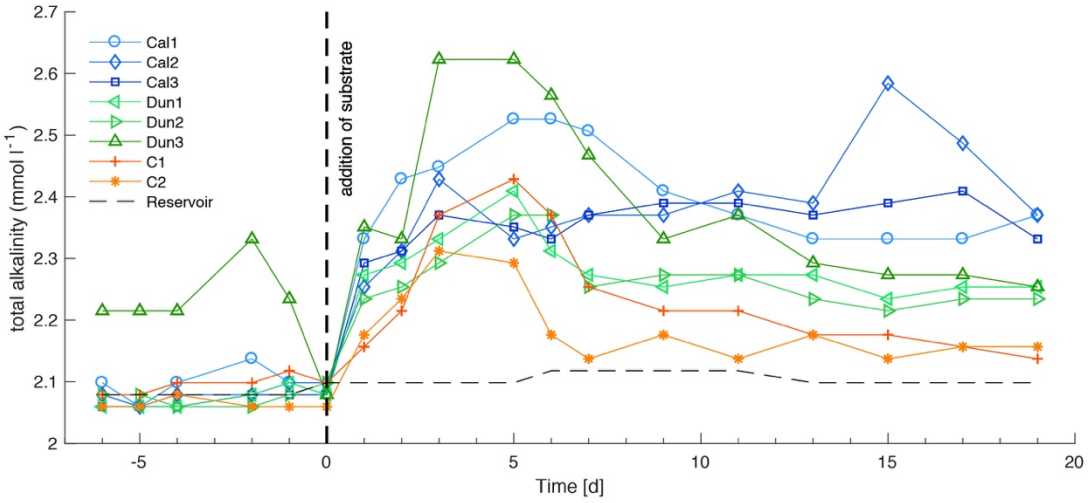

Figure S21: Total alkalinity (TA) in bottom waters in all cores over the entire course of the experiment. Dashed vertical line denotes addition of substrates. Vertical line shows TA in the reservoir.

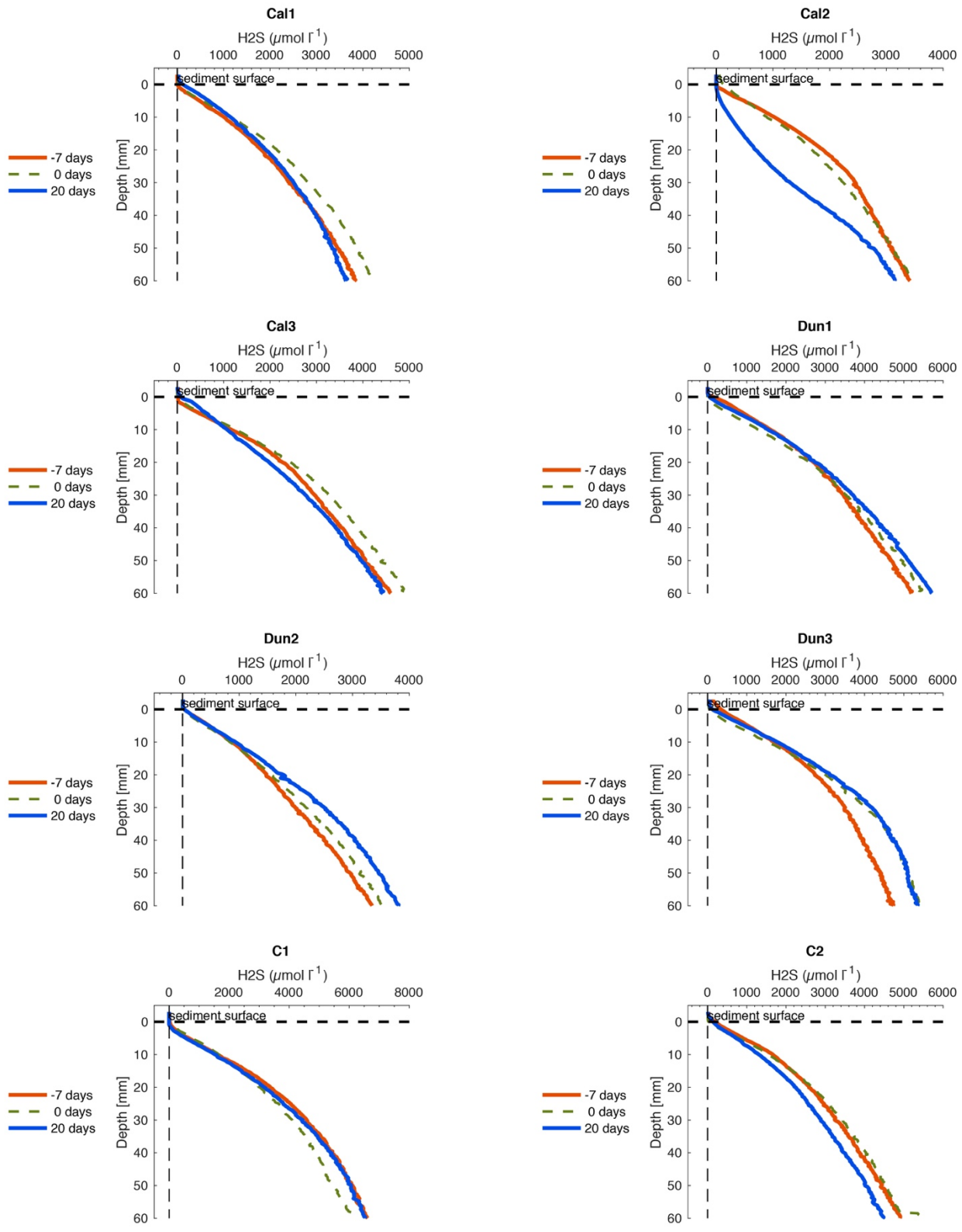

Figure S22: H_2S profiles obtained over the course of the experiment. The profiles at t=0 d were obtained directly before the addition of substrates.

Supplementary material to "Calcite takes it all: Benthic weathering potential and costs of alkaline mineral addition to muddy shelf sediments"

S1 Supplementary methods

S1.1 Model set-up

S1.1.1ODE system

For the four boxes of the model an ODE system was set up as followed:

ODEs for TA:

$$\text{Box1: } \frac{dC_{TA1}}{dt} = -r_{ex} \times C_{TA1}(t) + r_{ex} \times C_{TA3}(t) + r_{mix} \times C_{TA2}(t) - r_{mix} \times C_{TA1}(t) - r_{upw} \times \frac{v_2}{v_1} \times C_{TA1}(t) + r_{upw} \times \frac{v_2}{v_1} \times C_{TA2}(t) \quad \text{(S1)}$$

$$\text{Box2: } \frac{dC_{TA2}}{dt} = \frac{F_{TAnat}}{v_2} + \frac{F_{TAweath}}{v_2} + r_{mix} \times \frac{v_1}{v_2} \times C_{TA1}(t) - r_{mix} \times \frac{v_1}{v_2} \times C_{TA2}(t) - r_{upw} \times C_{TA2}(t) + r_{upw} \times C_{TA4}(t) \quad \text{(S2)}$$

$$\text{Box3: } \frac{dC_{TA3}}{dt} = -r_{ex} \times \frac{v_3}{v_1} \times C_{TA3}(t) + r_{ex} \times C_{TA3}(t) + r_{mix} \times \frac{v_4}{v_3} \times C_{TA2}(t) - r_{mix} \times \frac{v_4}{v_3} \times C_{TA1}(t) - r_{upw} \times \frac{v_2}{v_1} \times C_{TA1}(t) + r_{upw} \times \frac{v_2}{v_1} \times C_{TA2}(t) \quad \text{(S3)}$$

$$\text{Box4: } \frac{dC_{TA4}}{dt} = r_{mix} \times C_{TA3}(t) - r_{mix} \times C_{TA4}(t) \quad \text{(S4)}$$

ODEs for DIC:

$$\text{Box1: } \frac{dC_{DIC1}}{dt} = -r_{ex} \times C_{DIC1}(t) + r_{ex} \times C_{DIC3}(t) + r_{mix} \times C_{DIC2}(t) - r_{mix} \times C_{DIC1}(t) - r_{upw} \times \frac{v_2}{v_1} \times C_{DIC1}(t) + r_{upw} \times \frac{v_2}{v_1} \times C_2(t) - F_{CO2\,1} - \frac{PP(t)}{v_1} \quad \text{(S5)}$$

$$\text{Box2: } \frac{dC_{DIC2}}{dt} = \frac{F_{DICnat}}{v_2} + \frac{F_{DICweath}}{v_2} + r_{mix} \times \frac{v_1}{v_2} \times C_{DIC1}(t) - r_{mix} \times \frac{v_1}{v_2} \times C_{DIC2}(t) - r_{upw} \times C_{DIC2}(t) + r_{upw} \times C_{DIC4}(t) + \frac{r_{POC}(t) \times POC_2(t)}{v_2} \quad \text{(S6)}$$

$$\text{Box3: } \frac{dC_{DIC3}}{dt} = -r_{ex} \times \frac{v_3}{v_1} \times C_{DIC3}(t) + r_{ex} \times C_{DIC3}(t) + r_{mix} \times \frac{v_4}{v_3} \times C_{DIC2}(t) - r_{mix} \times \frac{v_4}{v_3} \times C_{DIC1}(t) - r_{upw} \times \frac{v_2}{v_1} \times C_{DIC1}(t) + r_{upw} \times \frac{v_2}{v_1} \times C_{DIC2}(t) - F_{CO2\,3} \quad \text{(S7)}$$

$$\text{Box4: } \frac{dC_{DIC4}}{dt} = r_{mix} \times C_{DIC3}(t) - r_{mix} \times C_{DIC4}(t) + \frac{r_{POC}(t) \times POC_4(t)}{v_4} \quad \text{(S8)}$$

ODEs for POC:

Box2: $\frac{dPOC_2}{dt} = -r_{POC}(t) \times POC_2(t) + (1 - r_r) \times PP_1(t)$ (S9)

Box4: $\frac{dPOC_4}{dt} = -r_{POC}(t) \times POC_4(t) + (1 - r_r) \times PP_3(t)$ (S10)

where v_1, v_2, v_3 and v_4 are the volumes of the four boxes, defined as 15 m^3, 10 m^3, 100 m^3 and 86 m^3, respectively.

ODEs for calcite/dunite in the four sediment layers (M_i)

Sediment surface: $\frac{dM_i}{dt} = -r_{MiDiss}(t) - k_{transp} \times M_i(t) + r_{Add}$ (S11)

Upper (0 – 3.33 cm): $\frac{dM_{iUp}}{dt} = -r_{MiDissSed}(t, z) - k_{transpSED} \times M_{iup}(t) + k_{transp} \times M_i(t)$ (S12)

Middle (3.33 – 6.66 cm): $\frac{dM_{iMid}}{dt} = -r_{MiDissSed}(t, z) - k_{transpSED} \times M_{iMid}(t) + k_{transpSED} \times M_{iup}(t)$ (S13)

Lower (6.66 – 10 cm): $\frac{dM_{iLow}}{dt} = -r_{MiDissSed}(t, z) - k_{transpSED} \times M_{iLow}(t) + k_{transpSED} \times M_{iMid}(t)$ (S14)

In the above equations, *t* is time in d and z (cm) is the average sediment depth of each box. $F_{TAweath}$ and $F_{DICweath}$ denote, respectively, the combined TA and DIC flux derived from calcite/dunite dissolution on and in the sediment. Numbered indices correspond to the individual boxes (Additional data figure 1).

S1.1.2Hydrological boundary conditions

To set up the model, certain assumptions concerning the hydrological properties were made. These include the parameterization of the water exchange between the different boxes and the implementation of quasi-upwelling induced by salty and dense waters invading and replacing the bottom water, which is difficult to assess with fixed box sizes. For this reason, the mixing rate between the boxes was kept very low during times where the water body is strongly stratified. The mixing rates ($r_{premix}(t)$, d^{-1}) were qualitatively estimated based on residence times and age of single water parcels in Eckernförde Bay determined using a 3-D model by Dietze and Löptien (2021). To simulate the bottom water pCO_2 values published by Melzner et al. (2013), the model additionally included a tuning parameter, leading to the vertical mixing rate r_{mix} (d^{-1}) defined as:

$$r_{mix} = k_{premix} \times r_{premix}(t) \quad \text{(S15)}$$

where k_{premix} (dimensionless) is a tuning parameter and $r_{premix}(t)$ is the qualitative estimate of mixing rates for each month. The mixing was subsequently assumed to be lower (factor 0.5) in the two large boxes, representing the adjacent Kiel Bight (Figure S1). This was done to account for the larger distance from the coast and to reduce recycling of water in the model.

Additionally, to reflect the quasi-upwelling, the water exchange with Kiel Bight ($r_{ex}(t)$ (d^{-1})) had to be adopted in a way that water exchange was only assumed between the surface boxes and that this exchange is higher during phases with strong stratification and low during phases with strong mixing. Subsequently, the overall upwelling regime was introduced via an upwelling term ($r_{upw}(d^{-1})$) that transports water from the deeper Kiel Bight into the deeper Eckernförde Bay, upwards to the surface, and then out of the system via the upper Kiel Bight. This upwelling term was defined as a function of the vertical mixing rate as:

$$r_{upw} = r_{upwind} + k_{upw} \times r_{mix} \quad \text{(S16)}$$

where r_{upwind} (d^{-1}) accounts for wind induced upwelling that was assumed to occur constantly throughout the year and k_{upw} is a dimensionless constant. In order to maintain conservation of mass, the amount of water in the deeper Kiel Bight was replaced with water that has the same properties as the deeper Kiel Bight. Box 4, therefore, serves to pre-form the upwelling bottom water entering the deep Eckernförde Bay box.

S1.1.3Geochemical forcing, boundary and initial conditions

The model considers that mineral transport into the sediment by bioturbation is a functions of bottom water oxygen levels. Dissolved O_2 concentrations were adapted from Melzner et al. (2013) and recalculated based on the observed temporal decrease reported by Lennartz et al. (2014) as:

$$O_2(t) = O_2(0) - t \times r_{oxy} \quad \text{(S17)}$$

where $O_2(t)$ is the oxygen concentration in bottom waters in µmol l^{-1}, $O_2(0)$ is the initial seasonal concentration in the first year of the model run (Melzner et al., 2013), reported in Table S2, *t* is the time in days and r_{oxy} is the daily decline (d^{-1}) based on Lennartz et al. (2014). Since the mineral addition experiment is assumed to start in 2024, the historical trend in oxygen decrease was imposed on 2024 values.

The increase in atmospheric CO_2 concentrations (Lan et al., 2024) was calculated as:

$$CO_2(t) = CO_2(0) + t \times r_{CO2} \quad \text{(S18)}$$

where $CO_2(t)$ is the CO_2 concentration in the atmosphere in µatm, $CO_2(0)$ is the CO_2 concentration at the start of the model run, and r_{CO2} is the daily increase in d^{-1}.

The natural benthic TA fluxes (F_{TAnat}, µmol cm^{-2} d^{-1}, Table S4) were taken as the average from the untreated benthocosm experiments. These fluxes were assumed to derive from natural calcite dissolution and iron sulfide formation at a ratio (rat_{TA} = dissolution : sufide formation) derived from Dale et al. (2024, in review).

Subsequently natural DIC (F_{DICnat}) fluxes (excluding remineralization) were calculated as:

$$F_{DICnat} = F_{TAnat} \times 0.5 \times rat_{TA} \quad \text{(S19)}$$

Note that for the model the measured values reported in Table 4S were transposed to mmol m^{-2}.

Primary production over the course of a year (PP(t), mol m^{-2} yr^{-1}) was inferred based on monthly chlorophyll *a* concentrations (Chl, µg L^{-1}) reported by Lennartz et al. (2014). Subsequently, these values were normalized by dividing by the sum of all values. Hence, the primary production was defined as

$$PP(t) = PP_a \times \frac{Chl}{\sum Chl} \quad \text{(S20)}$$

where PP_a is the annual mean primary production (mol m^{-2} yr^{-1}). This value was adapted in a way that the bottom water pCO_2 values corresponded to values reported by Melzner et al. (2013) and were further verified by comparison to values reported by Balzer (1984) (Table S1).

The model does not differentiate between PP and export production and assumes that exported particulate organic carbon (POC) equals PP. The POC degradation rate (r_{POC}, mmol m^2 d^{-1}) in the bottom water box was defined as:

$$r_{POC} = \left(1 - \frac{r_b}{100}\right) \times \frac{PP_a}{t_{POC}} \times rT \quad \text{(S21)}$$

t_{POC} is the residence time of POC in the sediment before burial at 10 cm depth defined as:

$$t_{POC} = \frac{10\ cm}{r_{sed}} \quad \text{(S22)}$$

where r_{sed} is the sedimentation rate in cm d^{-1} (Nittrouer et al., 1998; Whiticar, 2002). The amount of POC buried below 10 cm depth in the sediment (r_b, % of POC) was inferred from export production and carbon burial reported for Eckernförde Bay by Balzer (1984). rT is the temperature dependence of POC remineralization defined as:

$$rT_{POC} = e^{\frac{E_{ActPOC}}{R} \times \left(\frac{1}{T_{mean}} - \frac{1}{T_{down}}\right)} \quad \text{(S23)}$$

where E_{ActPOC} (J mol^{-1}) is the activation energy for POC degradation, R (J mol^{-1} K^{-1}) is the ideal gas constant, T_{down} (°C) is the bottom water temperature and T_{mean} (°C) is the mean bottom water temperature. Remineralized POC was assumed to directly contribute to DIC in bottom waters. For the Kiel Bight bottom water box, the residence time for POC was defined 10-fold lower as this box is supposed to reflect sandy sediments depleted in POC.

Initial conditions for POC, DIC and pCO_2 were derived by running the model into steady state with constant atmospheric pCO_2 and fixed TA. All model parameters are reported in Tables S1 and S2. Initial conditions are reported in Table S3.

S1.2 Transport of added materials through the sediment

The transport from the sediment surface to the upper sediment layer prior to mineral addition (0 - 3.33 cm) was defined as a first-order rate constant $r_{transp} = 0.07$ d^{-1}. Since the upper 3 cm are assumed to be well mixed, this implies that after 50 days, the material has reached a depth of 3.33 cm. Based on the residence time of the material in the entire upper 10 cm of sediment (equal to t_{POC}), the residence time of the added material in the lower two sediment boxes is 30 years minus 50 days. For simplicity reasons, the initial 50 days were ignored. Assuming negligible compaction and bioturbation in these deeper layers, the residence time (t_{res}) in each of the lower two boxes must be half as long as t_{POC}, 15 years. Furthermore, the assumption was made, that after 30 years, only 1% of the material remains in the sediment box from which it is transported downwards. Subsequently, the rate constant for the downward transport into deeper sediments ($r_{transSED}$, d^{-1}) was calculated as:

$$r_{transpSED} = \frac{\ln\left(\frac{C_{ini}}{C_{final}}\right)}{t_{res}} \quad \text{(S24)}$$

where C_{ini} is the initial concentration (100%) and C_{final} is the concentration after r_{res} (1%).

The burial of added material from the lower box into deeper sediment was then also defined by $r_{transpSed}$.

S1.3 Additional calculations

S1.3.1Calculation of calcite and dunite dissolution from the benthocosm experiments

The dissolution of calcite in the sediment was calculated from the TA fluxes measured during the benthocosm experiments as:

$$r_{calmeasured} = \frac{0.5 \times \Delta F_{TAmeasured}}{A_{BET}} \quad \text{(S25)}$$

Where $\Delta F_{TAmeasured}$ (µmol cm^{-2} d^{-1}) is the difference between the mean flux measured in the three calcite treated experiments and the mean TA flux measured in the control experiment for each time a sample was taken and A_{BET} is the BET surface of the used calcite material. 0.5 is a stoichiometric factor as per mol of calcite, 2 mol of alkalinity are released.
For dunite the procedure was similar. Instead of a stoichiometric factor of 0.25 a factor of 0.268795 was used, based on previous dissolution experiments (Fuhr et al., 2022), to account for the iron content in the used olivine material and subsequent loss of TA due to iron oxidation.
From these values and the measured temperature, the temperature dependences were defined as:

$$\mathrm{rT}_{Cal/Dun} = e^{\frac{E_{ActCal/Dun}}{R} \times \left(\frac{1}{T_{mean}} - \frac{1}{T_{down}}\right)} \quad \text{(S26)}$$

Where $E_{ActCal/Dun}$ (J) is the activation energy for calcite and dunite dissolution, respectively, R (J mol^{-1} K^{-1}) is the ideal gas constant, T_{mean} is the mean absolute temperature in bottom waters and T_{down} is the absolute temperature in bottom waters, both in °C. E_{actCal} was then chosen to achieve the best fit, and compared to literature values (Naviaux et al., 2019b; Rimstidt et al., 2012). Values used for these calculations as well as literature values are reported in Tables S4 – S7.

S1.4 Cost and efficiency calculations

S1.4.1Costs for transportation

Since the large scale spreading of rock powder by ships has not been undertaken to date, the assumptions transportation costs were adapted from inland shipping (Hofbauer and Putz, 2020).

S1.4.2Cost estimates for dunite production

The primary assumption was that dunite would be acquired from Sibelco™ and produced in their facilities in Åarheim, Norway, which is the closest available source of quarried dunite and one of the world's largest. Based on personal communication with Sibelco™, the CO_2 footprint of producing 1 mm grain size olivine is 2 kg/t (*CO_2baseDun*). Hence, energy costs and CO_2-footprints for production were not further considered. In a second step, the energy demand for grinding olivine to a defined grain size was calculated following Eq. 22, which is valid for the feed grain size of 1000 µm (Strefler et al., 2018). This energy in kWh was then translated into costs and CO_2 emissions based on the current energy price for industries and the current energy mix in Germany. The total CO_2 footprint per ton of dunite *CO_2totDun* was subsequently calculated as

$$CO_2totDun = E_{gr} \times r_{en} + CO_2baseDun + CO_2totTranspDun \quad \text{(S27)}$$

where E_{gr} is the energy for grinding in kWh, r_{en} is the CO_2 emission per kWh of electric energy, and $CO_2totTranspDun$ is the combined emission for transport of dunite (see section S1.3.4).
The base product price (*CostBaseDun*) was estimated as 30€/t based on pricing suggested by Strefler et al. (2018). Additionally, the price for electricity and transportation was considered leading to:

$$CostTotDun = E_{gr} \times c_{en} + CostBaseDun + CostTotTranspDun \quad \text{(S28)}$$

where *CostTotDun* is the final price per ton of dunite, c_{en} is price per kWh of electricity, and *CostTotTranspDun* are the total costs for transportation (see section S1.3.4). c_{en} was reported by the German Limestone Association (GLA) as 0.15 € kWh^{-1}. For r_{en}, a value of 380 g kWh^{-1} was assumed (Blizniukova et al., 2023). Results of these calculations are reported in Table S8.

S1.4.3Cost estimates for calcite production

The cost estimates for grinding and drying of calcite were provided directly by the German Limestone Association (GLA) and listed in Table S10. Additionally to those costs, 10 kWh for mining were accounted for with a CO emission of 2.538 kg kWh^{-1} (Hangx and Spiers, 2009). The base price for excavation, investment and maintenance as well as factory margins is 18.01 € t^{-1}.
The final costs and CO_2 emissions were then calculated by summing the respective values from production and transportation.

S1.4.4Estimates for transport

The costs for transport were based on the location of Sibelco™ in Åarheim, Norway for dunite, and in a near shore quarry in northern Germany for calcite, respectively. Precise values are provided in Table S9

S2 Supplementary Tables

Table S1: Constants used for the box model.

Term	Description	Value/formula	Reference
$k_{CalDIss}$	First-order reaction constant for calcite dissolution (mol cm^{-2} s^{-1})	For $\Omega_{Cal}<0.75$: $10^{-9.95}$ For $\Omega_{Cal}\geq0.75$: $10^{-12.106}$	Naviaux et al. (2019a)
$n_{CalDiss}$	Reaction order of calcite dissolution (-)	For $\Omega_{Cal}<0.75$: 4.09 For $\Omega_{Cal}\geq0.75$:1.92	Naviaux et al. (2019a)
k_{premix}	Dimensionless mixing rate parameter (-)	0.08	This study
r_{upwind}	Upwelling exchange factor (d^{-1})	0.005	This study
k_{upw}	Constant to define upwelling as a function of mixing (-)	0.1	This study
r_{ox}	Rate of bottom water oxygen decrease (yr^{-1})	1.14	Lennartz et al. (2014)
r_{CO2}	Rate of atmospheric CO_2 increase (yr^{-1})	2.4	Lan et al. (2024)
rat_{TA}	Ratio for TA flux from natural calcite dissolution (-)	0.4	Dale et al. (2024, under review)
PP_a	Annual primary production (mol m^{-2} yr^{-1})	Box1: 4.8 Box3: 3.9	Fitted to bottom water pCO_2 Based on Balzer (1984): 3.3
r_b	Burial rate for POC (% of primary production)	17.5	Balzer (1984)
r_{sed}	Sedimentation rate (cm yr^{-1})	0.33	Nittrouer et al. (1998), Whiticar (2002)
E_{ActPOC}	Activation energy for POC degradation (J mol^{-1})	70000	Robador et al. (2016)
T_{mean}	Mean bottom water temperature (°C)	7.54	Melzner et al. (2013)
R	Ideal gas constant (J K^{-1} mol^{-1})	8.314	-
E_{ActCal}	Activation energy for calcite degradation (J mol^{-1})	58500	This study (best fit) Naviaux et al. (2019b): 25000
E_{ActDun}	Activation energy for dunite degradation (J mol^{-1})	98500	This study (best fit) Rimstidt et al. (2012): 66400

Table S2: Time-dependent model parameters for both upper (x_{up}) and lower(x_{down}). For daily resolution, these values were interpolated linearly and repeated each year, except for oxygen (see section S1.1.2)

Time (d)	T_{up} (°C)	T_{down} (°C)	Sal_{up} (-)	Sal_{down} (-)	Chl *a* $\mu g\ L^{-1}$	O_2 $\mu mol\ l^{-1}$	u_{10m} $m\ s^{-1}$	r_{premix} d^{-1}	r_{ex} d^{-1}
0	15	8	15	22.3	3.00	48	8.85	0.003	0.5
31	19	10	16	22.7	3.50	19	8.86	0.003	0.4
62	15	12	17	22.7	4.30	17	7.94	0.003	0.3
92	12	12.5	18	22.1	5.00	80	7.00	0.005	0.05
123	9.5	9.5	19	22	5.80	170	6.77	0.09	0.001
153	5	7	19.5	21	4.50	240	6.52	0.6	0.05
184	4.5	5	19	20.5	5.00	270	6.68		0.05
215	4.5	4.5	18.5	20.3	6.00	320	6.77	0.99	0.05
243	4.7	4.5	17.5	20	10.00	322	7.38	0.6	0.075
274	5.6	4.7	16.2	20.2	5.30	250	8.40	0.2	0.1
304	10	5.2	15	20.2	2.50	180	8.60	0.02	0.21
335	13	7.2	14	21	3.00	121	8.91	0.12	0.35
365	15	8	15	22.3	3.00	48	8.85	0.003	0.5

Table S3: Initial conditions from which all other model variables were calculated.

Box	DIC (mmol kg^{-1})	TA (mmol kg^{-1})	POC (mmol m^{-2})	PIC (mmol m^{-2})
1	1.742	1.847	-	-
2	1.842	1.847	29.1416	0
3	1.742	1.847	-	-
4	18.42	1.847	0.637065	0

Table S4: TA fluxes (F_{TAnat}) measured during the benthocosm experiments in µmol cm^{-2} d^{-1}. C (1-3) refers to the control experiment. Cal (1-3) refers to calcite addition and Dun (1-3) to dunite addition.

Time (d)	C1	C2	C3	Cal1	Cal2	Cal3	Dun1	Dun2	Dun3
0	0.6	0.6	0.6	0.6	0.6	0.6	0.6	0.0	0.6
15	0.0	0.6	1.2	2.5	3.7	2.5	1.9	1.9	1.2
77	0.0	0.0	0.0	1.2	1.9	1.2	0.6	0.6	0.6
133	0.0	0.0	0.0	0.6	1.9	0.6	0.0	0.0	0.0
183	0.0	0.0	0.0	1.2	1.2	1.9	0.0	0.0	0.0
224	0.0	0.0	0.0	1.9	2.5	1.9	0.6	0.0	1.2
283	0.0	0.6	0.6	1.2	1.9	1.2	0.6	1.9	1.2
345	1.9	0.0	0.0	2.5	1.9	1.2	0.6	0.6	1.2

Table S5: Bottom water oxygen concentrations in µmol l^{-1} and temperature in °C measured during the benthocosm experiments.

Time (d)	Temperature	C1	C2	C3	Cal1	Cal2	Cal3	Dun1	Dun2	Dun3
0	16.4	261	261	259	204	200	221	224	221	227
77	5.7	245	242	236	237	246	219	238	171	168
133	4.7	230	244	233	230	254	237	250	263	238
183	4.7	235	281	270	277	270	262	269	266	260
224	9.5	195	209	214	204	257	265	246	234	240
283	16.6	88	93	109	88	121	71	69	85	81
345	18.0	88	42	49	42	81	94	99	114	114

Table S6: pH values (total scale) measured in bottom waters during the benthocosm experiments.

Time (d)	C1	C2	C3	Cal1	Cal2	Cal3	Dun1	Dun2	Dun3
0	8.01	8.02	8.05	7.96	7.94	8.04	8.09	8.06	8.06
77	7.87	7.89	7.98	7.98	7.96	7.93	7.94	8.00	7.99
133	7.82	7.88	7.87	7.87	7.83	7.89	7.87	7.87	7.98
183	7.96	7.91	7.94	7.86	7.95	7.93	7.89	7.87	7.83
224	7.47	7.52	7.35	7.61	7.85	7.73	7.48	7.58	7.66
283	7.42	7.45	7.34	7.36	7.26	7.32	7.33	7.33	7.37
345	7.28	7.33	7.31	7.43	7.29	7.39	7.39	7.50	7.40

Table S7: Bottom water calcium concentrations in mmol l^{-1} measured during the benthocosm experiment.

Time (d)	C1	C2	C3	Cal1	Cal2	Cal3	Dun1	Dun2	Dun3
0	4.5	4.4	4.4	4.4	4.5	4.5	4.4	4.4	4.5
15	5.6	5.6	5.6	5.6	5.6	5.6	5.6	5.6	5.7
77	6.2	6.2	6.2	6.2	6.2	6.2	6.1	6.1	6.2
133	6.6	6.6	6.6	6.6	6.6	6.6	6.6	6.5	6.6
183	6.3	6.3	6.3	6.3	6.4	6.3	6.3	6.2	6.3
224	5.1	5.1	5.1	5.1	5.1	5.1	5.1	5.1	5.1
283	5.4	5.3	5.4	5.4	5.4	5.9	5.9	5.9	6.0
345	6.6	6.6	6.6	6.6	6.6	6.5	6.6	6.6	6.6

Table S8: Cost and emission calculations for dunite. Final costs and CO_2 emissions include base price and emissions as well as costs and emissions from grinding and transportation.

A_{GEO} $cm^2\ g^{-1}$	Grain size (µm)	E_{gr} (GJ t^{-1})	E_{gr} (kWh t^{-1})	Costs (grinding) (€ t^{-1})	CO_2 (grinding) (kg t^{-1})	Final costs (€ t^{-1})	Final CO_2 (kg t^{-1})
1098.1	29.4	0.13	36.1	5.4	13.8	45.2	30.4
2196.2	14.7	0.29	80.8	12.1	30.8	51.9	47.4
3294.3	9.8	0.47	129.5	19.4	49.3	59.2	65.9
4392.3	7.4	0.65	180.9	27.1	68.9	66.9	85.5
5490.4	5.9	0.84	234.4	35.2	89.3	74.9	105.9
6588.5	4.9	1.04	289.7	43.5	110.3	83.2	126.9

Table S9: Cost and emission calculations for transport.

Transport	CO_2 (kg km^{-1} t^{-1})	Reference	Costs (€ km^{-1} t^{-1})	Reference	Distance (km)		CO_2 (Transport) (kg t^{-1})		Costs (Transport) (€ t^{-1})	
					Dun	Cal	Dun	Cal	Dun	Cal
Bulk carrier	0.007	Renforth (2012)	0.005	Renforth (2012)	1400	0	9.8	0	7.00	0
Rail	0.022	Renforth (2012)	0.083	GLA*	0	50	0	1.1	0	4.15
Inland ship	0.032	Renforth (2012)	0.0183	Hofbauer & Putz (2020)	150	150	4.8	4.65	2.745	2.745
						Total:	**14.6**	**5.75**	**9.75**	**6.90**

*German Limestone Association

Table S10: Cost and emission calculations for calcite. Final costs and CO_2 emissions include base price and emissions as well as costs and emissions from transportation.

A_{BET} cm^2 g^{-1}	Grain size (µm)	Drying (kWh t^{-1})	Grinding (kWh t^{-1})	Costs (electr.) (€ t^{-1})	CO2 (electr.) (kg t^{-1})	Final costs (€ t^{-1})	Final CO_2 (kg t^{-1})
5000	29.4	40.0	10.5	7.6	19.2	32.5	44.5
10000	14.7	40.0	25.2	9.8	24.8	34.7	50.1
15000	9.8	40.0	34.0	11.1	28.2	36.0	53.4
20000	7.4	40.0	40.0	12.0	30.4	36.9	55.7
25000	5.9	40.0	44.3	12.6	32.1	37.5	57.3
30000	4.9	40.0	47.5	13.1	33.3	38.0	58.6

Table S11: Overview of treatments in the benthocosm experiment.

Experiment	Cal (1-3)	Dun (1-3)	C (1-3)
Addition (g cm^{-2})	0.22	0.36	-
A_{BET} (m^2 cm^{-2})	1.82	-	-
A_{GEO} (m^2 cm^{-2})	0.400	0.699	-
Grain size	D_{50} = 19.39	D_{50} = 5.85	-

Table S12: Pore water calcium concentrations in mmol l^{-1} measured at the beginning of the benthocosm experiments. Depth 0 cm denotes bottom water concentration. (-) denotes depths where no sample could be taken.

Depth (cm)	C1	C2	C3	Cal1	Cal2	Cal3	Dun1	Dun2	Dun3
0	4.44	4.43	4.42	4.39	4.41	4.39	4.40	4.40	4.39
0.5	4.45	4.43	4.44	4.42	4.42	4.39	4.38	4.40	4.38
1.5	4.44	4.42	4.50	4.42	4.47	4.41	4.41	4.41	4.41
2.5	4.45	4.46	4.58	4.55	4.61	4.42	4.53	4.46	4.42
3.5	-	4.64	5.19	4.67	4.70	4.59	4.45	4.58	4.77
5.5	4.54	4.79	5.32	4.74	5.12	4.85	5.27	4.60	5.55
7.5	4.48	5.07	5.84	4.95	5.54	-	5.81	5.40	5.74

Table S13: Pore water TA concentrations in mmol l^{-1} measured at the beginning of the benthocosm experiments. Depth 0 cm denotes bottom water concentration. (-) denotes depths where no sample could be taken.

Depth (cm)	C1	C2	C3	Cal1	Cal2	Cal3	Dun1	Dun2	Dun3
0	1.90	1.94	1.92	1.90	1.92	1.86	1.88	1.98	1.90
0.5	1.98	1.86	1.86	1.86	2.06	2.00	1.90	1.88	1.98
1.5	2.08	1.96	2.31	1.98	2.17	2.06	1.96	2.06	2.00
2.5	2.08	2.04	2.56	2.86	2.63	2.33	2.75	2.27	2.19
3.5	-	2.54	5.09	3.55	2.88	3.07	2.11	2.69	4.05
5.5	2.17	2.67	6.90	3.96	4.40	3.48	5.44	2.71	6.26
7.5	2.29	3.17	14.60	4.65	6.48	-	7.92	-	6.96

Table S14: $Diss_{pot}$ values (cm) calculated based on the pH profiles obtained during the benthocosm experiments.

Time (d)	C1	C2	C3	Cal1	Cal2	Cal3	Dun1	Dun2	Dun3
0	3.0	1.8	1.3	2.4	2.9	1.8	1.4	2.6	0.8
77	1.7	1.5	0.4	0.3	1.6	0.1	0.8	0.1	0.2
133	1.6	3.1	1.8	1.5	2.5	0.2	1.2	0.5	1.2
183	0.1	0.3	0.2	0.6	0.7	0.0	0.3	0.5	0.2
224	2.5	3.3	2.8	2.3	1.5	0.1	3.0	1.1	1.6
283	0.1	0.1	0.4	0.4	0.7	0.3	0.7	0.5	0.4
345	2.5	2.4	0.7	0.1	1.7	0.1	0.2	0.0	0.7

S3 Supplementary figures

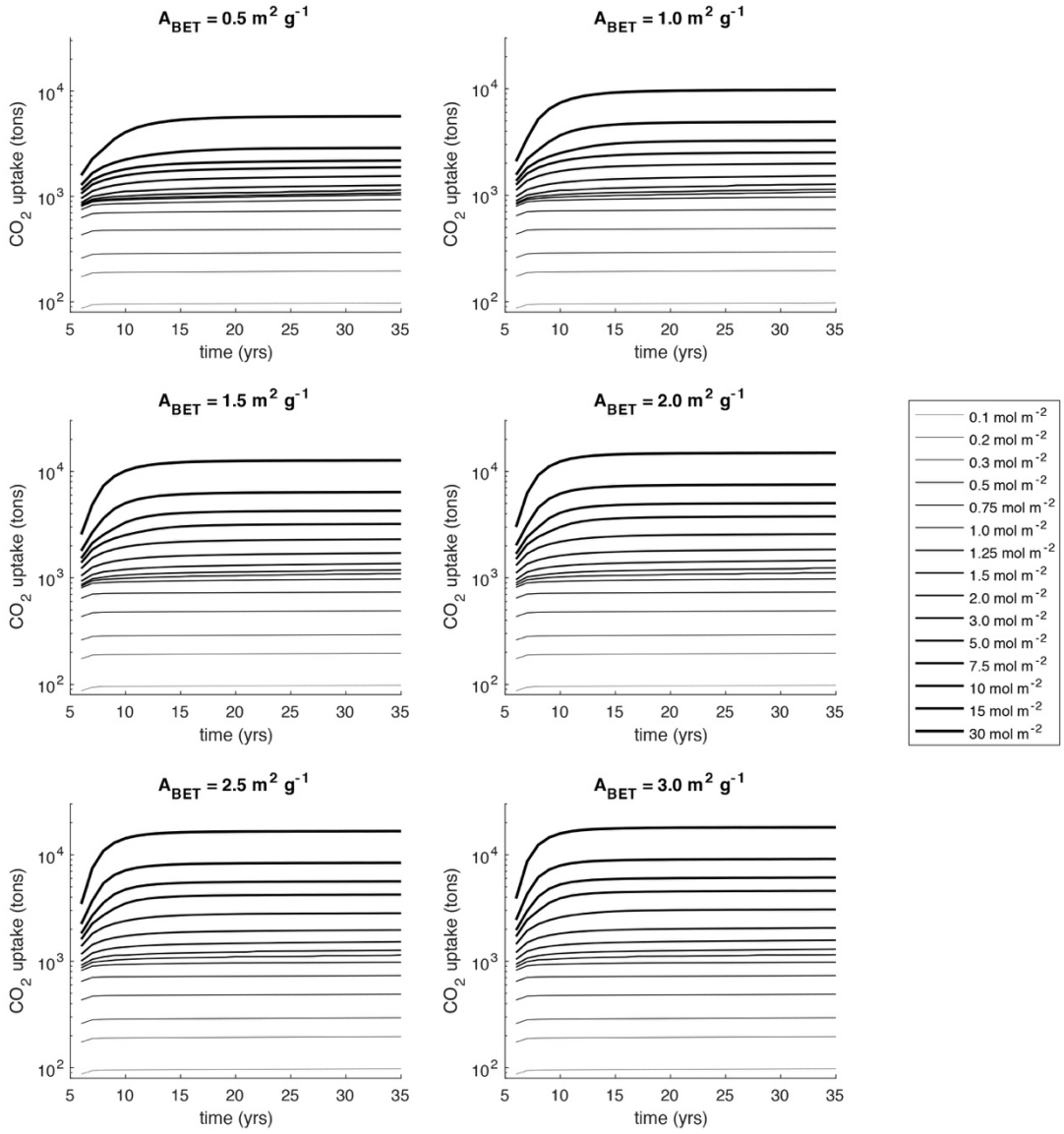

Figure S1: Additional CO_2 uptake for all BET surfaces and calcite addition scenarios over the entire modelling period. Thickness of lines represents the amount of added material.

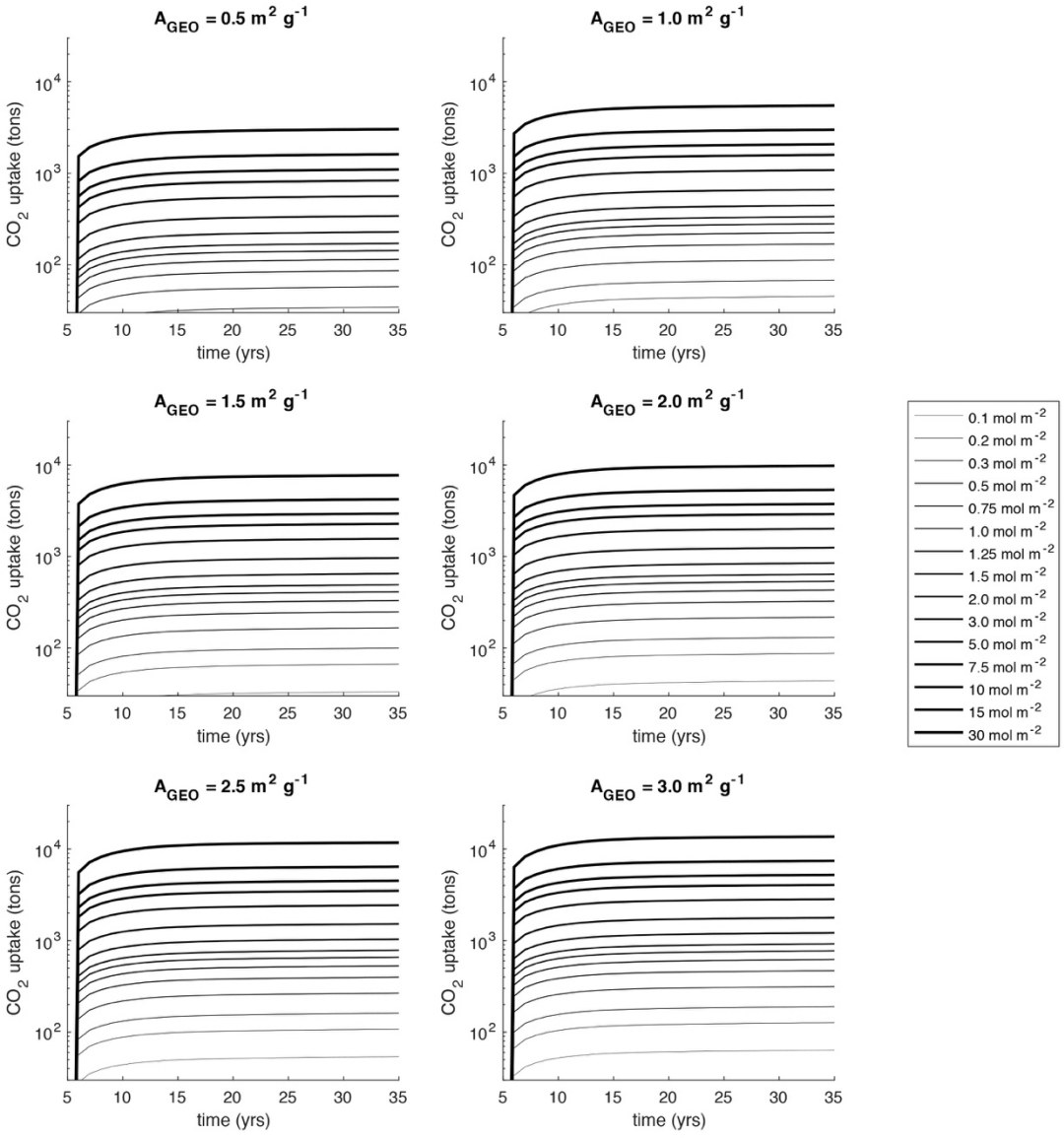

Figure S2: Additional CO_2 uptake for all geometrical surfaces and dunite addition scenarios over the entire modelling period. Thickness of lines represents the amount of added material.

Supplementary references

Balzer, W., 1984. Organic matter degradation and biogenic element cycling in a nearshore sediment (Kiel Bight)1. Limnol. Oceanogr. 29, 1231–1246. https://doi.org/https://doi.org/10.4319/lo.1984.29.6.1231

Blizniukova, D., Holzapfel, P., Unnewehr, J.F., Bach, V., Finkbeiner, M., 2023. Increasing temporal resolution in greenhouse gas accounting of electricity consumption divided into Scopes 2 and 3: case study of Germany. Int. J. Life Cycle Assess. 28, 1622–1639. https://doi.org/10.1007/s11367-023-02240-3

Dietze, H., Löptien, U., 2021. Retracing Hypoxia in Eckernförde Bight (Baltic Sea). Biogeosciences Discuss. 2021, 1–42. https://doi.org/10.5194/bg-2021-31

Fuhr, M., Geilert, S., Schmidt, M., Liebetrau, V., Vogt, C., Ledwig, B., Wallmann, K., 2022. Kinetics of Olivine Weathering in Seawater: An Experimental Study. Front. Clim. 4:831587. https://doi.org/10.3389/fclim.2022.831587

Fuhr, M., Wallmann, K., Dale, A.W., Diercks, I., Kalapurakkal, H.T., Schmidt, M., Sommer, S., Böhnke, S., Perner, M., Geilert, S., 2023. Disentangling artificial and natural benthic weathering in organic rich Baltic Sea sediments. Front. Clim. https://doi.org/10.3389/fclim.2023.1245580

Hangx, S.J.T., Spiers, C.J., 2009. Coastal spreading of olivine to control atmospheric CO2 concentrations: A critical analysis of viability. Int. J. Greenh. Gas Control 3, 757–767. https://doi.org/10.1016/j.ijggc.2009.07.001

Hofbauer, F., Putz, L.-M., 2020. External Costs in Inland Waterway Transport: An Analysis of External Cost Categories and Calculation Methods. Sustainability. https://doi.org/10.3390/su12145874

Lan, X., Tans, P., Thoning, K.W., 2024. Trends in globally-averaged CO2 determined from NOAA Global Monitoring Laboratory measurements. Version 2024-03. https://doi.org/10.15138/9N0H-ZH07

Lennartz, S.T., Lehmann, A., Herrford, J., Malien, F., Hansen, H.-P., Biester, H., Bange, H.W., 2014. Long-term trends at the Boknis Eck time series station (Baltic Sea), 1957–2013: does climate change counteract the decline in eutrophication? Biogeosciences 11, 6323–6339. https://doi.org/10.5194/bg-11-6323-2014

Melzner, F., Thomsen, J., Koeve, W., Oschlies, A., Gutowska, M.A., Bange, H.W., Hansen, H.P., Körtzinger, A., 2013. Future ocean acidification will be amplified by hypoxia in coastal habitats. Mar. Biol. 160, 1875–1888. https://doi.org/10.1007/s00227-012-1954-1

Naviaux, J.D., Subhas, A. V, Dong, S., Rollins, N.E., Liu, X., Byrne, R.H., Berelson, W.M., Adkins, J.F., 2019a. Calcite dissolution rates in seawater: Lab vs. in-situ measurements and inhibition by organic matter. Mar. Chem. 215, 103684. https://doi.org/https://doi.org/10.1016/j.marchem.2019.103684

Naviaux, J.D., Subhas, A. V, Rollins, N.E., Dong, S., Berelson, W.M., Adkins, J.F., 2019b. Temperature dependence of calcite dissolution kinetics in seawater. Geochim. Cosmochim. Acta 246, 363–384. https://doi.org/https://doi.org/10.1016/j.gca.2018.11.037

Nittrouer, C.A., Lopez, G.R., Donelson Wright, L., Bentley, S.J., D'Andrea, A.F., Friedrichs, C.T., Craig, N.I., Sommerfield, C.K., 1998. Oceanographic processes and the preservation of sedimentary structure in Eckernförde Bay, Baltic Sea. Cont. Shelf Res. 18, 1689–1714. https://doi.org/https://doi.org/10.1016/S0278-4343(98)00054-5

Renforth, P., 2012. The potential of enhanced weathering in the UK. Int. J. Greenh. Gas Control 10, 229–243. https://doi.org/https://doi.org/10.1016/j.ijggc.2012.06.011

Rimstidt, J.D., Brantley, S.L., Olsen, A.A., 2012. Systematic review of forsterite dissolution rate data. Geochim. Cosmochim. Acta 99, 159–178. https://doi.org/10.1016/j.gca.2012.09.019

Robador, A., Müller, A.L., Sawicka, J.E., Berry, D., Hubert, C.R.J., Loy, A., Jørgensen, B.B., Brüchert, V., 2016. Activity and community structures of sulfate-reducing microorganisms in polar, temperate and tropical marine sediments. ISME J. 10, 796–809. https://doi.org/10.1038/ismej.2015.157

Strefler, J., Amann, T., Bauer, N., Kriegler, E., Hartmann, J., 2018. Potential and costs of carbon dioxide removal by enhanced weathering of rocks. Environ. Res. Lett. 13. https://doi.org/10.1088/1748-9326/aaa9c4

Whiticar, M.J., 2002. Diagenetic relationships of methanogenesis, nutrients, acoustic turbidity, pockmarks and freshwater seepages in Eckernförde Bay. Mar. Geol. 182, 29–53. https://doi.org/https://doi.org/10.1016/S0025-3227(01)00227-4

Acknowledgements

First and most of all, I want to thank Klaus Wallmann for giving me the great opportunity to work on these experiments and write this thesis. Thanks for your guidance, the time you took, whenever I needed anything and for teaching me how to play Candy Crush!

Secondly, I want to thank Andy W. Dale. Working with you was the greatest pleasure. Thanks for sharing your experience and knowledge and of course for all the poker money!

A massive "Thank you!!" goes to the entire lab team!! Anke, Bettina, Regina and Alex, you guys are doing such a great job providing everyone with everything they ever needed! Special thanks to Anke for always having a cheerful word and being my Lab-Mummy

And finally, I want to thank Mareike Steinmetzer for all the support during the last three years. I owe you, big time!